Discovery and Morphology of Complex Molecules toward Interstellar Molecular Clouds

Ci Xue
Haikou, Hainan

B.Sc. Biotechnology, Xiamen University, 2015

A Dissertation Presented to the
Graduate Faculty of the
University of Virginia
in Candidacy for the Degree of
Doctor of Philosophy

Department of Chemistry

University of Virginia
December 2021

Committee Members:
Eric Herbst
Anthony J. Remijan
Robin T. Garrod
Brooks H. Pate
Al Wootten
Zhi-Yun Li

Abstract

Up to now, more than 250 individual molecular species have been detected toward both interstellar and circumstellar mediums with astronomical facilities. This dissertation presented two cases of investigations focusing on the chemical composition as well as the molecular spatial distributions of complex astronomical molecules in interstellar clouds, the chemistry in which sets the initial conditions of the chemical processes in the late stages of star formation.

We leveraged the GOTHAM high-sensitivity and high-spectral-resolution survey as well as cutting edge spectral line stacking and match filtering techniques to conduct molecular census towards the Taurus molecular cloud-1 (TMC-1). TMC-1 is a prototypical object of study in the quest for an understanding of dark cloud chemistry. The large observational program GOTHAM (Green Bank Telescope Observations of TMC-1: Hunting for Aromatic Molecules) is undertaking a radio survey with a combined observation time of ~850 hours directed toward TMC-1. The GOTHAM project has provided extremely sensitive data at a sensitivity of 2 mK and a spectral resolution of $0.05\,\mathrm{km\,s^{-1}}$, which is essential for searching complex interstellar molecules. Our work has led to the first astronomical detections of numerous new complex molecules and greatly expanded the molecular inventory in the interstellar medium. Of the newly

detected species, this dissertation specifically presents the discoveries of two unsaturated carbon-chain molecules, isocyanodiacetylene (HC_4NC) and thiopropadienone (H_2C_3S) in space. These studies provided new mechanistic insights into CN-vs-NC chemistry as well as the sulfur evolution under dark-cloud conditions.

An innovation of this dissertation is the development of a quantitative data-filtering method for molecular line identification and multiple-transition imaging to represent the intrinsic spatial distribution of a molecule. Guided by these methods, the morphological investigations of terrestrial-type molecules were composed of three projects directed toward two massive molecular clouds, namely Sagittarius (Sgr) B2 and NGC 6334I. Sgr B2(N) is the richest known source for molecular detections and has contributed to 69 new interstellar molecules, (27%) of the interstellar molecular census. The first project revealed the spatial differentiation of the $C_2H_4O_2$ isomers towards Sgr B2(N), which demonstrated the distinct morphology can help to constrain the formation mechanisms and the chemical relations of the isomeric molecules. The second project, focusing on precisely locating the emission region of acetic acid with a wide range of excitation energy toward NGC 6334I, uncovered the dependence of the molecular emission peak positions on the excitation levels and brought to light the potential unresolved sub-structures of the source. In synergies with VLA observations, the last project performed a multi-wavelength investigation for the origin, distribution, relationships of molecular masers toward Sgr B2(N).

Acknowledgements

A unifying goal of my research is to spend my whole efforts, though a drop in the ocean, to understand one of the most fundamental scientific questions, the origin of life. My scientific voyage started with Biology, where the rare microbes surviving in extreme environments - and even in space - broadened my mindset and made me open to not only the potential existence of extraterrestrial life but also the possibility of the cosmic origins of life. Astrochemistry has since become a passion of mine along with Biology. Leaping from Biology, my journey in Astrochemistry would not have been even possible without the appearances of the following wonderful people in my life.

I wish to firstly express my sincerest gratitude to my graduate advisors, Eric Herbst and Anthony (Tony) Remijan, for their instruction, patience, and care. In 2020, I was stuck in China due to the Covid-19 pandemic and had to stay in the third country in order to fly back to the US. Eric and Tony supported me with the expense of the entire trip. Their care and concern for my safety along the trip were the best comforts for me on those rough days. However, it would not have happened without the email sent to Eric back in 2016. Without Eric's help, I would not have had the opportunity to pursue my Ph.D. studies at UVa, and he always patiently

edit my writing. Tony is the greatest ever advocate for my work, and he might never understand how much I appreciate his support. He provided me with all the security to worry about nothing but devote myself to astrochemical research; it was a luxury for me. He warned me from staying too long in the rabbit holes but still gave me the freedom to explore the holes. I have had the honor of being the Secretary of Defense of the "Kingdom of Remijanistan".

In addition, I wish to express my gratitude to my undergraduate mentor in Astronomy, Taotao Fang. Taotao is my first astronomer contact who firmly support my transfer from Biology to Astronomy. The printed copies of all my literature reading assignments that Taotao provided, in total ~ 30 cm thick, not only laid the foundation for my scientific research ability but also cultivated my old-school habit of reading hard-copy literature.

I would like to thank my committee, Robin Garrod, Brooks Pate, Zhi-Yun Li, and Al Wootten, for their insightful questions and comments that pinpointed the essence of my work. I was touched by the seriousness with which they approached my dissertation and the amount of attention they paid to details, much more than what I ever had and expected. I believe that the discussion I had with them will be one of the most delightful ones I have ever had.

I wish to thank my academic colleagues, especially Brett McGuire, Ryan Loomis, Emmanuel Momjian, Todd R. Hunter, Crystal Brogan, and Romane Le Gal, for all the inspiring discussion and their generous help with all my naïve questions. Brett has fascinated me with his enthusiasm, expertise, and inventiveness in Astrochemistry. I am always impressed by the breadth and depth of Ryan's scientific knowledge, and he always provides the most insightful advice and comments. I would also like to thank my group members, Andrew Burkhardt, Christopher Shingledecker, Alec Paulive, Jessica Tennis, Mark Siebert, Joshua Carder, Haley Scolati, and Weikai Cui, for their

help and the good times.

I wish to next thank my friends, especially Chen Tian, Yumeng Wen, Yiqing Song, Allison Costa, and Molly Finn. Chen is my biggest cheerleader; she has encouraged me countless times as well as shared the smile, tears, and every bit of life as a Ph.D. student. Yumeng has been my life coach since I was a teenager; her maturity and calmness of mind are beyond our years and I have benefited from her sage advice on life. I am lucky to share an office with Yiqing and she has been always willing to lent me the office keys, even at the night right before my defense. Without Allie and Molly, I would not be exposed to the beautiful city of Santa Fe and the fantastic musical Hamilton on our trip to New Mexico.

These thanks extend to my family, my parents and Didi, for their constant love and unwavering support. Didi's sparkling eyes as well as his furry body have calmed and healed my emotions over the past five and half years.

Finally but most importantly, I would like to express my deep gratitude to my lover and my closest friend, Ka Ho Lam. He always unconditionally support me, from preparing foods to debugging my codes, from driving me to all the places to editing my manuscripts, from listening to all my complaint to teaching me physics and statistics. He has been very picky about all the formatting of my work, yet it in turn shaped my coding habits and led to my highly rigid formatting style. His company is the most indispensable part of my graduate life. There are never enough times for me to express my thanks to him.

Table of Contents

List of Figures

List of Tables

Part I

Introduction

Chapter 1

Introduction

Up to now, more than 250 individual molecular species have been detected toward both interstellar and circumstellar medium (ISM and CSM) with astronomical facilities (McGuire, 2021, and The Astrochymist[1]), for which single-dish telescopes working at radio wavelength have contributed to ~80% of the discoveries. In the past, searches for interstellar molecules were targeted toward narrow astronomical regions around certain laboratory-measured transitions of specific molecules (Ziurys et al., 1984; Millar et al., 1987; Combes & Wiklind, 1995). In addition to the observations of individual spectral lines, the improvements in receiver technology have enabled us to efficiently perform wide-band and high-sensitive molecular line surveys. The first spectral survey was targeted at the most chemically-rich molecular cloud, Sagittarius B2 (Sgr B2), at the Galactic center with a bandwidth of 72 GHz but took 600 hours over 5 years to complete (Cummins et al., 1986). As a comparison, modern facilities require less than five minutes to reach the same sensitivity with the same bandwidth. Until recently, molecular line surveys have been expanded to various astronomical sources ranging from dark clouds (Kaifu et al., 2004; McGuire

[1] `http://astrochymist.org/astrochymist_ism.html`

et al., 2020), star-forming regions (Neill et al., 2012; Belloche et al., 2019), young stellar objects (Jørgensen et al., 2016; Bianchi et al., 2020), stellar envelopes of evolved stars (Kawaguchi et al., 1995; Tenenbaum et al., 2010; Cernicharo et al., 2019), to proto-planetary nebulae (Fontani et al., 2017).

The diverse astronomical environment serves as unique laboratories for investigating molecular behaviors and chemical evolution under extreme extraterritorial conditions. Leveraging with astronomical observations constraining molecular abundances, theoretical and experimental approaches are employed to examine the formation mechanisms of interstellar molecules. We concentrate in the following on two types of the richest sources for molecular detections: prestellar dark clouds as well as protostellar hot cores. Dark clouds prior to star formation represent a dense and cold environment with typical temperatures of 10 K and densities of $10^4 - 10^5\,\mathrm{cm}^{-3}$ (van Dishoeck, 2018). The chemical signatures of dark clouds include gas-phase dominated chemistry and abundant unsaturated carbon-chain molecules with up to 11 carbon atoms ($HC_{11}N$, Loomis et al., 2021). For ~80% of the detected molecules in dark clouds, gas-phase astrochemical models utilizing rate equations in combination with appropriate reaction networks (e.g. Wakelam et al., 2012; McElroy et al., 2013) demonstrated an order of magnitude agreement or better with the observations (Hincelin et al., 2011; Loison et al., 2014b; Ruaud et al., 2016; Burkhardt et al., 2018). In contrast, protostar-forming hot cores have typical temperatures of $100 - 300\,\mathrm{K}$ and densities of $>10^7\,\mathrm{cm}^{-3}$ (Williams & Viti, 2014) and exhibit astonishingly dense gas-phase molecular spectra at millimeter (Blake et al., 1987; Lee et al., 2001; Belloche et al., 2013). Unlike the unsaturated molecules found in dark clouds, saturated terrestrial-type molecules prevail in hot cores while reaching thermal equilibrium (Herbst & van Dishoeck, 2009).

Astrochemical observations not only discover new molecular species and reveal

the diverse chemistry in astronomical environments, but they also provide probes to characterize the physical properties of the gas and dust where molecules reside. The advent of interferometer technologies drives the field of astrochemistry further forward. With the improved capabilities of resolving the molecular emission regions, high-resolution interferometric line images provides crucial spatial information to pinpoint the physical conditions, such as kinetic motions and temperatures, of such regions. For example, HCO^+ is a molecular tracer of infall motions caused by gravitational collapse (Morata et al., 2005; Contreras et al., 2018) whereas H_2S and SiO trace bipolar out-flows (Hatchell et al., 2001; Gibb et al., 2004; Feng et al., 2016; Lu et al., 2021). In addition, NH_3 and HCN-to-HNC ratios are sensitive to kinetic temperatures, making them good chemical thermometers (Friesen et al., 2009; Hacar et al., 2020).

1.1 Molecular Assignment

The assignment of an interstellar molecule is facilitated by the availability of spectroscopic databases for molecular rotational transitions. The databases still being maintained include the Cologne Database for Molecular Spectroscopy (CDMS, `http://www.astro.uni-koeln.de/site/vorhersagen/`), the Jet Propulsion Laboratory (JPL) molecular spectroscopy catalog (`https://spec.jpl.nasa.gov`), and the Splatalogue database (`https://splatalogue.online/index.php`). In addition to inheriting data from the JPL and CDMS catalogs, the Splatalogue database also contains data from the Spectral Line Atlas of Interstellar Molecules (SLAIM), a compilation of spectroscopic analysis of detected molecules performed by F. J. Lovas [2]. Despite the great contribution from those databases, they still tend to be incomplete in terms of limited frequency coverages, hyperfine structures, and vibrational

[2] `https://www.nist.gov/people/francis-j-lovas`

excited states. Individually reported laboratory measurements dedicated to specific molecules have also contributed to the searching campaign of astronomical molecules (e.g., Ilyushin et al., 2013; Maris et al., 2019; Chitarra et al., 2020; McCarthy et al., 2021; Zou et al., 2021).

With the knowledge of spectroscopic properties of a target molecule (e.g., transition frequencies and line strengths) and telescope characteristics (e.g., dish size and efficiency), we can simulate a molecular spectral emission which can be compared directly with observations. In the radio regime, observed spectra are often dominated by rotational emission of interstellar molecules that are excited by collisions with other molecules or by radiation. The strength of rotational emission can be calculated as the following (see also Mangum & Shirley, 2015). For a single excitation temperature $T_{\rm ex}$, assuming a Gaussian line profile $\phi(\nu; \nu_0, \Delta V)$ with a FWHM ΔV, a transition at a frequency ν_0 with upper state energy $E_{\rm u}$ and upper state degeneracy $g_{\rm u}$ would have a peak optical depth

$$\tau_0 = \sqrt{\frac{4\ln 2}{\pi}} \frac{A_{ij}\, c^3\, N_{\rm T}\, g_{\rm u}\, {\rm e}^{-\frac{E_{\rm u}}{T_{\rm ex}}} \left({\rm e}^{\frac{h\nu_0}{kT_{\rm ex}}} - 1\right)}{8\pi\, \nu^3\, \Delta V\, Q(T_{\rm ex})}, \tag{1.1}$$

where A_{ij} is the spontaneous emission coefficient, $N_{\rm T}$ is the molecular column density, and $Q(T)$ is the partition function. For a background temperature $T_{\rm bg}$, the background specific intensity is simply $I_{\rm bg}(\nu) = B_\nu(T_{\rm bg})$, where $B_\nu(T)$ is the Planck function. Considering the optical depth $\tau = \tau_0\, \phi(\nu; \nu_0, \Delta V)$, antenna efficiency η, emission source size ss^2 and telescope's beam size Ω, the specific intensity with background subtracted is

$$I_\nu = \left(B_\nu(T_{\rm ex}) - B_\nu(T_{\rm bg})\right)\left(1 - {\rm e}^{-\tau}\right)\eta \frac{{\rm ss}^2}{\Omega + {\rm ss}^2}. \tag{1.2}$$

In low-frequency limit, the Planck function can be approximated by the Rayleigh-Jeans laws: $B_\nu(T) = 2k_B T \nu^2/c^2$. After converting the specific intensity into brightness temperature, we obtain

$$T_B = \left(T_{ex} - T_{bg}\right)\left(1 - e^{-\tau}\right)\eta \frac{ss^2}{\Omega + ss^2}. \tag{1.3}$$

The simulated molecular spectra, either in I_ν or T_B that are commonly used for interferometric and single-dish observations respectively, are further used to evaluate the consistency between the assumption and observations and, in turn, constrain the molecular excitation conditions (e.g., T_{ex} and N_T). If the spectral profile meets the Snyder Criteria (detailed in Section 4.3), the observed emission features can then be assigned to a certain molecular species.

1.2 Chemically Rich Sources

In this dissertation, we present the astrochemical investigation toward three molecular clouds, Taurus Molecular Cloud-1 (TMC-1), Sagittarius (Sgr) B2, and NGC 6334 I, among which Sgr B2 and TMC-1 are the richest two known sources for molecular detections. TMC-1, a filamentary condensation within the extended Taurus cloud, is a prototypical target to be studied in the quest for an understanding of dark cloud chemistry (Fuente et al., 2019). It has a mass of ~8 $M_\odot$, a central density ~2×10^4 cm^{-3}, and a distant of ~130 pc (Nutter et al., 2008); the closest molecular cloud discussed in this dissertation. Observations toward TMC-1 have contributed to 63 new interstellar molecules, ~25% of the interstellar molecular census, ranging from C_3N in 1980 to most recent CH_2C_3N (Friberg et al., 1980; Cabezas et al., 2021). In particular, the very recent discoveries of monocyclic and bicyclic aromatic molecules in TMC-1 (McGuire et al., 2018a, 2021) are the first identified individual

aromatic molecules in the ISM, more than 40 years after the birth of the PAH hypothesis. Several spectral surveys toward its cyanopolyyne peak (CP) position carried out with single-dish observations have expanded the molecular census in TMC-1 and constrained the chemical abundances toward this source (e.g. Kaifu et al., 2004; Gratier et al., 2016; Soma et al., 2018). In addition to expanding the molecular inventory, as the initial stage of star formation, TMC-1 provides the initial conditions for chemical models of later phases (Hatchell et al., 2001).

Sgr B2 is a giant molecular cloud located near the galactic center (~8.2 kpc, Reid et al., 2019). As the most massive star-forming region, Sgr B2 consists of three clumps, South, Main, and North, spanning over 2.5 pc × 5 pc (Schmiedeke et al., 2016). The North clump, Sgr B2 (N), displays remarkable chemical richness (Friedel et al., 2004; Belloche et al., 2013; Loomis et al., 2015; Corby et al., 2018) and 69 interstellar molecules were first discovered toward this region. These include terrestrial-type biologically relevant molecules such as sugar-related glycolaldehyde and dihydroxyacetone (Hollis et al., 2004a; Apponi et al., 2006), peptide-bond-bearing acetamide (Hollis et al., 2006), urea (Remijan et al., 2014; Belloche et al., 2019), and the only chiral molecule in space, propylene oxide (McGuire et al., 2016). These species contain the same functional groups as the biotic building blocks of sugars, lipids, proteins, and other bio-macromolecules, which are key to an understanding of the cosmic origins of life. Its chemical richness causes the millimeter spectrum toward Sgr B2 to be full with molecular rotational lines. As shown in Figure 1.1, there are more than 10 lines every 100 MHz. Because of the relatively wide line widths and high density of lines, most of them are contaminated with other molecules.

NGC 6334, also known as Cat's Paw Nebula due to its similar shape to cat paw, is a massive protocluster undergoing active star formation at a distance of 1.3 kpc (Reid et al., 2014). It contains multiple sites of high-mass star forming regions. The

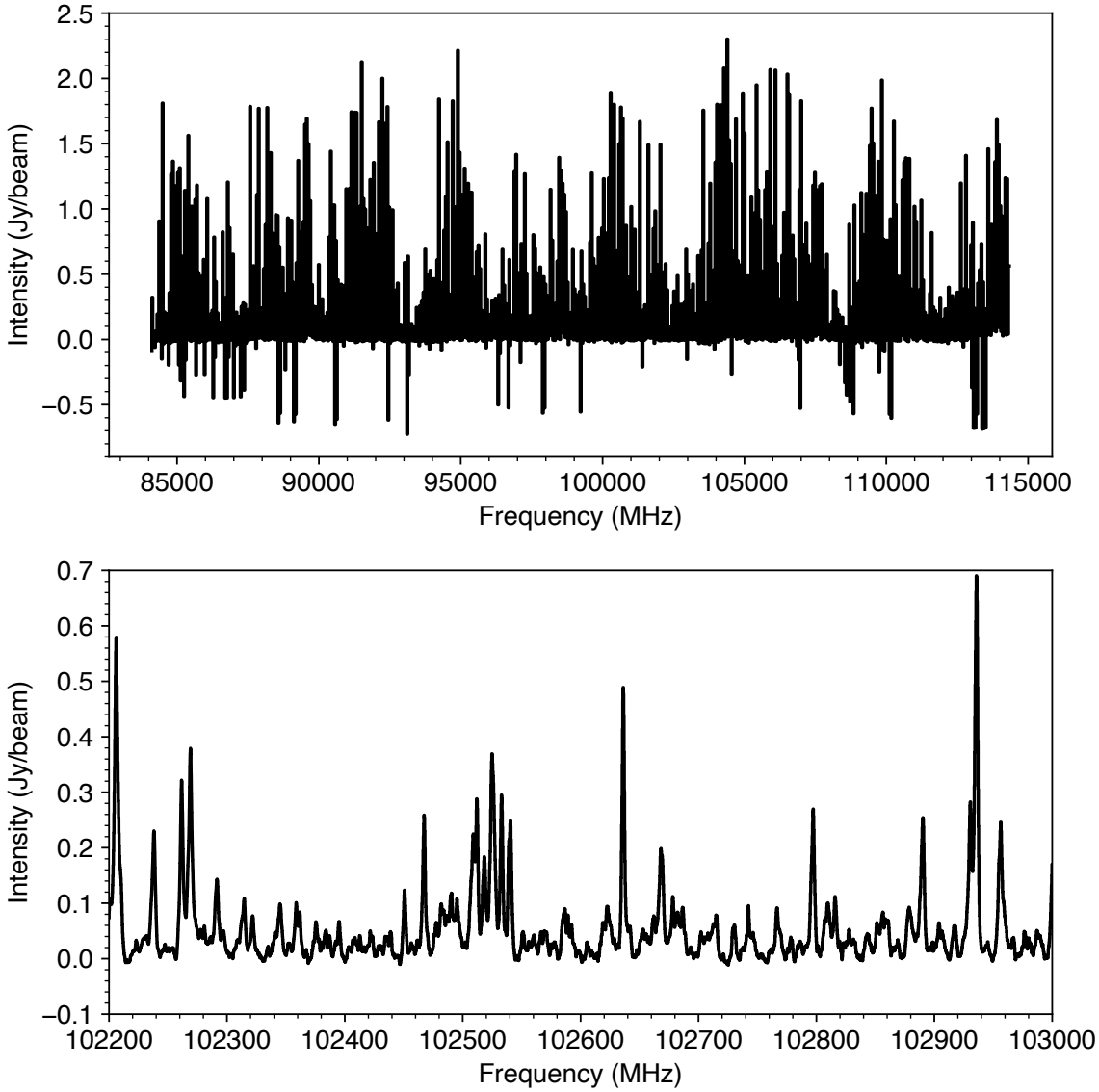

Figure 1.1: The top row shows a millimeter spectrum with a 30-GHz bandwidth toward the SgrB2-N LMH region observed with ALMA. The bottom row shows the same observation, zoomed in to show the high spectral line densities toward Sgr B2(N).

deeply embedded source "I" is at the northeastern end of the region and has been resolved into four main sources, ultra-compact region MM3, dust core MM4, and chemically rich hot core MM1 and MM2 (Brogan et al., 2016; Hunter et al., 2017). NGC 6334 I has been revealed with rich hot-core chemistry (McGuire et al., 2018b; Bøgelund et al., 2019; Melosso et al., 2020; Ligterink et al., 2020). This source was the site of the first interstellar detections of methoxymethanol (CH_3OCH_2OH) (McGuire et al., 2017b) and the first two vibrationally excited torsional states of acetic acid (CH_3COOH, Xue et al., 2019a).

1.3 Outline of the Thesis

In this dissertation, we present two cases of investigations focusing on complex astronomical molecules in molecular clouds. Part II reported the discoveries of two unsaturated carbon-chain molecules toward the TMC-1 dark cloud, namely HC_4NC (Chapter 2) and H_2C_3S (Chapter 3). These discoveries were achieved with a deep chemical survey with ~850 hours observational time directed toward TMC-1, the GOTHAM (Green Bank Telescope Observations of TMC-1: Hunting for Aromatic Molecules) observational program. By conducting high-sensitivity (2 mK) and high-resolution ($0.05\,\mathrm{km\,s^{-1}}$) observations, our team has reported the first astronomical detections of numerous new complex molecules, largely expanding the molecular inventory in ISM. By comparing the observed abundances with the astrochemical models, we provided further insights into the isocyanide and sulfur chemistry as well as their evolution.

Through characterizing spatial distributions of saturated terrestrial-type interstellar molecules, Part III disentangled a wealth of chemical and physical information about massive molecular hot cores. The morphological investigations are composed of three ALMA projects directed toward two massive hot molecular clouds, namely

Sgr B2 and NGC 6334 I. Chapter 4 described the distinct morphologies of an isomeric molecular family toward the Sgr B2 (N) hot core while Chapter 5 examined the distributions of a molecule with a wide range of excitation energy levels toward a second hot core, NGC 6334 I. In synergies with VLA observations, Chapter 6 presented the preliminary results of a multi-wavelength investigation for the origin, distribution, relationships of molecular masers toward Sgr B2 (N).

Part II

Molecular Census

Chapter 2

Interstellar HC_4NC and Isocyanopolyyne Chemistry

We report an astronomical detection of HC_4NC for the first time in the interstellar medium with the Green Bank Telescope toward the TMC-1 molecular cloud with a minimum significance of $10.5\,\sigma$. The total column density and excitation temperature of HC_4NC are determined to be $3.29^{+8.60}_{-1.20} \times 10^{11}$ cm^{-2} and $6.7^{+0.3}_{-0.3}$ K, respectively, using the MCMC analysis. In addition to HC_4NC, HCCNC is distinctly detected whereas no clear detection of HC_6NC is made. We propose that the dissociative recombination of the protonated cyanopolyyne, HC_5NH^+, and the protonated isocyanopolyyne, HC_4NCH^+, are the main formation mechanisms for HC_4NC while its destruction is dominated by reactions with simple ions and atomic carbon. With the proposed chemical networks, the observed abundances of HC_4NC and HCCNC are reproduced satisfactorily. *The following chapter is primarily reproduced from Xue, C.; Willis, E. R.; Loomis, R. A. et al. Astrophysical Journal Letters* ***2020****, 900, L9.*

2.1 Introduction

Understanding the formation and destruction routes of molecules in astronomical environments remains one of the challenging issues in modern astrochemistry. Increasingly sensitive astronomical observations can reveal detailed information about the chemical inventories present in interstellar sources. Laboratory experiments and astrochemical modelling can then work in tandem to uncover the chemical mechanisms underlying these molecular inventories. However, there are still deficiencies in our understanding of the chemistry of interstellar sources. For example, in spite of proposed formation routes through grain chemistry, gas-phase formation routes cannot be ruled out as a viable pathway for the formation of large astronomical molecules (LAMs) (Balucani et al., 2015; Coutens et al., 2017; Acharyya & Herbst, 2017, and references therein). The question remains as to how to better model the chemistry present in these astronomical environments and make the models more predictive. In turn, these robust models could then suggest further chemical species to be investigated both in the laboratory and through astronomical observations.

Structural isomers are a promising class of molecules for improving the accuracy of models. Structural isomers contain the same constituent atoms but are arranged in different elemental configurations (Xue et al., 2019b). One of the most well studied isomeric pairs in astronomical environments is that of hydrogen cyanide (HCN) and isocyanide (HNC) (Schilke et al., 1992; Turner et al., 1997; Hirota et al., 1998; Herbst et al., 2000; Tennekes et al., 2006; Graninger et al., 2015). At 100 K, under thermal equilibrium conditions, the relative abundance ratio between HNC and HCN is $\sim 10^{-30}$ (Brown, 1977). However, it is well known that under dark cloud conditions, such as those found in the Taurus Molecular Cloud 1 (TMC-1), the abundance ratio approaches ~1 (Irvine & Schloerb, 1984), indicating that thermodynamic equilibrium

certainly does not apply to the two species in these regions (Brown et al., 1989). Instead, measured column densities toward these sources are dominated by the kinetics of chemical reactions in the gas phase; these measurements give observational constraints on the chemical formation and destruction networks (Graninger et al., 2014). As such, measuring the relative abundance ratios for pairs of chemical isomers, and incorporating isomer-specific chemistry into chemical networks, can be a powerful tool to improving the predictive power of these models. Here, we focus on exploiting the cyanide and isocyanide pairs of isomers.

The family of astronomically-detected cyanides includes HCN, methyl cyanide (CH_3CN), vinyl cyanide (CH_2CHCN), ethyl cyanide (CH_3CH_2CN), and other species including isocyanogen (CNCN), E-cyanomethanimine (E−HNCHCN), glycolonitrile ($HOCH_2CN$) and many others (McGuire, 2018; Zeng et al., 2019, and references therein). Some of these species are found in high abundance and are readily detectable in a variety of interstellar environments (Miao & Snyder, 1997; Araya et al., 2005; López et al., 2014; Hung et al., 2019). In contrast to the numerous detection of cyanides in astronomical environments, there have been very few confirmed detection of isocyanides, such as methyl isocyanide (CH_3NC) (Remijan et al., 2005; Gratier et al., 2013). Most recently, the Protostellar Interferometric Line Survey (PILS) observed CH_3NC in a solar-type star, IRAS 16293-2422, for the first time toward a source of this type (Calcutt et al., 2018). Despite that, there have been no successful detections of CH_2CHCH_2NC (Haykal et al., 2013) or CH_3CH_2NC (Remijan et al., 2005; Margulès et al., 2018).

Alongside CH_3CN, one of the most frequently observed families of cyanide species, especially in cold sources, are the cyanopolyynes ($HC_{2n}CN$) (Broten et al., 1978; Little et al., 1978; Bell et al., 1998). Yet, despite their relative ubiquity, the only isocyanide version that has been successfully detected is HCCNC (Kawaguchi et al., 1992), the

isomer of HC_3N. Remijan et al. (2005) first searched for isocyanodiacetylene (HC_4NC), the isomer of HC_5N, toward Sagittarius B2(N). To the best of our knowledge, this has been the only attempt to detect this molecule in astronomical environments, setting an upper limit on the abundance ratio to HC_5N as 0.03. In this work, we report the first astronomical detection of HC_4NC using the data available from the GOTHAM (Green Bank Telescope Observations of TMC-1: Hunting for Aromatic Molecules) observational program of TMC-1 (McGuire et al., 2020). The detection of HC_4NC along with new observations of HCCNC and an upper limit to the abundance of HC_6NC, have been used to better constrain the gas-phase formation models of both cyanopolyynes and isocyanopolyynes ($HC_{2n}NC$) under TMC-1 conditions. The interplay between –CN and –NC formation chemistry can also provide insights into the physical conditions and history of the sources where these species are detected, therefore making new mechanistic insights into -CN vs -NC chemistry particularly relevant for both new and continuing problems such as the HCN/HNC abundance ratio (e.g. Hacar et al., 2020).

In Section 2.2, we describe the molecular properties of HC_4NC. Section 2.3 presents the detection of HC_4NC with the GOTHAM observations and the observational analyses. The results of the analyses are used to constrain the new chemical formation network developed to account for the formation of HC_4NC in Section 2.4. Finally, in Section 2.5, we summarize our results and describe the next steps in refining the chemical network and searches for larger isocyanopolyynes towards other astronomical sources.

2.2 Spectroscopic Properties

The HC_4NC molecule has a linear equilibrium structure (Gronowski & Kołos, 2006). For this work, transition frequencies of HC_4NC were taken from the CDMS

catalog (Müller et al., 2005); the entry was based on Fourier transform microwave (FTMW) spectroscopy data and *ab initio* calculations reported by Botschwina et al. (1998).

In addition to the molecular structure, Botschwina et al. (1998) also provide estimates of the electric dipole moment. However, the authors did not report the dipole polarizability, which is required for estimating reaction rate coefficients, as will be discussed in Section 2.4. To this end, we carried out new calculations with the CFOUR (Coupled-Cluster techniques for Computational Chemistry) suite of electronic structure programs (Stanton et al., 2017), employing the coupled-cluster method with single, double, and perturbative triple excitations [CCSD(T)] under the frozen-core approximation, paired with a Dunning's correlation-consistent quadruple-ζ (cc-pVQZ) basis set. At this level of theory, we obtain an equilibrium dipole moment of 3.24 D in agreement with the value of 3.25 D obtained by Botschwina et al. (1998) employing a smaller Dunning's triple-ζ (cc-pVTZ) basis set. The small change between the cc-pVTZ and cc-pVQZ values suggests that the one-electron properties have effectively converged with respect to basis set, thereby lending confidence in our calculations. With the same method and the cc-pVQZ basis set, we obtain a value of 10.3501 Å^3 for the average dipole polarizability listed in Table 2.1.

2.3 Observations

The capabilities of the Green Bank Telescope (GBT) have expanded the molecular census in TMC-1 and, thereby, increased the known molecular inventory in the interstellar medium (McGuire et al., 2017a, 2018a). The GBT observations of the GOTHAM project targeted the TMC-1 cyanopolyyne peak (CP) centered at $\alpha_{\text{J2000}} = 04^{\text{h}}41^{\text{m}}42.5^{\text{s}}$, $\delta_{\text{J2000}} = 25^{\circ}41'26.8''$, where the column densities of the carbon-chain species peak. The GOTHAM spectral line survey covers the GBT X-, K- and

Table 2.1: Calculated dipole and polarizability for the related cyanopolyynes and isocyanopolyynes

Parameter	μ_e (D) [a]	α (Å^3) [b]	Reference
HC_3N	3.788	5.848	Woon & Herbst (2009)
HCCNC	2.990	6.221	Woon & Herbst (2009)
HC_5N	4.55	9.61	Loison et al. (2014b)
HC_4NC	3.24	10.3501	This work
CH_3C_3N	5.041	8.008	Woon & Herbst (2009)

[a] The equilibrium electric dipole moment in units of Debye.
[b] The average dipole polarizability, in units of Å^3.

Ka-Bands with total 13.1 GHz frequency coverage from 7.906 to 29.827 GHz. The beam size varies between ~90″ at 8 GHz and ~26″ at 29 GHz. At a uniform 0.05 km s^{-1} velocity resolution, the RMS noise ranges from $\sim 2 - 20$ mK across the dataset. Detailed information concerning the GOTHAM observations and the data calibration can be found in McGuire et al. (2020).

As presented in Figure 2.1, we identified three emission features above the noise level of the observations assigned to HC_4NC with the GOTHAM survey. Each feature comprises three hyperfine components of the rotational transition. Table 2.2 summarizes the spectroscopic properties of the nine transitions. The HC_4NC lines show a good match between the observed frequencies and the calculated frequencies from the CDMS database assuming a systematic Local Standard of Rest velocity ($V_{\rm lsr}$) of 5.8 km s^{-1}.

2.3.1 Determinations of Column Density and Excitation Conditions

A total of 13 transitions of HC_4NC (See Section 2.7) were used to rigorously determine the molecular abundance and excitation conditions using the Markov chain

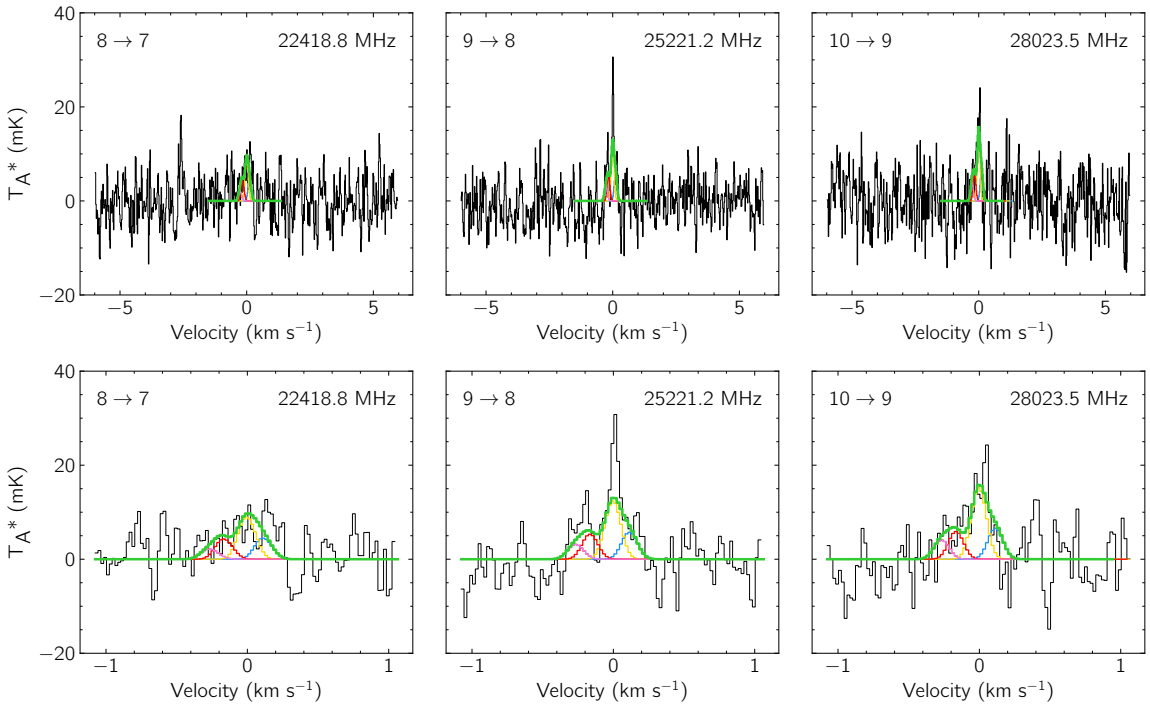

Figure 2.1: Individual line detections of HC_4NC in the GOTHAM data. The top row shows a wider view to provide context on the noise levels, ~5 mK. The bottom row shows the same transitions, zoomed in to show detail. The spectra (black) are displayed in velocity space relative to 5.8 km s^{-1}, and using the rest frequency given in the top right of each panel. Quantum numbers are given in the top left of each panel, neglecting hyperfine splitting. The best-fit model to the data, including all velocity components, is overlaid in green. Simulated spectra of the individual velocity components are shown in: blue (5.63 km s^{-1}), yellow (5.75 km s^{-1}), red (5.91 km s^{-1}), and violet (6.01 km s^{-1}). See Table 2.3.

Table 2.2: Spectroscopic Properties of Observed Transitions

Transitions $J' \rightarrow J''$	Transitions $F' \rightarrow F''$	Frequency (MHz)	$E_{\rm up}$ (K)	$\log_{10} \frac{A_{\rm ul}}{\rm s^{-1}}$	$S_{ij}\mu^2$ ($\rm D^2$)
8 → 7	9 → 8	22418.8438(10)	4.84	-6.1859	94.43
	8 → 7	22418.8461(10)	4.84	-6.1927	83.18
	7 → 6	22418.8498(10)	4.84	-6.1936	73.24
9 → 8	10 → 9	25221.1790(16)	6.05	-6.0295	105.07
	9 → 8	25221.1808(17)	6.05	-6.0350	93.88
	8 → 7	25221.1837(17)	6.05	-6.0356	83.88
10 → 9	11 → 10	28023.5067(25)	7.40	-5.8899	115.69
	10 → 9	28023.5082(26)	7.40	-5.8943	104.57
	9 → 8	28023.5105(26)	7.40	-5.8948	94.52

NOTE — The spectroscopic data of the HC_4NC transitions corresponding to the three detected emission features are taken from the CDMS catalogue (Müller et al., 2005) and the SPLATALOGUE spectroscopy database [1].

Monte Carlo (MCMC) fitting method described in Loomis et al. (2021). Each of the identified emission features consists of four individual velocity components (Loomis et al., 2021), indicating that TMC-1 is not quiescent and isotropic in terms of physical structure. This is supported by recent CCS and HC_3N observations performed with the 45 m telescope at the Nobeyama Radio Observatory (Dobashi et al., 2018).

A uniform excitation temperature ($T_{\rm ex}$) and line width (ΔV) for each velocity component are assumed, while source velocity ($V_{\rm lsr}$), source size, and column density ($N_{\rm T}$) are variable among different velocity components. Therefore, there are 14 free parameters in total to be adjusted in the MCMC analysis. A forward model with 14 free parameters is used to iteratively generate model spectra which are compared with the observations. Posterior probability distributions for each parameter and their covariances are generated via several million of these parameter draws, populating the corner plot in Section 2.7. The resulting best-fit parameters of each velocity component of HC_4NC are summarized in Table 2.3. As shown in Figure 2.1, if we

take the noise level measured in each passband into account, the constructed profiles fit reasonably well with the observed spectra for the individual emission features. A total $N_{\rm T}$ of $3.29^{+8.60}_{-1.20} \times 10^{11}\,{\rm cm}^{-2}$ with a $T_{\rm ex}$ of $6.7^{+0.3}_{-0.3}$, K is determined for HC_4NC.

The $N_{\rm T}$ per velocity components show variation on the order of a factor of a few but have consistency in the order of magnitude, unlike the case of HC_3N and CCS presented in Dobashi et al. (2018). The variation of $N_{\rm T}$ arises from the degeneracy between the $N_{\rm T}$ of each component and its source size, found by the MCMC analysis. Without any spatial information to constrain the source sizes, we cannot conclude much about their chemical properties.

In addition to the HC_4NC analysis, we have also analyzed HCCNC and HC_6NC in these observations; the results of these analyses are presented in Appendices 2.8 and 2.9. HCCNC is definitively detected with six emission features whereas there is no obvious emission detected for HC_6NC. The $N_{\rm T}$ for HCCNC is measured to be $3.82^{+1.06}_{-0.53} \times 10^{12}\,{\rm cm}^{-2}$, while a $2\,\sigma$ upper limit of $<4.04 \times 10^{11}\,{\rm cm}^{-2}$ for the HC_6NC column density is determined. HCCNC has been previously detected in TMC-1 with Nobeyama 45-m observations (Gratier et al., 2016), which reported $N_{\rm T}$(HCCNC) to be $8.51^{+8.87}_{-1.9} \times 10^{12}\,{\rm cm}^{-2}$, consistent with our GOTHAM result. The column densities listed in Table 2.4 are the sums of the four detected velocity components, where the column densities of HC_3N and HC_5N are from Loomis et al. (2021). The detection of HCCNC and HC_4NC in GOTHAM data gives column density ratios to their corresponding cyanide isomers of $2.2^{+0.7}_{-0.4}$% for HCCNC/HC_3N and $0.49^{+1.32}_{-0.19}$% HC_4NC/HC_5N toward TMC-1. The observed results are used to constrain the reaction rate coefficients and branching ratios of the formation routes of HC_4NC, as will be discussed in Section 2.4.2.

Table 2.3: HC_4NC best-fit parameters from the MCMC analysis

Component	$V_{\rm lsr}$ ($\rm km\,s^{-1}$)	Size ($''$)	$N_{\rm T}$ [a] ($10^{11}\,\rm cm^{-2}$)	$T_{\rm ex}$ (K)	ΔV ($\rm km\,s^{-1}$)
C1	$5.628^{+0.045}_{-0.038}$	42^{+9}_{-9}	$0.30^{+0.19}_{-0.13}$	$6.7^{+0.3}_{-0.3}$	$0.120^{+0.012}_{-0.010}$
C2	$5.745^{+0.021}_{-0.015}$	21^{+7}_{-8}	$1.35^{+1.38}_{-0.50}$		
C3	$5.907^{+0.038}_{-0.046}$	62^{+20}_{-20}	$0.23^{+0.12}_{-0.12}$		
C4	$6.009^{+0.044}_{-0.032}$	9^{+11}_{-6}	$1.40^{+8.48}_{-1.07}$		
$N_{\rm T}$(Total)[b]	$3.29^{+8.60}_{-1.20} \times 10^{11}\,\rm cm^{-2}$				

NOTE — The quoted uncertainties represent the 16^{th} and 84^{th} percentile ($1\,\sigma$ for a Gaussian distribution) uncertainties.

[a] Column density values are highly covariant with the derived source sizes. The marginalized uncertainties on the column densities are therefore dominated by the largely unconstrained nature of the source sizes, and not by the signal-to-noise of the observations. See Figure 2.4 for a covariance plot, and Loomis et al. (2021) for a detailed explanation of the methods used to constrain these quantities and derive the uncertainties.

[b] Uncertainties derived by adding the uncertainties of the individual components in quadrature.

Table 2.4: Column Densities and XNC/XCN Ratios

Species	$N_{\rm T}$ ($\rm cm^{-2}$)	$N_{\rm T}$ with the Nobeyama Observations [b] ($\rm cm^{-2}$)	$N_{\rm T}$(XNC)/$N_{\rm T}$(XCN) Observation	High HC_4NC BF [c]	Low HC_4NC BF [c]
HCCCN	$1.75^{+0.05}_{-0.05} \times 10^{14}$ [a]	$2.34^{+0.82}_{-0.30} \times 10^{14}$			
HCCNC	$3.82^{+1.06}_{-0.53} \times 10^{12}$	$8.51^{+8.87}_{-1.90} \times 10^{12}$	$2.2^{+0.7}_{-0.4}$%	3.0%	3.0%
HC_4CN	$6.69^{+0.13}_{-0.13} \times 10^{13}$ [a]	$5.89^{+1.52}_{-1.10} \times 10^{13}$			
HC_4NC	$3.29^{+8.60}_{-1.20} \times 10^{11}$		$0.49^{+1.32}_{-0.19}$%	2.6%	0.34%
HC_6CN	$3.65^{+0.13}_{-0.12} \times 10^{13}$ [a]	$4.57^{+1.74}_{-0.94} \times 10^{13}$			
HC_6NC	$< 4.04 \times 10^{11}$		< 1.1%		

[a] Loomis et al. (2021) estimated the column densities of cyanopolyynes with similar MCMC analyses of the GOTHAM data, assuming the four velocity components are cospatial.

[b] The column density estimated by the Bayesian approach of the spectral survey performed with the Nobeyama 45-m dish (Gratier et al., 2016)

[c] "High HC_4NC BF" corresponds to the model with a high branching fraction to form HC_4NC in the HC_5NH^+ dissociative recombination, i.e. shown in solid lines in Figure 2.3, while "Low HC_4NC BF" is the modeled result with a low branching fraction shown in dashed lines in Figure 2.3.

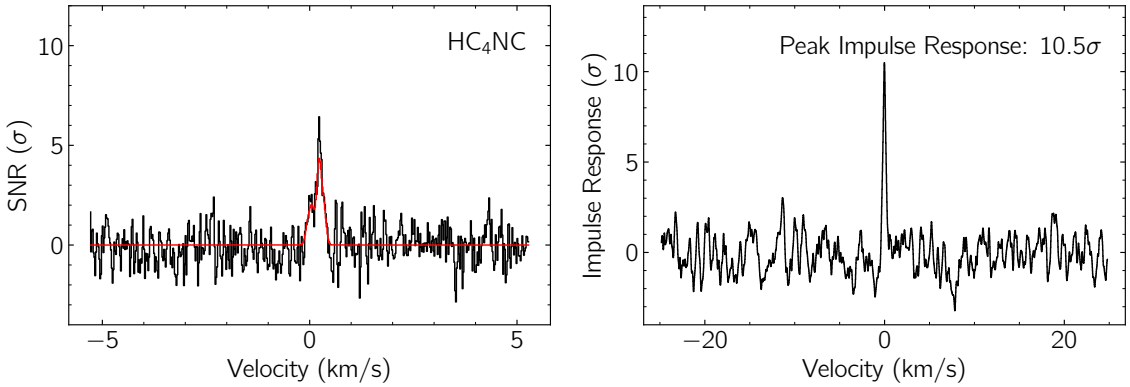

Figure 2.2: *Left:* Velocity-stacked spectra of HC_4NC in black, with the corresponding stack of the simulation using the best-fit parameters to the individual lines in red. The data have been uniformly sampled to a resolution of $0.02\,\mathrm{km\,s^{-1}}$. The intensity scale is the signal-to-noise ratio of the spectrum at any given velocity. *Right:* Impulse response function of the stacked spectrum using the simulated line profile as a matched filter. The intensity scale is the signal-to-noise ratio of the response function when centered at a given velocity. The peak of the impulse response function provides a minimum significance for the detection of $10.5\,\sigma$. See Loomis et al. (2021) for details.

2.3.2 Visualization of the Detection

To better visualize the detection, and determine a minimum statistical significance, we constructed an intensity- and noise-weighted stacked composite spectrum using the GOTHAM data (Loomis et al., 2021). The spectral stacking was performed in velocity space using the 13 HC_4NC transitions covered by the survey. Another composite line profile using the best-fit parameters was constructed, and used as a matched filter to perform the cross-correlation and determine the statistical significance of the detection (Loomis et al., 2021). The results are shown in Figure 2.2, and indicate a minimum significance to the detection of HC_4NC of $10.5\,\sigma$.

2.4 Discussion

2.4.1 Chemical Networks

A number of prior investigations have attempted to address the chemical origins of many of the cyanopolyynes observed in TMC-1 (Takano et al., 1998; Taniguchi et al., 2016; Burkhardt et al., 2018). For example, due to the significant abundance enhancement of HCC^{13}CN relative to HC^{13}CCN and H^{13}CCCN, the formation of HC_3N was suggested to be dominated by the neutral-neutral reaction of C_2H_2 and the CN radical (Takano et al., 1998). On the other hand, HC_5N and HC_7N show no such enhancement for the analogous ^{13}C position, implying that the primary formation route for HC_5N is the dissociative recombination (DR) reaction between the N-bearing hydrocarbon ions and electrons in cold environments (Burkhardt et al., 2018). Furthermore, Loison et al. (2014a) pointed out that the $H_2CCN + C \longrightarrow HC_3N + H$ reaction is also involved in producing HC_3N.

On the other hand, the chemistry of the corresponding isocyanopolyynes ($HC_{2n}NC$) is less well known. Compared with neutral-neutral reactions, reaction schemes involving the DR process of protonated molecular ions such as HC_3NH^+ and HC_2NCH^+ are more likely to be the main production mechanisms for HCCNC (Kawaguchi et al., 1992; Gensheimer, 1997; Osamura et al., 1999; Vastel et al., 2018a). These protonated ions can be formed through ion-molecule reactions such as $HCCH^+ + HNC/HNC$ and $CH_3CN + C^+$ (Takagi et al., 1999; Quénard et al., 2017). Even though the chemistry of HC_4NC is less well-studied compared to HCCNC, both of them belong to the same homologous series. We therefore assumed analogous formation schemes of HCCNC and HC_4NC. In other words, HC_4NC would mainly form through the DR of the protonated cyanopolyynes HC_5NH^+ and protonated isocyanopolyynes HC_4NCH^+.

One of the most prevalent destruction mechanisms of cyano- and isocyanopolyynes is ion-molecule chemistry, particularly reactions with C^+, H_3^+, and HCO^+ (Woon & Herbst, 2009). In addition, as described in Loison et al. (2014b), reactions with carbon atoms are also efficient. Therefore, we extrapolate the mechanisms involving carbon atoms to isocyanopolyynes and propose that the main destruction mechanisms of HC_4NC are with the ions mentioned above, neutral carbon, and photons.

In this work, we adopted the chemical network of `kida.uva.2014` (Wakelam et al., 2015), modified as described in McGuire et al. (2018a), as the basis and added or updated the reactions related to HC_3N, HCCNC, HC_5N, and HC_4NC. Note that we introduce HC_4NC as the only isomer of HC_5N in the network. We neglected the other HC_5N isomers to avoid adding more new species of which we have even less knowledge. In the following sections, we will discuss the choices and estimations of the reaction rate coefficients of the formation and destruction pathways of the four molecules of interest. The production and destruction routes regarding HC_4NC are summarized in Table 2.5 with the corresponding rate coefficients.

Formation Mechanisms – Dissociative Recombination Reactions

The estimation of the branching ratios and rate coefficients of the HC_3NH^+ DR are constrained by the laboratory measurements of the DR of DC_3ND^+ and the consideration of isomerization among the products (Vastel et al., 2019, and references therein). Here, we adopted their values in this chapter.

Since HC_3N and HCCNC are both products of the HC_3NH^+ DR reactions, the HC_5NH^+ DR, originally included in the `kida.uva.2014 network`, is amended to

include HC_4NC as another product:

$$HC_5NH^+ + e^- \longrightarrow C_4H + HCN \qquad 22\% \qquad (2.1)$$

$$\longrightarrow C_4H + HNC \qquad 22\% \qquad (2.2)$$

$$\longrightarrow CCH + HC_3N \qquad 6\% \qquad (2.3)$$

$$\longrightarrow C_5N + H_2 \qquad 4\% \qquad (2.4)$$

$$\longrightarrow HC_5N + H \qquad 43.8\% \qquad (2.5)$$

$$\longrightarrow HC_4NC + H \qquad 2.2\% \qquad (2.6)$$

The particular choice of the branching ratio is explained below.

Based on the potential energy surface of the various HC_3N isomers, Vastel et al. (2019) suggested the branching fraction for the HC_3NH^+ DR forming HC_3N to be 20 times greater than that for the process forming HCCNC (private communication with J. Loison). The energy difference between HC_4NC and HC_5N is calculated to be ~114.5 kJ/mol (or 13771 K) with the W1BD thermochemical method, which is similar to the difference between HCCNC and HC_3N, ~113.1 kJ/mol (or 13603 K). Because of the lack of a laboratory measurement of the branching ratio in the HC_5NH^+ DR, we assume a fiducial ratio between the branching fractions for the HC_5N isomers to be 20, analogous to that of the HC_3N isomers. The total rate coefficient for the HC_5NH^+ DR, $2.0 \times 10^{-6}(T/300)^{-0.7}\,\mathrm{cm^3\,s^{-1}}$, and the branching ratios for the other product species are followed as suggested in `kida.uva.2014`.

The dissociative recombination of HC_2NCH^+ is another important pathway leading to HCCNC (Botschwina et al., 1993). In `kida.uva.2014`, the rate coefficient for the DR of HC_2NCH^+ is $6.0 \times 10^{-7}(T/300)^{-0.5}\,\mathrm{cm^3\,s^{-1}}$, which seems to be underestimated compared with the experimentally measured rate coefficient for the DR of

DC_3ND^+, $1.5 \times 10^{-6}(T/300)^{-0.7}\,cm^3\,s^{-1}$ (Geppert et al., 2004; Vigren et al., 2012). We expect these rate coefficients to be similar because rate coefficients for DR tend to increase with complexity (Larsson et al., 2012), and because the two cations are of similar complexity. Considering that, we modified the total rate coefficient for the HC_2NCH^+ DR to be analogous with that of DC_3ND^+.

Furthermore, we also added HC_4NCH^+ as secondary precursor of HC_4NC. For the HC_4NCH^+ DR, we assume the total rate coefficient to be consistent with the HC_5NH^+ DR rate coefficient of $2.0 \times 10^{-6}(T/300)^{-0.7}\,cm^3\,s^{-1}$. The channels and branching ratios of the DR of HC_4NCH^+ are assumed to be equal to that of HC_2NCH^+ in the `kida.uva.2014 network`:

$$HC_4NCH^+ + e^- \longrightarrow C_4H + HCN \qquad 38\% \qquad (2.7)$$

$$\longrightarrow C_4H_2 + CN \qquad 38\% \qquad (2.8)$$

$$\longrightarrow HC_5N + H \qquad 4\% \qquad (2.9)$$

$$\longrightarrow HC4NC + H \qquad 20\% \qquad (2.10)$$

Note that, while HC_4NC can be protonated to form HC_4NCH^+, the formation of HC_4NCH^+ is dominated by the proposed reaction between CH_3C_3N and the C^+ ion. Thus, consecutive protonation and de-protonation of HC_4NC, resulting in a zero net abundance change, is avoided.

Since the barrierless DR reactions contribute dominantly to the formation of isocyanopolyynes, we emphasize that the determination of the branching ratios are usually more crucial than those of the overall rate coefficients for the case of DR in astronomical environments (Larsson et al., 2012). Nonetheless, although the branching ratios of the related DR reactions are mostly estimated and relatively arbitrary

due to the lack of experimental measurement other than for DC_3ND^+ (Geppert et al., 2004), we believe that the values we estimated are reasonable, as supported by the reproduction of observed values discussed below.

Destruction Mechanisms

As previously mentioned, the destruction of the cyano- and isocyanopolyynes is dominated by ion-molecule reactions and reactions with atomic carbon. The reaction coefficient of the related ion-molecule reactions are estimated with equation (3) from Woon & Herbst (2009), which can be rewritten as

$$k_{\mathrm{D}} = 0.4767 \frac{2\pi e \mu_{\mathrm{D}}}{\sqrt{2kT\mu}} + 0.62 \times 2\pi e \sqrt{\frac{\alpha}{\mu}}, \tag{2.11}$$

where μ_{D} and α are the dipole moment and the average dipole polarizability of the neutral molecule, respectively, and μ is the reduced mass of the reactants. In addition to adding the new destruction routes proposed for HC_4NC, we also updated the ion-molecule reaction rate coefficients of HCCNC, HC_5N, and CH_3C_3N from the kida.uva.2014 network with this formula and the dipole moments and polarizabilities listed in Table 2.5. The reaction rate coefficients for the reactions of isocyanopolyynes with carbon atoms are estimated to be the same as those of the cyanopolyynes (Loison et al., 2014b), while the reaction coefficients for the UV photon dissociation and cosmic-ray ionization reactions of HC_4NC are assumed to be the same as those of HCCNC in `kida.uva.2014` respectively.

2.4.2 Chemical Modeling

We used the three-phase gas-grain astrochemical model `NAUTILUS 1.1` (Ruaud et al., 2016) together with our updated network to attempt to reproduce the abundances of HC_4NC and the related species. Physical conditions are assumed to follow

typical cold dense cloud conditions, i.e. a gas and dust temperature of 10 K, a gas density $n_{\rm H}$ of $2\times10^{4}\,{\rm cm}^{-3}$, a visual extinction ($A_{\rm v}$) of 10, and a cosmic ray ionization rate (ζ) of $1.3\times10^{-17}\,{\rm s}^{-1}$ (Ruaud et al., 2016). We adopted assumed initial elemental abundances in TMC-1 CP as described in Hincelin et al. (2011) with the exception of atomic oxygen. The resulting abundances, with respect to the $N_{\rm T,(H_2)} \sim 10^{22}\,{\rm cm}^{-2}$ (Gratier et al., 2016), were converted to column densities and compared with the observed values.

We found that both cyano- and isocyanopolyynes are highly sensitive to the initial oxygen elemental abundance. A higher oxygen abundance would result in lower abundances of the HC_3N, HCCNC, HC_5N, and HC_4NC molecules because the majority of C is being locked into CO while reacting with the abundant O. In Figure 2.3, we present the results of the chemical modeling with an initial C/O ratio of 1.1, in which the model at an age of $\sim3.5\times10^{5}$ yr gives satisfactory agreement with the observations for HC_3N,HCCNC,andHC_5N. The initial physical conditions and elemental abundances are all homogeneous among the series of GOTHAM Data Reduction 1 (DR1) papers (McGuire et al., 2021; Loomis et al., 2021; McCarthy et al., 2021; Xue et al., 2020; Burkhardt et al., 2021) and have reproduced the observed abundances of the other cyanopolyynes species HC_7N, HC_9N, and $HC_{11}N$ well. Compared with previous astrochemical modelling on TMC-1, the modelled results produce a similar agreement. For example, in Loison et al. (2014b), when assuming the C/O ratio to be 0.95, the peak abundances for HC_3N and HC_5N are $\sim4\times10^{-8}$ and $\sim7\times10^{-9}$ respectively and occur at $\sim3\times10^{5}$ yr, which are consistent with our results.

The overproduction of HC_4NC could be explained by the defects in the chemical network. Concerning destruction, there could be secondary destruction mechanisms that we have not accounted for, while concerning production, the branching ratios in the related DR processes could be inaccurate. Firstly, the ratio between the branching

fraction for forming HC_5N and that for forming HC_4NC in the HC_5NH^+ DR was assumed to be an analogous value of 20 from the HC_3NH^+ DR, which could be underestimated. We conducted additional models by varying this ratio and found that increasing it would result in a significant decrease in the simulated abundance of HC_4NC while the increase in HC_5N is less significant, as shown in Figure 2.3. When this ratio is set to be 200, the modeled abundance ratio for HC_4NC/HC_5N can reach 0.34%, which matches well with the observed value, $0.49^{+1.32}_{-0.19}$%. Therefore, as constrained by the observed abundances, this ratio is suggested to fall within a range of 20 to 200. Secondly, neglecting other possible HC_5N isomers in the DR processes would also lead to an overestimation of the branching fractions for forming HC_4NC and HC_5N in the HC_4NCH^+ DR. A reduction in the branching ratio could easily reduce the simulated HC_4NC abundance. Experimental studies on the formation and destruction pathways of this molecule are rare, and its detection in TMC-1 therefore highlights the need for more experimental and theoretical work

2.4.3 CN/NC Formation Chemistry

In the current study, we have assumed the formation mechanism of HC_4NC to be analogous to that of HCCNC with the understanding that HC_3N and HC_5N, and thus HCCNC and HC_4NC, might have different dominant formation pathways. As such, the model results presented here are only a first attempt at understanding this chemistry with the knowledge that refinements to the models will be necessary as more experimental studies become available.

The current model shows that the HC_nNH^+ DR is the dominant pathway in the formation of HCCNC and HC_4NC, whereas there are several reaction channels contributing to the HCCCN and HC_4CN production and different pathways dominate at different times, in disagreement with what the ^{13}C-isotopologue observation suggests.

The resultant model abundance ratios are comparable for HCCNC/HCCCN (~3.0%) and HC_4NC/HC_4CN (~2.6%) at $\sim 3.5 \times 10^5$ yr.

In contrast, the observed HC_4NC/HC_4CN abundance ratio in TMC-1, $0.49^{+1.32}_{-0.19}$%, is lower than the HCCNC/HCCCN abundance ratio, $2.2^{+0.7}_{-0.4}$%, within $1\,\sigma$ uncertainty. The uncertainties in the observed ratios are largely introduced by the poor constraint on the spatial distribution of these molecules. One caveat is that, as Remijan et al. (2005) highlighted, a necessary prerequisite to interpret the relative abundance ratio between any molecular species detected in astronomical environments, including cyanide and isocyanide isomers, is that they must be co-spatial.

A subsequent dedicated search for cyanide and isocyanide pairs in different interstellar sources is justified, because the abundance ratio between cyanide and isocyanide isomers could also vary among sources. For example, the HCCNC/HCCCN abundance ratio toward the L1544 pre-stellar core, $\sim(3.5 - 13.8)$%, is elevated relative to that in the TMC-1 dark cloud (Vastel et al., 2018a). Compared with TMC-1, L1544 is at a later stage along the path of star formation and has a slightly higher excitation temperature of 6 - 8 K (Vastel et al., 2018a). Determining the cause of the variation in CN/NC isomeric ratios may prove useful in constraining the dominant pathways and their dependence on the physico-chemical history of the source.

In addition, studies on other cyanide/isocyanide isomers in TMC-1 would help to address how the NC/CN ratio varies among different pairs of species, such as CH_3CN and CH_3NC. To date, only CH_3CN has been detected towards TMC-1 (Irvine & Schloerb, 1984; Gratier et al., 2016), while CH_3NC may be detected as the GOTHAM survey progresses.

Table 2.5: Summary of the Proposed Dominant Reactions For HC_4NC

Reactions	α	β	γ	Formula Type	$k(10\,\mathrm{K})$
Production Routes:					
$HC_5NH^+ + e^- \longrightarrow HC_4NC + H$	4.400×10^{-8}	-0.7	0	3	4.758×10^{-7} [a]
$HC_4NCH^+ + e^- \longrightarrow HC_4NC + H$ [b]	4.000×10^{-7}	-0.7	0	3	4.326×10^{-6} [c]
Destruction Routes:					
$HC_4NC + C^+ \longrightarrow HC_5N^+ + C$	0.2	2.334×10^{-9}	3.499	4	4.554×10^{-9} [d]
$HC_4NC + C^+ \longrightarrow CNC^+ + C_4H$	0.2	2.334×10^{-9}	3.499	4	4.554×10^{-9} [d]
$HC_4NC + C^+ \longrightarrow C_6N^+ + H$	0.2	2.334×10^{-9}	3.499	4	4.554×10^{-9} [d]
$HC_4NC + C^+ \longrightarrow C_5H^+ + CN$	0.2	2.334×10^{-9}	3.499	4	4.554×10^{-9} [d]
$HC_4NC + C^+ \longrightarrow C_4H^+ + CCN$	0.2	2.334×10^{-9}	3.499	4	4.554×10^{-9} [d]
$HC_4NC + H_3^+ \longrightarrow HC_4NCH^+ + H_2$	1.0	4.420×10^{-9}	3.499	4	4.312×10^{-8} [d]
$HC_4NC + HCO^+ \longrightarrow HC_4NCH^+ + CO$	1.0	1.642×10^{-9}	3.499	4	1.602×10^{-8} [d]
$HC_4NC + H_3O^+ \longrightarrow HC_4NCH^+ + H_2O$	1.0	1.928×10^{-9}	3.499	4	1.881×10^{-8} [d]
$HC_4NC + H^+ \longrightarrow CN + C_4H_2^+$	0.333	7.557×10^{-9}	3.499	4	2.455×10^{-8} [d]
$HC_4NC + H^+ \longrightarrow H_2 + C_5N^+$	0.333	7.557×10^{-9}	3.499	4	2.455×10^{-8} [d]
$HC_4NC + H^+ \longrightarrow C + H_2C_4N^+$	0.333	7.557×10^{-9}	3.499	4	2.455×10^{-8} [d]
$HC_4NC + He^+ \longrightarrow He + C_4H + CN^+$	0.5	3.852×10^{-9}	3.499	4	1.879×10^{-8} [d]
$HC_4NC + He^+ \longrightarrow He + C_4H^+ + CN$	0.5	3.852×10^{-9}	3.499	4	1.879×10^{-8} [d]

Table 2.5 continued

Table 2.5: Summary of the Proposed Dominant Reactions For HC_4NC (continued)

Reactions	α	β	γ	Formula Type	$k(10\,\mathrm{K})$	
$HC_4NC + C \longrightarrow C + HC_5N$	1.000×10^{-10}	0	0	3	1.000×10^{-10}	e
$HC_4NC + CRPh \longrightarrow CN + C_4H$	3.450×10^{3}	0	0	1	4.485×10^{-14}	f
$HC_4NC + Photon \longrightarrow CN + C_4H$	9.540×10^{-10}	0	1.830	2	1.076×10^{-17}	f

NOTE — Definitions of α, β, and γ can be found on the KIDA online database (`http://kida.astrophy.u-bordeaux.fr/help.html`). Formulae of type 1 and 2 are $k = \alpha\zeta$ and $k = \alpha e^{-\gamma A_\nu}$, where k is in s^{-1}, and formulae of type 3 and 4 are $k(T) = \alpha\,(T/300)^{\beta}\,e^{-\gamma/T}$ and $k(T) = \alpha\beta\left(0.62 + 0.4767\gamma\,(300/T)^{0.5}\right)$, where k is in $\mathrm{cm}^3\,\mathrm{s}^{-1}$ and T is in K, respectively.

[a] The total reaction coefficient of the HC_5NH^+ DR is $2.0 \times 10^{-6}(T/300)^{-0.7}\,\mathrm{cm}^3\,\mathrm{s}^{-1}$ followed as suggested in `kida.uva.2014` while the branching ratio leading to HC_4NC is assumed to be one-twentieth of that leading to HC_5N, which is based on the branching fractions for producing HC_3N and HCCNC of the HC_3NH^+ DR (Vastel et al., 2019).

[b] HC_4NCH^+ is mainly produced through the reaction between CH_3C_3N and the C^+ ion.

[c] The reaction coefficient of the HC_4NCH^+ DR is assumed to have the same rate coefficient as that of HC_5NH^+: $2.0 \times 10^{-6}(T/300)^{-0.7}\,\mathrm{cm}^3\,\mathrm{s}^{-1}$, while the branching ratio is assumed to be similar to that of HC_2NCH^+, which is included in `kida.uva.2014`.

[d] Rate coefficient estimated from Equation (2.11) with μ of 3.24 D and α of 10.3501 $\mathrm{Å}^3$.

[e] Rate coefficient same as the family reacting with atomic carbon (Loison et al., 2014b).

[f] Rate coefficient same as that of the HCCNC + CRPh and HCCNC + Photon reactions in `kida.uva.2014` respectively.

2.5 Summary

In this chapter, we report the astronomical detection of HC_4NC for the first time in the interstellar medium using the GOTHAM survey at a minimum significance of $10.5\,\sigma$. Three emission features above the noise level of the observations are assigned to HC_4NC. Our analysis indicates a total of four distinct velocity components contribute to the emission signal observed for this species. The observed ratio between HC_4NC and its cyanopolyyne counterpart HC_5N is $\sim 0.49^{+1.32}_{-0.19}\%$ while the observed relative abundance ratio between HCCNC and HC_3N is $\sim 2.2^{+0.7}_{-0.4}\%$.

The synthesis of the HC_4NC molecule is linked to the chemistry of the protonated cyanides and isocyanides. We attempted to reproduce the observed abundances of the selected cyano- and isocyanopolyynes with the inclusion of dissociative recombination as major formation routes and ion-molecule reactions, as well as reactions with atomic carbon as dominant destruction routes. We are aware that HC_3N and HC_5N have different dominant formation pathways whereas the chemical network of HC_4NC in the current study is assumed to be analogous to that of HCCNC. The similar molecular structure of the two isocyanopolyynes makes it the best assumption we can posit.

The chemical modelling presented reproduces the observed abundance of HC_4NC within an order of magnitude. The result of the chemical modelling suggests that the considered formation and destruction routes are reasonable and relevant for HC_4NC and has enabled us to constrain the reaction rate coefficients to some extent. With the increasing number of detected cyano- and isocyanopolyynes in astronomical environments, accurate laboratory measurements of the rate coefficients and branching ratios for reactions of interest would certainly help to better reproduce the observed results.

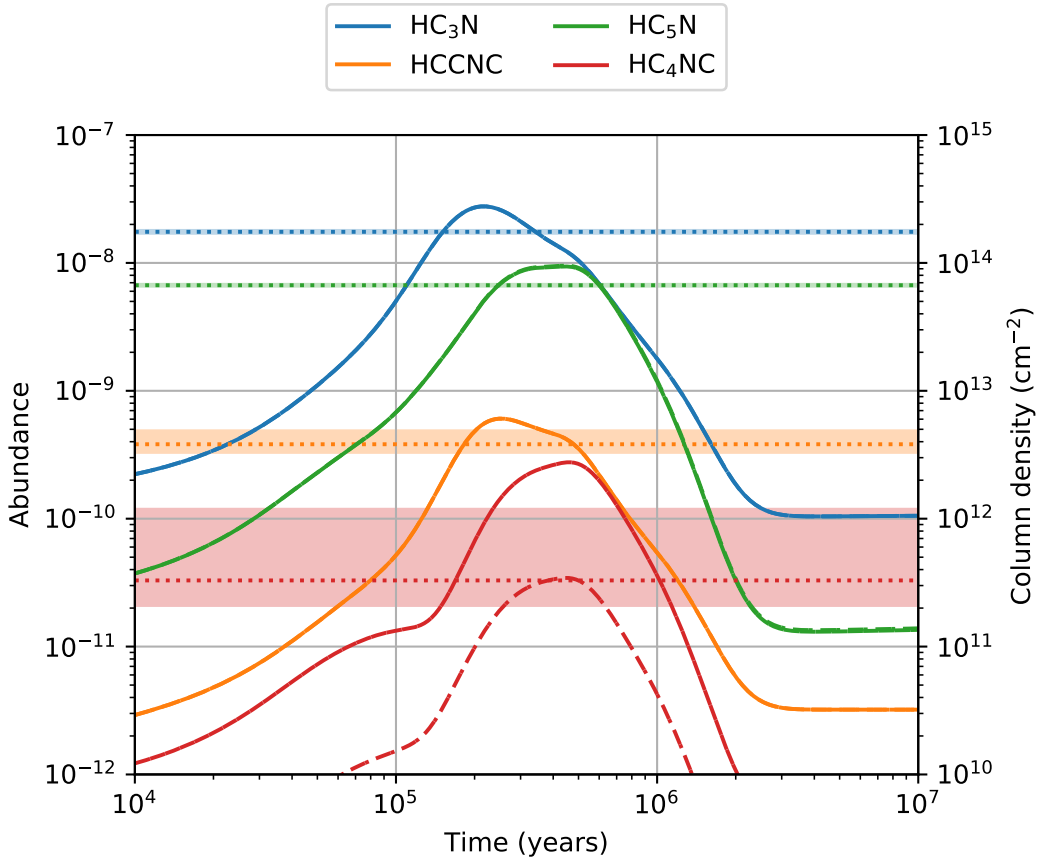

Figure 2.3: The observed and predicted abundances of HC_3N, HC_5N, HCCNC, and HC_4NC are shown in blue, orange, green, and red respectively. The dotted lines and the shaded regions correspond to the mean and the $1\,\sigma$ range of the observed abundances. The solid and dashed lines represent two models with HC_5N/HC_4NC branching ratios for HC_5NH^+ DR of 20 and 200 respectively. Note that the predicted abundances of HC_3N, HC_5N, and HCCNC from the two models overlap and are indistinguishable in the figures.

2.6 Acknowledgments

A.M.B. acknowledges support from the Smithsonian Institution as a Submillimeter Array (SMA) Fellow. M.C.M and K.L.K.L. acknowledge financial support from NSF grants AST-1908576, AST-1615847, and NASA grant 80NSSC18K0396. Support for B.A.M. was provided by NASA through Hubble Fellowship grant #HST-HF2-51396 awarded by the Space Telescope Science Institute, which is operated by the Association of Universities for Research in Astronomy, Inc., for NASA, under contract NAS5-26555. C.N.S. thanks the Alexander von Humboldt Stiftung/Foundation for their generous support, as well as V. Wakelam for use of the `NAUTILUS` v1.1 code. C.X. is a Grote Reber Fellow, and support for this work was provided by the NSF through the Grote Reber Fellowship Program administered by Associated Universities, Inc./National Radio Astronomy Observatory and the Virginia Space Grant Consortium. E.H. thanks the National Science Foundation for support through grant AST 1906489. S.B.C. and M.A.C. were supported by the NASA Astrobiology Institute through the Goddard Center for Astrobiology. The National Radio Astronomy Observatory is a facility of the National Science Foundation operated under cooperative agreement by Associated Universities, Inc. The Green Bank Observatory is a facility of the National Science Foundation operated under cooperative agreement by Associated Universities, Inc.

2.7 Appendix: MCMC Fitting Detail for HC_4NC

A total of 13 transitions (including hyperfine components) of HC_4NC were covered by GOTHAM observations at the time of analysis and were above the predicted flux threshold of 5%, as discussed in Loomis et al. (2021). Of these transitions, none were coincident with interfering transitions of other species, and thus a total of 13 transitions were considered. Observational data windowed around these transitions, spectroscopic properties of each transition, and the partition function used in the MCMC analysis are provided in the Harvard Dataverse repository (GOTHAM Collaboration, 2020). A corner plot of the parameter covariances and their distribution for the HC_4NC MCMC fit is shown in Figure 2.4. Worth noting are the strong covariances between the column density and the source size for sources #2 and #4. The poor constraint on these source sizes leads to a large uncertainty in the total column density. Future detections of lines at lower or higher frequencies to anchor the source size fit (through measured beam dilution) would greatly enhance the precision of the column density measurement.

2.8 Appendix: HCCNC Analysis Results

An identical analysis to that for HC_4NC was carried out for HCCNC. Six emission features contributed by the nine rotational transitions (including hyperfine components) of HCCNC are well-detected above the noise, as shown in Figure 2.5. The top three panels are the three hyperfine components of the 1 – 0 transition respectively while the bottom panel shows all the hyperfine components of the 3 – 2 transition. The spectroscopic properties of the nine transitions are summarized in Table 2.6.

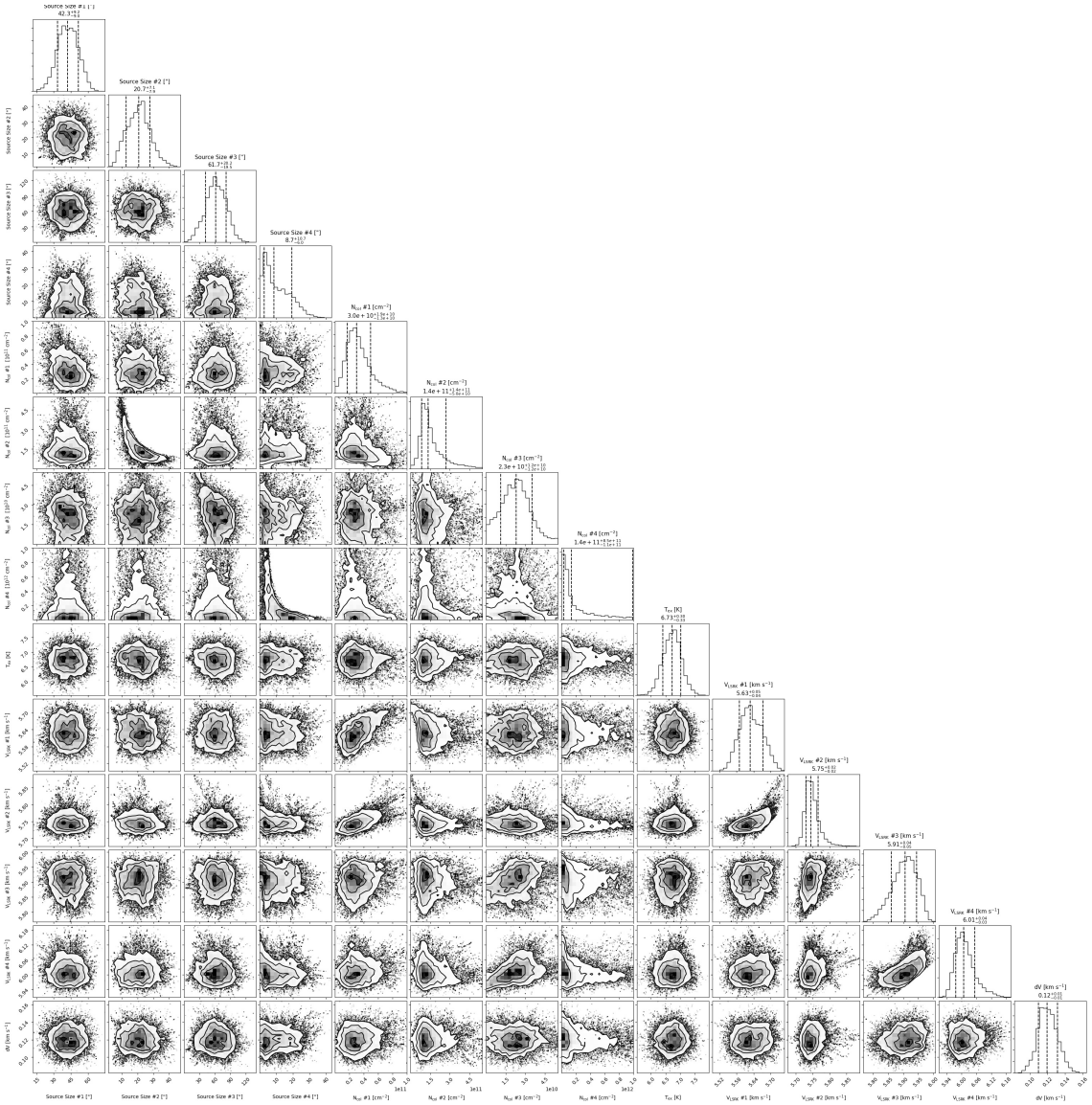

Figure 2.4: Parameter covariances and marginalized posterior distributions for the HC_4NC MCMC fit. 16^{th}, 50^{th}, and 84^{th} confidence intervals (corresponding to $\pm 1\,\sigma$ for a Gaussian posterior distribution) are shown as vertical lines.

Table 2.6: Spectroscopic Properties of the HCCNC lines

Transitions J' → J''	Transitions F' → F''	Frequency (MHz)	$E_{\rm up}$ (K)	$\log_{10}\frac{A_{\rm ul}}{\rm s^{-1}}$	$S_{ij}\mu^2$ ($\rm D^2$)
1 → 0	0 → 1	9935.2000(150)	0.48	-7.4859	2.86
1 → 0	2 → 1	9935.6270(150)	0.48	-7.4859	14.31
1 → 0	1 → 1	9935.9100(150)	0.48	-7.4858	8.59
3 → 2	2 → 2	29806.5354(122)	2.86	-6.7535	2.86
	2 → 3	29806.8398(39)	2.86	-8.2976	0.08
	4 → 3	29806.9503(20)	2.86	-5.9454	33.11
	3 → 2	29806.9615(20)	2.86	-5.9965	22.89
	2 → 1	29807.0089(25)	2.86	-6.0211	15.45
	3 → 3	29807.2660(89)	2.86	-6.8996	2.86

NOTE — The spectroscopic data of the HCCNC transitions corresponding to the six detected lines are taken from the JPL catalogue[2] and the SPLATALOGUE spectroscopy database, which are based on the FTMW and millimetre-wave measurements of Guarnieri et al. (1992) and Kruger et al. (1993).

Of these transitions, 6 transitions are above the 5% threshold, which was uniformly applied to the whole GOTHAM dataset, and were therefore considered for the MCMC fitting and spectral stacking process, the data used in which are available in GOTHAM Collaboration (2020). The resulting best-fit parameters are given in Table 2.7. The noise level of the $1_0 \rightarrow 0_1$ spectrum is ~3 mK, which accounts for the apparent difference seen between the constructed and observed profiles. The stacked spectrum and matched filter results are shown in Figure 2.6, while a corner plot of the parameter covariances for the HCCNC MCMC fit is shown in Figure 2.7.

2.9 Appendix: HC_6NC Analysis Results

Following the similar line-selection process with HC_4NC, a total of 10 transitions (including hyperfine components) of HC_6NC were considered and the data are again available in GOTHAM Collaboration (2020). In our observation, no signal beyond

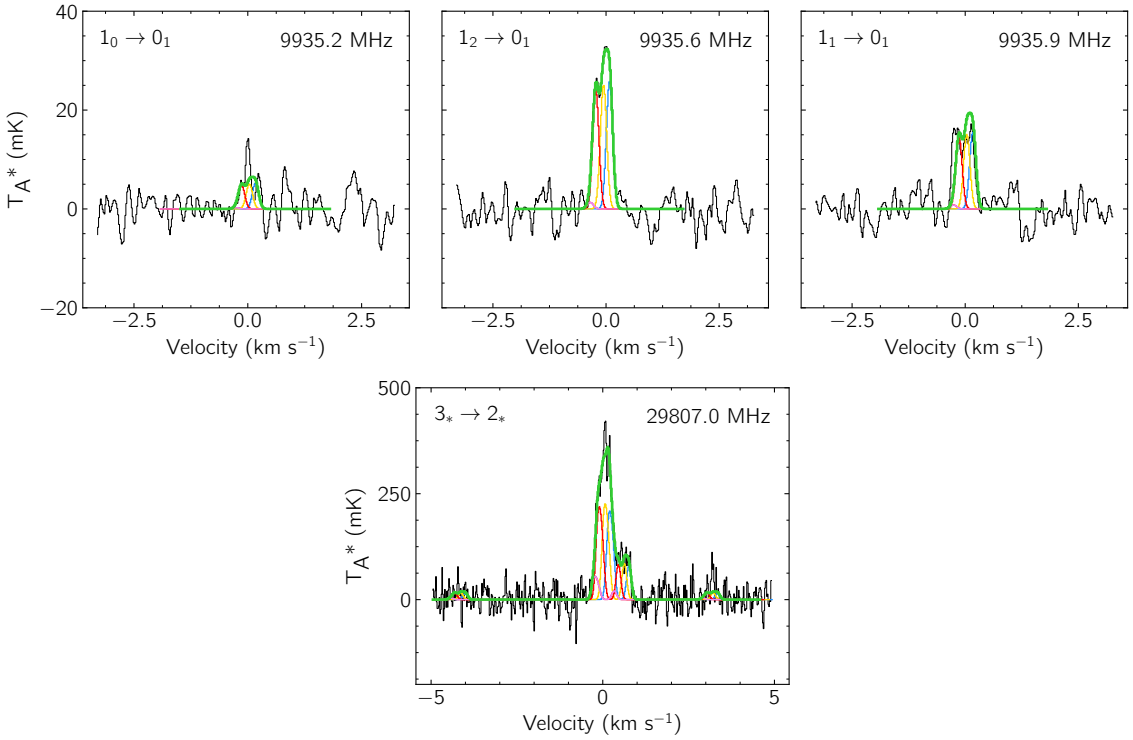

Figure 2.5: Similar with Figure 2.1. Individual line detections of HCCNC in the GOTHAM data. The observed spectra (black) are displayed in velocity space relative to 5.8 km s^{-1} and the simulated spectra of the individual velocity components are shown in blue (5.62 km s^{-1}), yellow (5.76 km s^{-1}), red (5.93 km s^{-1}), and violet (6.05 km s^{-1}), which are summarized in Table 2.7, with the best-fit model including all velocity components overlaid in green.

Table 2.7: HCCNC best-fit parameters from the MCMC analysis

Component	$V_{\rm lsr}$ ($\rm km\,s^{-1}$)	Size ($''$)	$N_{\rm T}$ [a] ($10^{12}\,\rm cm^{-2}$)	$T_{\rm ex}$ (K)	ΔV ($\rm km\,s^{-1}$)
C1	$5.622^{+0.016}_{-0.011}$	140^{+34}_{-27}	$0.97^{+0.18}_{-0.16}$	$6.9^{+0.3}_{-0.3}$	$0.166^{+0.017}_{-0.014}$
C2	$5.756^{+0.022}_{-0.020}$	117^{+38}_{-25}	$1.04^{+0.15}_{-0.16}$		
C3	$5.926^{+0.015}_{-0.017}$	110^{+40}_{-23}	$1.06^{+0.16}_{-0.19}$		
C4	$6.051^{+0.066}_{-0.045}$	17^{+26}_{-9}	$0.75^{+1.02}_{-0.44}$		
$N_{\rm T}$(Total)[b]	$3.82^{+1.06}_{-0.53} \times 10^{12}\,\rm cm^{-2}$				

NOTE — The quoted uncertainties represent the 16^{th} and 84^{th} percentile ($1\,\sigma$ for a Gaussian distribution) uncertainties, which are derived with the same methods mentioned in Table 2.3. See Figure 2.7 for a covariance plot.

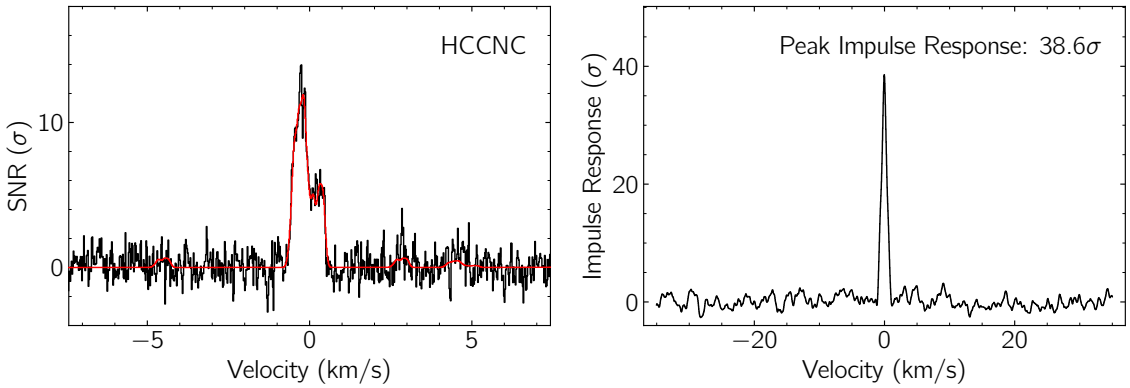

Figure 2.6: Similar with Figure 2.2. *Left:* Velocity-stacked spectra of HCCNC in black, with the corresponding stack of the simulation using the best-fit parameters to the individual lines in red. *Right:* Impulse response function of the stacked spectrum using the simulated line profile as a matched filter. The peak of the impulse response function provides a minimum significance for the detection of $38.6\,\sigma$.

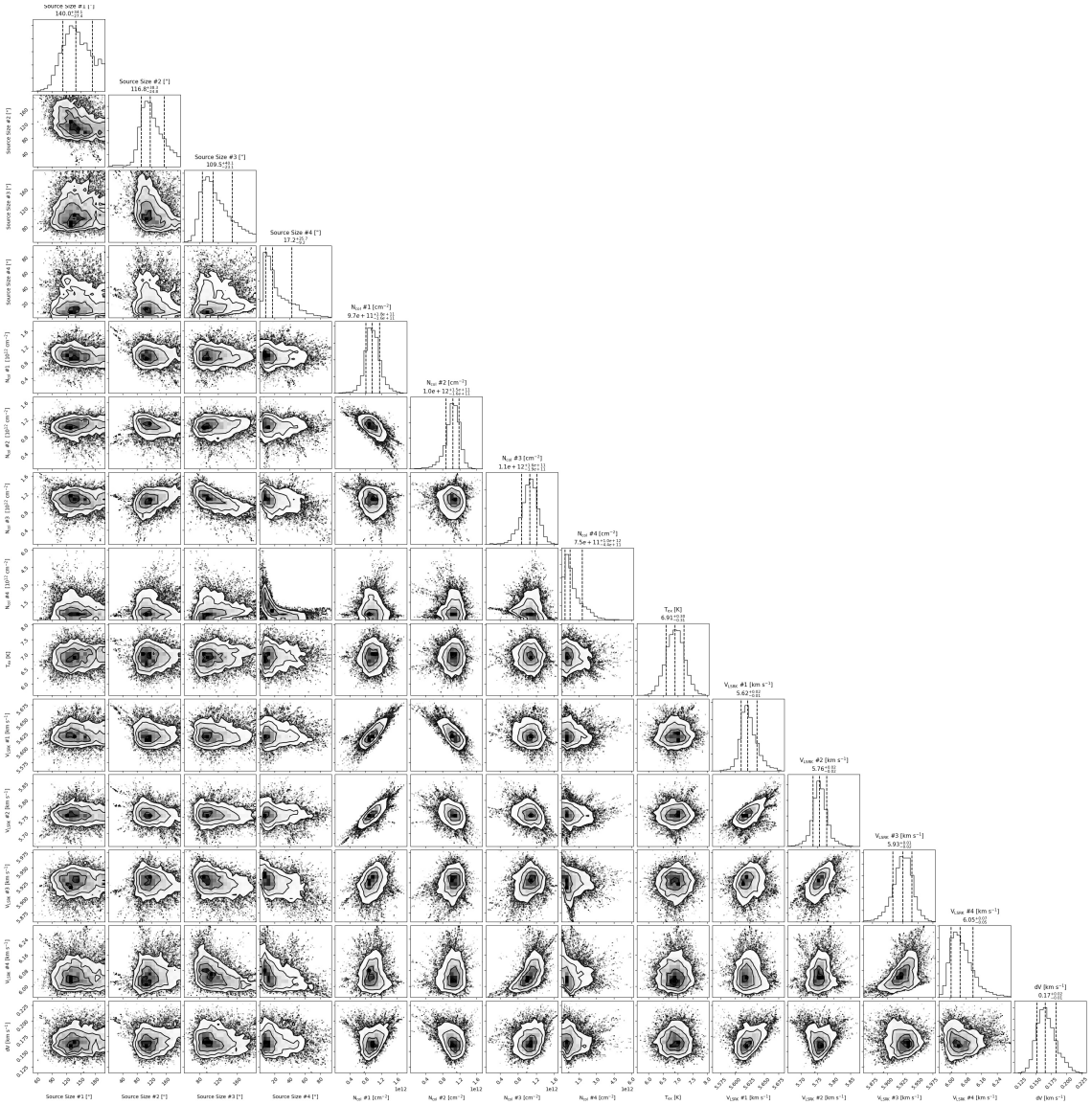

Figure 2.7: Parameter covariances and marginalized posterior distributions for the HCCNC MCMC fit. 16^{th}, 50^{th}, and 84^{th} confidence intervals (corresponding to $\pm 1\,\sigma$ for a Gaussian posterior distribution) are shown as vertical lines.

Table 2.8: HC_6NC derived upper limit column densities from the MCMC analysis

Component	$V_{\rm lsr}$ ($\rm km\,s^{-1}$)	Size ($''$)	$N_{\rm T}$ [a] ($10^{11}\,\rm cm^{-2}$)	$T_{\rm ex}$ (K)	ΔV ($\rm km\,s^{-1}$)
C1	[5.624]	[33]	<0.65	[6.5]	[0.117]
C2	[5.790]	[22]	<0.64		
C3	[5.910]	[50]	<0.35		
C4	[6.033]	[18]	<2.39		
$N_{\rm T}$(Total)[b]	$< 4.04 \times 10^{11}\,\rm cm^{-2}$				

NOTE — Upper limits are given as the 97.8^{th} percentile ($2\,\sigma$) value. Parameters in brackets were held fixed to the 50^{th} percentile value. See Figure 2.8 for a covariance plot.

a $1\,\sigma$ detection limit can be assigned to HC_6NC. Column density upper limits are therefore constrained using the modified fitting process described in Loomis et al. (2021), the results of which are given in Table 2.8. A corner plot of the parameter covariances for the HC_6NC MCMC fit is shown in Figure 2.8.

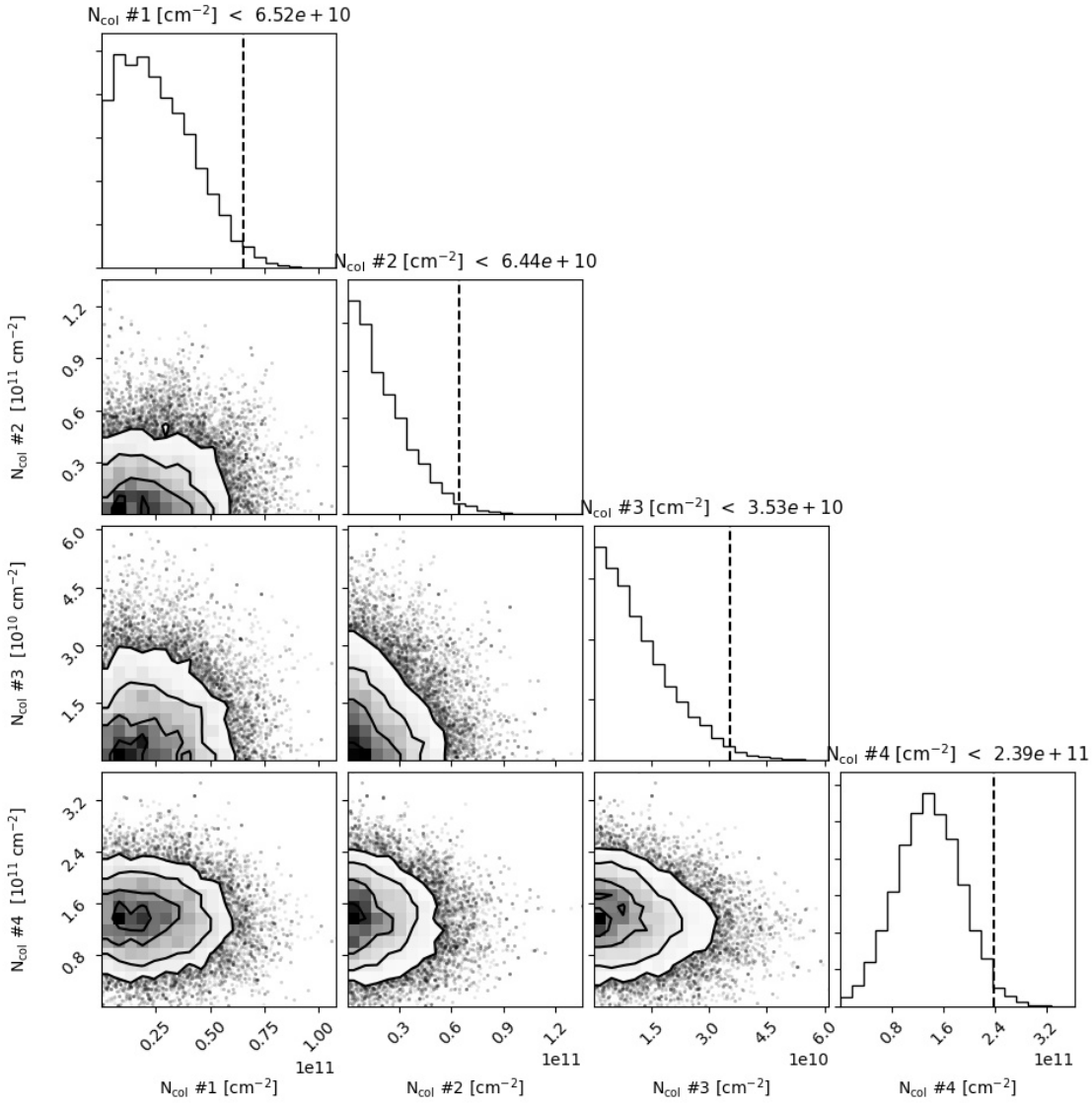

Figure 2.8: Parameter covariances and marginalized posterior distributions for the HC_6NC MCMC fit. The 97.8^{th} confidence interval (corresponding to $2\,\sigma$ for a Gaussian posterior distribution) is shown as a vertical line.

Chapter 3

Confirmation of H_2C_3S Detection and H_2C_NS Molecular Family

3.1 Introduction

The sulfur depletion problem has long been a puzzle of the chemistry in dense clouds (Ruffle et al., 1999; Vidal et al., 2017). The elemental sulfur abundance shows excellent consistency among the solar system (S/H of $1.41 \pm 0.03 \times 10^{-5}$, Asplund et al., 2005) and the diffuse interstellar medium (S/H of $1.35 \pm 0.09 \times 10^{-5}$, Howk et al., 2006). On the contrary, in dense dark clouds, the sulfur budget probed by gas-phase sulfur(S)-bearing molecules only account for a tiny fraction of the cosmic elemental sulfur abundance. While there are hypotheses that the missing sulfur is on dust grains and/or in its atomic form, detailed infrared observations have found very few S-bearing molecules on ice mantles (Vastel et al., 2018b; Shingledecker et al., 2020, and reference therein). Modern astrochemical models also have to adopt a depleted S/H value of 8×10^{-8} in order to reproduce the chemistry under dark cloud conditions (Agúndez & Wakelam, 2013), rendering the mystery unsolved. Therefore, it remains

important to search for new unknown S-bearing molecules and rigorously determine the abundances of the known S-bearing species.

The study of interstellar sulfur-bearing molecules has become a hot topic lately on both observational and theoretical sides (e.g. Luo et al., 2019; McGuire et al., 2019; Margulès et al., 2020; Lorand et al., 2020). Notably, the very recent discoveries of H_2C_2S and H_2C_3S along with other four S-bearing species in the dark cloud TMC-1 have expanded the sulfur molecular inventory and characterized the previously unknown richness of sulfur chemistry in dark clouds (Cernicharo et al., 2021a,b). Furthermore, of the H_2C_nS family, quantum chemical calculation and astrochemical kinetics modeling suggest an efficient but exclusive destruction pathway of H_2C_2S with atomic hydrogen (Shingledecker & Kang, in preperation). The diverse chemical behaviours of this family by itself is worth a throughout investigation of their molecular abundance ratios and a systematic investigation of this family can certainly enrich our understanding of the sulfur chemistry of dark clouds.

The simplest member, H_2CS, was firstly detected in interstellar medium (ISM) in 1973 by Sinclair et al. (1973) and towards TMC-1 in 1989 by Irvine et al. (1989). The spectral line survey of TMC-1 performed with the 45 m telescope at the Nobeyama Radio Observatory subsequently detected the $J_{K_a,K_c} = 1_{0,1} - 0_{0,0}$ transition of H_2CS at 34.3 GHz (Kaifu et al., 2004). Later, Gratier et al. (2016) imposed a $N_{\rm T}$ of $4.17^{+9.96}_{-1.08} \times 10^{13}\,{\rm cm}^{-2}$ using Kaifu's data. It remained the only known member until very recent discovery of the second and third member, H_2C_2S and H_2C_3S reported with the Yebes 40 m telescope observations (Cernicharo et al., 2021b). The column densities were suggested to be $7.8 \pm 0.8 \times 10^{11}\,{\rm cm}^{-2}$ for H_2C_2S and $3.7 \pm 0.4 \times 10^{11}\,{\rm cm}^{-2}$ for H_2C_3S respectively. However, comparisons of molecular ratios of the H_2C_nS family between different telescopes suffer from differences in beam dilution corrections and beam efficiencies. For example, a Gaussian source with an FWHM of $160''$ was as-

sumed in Kaifu et al. (2004), whereas a source size of $40''$ was adopted in Cernicharo et al. (2021b).

Moreover, these observations also suffered from the limited spectral resolutions, which prevent us from precisely constraining the excitation conditions and column densities of these molecules. Recently, the high spectral resolution observations of the CCS and HC_3N emission lines performed with the Nobeyama 45 m telescope revealed multiple cloud components with distinct systematic velocities toward TMC-1 CP (Dobashi et al., 2018). The detailed analysis of the spectra from the GOTHAM program confirmed the presence of up to four individual velocity components for all molecules in the survey (Loomis et al., 2021). The low frequency resolution of the previous observations of H_2C_nS, ~40 kHz (corresponding to 0.35 $km\,s^{-1}$ at 34 GHz), was insufficient to resolve the multiple velocity components where adjacent components can be separated by as close as ~0.1 $km\,s^{-1}$. The poor characterization of the emission profile makes the assignments of column densities among components impossible and leads to a high degree of uncertainties in the analysis of sulfur chemistry in TMC-1.

In this chapter, we confirm the detection of H_2C_3S and present a rigorously investigation of the H_2C_nS molecular family for n = 1, 2, and 3 toward TMC-1 with an uniform set of high-resolution observations. In Section 3.2, we describe the used spectroscopy data of H_2C_3S and the molecular properties of the three H_2C_nS molecules. Section 3.3 describes the observing strategy and Section 3.4 presents the observational results of three molecules. The abundance ratios among the H_2C_nS family and the differences in chemistry among the TMC-1's sub-components are discussed in Section 3.5.

Table 3.1: Properties of thioformaldehyde, thioketene, and thiopropadienone

Molecules	α (Å^3) [a]	μ_e (D) [a] (calc)	μ_e (D) (exp)	Reference
H_2CS	4.450	1.68	1.6491	Fabricant et al. (1977)
H_2C_2S	6.551	1.01	1.01	Winnewisser & Schäfer (1980)
H_2C_3S	9.329	2.12	2.064	Brown et al. (1988)

[a] Entries are based on cc-pVQZ calculations using `CFOUR` done in this work.

3.2 Spectroscopic Properties

For this work, transition frequencies of H_2CS, H_2C_2S, and H_2C_3S were taken from the CDMS catalog (Müller et al., 2005). In particular, the entry of H_2C_3S was based on Fourier transform microwave (FTMW) spectroscopy data and *ab initio* calculations reported by Botschwina et al. (1998). We performed the calculations with the `CFOUR` suite of electronic structure programs (Stanton et al., 2017), employing the coupled-cluster method with single, double, and perturbative triple excitations [CCSD(T)] under the frozen-core approximation, paired with a Dunning's cc-pVQZ basis set (Xue et al., 2020). At this level of theory, we re-examine equilibrium electric dipole moments and average dipole polarizabilities of H_2C_nS for n = 1, 2, and 3, as listed in Table 3.1. The calculated dipole moments of these species are consistent with the values measured with laboratory stark effect measurements (Fabricant et al., 1977; Winnewisser & Schäfer, 1980; Brown et al., 1988). The other spectroscopic information of the observed transitions are listed in Table 3.2.

3.3 GBT Observations

Two sets of data were used to investigate the three members of the H_2C_nS family: the GOTHAM observations as well as a Director's Discretionary Time (DDT)

observation. All the observations were performed with the Robert C. Byrd 100 m Green Bank Telescope and directed toward the TMC-1 cyanopolyyne peak (CP) centered at $\alpha_{\rm J2000} = 04^{\rm h}41^{\rm m}42.5^{\rm s}$, $\delta_{\rm J2000} = 25^{\circ}41'26.8''$, where the column densities of the carbon-chain species peak.

The first and second data reduction of the large observational program GOTHAM (hereafter referred as DR1 and DR2) comprise observations obtained between February 2018 - May 2019 (DR1) and May 2019 - June 2020 (DR2). Detailed information concerning the GOTHAM DR1 and DR2 observations and the data calibration can be found in McGuire et al. (2020, 2021). The GOTHAM observations used here are the third data reduction with completed observations through April 2021 (hereafter referred as DR3), which extended the frequency coverage to $7.906 - 35.434$ GHz with a few gaps and improved the sensitivity in some frequency coverage already covered by DR2. The beam size varies between $\sim 90''$ at 8 GHz and $\sim 20''$ at 35 GHz. At a uniform 0.05 km s^{-1} velocity resolution, the RMS noise ranges from $\sim 2 - 20$ mK across the dataset.

In parallel, a supportive Ka-Band DDT observation with frequency coverage of $33.296 - 35.433$ GHz (Project code: GBT21A-414) was proposed dedicatedly for the principle transitions of H_2CS. The observation was performed on 2021 April 13 with the Ka-band receiver with a requested 1.431 kHz resolution (corresponding to 0.0125 km s^{-1} at 34 GHz). The pointing and focus calibrator was J0359+5057. Data were taken in the position-switching mode with the off reference position throw of 1°. The spectra were smoothed to a 0.05 km s^{-1} resolution for consistency with the GOTHAM data sets and had an RMS noise level of $\sim$40 mK.

Table 3.2: Spectroscopic Properties of Observed H_2C_nS Transitions

Molecule	Transitions $J_{K_a,Kc}$	Rest Frequency (MHz)	$E_{\rm up}$ (K)	$\log_{10}\frac{A_{ul}}{\rm s^{-1}}$	$S_{ij}\mu^2$ (D^2)	Setup
H_2CS	$1_{0,1} \rightarrow 0_{0,0}$	34351.4300(200)	1.65	-6.369	2.719	DDT
H_2C_2S	$2_{1,2} \rightarrow 1_{1,1}$	22292.3150(200)	15.09	-7.404	4.591	GOTHAM #4
	$2_{0,2} \rightarrow 1_{0,1}$	22407.9070(200)	1.61	-7.272	2.040	GOTHAM #4
	$2_{1,1} \rightarrow 1_{1,0}$	22522.2220(200)	15.11	-7.390	4.591	GOTHAM #4
	$3_{1,3} \rightarrow 2_{1,2}$	33438.3700(200)	16.70	-6.772	8.161	GOTHAM #17
	$3_{0,3} \rightarrow 2_{0,2}$	33611.7000(200)	3.23	-6.714	3.060	DDT
	$3_{1,2} \rightarrow 2_{1,1}$	33783.2300(200)	16.73	-6.758	8.161	DDT
H_2C_3S	$5_{1,5} \rightarrow 4_{1,4}$	25215.0579	19.27	-6.460	61.347	GOTHAM #6
	$5_{0,5} \rightarrow 4_{0,4}$	25274.6794	3.64	-6.439	21.301	GOTHAM #6
	$5_{1,4} \rightarrow 4_{1,3}$	25333.0329	19.29	-6.454	61.345	GOTHAM #6
	$6_{1,6} \rightarrow 5_{1,5}$	30258.0232	20.73	-6.210	74.553	GOTHAM #13
	$6_{0,6} \rightarrow 5_{0,5}$	30329.5584	5.09	-6.195	25.561	GOTHAM #13
	$6_{1,5} \rightarrow 5_{1,4}$	30399.5932	20.75	-6.204	74.543	GOTHAM #13

NOTE — The spectroscopic data are taken from the CDMS catalogue (Müller et al., 2005) and the SPLATALOGUE spectroscopy database [1].

3.4 Results

3.4.1 Thioformaldehyde (H_2CS)

The principle transition of H_2CS ($J_{K_a,K_c} = 1_{0,1} - 0_{0,0}$ at 34351.417 MHz was firstly detected in the spectral survey toward TMC-1 CP performed with the Nobeyama telescope (Kaifu et al., 2004). The observed line profile obtained with the Nobeyama telescope is shown in Figure 3.1(b). From the Nobeyama observation, Gratier et al. (2016) obtained a column density of $4.17^{+9.96}_{-1.08} \times 10^{13}\mathrm{cm}^{-2}$ for H_2CS with a T_{ex} of $5.16^{+1.55}_{-1.55}$ K. However, limited by the spectral resolution, the Nobeyama observation prevented their analysis from characterizing the emission profiles and, therefore, observed behaviours of each velocity component. Moreover, the frequency coverage of GOTHAM covered no transitions of H_2CS with intensities over the noise levels.

Therefore, a supportive GBT observation at the same spectral resolution with the GOTHAM program (~1.4 kHz) was performed to self-consistently determine the column density and excitation conditions of H_2CS with other H_2C_nS family members. The observed spectrum of the $J_{K_a,Kc} = 1_{0,1} - 0_{0,0}$ transition of H_2CS with multi-peak features is shown in Figure 3.1(a). The high spectral resolution enabled us to resolve four sub-components with distinct velocity. The synthetic spectra simulated with four velocity components are overlaid in Figure 3.1(a) with a velocity difference of $>0.1\,\mathrm{km\,s^{-1}}$. A total column density of H_2CS was determined to be $(5.24 \pm 1.09) \times 10^{13}\,\mathrm{cm}^{-2}$ with a T_{ex} of ~5.2 K, while the observed properties per each velocity component are summarised in Table 3.3.

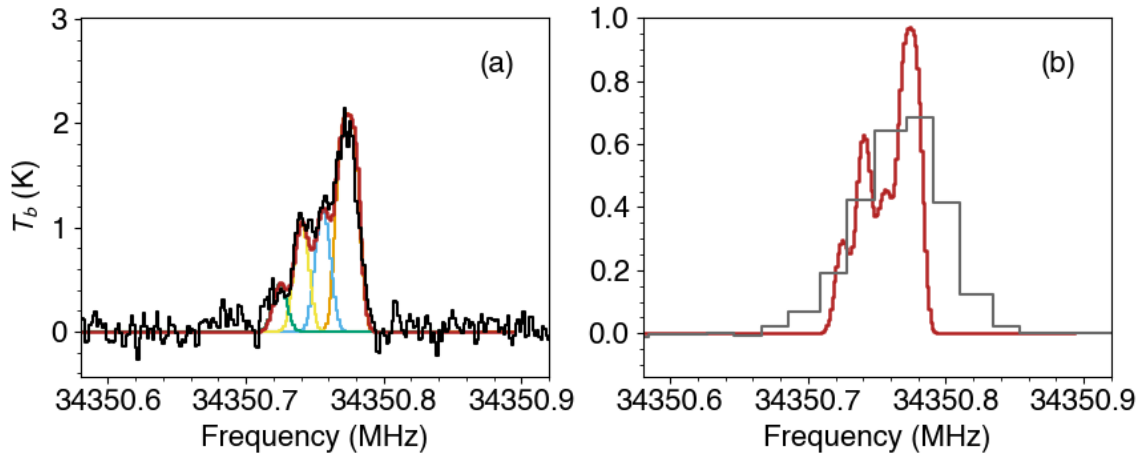

Figure 3.1: The observed spectra of H_2CS from the GBT data shown in black in panel (a) while the Nobeyama observation (Kaifu et al., 2004) shown in grey in panel (b). The best-fit simulated spectra of the individual velocity components are shown in: orange ($5.61\,\mathrm{km\,s^{-1}}$), blue ($5.79\,\mathrm{km\,s^{-1}}$), yellow ($5.91\,\mathrm{km\,s^{-1}}$), and green ($6.04\,\mathrm{km\,s^{-1}}$). The sum of all four velocity components is overlaid in red. The simulated spectrum with multiple velocity components scaled with beam dilution effect is also shown in panel (b) for illustration.

Table 3.3: H_2CS best-fit parameters from the MCMC analysis

Component	$V_{\rm lsr}$ ($\mathrm{km\,s^{-1}}$)	Size ($''$)	$N_{\rm T}$ [a] ($10^{13}\,\mathrm{cm^{-2}}$)	$T_{\rm ex}$ (K)	ΔV ($\mathrm{km\,s^{-1}}$)
C1	5.608 ± 0.007	65.3 ± 63.6	3.51 ± 0.14	5.2 ± 0.5	0.120 ± 0.006
C2	5.792 ± 0.011	47.0 ± 61.9	0.92 ± 0.36		
C3	5.906 ± 0.018	146.2 ± 117.6	0.60 ± 0.38		
C4	6.039 ± 0.011	234.8 ± 104.3	0.22 ± 0.21		
$N_{\rm T}$(Total)[b]	$(5.24 \pm 1.09) \times 10^{13}\,\mathrm{cm^{-2}}$				

NOTE — The quoted uncertainties represent the $1\,\sigma$ uncertainties for a Gaussian distribution.

3.4.2 Thiopropadienone (H_2C_3S)

As presented in Figure 3.2, we identified three H_2C_3S emission features above the observational noise levels with the GOTHAM DR3. The stacking and match-filtering results of H_2C_3S are shown in Figure 3.3. Assisted by the joint effort of the deep observations and the detection techniques, the detection significance of H_2C_3S of $\sim 9\,\sigma$ was achieved. One caveat of this detection, however, is that there is a possible interfering line from DCC^{13}CN $J = 3 - 2$ toward the 25215 MHz emission feature. Since it is the only transition of DCC^{13}CN with detectable intensities in our current data, it cannot be ruled out as a possible contribution. With the knowledge of the HC_3N abundance ($(1.8 \pm 0.05) \times 10^{14}$, Loomis et al., 2021), the deuterium ratio (i.e. DC_3N:HC_3N of 1.41%, Turner, 2001), and the ^{13}C ratio (i.e. HCC^{13}CN:HC_3N of 1.30%, Takano et al., 1998), a column density of $3.3 \times 10^{10}\,\mathrm{cm}^{-2}$ was estimated for DCC^{13}CN. Using this value, a synthetic spectrum was constructed, which matches with the residual after the H_2C_3S emission was subtracted (shown in Figure 3.2). A detailed discussion of the detections of cyanopolyynes isotopologues with the GOTHAM observations will be presented in Burkhardt et al. (in preparation).

A total of six H_2C_3S tranistions were covered by the GOTHAM observations, of which the spectroscopic properties is summarized in Table 3.2. The transitions were used to rigorously determine the molecular abundance and excitation conditions using the MCMC fitting method described in Section 2.3.1 and Loomis et al. (2021). A total column density of $4.17 \times 10^{11}\,\mathrm{cm}^{-2}$ was determined for H_2C_3S with a warmer T_{ex} of 8.8 K compared with that for H_2CS. The resulting best-fit parameters of each velocity component of H_2C_3S are listed in Table 3.4.

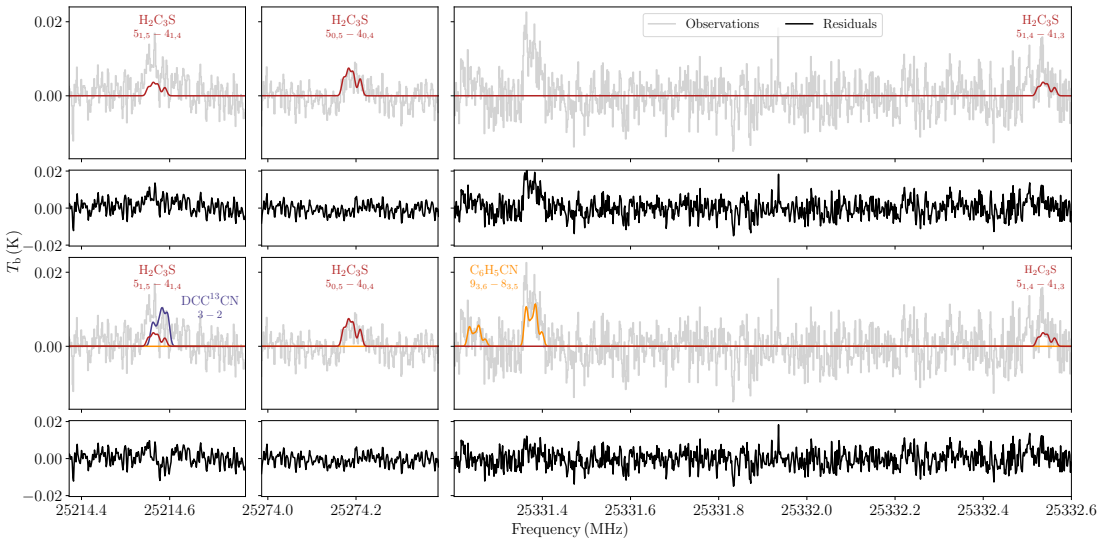

Figure 3.2: The observed spectra of H_2C_3S from the GOTHAM DR3 data. The observation is shown in grey while the residual spectra are shown in black. The best-fit simulated spectra of each molecule are shown in colors with the corresponding quantum numbers.

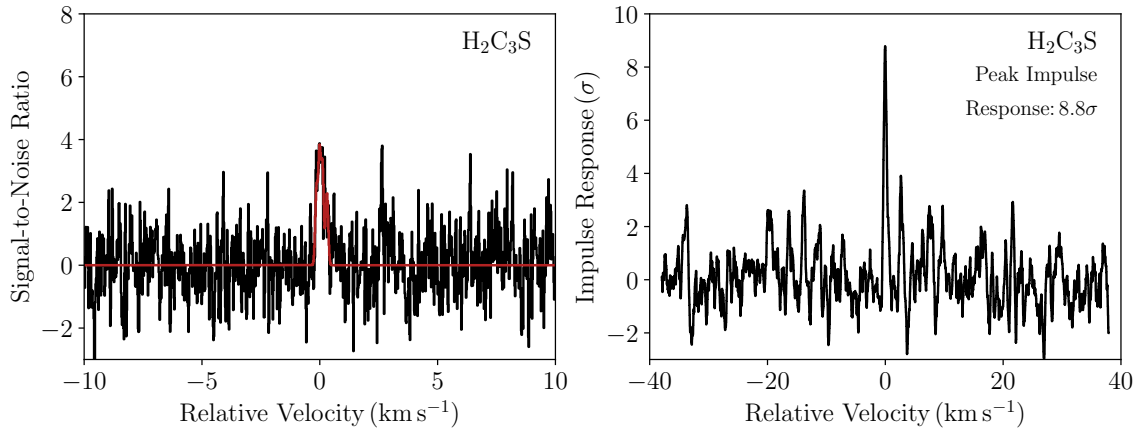

Figure 3.3: Left: velocity-stacked spectrum of H_2C_3S from the GOTHAM DR3 data in black, overlaid with the corresponding stack of the synthetic line profiles from the MCMC analysis in red. The spectra are shown relative to the TMC-1 systemic velocity of 5.8 km s^{-1}. The intensity scale is the signal-to-noise ratio on a per-channel basis. Right: impulse response function of the stacked spectrum using the synthetic line profile as a matched filter. The intensity scale is the signal-to-noise ratio of the response function when centered at a given velocity. The peak of the impulse response function provides a minimum significance for the detection of 8.8 σ for H_2C_3S.

Table 3.4: H_2C_3S best-fit parameters from the MCMC analysis

Component	$V_{\rm lsr}$ ($\rm km\,s^{-1}$)	Size ($''$)	$N_{\rm T}$ [a] ($10^{11}\,\rm cm^{-2}$)	$T_{\rm ex}$ (K)	ΔV ($\rm km\,s^{-1}$)
C1	5.576 ± 0.025	69.9	0.95 ± 0.10	8.8 ± 0.2	0.125 ± 0.003
C2	5.765 ± 0.014	98.0	1.18 ± 0.27		
C3	5.890 ± 0.013	254.0	1.22 ± 0.08		
C4	6.020 ± 0.012	259.5	0.82 ± 0.37		
$N_{\rm T}$(Total)[b]	$(4.17 \pm 0.40) \times 10^{11}\,\rm cm^{-2}$				

NOTE — The quoted uncertainties represent the $1\,\sigma$ uncertainties for a Gaussian distribution.

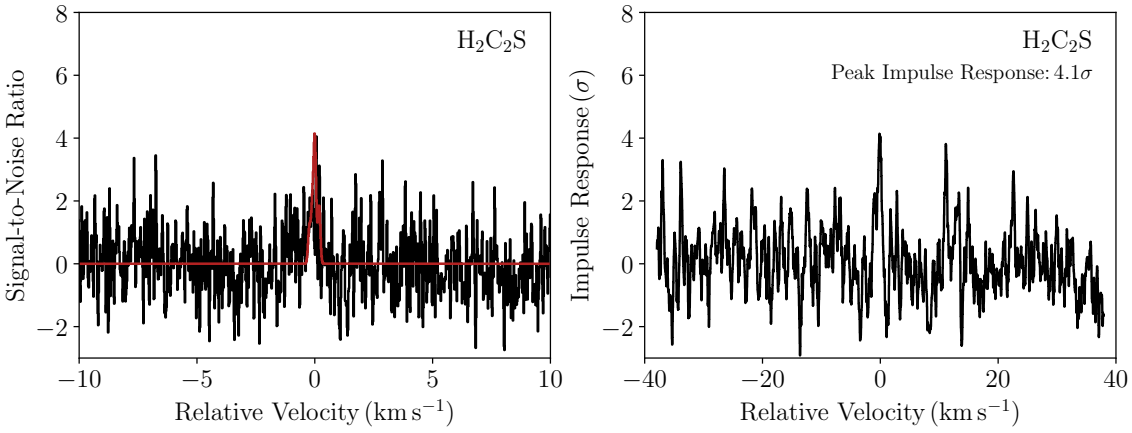

Figure 3.4: Left: velocity-stacked spectra of H_2C_2S. Right: impulse response function, the peak of which provides a minimum significance for the detection of 4.1 σ for H_2C_2S.

3.4.3 Thioketene (H_2C_2S)

In our observation, no signal beyond a 1 σ detection limit can be assigned to H_2C_2S. The peak impulse response for H_2C_2S of 4.1 σ prevented us from claiming a firm detection for it (Figure 3.4). Using the posterior of H_2CS as the prior for the MCMC fitting process, we derived an upper limit of $\leq 1.35 \times 10^{12}$ cm^{-2} for H_2C_2S. Recent observations with the Yebes 40 m telescope reported the detection of H_2C_2S toward TMC-1 CP with a total column density of 7.8×10^{11} cm^{-2} (Cernicharo et al., 2021b). While this value is consistent with our upper limit, Yebes' spectral resolution was insufficient to resolve the multi-peak features, so no information regarding each velocity component is available.

3.5 Discussion

It is worth investigating the molecular abundance ratios of the H_2C_nS family because of their diverse chemical behaviors. With our high-resolution observations, a total abundance ratio of [125:1] is determined for [H_2CS:H_2C_3S] toward TMC-1 CP. However, the ratios among the three members of the H_2C_nS family was reported

as [386:2:1] for [H_2CS:H_2C_2S:H_2C_3S] with the Yebes observations (Cernicharo et al., 2021b). The difference in abundance ratios may result from the different treatments of the excitation condition. Cernicharo et al. (2021b) assumed an excitation temperature of 10 K and fitted the observed emission feature with a single Gaussian profile. Correspondingly, we reported a lower excitation temperature, 5.2 K for H_2CS, and resolved four sub-components. Moreover, source size assumptions were not clarified in Cernicharo et al. (2021b). Whereas, through our analysis of all the molecules we have detected with GOTHAM, we have identified strong degeneracy between the molecular column densities for the different velocity components and their corresponding source sizes.

The sulfur chemistry vary among the four sub-components toward TMC-1 CP. The most abundant component for H_2CS is the C1 component whereas it is the C3 component for H_2C_3S. A direct evidence is the distinct emission profiles of H_2CS and H_2C_3S. The skewed emission profile for H_2CS and the symmetric profile for H_2C_3S lead to the conclusion that H_2CS is more abundant in the C1 component whereas H_2C_3S is more abundant in the C2 and C3 components. Different velocity components also exhibit different abundance ratios for [H_2CS:H_2C_3S]. The [H_2CS:H_2C_3S] ratio is [369:1], [78:1], [49:1], and [27:1] for the C1, C2, C3, and C4 component respectively. To confidently infer these ratios, more observations of TMC-1's substructures will be needed.

For a long time, TMC-1 CP had been assumed to be a relatively homogeneous cold, dark, starless cloud with an extended morphology (Bell et al., 1998; McGuire, 2018, and references therein). For the analysis of chemical abundances, most astrochemical models assumed that the physical conditions of TMC-1 CP are both temporally constant and spatially isotropic (e.g. Hincelin et al., 2011; Loison et al., 2014b; Ruaud et al., 2016). However, the recent observations of the emission lines of

CCS and HC_3N performed with the 45 m telescope at the Nobeyama Radio Observatory revealed multiple cloud components with distinct systematic velocities toward TMC-1 CP, indicating that it is not quiescent and isotropic (Dobashi et al., 2018). Furthermore, the detailed analysis of the GOTHAM spectra using the MCMC fitting method confirms the presence of up to four individual velocity components for the spectral profile of molecules in the survey. The improved spectral resolution makes it clear that we can no longer treat this source as a homogenous, extended cloud and must instead consider the morphology-dependent chemistry.

Part III

Molecular Spatial Distributions

Chapter 4

Molecular Isomers - Three $C_2H_4O_2$ Isomers towards Sgr B2(N)

The $C_2H_4O_2$ isomers have been previously investigated primarily via disparate sets of observations involving single dish and array measurements. The only attempt at using a uniform set of observations was performed with the IRAM 30 m observation in 2013 (Belloche et al., 2013). In this study, we present an intensive and rigorous spectral and morphological analysis of the $C_2H_4O_2$ isomers towards Sgr B2(N) with interferometers, *ALMA* Band 3 observations. We propose a quantitative selection method, which automates the determination of the most uncontaminated transitions and allows us to report the discovery of previously undetected transitions of the three isomers. With the least contaminated transitions, the high spatial-resolution millimeter (mm) maps of the $C_2H_4O_2$ isomers reveal that $HCOOCH_3$ and CH_2OHCHO each display two different velocity components, while only one velocity component of CH_3COOH is resolved. Moreover, the distribution of $HCOOCH_3$ is extended and off-

set from the continuum emission, unlike CH_2OHCHO and CH_3COOH, for which the low-velocity component is found to be compact and concentrated toward the continuum emission peak of Sgr B2(N). The distinct morphologies of these $C_2H_4O_2$ isomeric species indicate that $HCOOCH_3$ have significant differences in chemical processes than CH_2OHCHO and CH_3COOH, which display similar spatial distributions. *The following chapter is primarily reproduced from Xue, C.; Remijan A. J.; Burkhardt, A. M.; Herbst E. Astrophysical Journal* ***2019****, 871, 112.*

4.1 Introduction

Isomers are families of molecules that share the same constituent atoms, but are uniquely arranged and, as such, have very different chemical properties. Several isomeric groups are well known to exist in the interstellar medium (ISM). Examples include HCN and HNC towards translucent clouds (Turner, 1991) and proroplanetary disks (Graninger et al., 2015), as well as CH_3CN and CH_3NC (Remijan et al., 2005) and three isomers of C_3H_2O (Loomis et al., 2015) toward Sagittarius B2 North (Sgr B2(N)). Because isomers have different chemical and physical properties, further insight can be gained into the astrochemical evolution of different physical environments of astronomical sources by making use of isomers.

One way this can be accomplished is with the Minimum Energy Principle (Lattelais et al., 2009, 2010, 2011). However, it has already been refuted with numerous examples of isomers (Belloche et al., 2014; Karton & Talbi, 2014). Instead, it is widely accepted that the relative abundance of structural isomers in the ISM depends more on their formation mechanisms, i.e. kinetically controlled, than their relative energy differences, assuming they have same destruction routes, which has been further supported by Loomis et al. (2015). Thus, the study of isomers can help to constrain temperature- and density-dependent synthetic routes to complex

interstellar molecules (Mottl et al., 2007), which may in turn help to explain spatial distributions.

This work focuses on three isomers of $C_2H_4O_2$: glycolaldehyde (CH_2OHCHO, GLA), acetic acid (CH_3COOH, AcA) and methyl formate ($HCOOCH_3$, MF), the chemical evolution of which has been widely investigated (Laas et al., 2011; Skouteris et al., 2018; Linnartz et al., 2015). In astrochemical models, the most widely used mechanism to efficiently form the $C_2H_4O_2$ isomeric family in hot cores is through radical-radical recombination on interstellar grain surfaces (Garrod et al., 2008; Chuang et al., 2016). However, in addition to grain surface chemistry, it was also suggested that MF could be formed via gas-phase processes in cold regions (Laas et al., 2011; Balucani et al., 2015). An understanding of the astrochemical evolution of the $C_2H_4O_2$ isomers can shed light on calibrating astrochemical modeling networks. Furthermore, there has been increasing interest in studying these isomers towards astronomical environments because of their importance in the formation of large biologically-relevant molecules (Wächtershäuser, 2000; Liu et al., 2001, 2002; Puletti et al., 2010).

The northern clump of Sgr B2(N) molecular cloud, which lies ~120 pc from the Galactic center, is one of the most massive star-forming regions in the Galaxy. In 2011, observations with the SMA at a spatial resolution of $0.4'' \times 0.24''$ revealed two emission cores within the millimeter continuum map of Sgr B2(N) (Qin et al., 2011). One of these located at $\alpha_{\rm J2000} = 17^{\rm h}47^{\rm m}19.889^{\rm s}$, $\delta_{\rm J2000} = -28^\circ22'18.22''$ was designated as N1 in Belloche et al. (2016) and the other located at $\alpha_{\rm J2000} = 17^{\rm h}47^{\rm m}19.885^{\rm s}$, $\delta_{\rm J2000} = -28^\circ22'13.29''$ was designated as N2 in Belloche et al. (2016). The prominent core, N1, which contains the well known Sgr B2(N) Large Molecule Heimat (LMH) source (Snyder et al., 1994), is located ~5″ south of N2. The two cores have different systematic velocities, $V_{\rm lsr}$, ~64 km s^{-1} for N1 and ~73 km s^{-1} for N2 (Belloche et al.,

2013). Recently, the hot core structures in Sgr B2(N) was further characterized and up to 20 continuum sources were reported (Bonfand et al., 2017; Sánchez-Monge et al., 2017). Here, we adopt the naming conventions LMH and the shorthand notation of the continuum emission cores of N1, N2 and N3. The coordinates of N3 is $\alpha_{\rm J2000}$ = $17^{\rm h}47^{\rm m}19.248^{\rm s}$, $\delta_{\rm J2000}$ = $-28^{\circ}22'14.91''$ as described in Bonfand et al. (2017). See Section 4.4 for the corresponding positions.

Sgr B2(N) is one of the most prolific regions for detecting Large Astronomical Molecules (LAMs). Here, we move away from Complex Organic Molecules (COMs) (Herbst & van Dishoeck, 2009) and use LAMs as a more accurate definition for astronomical molecules with more than 6 atoms on account of the fact that, in astronomical environment, many detected molecules are not complex by chemical standards and have no direct relationship to organic or prebiotic chemistry. Many LAMs were first detected toward this source, such as CH_2CHCHO and CH_3CH_2CHO (Hollis et al., 2004b), NH_2CH_2CN (Belloche et al., 2008), CH_3NCO (Halfen et al., 2015) and CH_3CHCH_2O (McGuire et al., 2016). The first detection of all of the three $C_2H_4O_2$ isomers were also reported towards Sgr B2. The discovery of MF was achieved with the Parkes 64 m telescope in 1975 (Brown et al., 1975), while the lower abundance isomers, AcA and GLA, were not detected until several decades later due to the lack of accurate laboratory data. Mehringer et al. (1997) reported the first detection of 4 strong transitions of AcA towards the LMH region in Sgr B2(N) using the Berkeley Illinois Maryland Association (BIMA) Array and the Caltech Owens Valley Radio Observatory (OVRO) millimeter array, while the first detection of GLA was not reported until Hollis et al. (2000) who used the NRAO 12m telescope.

The $C_2H_4O_2$ isomers have been previously investigated primarily via disparate sets of observations involving single dish and array measurements. The MF and GLA abundance ratio, [$HCOOCH_3$]:[CH_2OHCHO], toward Sgr B2(N) was reported

to be ~6.7 : 1 as observed with the NRAO 12 m single-dish telescope (Hollis et al., 2000). Hollis et al. (2001) further studied MF and GLA with the BIMA array and found the abundance ratio to be ~52 : 1 for [$HCOOCH_3$]:[CH_2OHCHO]. The difference between the ratios was interpreted to be due to the different beam sizes between the single dish and interferometric array observations and to the size of the source of the molecular emission towards the LMH region. The one attempt at using a uniform set of observations was performed with the IRAM 30 m (Belloche et al., 2013). They deduced the abundance ratios among the three molecules [$HCOOCH_3$]:[CH_2OHCHO]:[CH_3COOH] to be 242:1:5.8 with unconstrained temperatures and source sizes. Regarding the spatial distributions, although Hollis et al. (2001) mapped both MF and GLA with the BIMA array, the images were only based on a single transition of GLA, $8(0,8) - 7(1,7)$, and the blended transitions of MF: $7(5,3) - 6(5,2)$ E and $7(5,2) - 6(5,1)$ A. The extended and cool distribution of GLA suggested with the BIMA array observations indicated a gas phase formation mechanism. MF is ubiquitous in molecular cores with various physical conditions, suggesting that its formation involves both gas-phase and grain-surface processes. AcA always possesses a warm, compact distribution, which favors grain surface formation mechanisms (Mehringer et al., 1997) followed presumably by thermal desorption.

Therefore, a rigorous comparison between the abundances and overall spatial distributions of these three isomers has not been achieved. High-sensitivity observations with better spatial and spectral resolution are necessary to determine accurate abundance ratios and molecular morphology in different regions towards Sgr B2(N). As such, a new careful comparison of these triplets towards the Sgr B2(N) region is needed. The Atacama Large Millimeter/submillimeter Array (ALMA) has the ability to carry out observations of molecules with low abundances and weak emission lines and to image LAMs at small spatial scales due to its high sensitivity and angular

resolution (Öberg et al., 2015).

This work reports a self-consistent and rigorous investigation of three $C_2H_4O_2$ isomeric species with interferometric observations towards Sgr B2(N). The observations are summarized in Section 4.2. Section 4.3 describes the methods and results of the data analysis, including the selection processes for selecting the unblended transitions of each species. The spatial distributions of $C_2H_4O_2$ isomers are presented in detail in Section 4.4. The possible explanations for the difference of the spatial distribution of each molecular species is discussed in Section 4.5, and the conclusion is given in Section 4.6.

4.2 Observations

The interferometric data used here were acquired from the ALMA Science Archive[1] of the EMoCA survey (Exploring Molecular Complexity with ALMA) (Belloche et al., 2016). This survey included 5 spectral setups as shown in Table 4.1 of which S1−S4 were performed during Cycle 0 (2012) with ALMA project code 2011.0.00017.S and S5 during Cycle 1 (2014) with project code 2012.1.00012.S. Each setup contains 4 spectral windows within the overall frequency range from 84.1 to 114.4 GHz. The phase center of the observations was pointed toward Sgr B2 with the field center at $\alpha_{\mathrm{J2000}} = 17^{\mathrm{h}}47^{\mathrm{m}}19.87^{\mathrm{s}}$, $\delta_{\mathrm{J2000}} = -28^{\circ}22'16''$. The Half Power Beam Width (HPBW) of the primary beam measured from actual 12 m ALMA antennas was $69''$ and $51''$ at 84 and 114 GHz respectively. The spectral resolution was 488.3 kHz, which corresponds to a velocity resolution of 1.29 to 1.70 $\mathrm{km\,s^{-1}}$ across the observing band. A detailed description of the observations and the data calibration was presented in Belloche et al. (2016).

[1] `http://almascience.nrao.edu/aq/`

The Common Astronomy Software Applications package (CASA[2]; McMullin et al., 2007) was used for imaging and analysis. For each spectral window, the relatively line-free continuum channel ranges were selected with the techniques, as described in McGuire et al. (2017b), which are based on the mean spectrum generated from the CASA image cube. Afterwards, the ranges were used to subtract the continuum emission in the UV-plane before imaging the spectral cubes. The imaging parameters of each spectral window are presented in Table 4.1. For all data sets, we used the Briggs scheme with a robust parameter of 0.5 and a cell size of $0.3''$ for imaging. The resulting size of the synthesized beam (HPBW) of each data cube has a medium value $\sim 1.6''$. The median of resultant typical rms noise levels is $4.4\,\mathrm{mJy\,beam^{-1}}$.

[2] https://casa.nrao.edu

Table 4.1: Summary of Analyzing Parameters

Setup	SPW	Frequency Range (GHz)	Primary Beam HPBW ($''$)	Synthesized Beam [a] HPBW ($'' \times ''$)	PA ($^\circ$)	Spectral Resolution ($\mathrm{km\,s^{-1}}$)	Median RMS Per Channel [b] ($\mathrm{mJy\,beam^{-1}}$)
S1	0	84.091 — 85.966	69	2.14×1.56	-85.5	1.70	4.1
	1	85.904 — 87.779	67	2.06×1.54	-84.4	1.69	3.5
	2	96.154 — 98.029	60	1.85×1.41	-87.2	1.51	3.5
	3	97.904 — 99.779	59	1.81×1.39	-86.7	1.48	3.8
S2	0	87.729 — 89.604	66	3.00×1.36	-82.8	1.65	4.5
	1	89.554 — 91.429	64	2.96×1.36	-83.4	1.62	4.5
	2	99.728 — 101.602	58	2.68×1.21	-83.7	1.46	4.4
	3	101.552 — 103.427	57	2.58×1.21	84.4	1.43	4.6
S3	0	91.368 — 93.242	63	3.01×1.47	84.8	1.59	5.7
	1	93.193 — 95.067	62	2.94×1.48	84.7	1.56	5.6
	2	103.365 — 105.239	56	2.68×1.32	85.1	1.40	6.8
	3	105.189 — 107.064	55	2.59×1.31	83.9	1.38	7.1
S4	0	95.021 — 96.896	61	1.82×1.40	-83.1	1.53	4.0
	1	96.846 — 98.720	60	1.80×1.38	-82.1	1.50	3.1
	2	107.019 — 108.893	54	1.62×1.24	-84.0	1.36	3.8
	3	108.843 — 110.718	53	1.58×1.22	-82.3	1.33	3.8
S5	0	98.672 — 100.546	58	1.79×1.46	-74.2	1.47	3.2
	1	100.496 — 102.370	57	1.76×1.43	-73.7	1.44	5.0
	2	110.669 — 112.543	52	1.61×1.30	-75.6	1.31	5.7
	3	112.494 — 114.368	51	1.56×1.29	-73.4	1.29	5.6

[a] The synthesized beam size varies depending on the *robust* parameter. Here we used a *robust* parameter of 0.5.

[b] The estimated rms noise level of each spectral window is the median of the noise levels measured in several channels with moderate emission, where the noise levels are each measured in the off-source region.

4.3 Spectral Analysis

4.3.1 Transition Selection Processes

Although MF, GLA and AcA have been unambiguously detected toward Sgr B2, the identification of clear individual spectral features of GLA and AcA were not obvious because of the spectral confusion, which limited the number of uncontaminated lines. Here, we propose a more reliable way to uniquely identify the spectral features of the $C_2H_4O_2$ isomers towards Sgr B2(N), particularly the spectral features of AcA and GLA. Through a more accurate continuum subtraction and our methods of line identification, we identified weaker, and previously undetected, transitions of this isomeric triplet from the EMoCA survey (Belloche et al., 2016) and further selected the least contaminated transitions for imaging.

Snyder et al. (2005) proposed five criteria, hereafter referred to as the Snyder Criteria, for line assignments, particularly toward interstellar clouds with high spectral line densities greater than 10 lines per 100 MHz, see also (Calcutt et al., 2014; Faure et al., 2014; Brouillet et al., 2015; Carroll et al., 2015). The Snyder Criteria, which are utilized in our study, include: (i) accurate rest frequencies, (ii) beam dilution, (iii) frequency agreement, (iv) line intensity and (v) presence of transitions with observable intensity. Here we applied these criteria for identifying the mostly uncontaminated transitions of the $C_2H_4O_2$ isomers. In the following, we discuss each criterion of the Snyder Criteria with our line identification process for the $C_2H_4O_2$ isomers. Details about other applications and the scope of the criteria are presented in Snyder et al. (2005).

(i) *Accurate Rest Frequencies.* The first criterion is the need for high degree of accuracy of the rest frequency of the target molecular transitions. The millime-

ter wave spectrum of GLA has been studied in the laboratory by Butler et al. (2001), Widicus Weaver et al. (2005), and Carroll et al. (2010); the spectrum of MF by Oesterling et al. (1999), Ogata et al. (2004), and Carvajal et al. (2007), and the spectrum of AcA by Ilyushin et al. (2001, 2013). Their transitions are included in the current public databases: the CDMS catalog[3] (Müller et al., 2005), the JPL catalog[4] (Pickett et al., 1998) and the Spectral Line Atlas of Interstellar Molecules (SLAIM) database, which are available in the SPLATALOGUE spectroscopy database[5]. For the analysis of the present ALMA observations, the rest frequencies and other spectral line parameters of the three isomers were taken from the above databases. In the range of $84-114$ GHz, the transition uncertainties of the three molecules were estimated to be less than 150 kHz, compared to a spectral resolution of 488.3 kHz. As a result, our study satisfied the criteria of the high accuracy in rest frequency.

In this study, we consider the transitions for both the ground and first vibrationally excited states of MF but only the vibrational ground state of AcA and GLA. The high hot cores temperatures ($\sim$150 $-$ 200 K, Belloche et al. (2016)) along with the high abundance of interstellar MF make the low-energy vibrationally excited states of MF (v_t = 1 at $\sim$132 cm^{-1} or 190 K) likely to be populated in hot cores (Sakai et al., 2015). In fact, transitions within v_t = 1 of MF have been reported toward Orion KL (Kobayashi et al., 2007) and W51 e2 (Demyk et al., 2008), which are comparable hot cores to Sgr B2. Belloche et al. (2016) derived the rotational temperatures in Sgr B2(N) ranging from 112 $-$ 278 K for different LAMs. Considering the excitation temperature and

[3] https://www.astro.uni-koeln.de/cdms/catalog
[4] https://spec.jpl.nasa.gov
[5] https://www.splatalogue.net

the previously determined column density of $N_{\mathrm{HCOOCH_3}} \sim 1.2 \times 10^{18}\,\mathrm{cm}^{-2}$ (Belloche et al., 2016), both the ground and $v_t = 1$ states are studied in this work. Even though the comparable first vibrationally excited state of AcA lies at about $170\,\mathrm{cm}^{-1}$ (or 245 K) above the ground state (Ilyushin et al., 2001) and that of GLA at $195\,\mathrm{cm}^{-1}$ (or 280 K) (Widicus Weaver et al., 2005), their abundances are not high enough to be detectable toward Sgr B2(N) like MF (Hollis et al., 2001; Remijan et al., 2002). Therefore, only the vibrational ground states for AcA and GLA are considered in this study.

(ii) *Beam Dilution.* The correction based on the beam dilution effects arises from the different synthesized beam sizes of the telescopes, which affect the relative intensities measured for spectral lines toward the same pointing position. Therefore, the relative observed intensities between any transitions need to be corrected for beam dilution effects when the observations are carried out with different telescopes (Faure et al., 2014). In this study, the observations were carried out in the same receiver band, ALMA Band 3. The minimum size of the synthesized beam of the EMoCA survey was reported as $1.58'' \times 1.22''$ while the source diameters, the FWHM from two-dimentional Gaussian fits to the integrated intensity maps, of many LAMs, including MF, were reported to be not larger than $1.5''$ (Belloche et al., 2016). Therefore beam dilution should not affect the corresponding line intensity difference of the three isomers if they have similar source sizes. In fact, we find that the three isomers have different source sizes as shown in Section 4.4. But, given the measurement accuracy and the resolution of the EMoCA survey, the angular extent of all emission above $3\,\sigma$ for the three isomers is larger than the synthesized beam of the observations. The beam dilution effect in our analysis is thus negligible.

To examine whether our line assignments satisfy the other three Snyder criteria, we applied a single-excitation temperature simulation followed with a quantitative analysis approach, which automatically reduces the number of emission line candidates by filtering out the obviously blended lines. The remaining less blended transitions go through a more rigorous analysis including spatial distribution imaging.

In this study, the observed spectra presented are extracted from the largest synthesized beam with a size of $3.01'' \times 1.47''$ centered at LMH with the centroid position at $\alpha_{\rm J2000} = 17^{\rm h}47^{\rm m}19.930^{\rm s}$, $\delta_{\rm J2000} = -28^{\circ}22'18.200''$. The LMH region is dense with $n_{\rm H_2}({\rm SgrB2(N)}) > 10^9\,{\rm cm}^{-3}$ (Sánchez-Monge et al., 2017), and hence LTE is assumed to be reached.Although there is still some likelihood of non-thermal excitation, the molecular emission toward LMH should be well-described by spectra simulated with a single-excitation temperature ($T_{\rm ex}$) (McGuire et al., 2017b). The single-excitation model follows the convention of Hollis et al. (2004a) with corrections for optical depth as discussed in Turner (1991) and Mangum & Shirley (2015). The spectra are simulated from the catalog data available in the public databases, which were generated from the laboratory data.

By comparing the simulated spectra with the observed spectra, we fit the observed spectrum of each molecule to constrain (1) the spectral line width (ΔV), (2) the source velocity ($V_{\rm lsr}$), (3) the molecular column density ($N_{\rm T}$), and (4) the excitation temperature ($T_{\rm ex}$) which contributes to the relative intensities among transitions of a certain species.

To determine the best fit to the observed spectrum, a variety of simulations with different values of these key quantities was constructed. We left both $N_{\rm T}$ and $T_{\rm ex}$ as free parameters to be adjusted and tried to obtain the best-fit simulation. By setting the ΔV to $6.5\,{\rm km\,s^{-1}}$, $V_{\rm lsr}$ to $64\,{\rm km\,s^{-1}}$, $T_{\rm ex}$ to $190\,{\rm K}$, we find that though subjective the single-excitation temperature simulations yield the most consistent fit

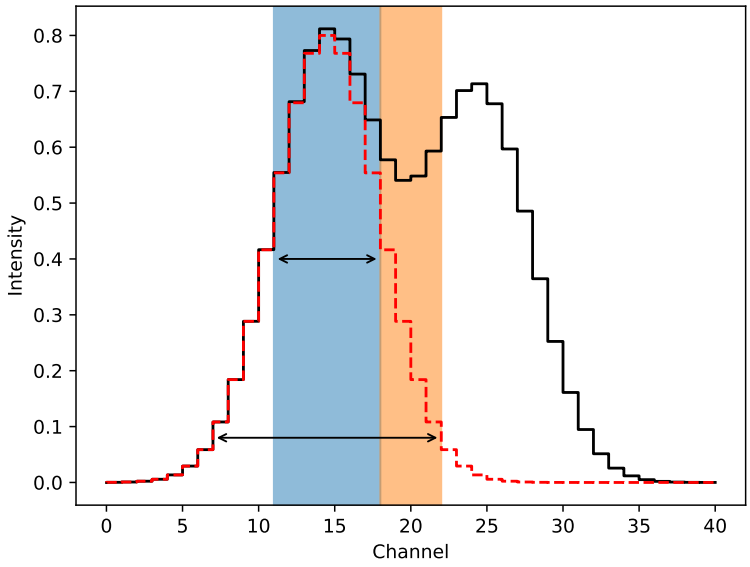

Figure 4.1: Illustration of the effect of different spectral range for comparing line profiles. Simulated spectrum and observed spectrum are shown in red dashed line and black solid line respectively.

to the observed spectra. The $V_{\rm lsr}$ and ΔV toward LMH were constrained by previous studies to the values of $64\,{\rm km\,s^{-1}}$ for $V_{\rm lsr}$ and $\sim 7\,{\rm km\,s^{-1}}$ for ΔV (Belloche et al., 2008). The parameter $T_{\rm ex}$ used here is consistent with the value of 200 K for $T_{\rm rot}$ used in Mehringer et al. (1997) for AcA and MF. It should be noted that these spectra are used for the initial analysis for identifying the potential uncontaminated transitions only and the values of $N_{\rm T}$ and $T_{\rm ex}$ will be refined later by χ^2 fitting using only the uncontaminated transitions as discussed in Section 4.3.3.

In order to quantify the degree of consistency between the simulated and observed spectra, we further defined two factors to describe this degree of consistency of line profiles, which quantify two of the Snyder Criteria: (iii) frequency and (iv) line intensity agreement.

The spectral range for comparing line profiles from observation and simulation is

crucial for calculating these consistency factors. As illustrated in Figure 4.1, within the small spectral range shown in blue, the simulated line shows a high degree of agreement in line intensity with the observed line. As a matter of fact there are two observed lines blended with each other. But, if a larger spectral range is used for comparing, the blended part colored in orange would be taken into account and thus reduce the degree of consistency. Therefore, using a large spectral range yields a value that describes the situation more accurately. In addition, as required by the Snyder criterion for frequency agreement, a resolved transition should be separated from its adjacent lines by more than its FWHM. So the spectral range for comparing line profiles should at least include the contiguous channels of which the simulated intensities are larger than 50% of the peak intensity. As it is critical to have a clean transition for imaging, in our study, we adopt an even wider spectral range where only the channels with intensities larger than 10% of the maximum are considered.

(iii) *Frequency agreement.* For characterizing the proximity in central frequencies, we define the P (Product) factor, which is based on the product of the observed and simulated line profiles, in the following manner:

$$P \text{ factor} = \frac{\sum_{\nu_1}^{\nu_2} I_{\text{obs}} \times I_{\text{sim}}}{\sum_{\nu_1}^{\nu_2} I_{\text{obs}}^{\text{sorted}} \times I_{\text{sim}}^{\text{sorted}}} \tag{4.1}$$

In Equation (4.1), I_{obs} and I_{sim} are the observed and simulated intensity as functions of frequency respectively. Figure 4.2(a) shows a fictitious simulated spectrum in red and a fictitious observed spectrum in black. The product of the profiles in each channel is first calculated and plotted in Figure 4.2(b). For example, in Figure 4.2(a), the observed value in channel 10 is 0.835 and the simulated value is 0.643. Therefore, the product is 0.537 as shown in channel

10 of Figure 4.2(b). The simulated and observed spectrum are then sorted in intensity bins from lowest intensity (left) to highest intensity (right) in Figure 4.2(c) and denoted by $I_{\rm sim}^{\rm sorted}$ and $I_{\rm obs}^{\rm sorted}$ respectively. Once again, similar to Figure 4.2(b), we derived the product of the sorted spectra for each bin as shown in Figure 4.2(d). Finally, the P factor is calculated by dividing the area in Figure 4.2(b) by the area in Figure 4.2(d). The denominator represents the maximum achievable value of the numerator and normalizes the P factor to 100%. In this example, since the central frequencies of the spectra are inconsistent, we obtain a rather low P factor, 82%.

If the central frequencies of the compared lines are same, the bin of the simulated and observed intensity in each channel would be the same. So, after sorting, only the order would change but the product of intensity would remain the same. The P factor thus would reach 100%. Figure 4.3 shows a couple of examples of the spectra with corresponding 5%, 25%, 50% and 100% P-values.

In our analysis, the summation operations in Equation (4.1) sum over the spectral range in which the simulated intensities larger than 10% of its maximum as mentioned above. The threshold P factor for assigning a line depends on the situation. In the study of $C_2H_4O_2$ toward Sgr B2(N), we have a high confidence of the accuracy of rest frequencies for the three molecules and the source velocity of LMH, which are the major factors affecting the frequency agreement. As a result, we are rigorous with the P factor and assign a transition with a P factor at least larger than 90% to be an unblended transition candidate.

(iv) *Line Intensity.* The difference of the line intensities is measured by the D (Difference) factor. It is the ratio between the difference of the integrated intensities of the compared spectra and the maximum of the two subtracted

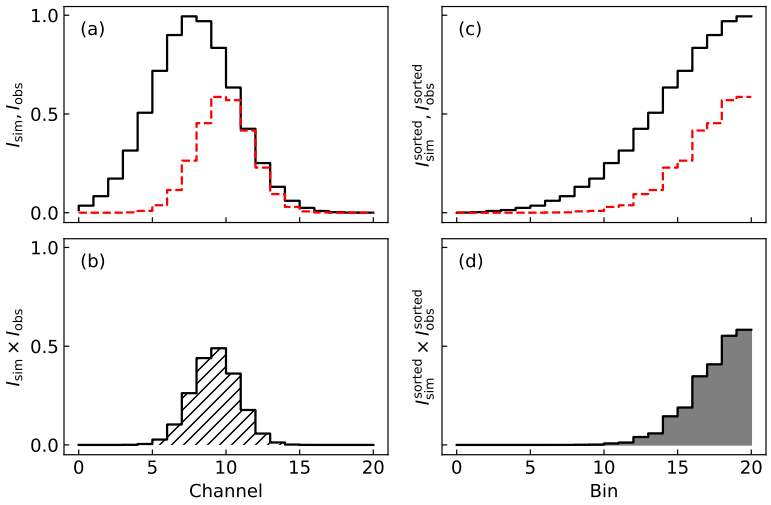

Figure 4.2: Illustration of the calculation of the P factor. In panel (a), the black solid lines represent the fictitious observed data while the red dashed lines represent the fictitious simulated data. Panel (b) represents the product of the compared spectra, i.e. the numerator in Equation (4.1). Panel (c) shows the spectra sorted in their intensities. The products of the sorted spectra are plotted in panel (d) of which the areas represents the denominator in Equation (4.1). The P factor is 82% in this case.

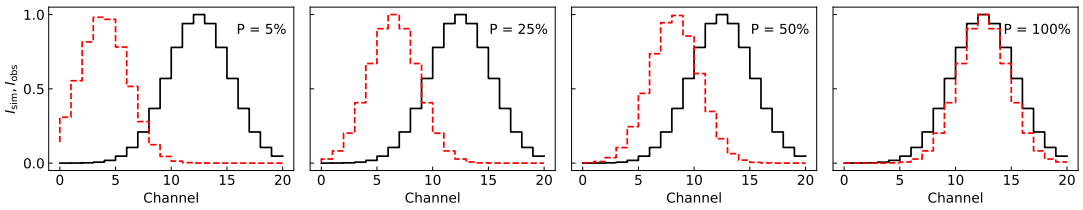

Figure 4.3: Examples of the compared spectra with P factors of 5%, 25%, 50% and 100% which are plotted in solid and dashed lines respectively.

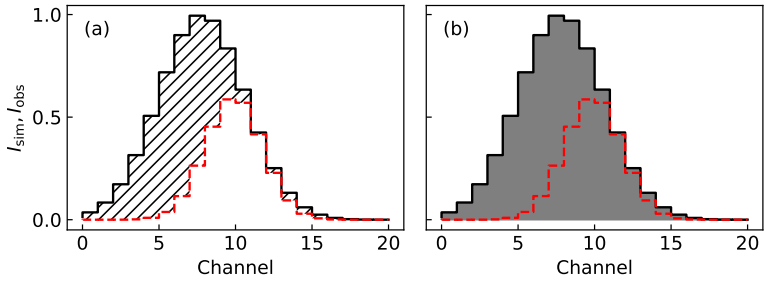

Figure 4.4: Illustration of the calculation of the D factor. The fictitious compared spectra are plotted in solid and dashed lines respectively. The hatched area in panel (a) represents the numerator in Equation (4.2) while the filled area in panel (b) represents the denominator. The D factor is 39% in this case.

from 1:

$$D \text{ factor} = 1 - \frac{\left|\sum_{\nu_1}^{\nu_2} I_{\text{obs}} - \sum_{\nu_1}^{\nu_2} I_{\text{sim}}\right|}{\max\left(\sum_{\nu_1}^{\nu_2} I_{\text{obs}}, \sum_{\nu_1}^{\nu_2} I_{\text{sim}}\right)} \tag{4.2}$$

Similar to Equation (4.1), in Equation (4.2), I_{obs} and I_{sim} are the observed and simulated intensity, respectively, and the D factor is calculated using the same spectral range of the P factor. Figure 4.4 shows fictitious observed and simulated lines with different intensities. The hashed area in Figure 4.4(a), which represents the numerator in Equation (4.2), is the difference in integrated line intensities while the filled area in Figure 4.4(b), which represents the denominator is the maximum of the two integrated intensities. In this example, the D factor is 39%.

When there is no difference in the intensities, the numerator is 0. As a result, the D factor is normalized to 100%. In the worst case, where there is no emission in one of the spectra, the numerator would be same as the denominator and the D factor equals 0%. Figure 4.5 shows a couple examples of the spectra with a 5%, 25%, 50% and 100% D-value correspondingly.

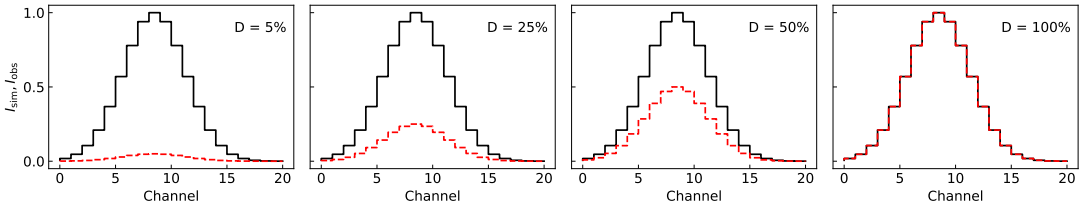

Figure 4.5: Examples of the compared spectra with D factors of 5%, 25%, 50% and 100% which are plotted in solid and dashed lines respectively. The compared spectra are given the same central frequencies.

The threshold of the D factor depends on the accuracy of the input temperature, line width and column density for simulating spectra to the actual values. However, there are still uncertainties in these input parameters, so that a relatively high tolerance of the difference of line intensities between the simulated and observed spectrum is needed. To decide the threshold of the D factor, many simulations were run over a wide range of temperature and column density, with significant deviation in line intensity occurring when the D factor dropped below 60%. Therefore, in this study, we set a threshold of 60% for the D factor.

(v) *Presence of Transitions with Observable Intensity.* The fifth and last Snyder criterion suggests that all transitions with intensity predictions leading to detectable signal levels must be present. We further confirmed the candidate transitions by checking their corresponding connected transitions, i.e. the transitions connected by favorable transition probabilities (Snyder et al., 2005). Similarly to the connected transitions, the A-E pair transitions for MF and AcA have similar line strengths, energy levels, and transition probabilities, and therefore each pair of transitions should have roughly the same intensity and line shape. Both the A and E state transitions must be detected if any of them

has a detectable signal level. In this work, all the transitions of the three isomers with observable intensities are present and none of the strong lines is missing within the observed spectra, although a large number of these lines are blended with neighboring features which leads to small P and D factors for these lines.

We are aware that our selection method suffers from several limitations: (1) There is the possibility of having absorption in the observed spectra. In that case, the methods of making use of the above consistency factors will be broken and the resulting factors would have abnormal values such as values larger than 100% or negative values. Therefore, we exclude the transitions when there is obvious absorption into our calculations of P and D values. (2) The transition maps of unblended transitions might suffer from the contamination of spatial distributions, which could not be recognized by analyzing the spectrum toward one region. To avoid this problem, we have additionally checked every interferometric transition map of the less contaminated transitions found by our methods and marked the spatially polluted transitions, as discussed in Section 4.4.1. (3) Unfortunately, due to the large line width and the high density of emission lines at mm wavelengths, lines could be blended very frequently with adjacent emission lines of the same molecule and appear as single-line spectral features. These transitions still have high values of P and D and would be identified as clean transitions. However, since their line profiles overlap with one another, they do not qualify for imaging. Thus, we carefully inspect the spectra of the transitions with the two consistency factors over our thresholds and highlight these kinds of "grouped" transitions, as discussed in Section 4.3.2-$HCOOCH_3$. These limitations reveal the complexity and difficulty of identifying and mapping a molecule in a source with high spectral line densities.

In spite of its shortcomings, as the focus of the study is on the rotational emission

transitions of the $C_2H_4O_2$ isomers, the transition selection processes in this study is in accordance with the rigorous Snyder criteria. This method also facilitated the detection of weaker and undiscovered transitions of our targets and enabled automation of the analysis of a survey with a large bandwidth by quantifying the consistency of the observed and simulated spectra. The details of the transition selection for the three isomers are summarized below.

4.3.2 Transitions of $C_2H_4O_2$

For assigning the least contaminated transitions, we set thresholds for both P and D factors respectively to select the corresponding transition candidates first. Theoretically, the two factors for a clean transition, which has no difference in either center frequency or line intensity between observed and simulated lines, are both 100%. In this study, we assign a transition with a P factor at least larger than 90% and a D factor larger than 60% to be an unblended transition candidate. After that, we further check if there is serious contamination from other transitions of the same molecule and if the spatial distribution is consistent with other transitions. The details of the selection of the most uncontaminated transitions of MF, GLA and AcA are now detailed.

$HCOOCH_3$ Within the observed spectral range, 84091 to 114368 MHz, there are 1516 transitions of MF recorded in the JPL catalog, including both the vibrationally ground state and first torsionally excited state. In the LTE simulated spectra of MF with an excitation temperature of T_{ex} = 190 K, 197 transitions were found to be above a signal-to-noise (S/N) level of 3 and are potentially detectable.

Through calculating the correlation factors, there are 26 MF transitions, which have P factors larger than 95% and D factors larger than 60% and satisfy our criteria.

These 26 transitions of MF are shown in Figure 4.6 and given in Table 4.2 with the following parameters: rest frequency(uncertainty) in MHz, rotational quantum number, upper-state energy ($E_{\rm u}$) in Kelvin, intensities expressed as the product of the relevant component of the dipole moment squared times transition strength ($S_{ij}\mu^2$) in D^2 (Townes & Schawlow, 1975), FWHM in MHz, critical density ($n_{\rm crit}$) in cm^{-3} and the two resulting correlation factors.

Many of A-E pairs and connected transitions of MF usually have little difference in frequencies compared to the observed line width, some of which are almost completely blended with each other and appear as a single line spectral feature. Therefore, as mentioned before, the strict use of our methodology for comparing spectral lines fails to identify these wide spectral features. As expected, there are several sets of transitions blended together among the 26 MF transitions. Therefore, we only imaged the transition maps of the remaining 10 transitions of MF which are the least contaminated, including 2 transitions in the $v_{\rm t}$ = 1 state, $9(1,8) - 8(1,7)$ A v = 1 and $8(3,5) - 7(3,4)$ A v = 1.

MF has been widely studied in the ISM. Previous studies that targeted Sgr B2(N) reported several transitions of MF, within the frequency coverage of the EMoCA survey (Hollis et al., 2001; Remijan et al., 2002, 2003; Requena-Torres et al., 2006). We critically examined seven transitions of MF from Hollis et al. (2001), two from Remijan et al. (2002), six from Remijan et al. (2003), and seven from Requena-Torres et al. (2006), and found that most of these previously reported transitions are contaminated by adjacent lines in the observed spectra toward LMH and have relatively low P and D values. Only the $7(3,5) - 6(3,4)$ A and E lines (Hollis et al., 2001), the $9(4,5) - 8(4,4)$ E transition (Requena-Torres et al., 2006), the $9(4,5) - 8(4,4)$ A transition (Remijan et al., 2003), and the $9(1,8) - 8(1,7)$ E transition (Requena-Torres et al., 2006) qualify for imaging.

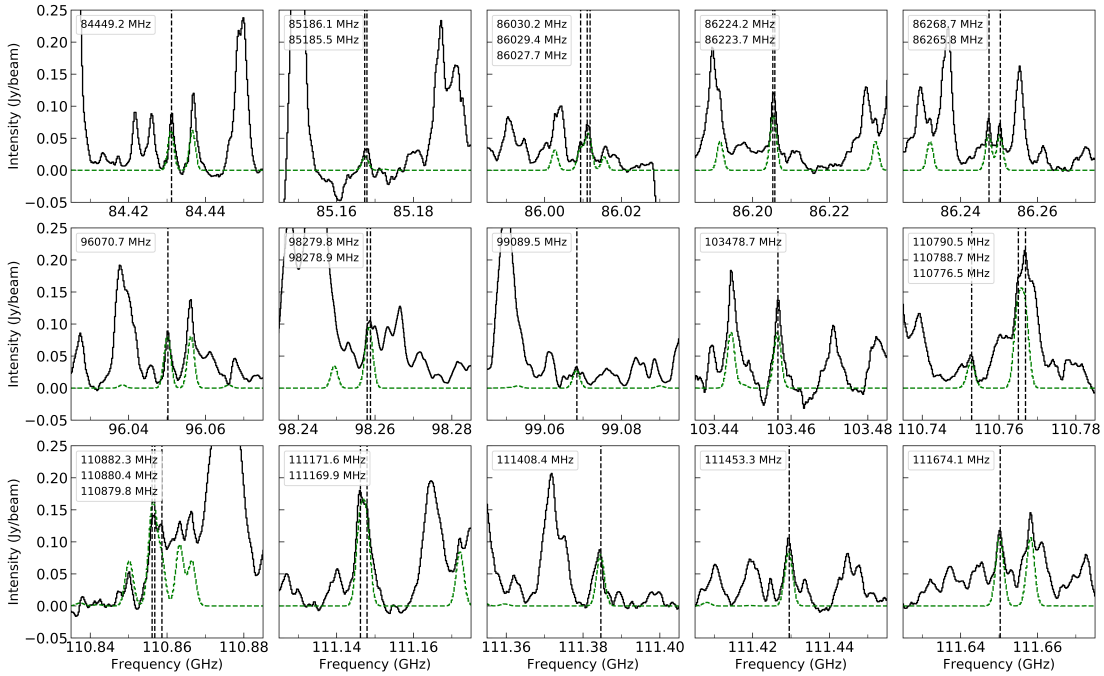

Figure 4.6: Observed spectra of the 26 transitions of MF with a P factor >95% and a D factor >60% toward LMH are plotted in black over the best-fit LTE simulated spectra of MF in green. The observed spectra are extracted from a uniform synthesized beam of $3.01'' \times 1.47''$. The observed frequencies in GHz are marked below each panel. The intensities are indicated in Jy beam^{-1}.

Table 4.2: The Most Uncontaminated Transitions of MF

Rest Frequency (MHz)	Transition	$E_{\rm u}$ (K)	$\log_{10}\frac{A_{ul}}{\rm s^{-1}}$	$S_{ij}\mu^2$ (D^2)	FWHM (MHz)	$n_{\rm crit}$ (cm^{-3})	P Factor (%)	D Factor (%)	Comments
84449.169(10)	$7(2,6)-6(2,5)$ E	19.00	-5.0992	17.0	1.533	1992.9	97.6	79.9	l, h
85185.466(10)	$7(5,3)-6(5,2)$ A $v=1$	220.89	-5.3602	9.1			97.4	63.4	
85186.063(10)	$7(5,2)-6(5,1)$ A $v=1$	220.89	-5.3602	9.1			"	"	
86027.723(10)[a]	$7(5,3)-6(5,2)$ E	33.12	-5.3461	9.1			99.6	70.8	
86029.442(10)[a]	$7(5,3)-6(5,2)$ A	33.11	-5.3459	9.1			"	"	
86030.186(10)[a]	$7(5,2)-6(5,1)$ A	33.11	-5.3459	9.1			"	"	
86223.655(10)	$7(4,3)-6(4,2)$ E	27.17	-5.2074	12.5			99.3	65.2	
86224.160(10)	$7(4,4)-6(4,3)$ E	27.16	-5.2075	12.5			"	"	
86265.796(10)[a]	$7(3,5)-6(3,4)$ A	22.51	-5.1209	15.2	1.739	1707.4	99.7	63.2	h
86268.739(10)[a]	$7(3,5)-6(3,4)$ E	22.52	-5.1248	15.1	1.800	1635.3	99.7	69.3	l
96070.725(10)	$8(2,7)-7(2,6)$ E	23.61	-4.9191	19.8	1.940	2712.5	97.7	97.6	l, h
98278.921(10)	$8(6,3)-7(6,2)$ E	45.13	-5.2179	9.3			96.4	65.3	
98279.762(10)	$8(6,3)-7(6,2)$ A	45.13	-5.2179	9.3			"	"	
99089.518(10)	$8(3,5)-7(3,4)$ A $v=1$	215.08	-4.9159	18.2	2.095	2609.9	98.7	64.8	l
103478.663(10)	$8(2,6)-7(2,5)$ A	24.63	-4.8188	20.0	2.326	3070.6	98.9	63.4	l, h
110776.499(10)	$9(1,8)-8(1,7)$ A $v=1$	215.75	-4.7151	23.1	2.320	4183.4	96.9	68.0	l, h
110788.664(10)	$10(1,10)-9(1,9)$ E	30.27	-4.7051	26.2			96.6 6 2.5		
110790.526(10)	$10(1,10)-9(1,9)$ A	30.26	-4.7049	26.2			"	"	
110879.766(10)	$9(3,7)-8(3,6)$ E	32.58	-4.7510	21.2			97.1 8 9.6		
110880.447(10)	$9(5,5)-8(5,4)$ A	43.16	-4.8592	16.6			"	"	
110882.331(10)	$9(5,5)-8(5,4)$ E	43.16	-4.8594	16.6			"	"	
111169.903(10)	$10(0,10)-9(0,9)$ E	30.25	-4.7002	26.2			99.6 8 2.7		
111171.634(10)	$10(0,10)-9(0,9)$ A	30.23	-4.7002	26.2			"	"	
111408.412(10)[b]	$9(4,5)-8(4,4)$ E	37.26	-4.8123	18.2	2.032	3841.2	94.8 8 6.1	l, h	
111453.300(10)[c]	$9(4,5)-8(4,4)$ A	37.24	-4.7878	19.2	2.681	3081.6	99.9 7 5.0	l, h	
111674.131(10)[b]	$9(1,8)-8(1,7)$ E	28.14	-4.7037	23.2	2.988	3362.0	99.6 7 8.7	l, h	

NOTE — Pertinent parameters of the transitions assigned to MF with $P > 95\%$ and $D > 60\%$ taken from JPL catalog. Here we consider the transitions for both the vibrational ground state and first excited state. $Q_{\rm r} = 12.45 \times T_{\rm r}^{1.5}$ Remijan et al. (2003). P and D factors are calculated based on the observed spectra toward LMH and the simulated spectra assuming an excited temperature of 190 K. "l" and "h" mark the transitions for which the low- and high-velocity components are used for generating the chemical map of MF. The transitions with ditto marks in the column of P and D factors are blended with the transitions in the previous row.

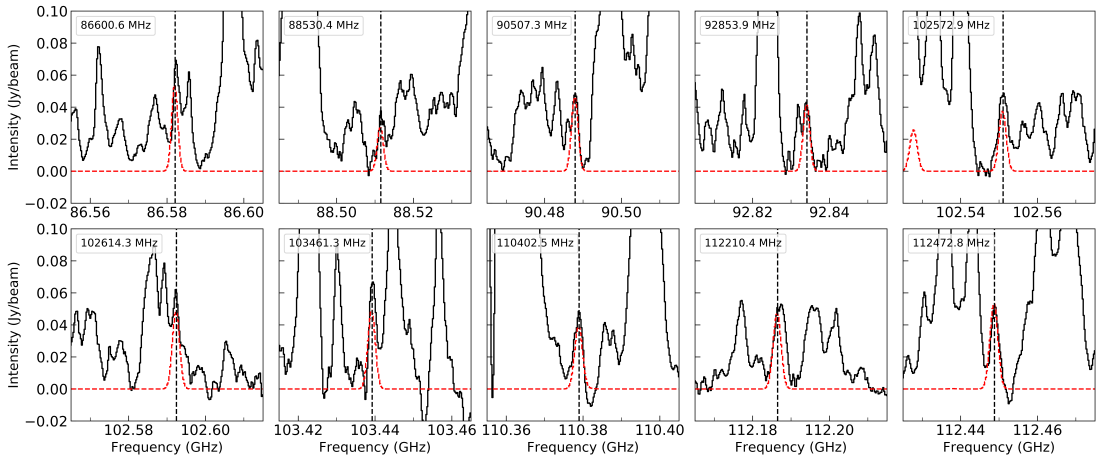

Figure 4.7: Same as Figure 4.6 for the 10 transitions of GLA. The best-fit LTE simulated spectra of GLA are shown in red.

CH_2OHCHO In the 84091 − 114368 MHz frequency range of the EMoCA survey, 402 ground-state transitions of GLA are listed in the CDMS catalog. We focused on the 83 transitions of GLA with S/N > 3 under the simulation condition T_{ex} = 190 K, covering J values up to 18. We found 10 such lines with a P factor >90% and a D factor >60% which were assigned to be the transitions of GLA. Table 4.3 summarizes the 10 most uncontaminated transitions with the pertinent molecular parameters and the P and D factors. The spectral lines used in the detection of GLA toward LMH are shown in Figure 4.7.

As in the case of MF, we studied the three lines of GLA reported by Hollis et al. (2000) and the 12 lines from Halfen et al. (2006). But none of them has consistency factors over our threshold. The observed line intensities of these 11 lines are much higher than the simulated values; this problem is interpreted as serious blending with other molecules. In contrast, the previously unreported 10 transitions, following our criteria, are the most uncontaminated lines identified with GLA at this frequency range toward Sgr B2(N).

Table 4.3: The Most Uncontaminated Transitions of GLA

Rest Frequency (MHz)	Transition	$E_{\rm u}$ (K)	$\log_{10}\frac{A_{ul}}{\rm s^{-1}}$	$S_{ij}\mu^2$ ($\rm D^2$)	FWHM (MHz)	$n_{\rm crit}$ ($\rm cm^{-3}$)	P Factor (%)	D Factor (%)	Comments
86600.5997(67)	$17(5,12)-17(4,13)$	101.14	-4.8624	63.6	1.684	3210.0	91.0	86.6	
88530.4001(46)	$8(4,5)-8(3,6)$	29.73	-4.9874	21.7	2.125	1950.2	94.9	68.9	l, h
90507.2610(133)	$17(3,14)-17(2,15)$	93.77	-4.9064	50.3	2.012	2536.7	98.1	80.4	l
92853.9487(49)	$12(4,9)-12(3,10)$	53.23	-4.8762	35.7	2.231	2517.1	97.2	79.2	l
102572.9391(82)	$14(3,12)-14(2,13)$	63.60	-4.8764	30.7	2.960	2094.5	99.0	62.2	l, h
102614.3429(137)	$18(3,15)-18(2,16)$	104.10	-4.7784	49.0	2.373	3274.6	97.9	64.4	l
103461.3106(66)	$15(4,12)-15(3,13)$	76.75	-4.7501	42.8	2.102	3979.1	95.0	77.7	h
110402.5367(87)	$15(3,13)-15(2,14)$	71.79	-4.8048	31.0	2.549	3087.6	99.4	80.3	h
112210.4422(52)	$12(5,8)-12(4,9)$	58.62	-4.6471	34.3	3.638	3161.2	92.2	70.7	l, h
112472.7946(50)	$14(5,10)-14(4,11)$	73.76	-4.6197	42.0	2.524	4862.7	98.6	98.4	l

NOTE — Pertinent parameters of the transitions assigned to GLA with $P > 90\%$ and $D > 60\%$ are taken from CDMS catalog. Here we only consider the transitions for vibrational ground state. $Q_{\rm r} = 6.868 \times T_{\rm r}^{1.5}$ is derived from the partition function at different temperatures given in CDMS. P and D Factors are calculated based on the simulated spectra assuming the excited temperature as 190 K. "l" and "h" mark the transitions of which the low- and high-velocity components are used for generating the chemical map of GLA respectively.

CH_3COOH There are 573 vibrational ground-state transitions of AcA from the SLAIM database in the 84091 − 114368 MHz spectral range; 136 of AcA transitions have S/N larger than 3 in the simulated spectra with T_{ex} = 190 K including the best known six four-fold degenerate transitions, 90203.35, 90246.26, 100855.43, 100897.46, 11507.27, and 111548.53 MHz lines (Mehringer et al., 1997; Remijan et al., 2003). However, the emission lines of AcA suffer seriously from contamination from other species. The observed intensity of some of the well-known four-fold degenerate transitions of AcA, for example $9(*,9) - 8(*,8)$ A at 100897.46 MHz where asterisks can be 0 or -1, are much higher than their simulated intensity and the observed intensity of their corresponding E pairs in spite of their similar upper-level energy.

There are only three transitions of AcA over the threshold P factor > 90% and D factor > 60% with S/N > 3 as shown in Table 4.4. If we go to weaker lines, there are two more transitions of AcA satisfying the requirement of the consistency factors but with lower S/N. They are the $23(15,9) - 23(14,10)$ transition with S/N ~ 2.7 and the $24(-13,11) - 24(-12,12)$ transition with S/N ~ 2.6. The relatively high values of the consistency factors and the similar spatial distribution of these two transitions with that of the three stronger lines make their assignments reliable. Therefore, we image the transition maps of the five transitions shown in Table 4.4. Figure 4.8 shows the observed and simulated spectra of these transitions toward the LMH region. Pertinent line parameters of all the detectable transitions of the isomeric species of $C_2H_4O_2$ observed in this survey with S/N larger than ~3 are summarized in Appendix Tables 4.6, 4.7 and 4.8 respectively.

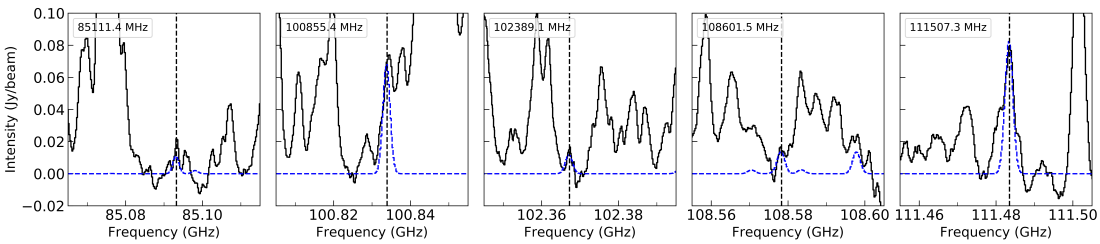

Figure 4.8: Same as Figure 4.6 for the five transitions of AcA. The best-fit LTE simulated spectra of AcA are shown in blue.

Table 4.4: The Most Uncontaminated Transitions of AcA

Rest Frequency (MHz)	Transition	$E_{\rm u}$ (K)	$\log_{10}\frac{A_{ul}}{\rm s^{-1}}$	${S_{ij}\mu}^2$ ($\rm D^2$)	FWHM (MHz)	$n_{\rm crit}$ ($\rm cm^{-3}$)	P Factor (%)	D Factor (%)	Comments
85111.3900(30)	$23(15,9)-23(14,10)$	251.54	-5.3344	30.3	1.201	1491.4	95.9	65.7	l
100855.4300(10)[a]	$9(*,9)-8(*,8)$ E^a	25.67	-4.5116	49.0	3.450	4092.4	94.7	70.7	l
102389.0800(10)	$24(-13,11)-24(-12,12)$	266.21	-5.1281	29.2	1.544	2244.7	96.7	86.0	l
108601.4600(10)	$21(-10,11)-21(-9,12)$	199.07	-5.1076	22.5	2.008	1919.4	90.1	82.6	
111507.2800(10)[b]	$10(*,10)-9(*,9)$ E^a	31.02	-4.3757	54.8	3.037	7029.4	99.4	86.7	

NOTE — Pertinent parameters of the transitions assigned to AcA with $P > 90\%$ and $D > 60\%$ are taken from SLAIM catalog. Here we only consider the transitions for vibrational ground state. $Q_{\rm r} = 14.10 \times T_{\rm r}^{1.5}$ Remijan et al. (2003). P and D Factors are calculated based on the simulated spectra assuming the excited temperature as 190 K. "l" marks the transitions that are most uncontaminated and of which the low-velocity component is used for generating the chemical map of AcA respectively. Each of the fourfold degenerate transitions consists of two a-type and two b-type degenerate transitions, and is shown with the K quantum numbers as substituted by an asterisk.

[a] Fourfold transition detected by Mehringer et al. (1997); asterisk could be 0 or -1.

[b] Fourfold transition detected by Remijan et al. (2003); asterisk could be 0 or 1.

4.3.3 Column Density

To more accurately determine the excitation temperature, we perform a χ^2 fitting over these less contaminated transitions to statistically determine $T_{\rm ex}$ toward the LMH region. The formula for χ^2 is defined as:

$$\chi^2 = \sum_{i=1}^{n} \frac{(I_{{\rm obs},i} - I_{{\rm sim},i})^2}{\sigma^2}, \tag{4.3}$$

where $I_{\rm sim}$ and $I_{\rm obs}$ represent the simulated peak intensity and the observed values at the corresponding frequency respectively, and σ is the rms noise level of the observed spectrum.

For MF, a $T_{\rm ex}$ of $201(12)$ K and a $N_{\rm T,MF}$ of $1.18(0.05) \times 10^{17}$ cm^{-2} minimized the χ^2 to 314.6 with the number of degrees of freedom of 15 and yield the best fit. The χ^2 fitting over these 10 GLA transitions suggested that a $T_{\rm ex}$ of $146(25)$ K and a $N_{\rm T,GLA}$ of $1.57(0.12) \times 10^{16}$ cm^{-2}, which minimized the χ^2 to 14.7 with the number of degrees of freedom of 8, best fit the observation data. A result of $T_{\rm ex} = 296(59)$ K and $N_{\rm T,AcA} = 4.63(0.92) \times 10^{16}$ cm^{-2} is obtained by χ^2 fitting using the five AcA transitions. The minimum value of χ^2 is 3.3 with a degree of freedom of 3.

Based on the ALMA Band 3 observations, the best fit to the observed spectra toward LMH in this study suggests abundance ratios of MF, AcA, and GLA [$HCOOCH_3$]:[CH_3COOH]:[CH_2OHCHO] of ~7.5 : 2.9 : 1. Although this result is in agreement with the suggested ratio of [$HCOOCH_3$]:[CH_2OHCHO] ~6.7 observed with the OVRO array (Hollis et al., 2000), we find an enhancement of the abundance of AcA with respect to those reported by Remijan et al. (2002). In Remijan et al. (2002), the observations conducted with the OVRO array reported an MF to AcA abundance ratio, [$HCOOCH_3$]:[CH_3COOH], of (16- 32):1 toward the LMH region.

Based on a uniform analysis of observations with the IRAM 30 m telescope, Belloche et al. (2013) suggest that $T_{\rm ex}$ = 80 K and $N_{\rm T,MF}$ = 4.37×10^{17} cm^{-2} with a source size of 4.0″ for MF; $T_{\rm ex}$ = 80 K and $N_{\rm T,GLA}$ = 1.8×10^{15} cm^{-2} with a source size of 10.0″ for GLA; and $T_{\rm ex}$ = 100 K and $N_{\rm T,AcA}$ = 1.05×10^{16} cm^{-2} with a source size of 4.0″ for AcA, based on which the abundance ratios among the three molecules are [$HCOOCH_3$]:[CH_3COOH]:[CH_2OHCHO] ~242 : 5.8 : 1. The inconsistency between the two values for [$HCOOCH_3$]:[CH_3COOH]:[CH_2OHCHO] can be justified in part by the different observations and data processing methods. The 30 m IRAM observation has beam sizes larger than 11″ and, therefore, cannot constrain the source sizes of the three molecules. In addition, the rotational diagram method that Belloche et al. (2013) used to determine column density requires a large number of the less contaminated transitions covering a large range of energy levels. But the detected AcA transitions in Belloche et al. (2013) have a narrow range of energy levels, $E_{\rm l}$ of $16 - 25$ K, and there are only 5 detected GLA transitions, which could introduce large uncertainties to the results. In contrast, in our study, we are more rigorous with line contamination and use χ^2 fitting to constrain the excitation temperature. In addition, the small synthesized beam sizes of the ALMA observations resolve the source sizes of the three molecules well.

4.4 Results

In order to determine the velocity components of the three isomers, we examined the spectral transitions of the three isomers as extracted from an aperture with a diameter of 11″ and covering most of the continuum emission region. Figure 4.9 shows the thermal dust continuum map of the Sgr B2(N) region as obtained with ALMA Band 3 observations at 85.9 GHz along with the LMH, N1, N2 and N3 emission cores (Belloche et al., 2016; Bonfand et al., 2017) which will be referenced below.

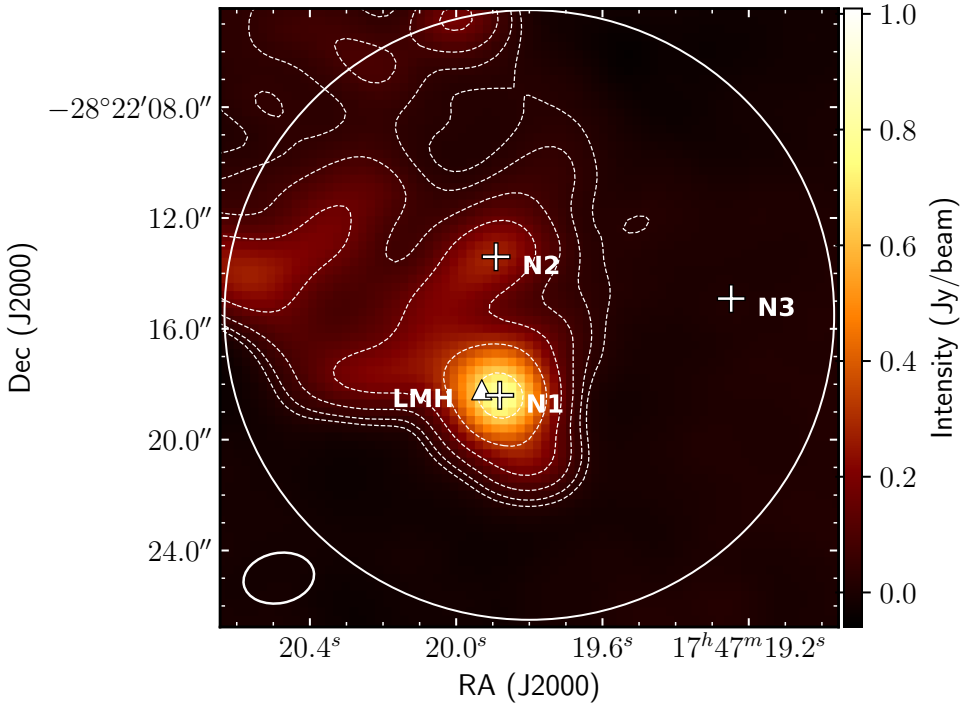

Figure 4.9: Continuum map of the Sgr B2(N) region obtained with EMoCA survey at 85.9 GHz (Belloche et al., 2016; Bonfand et al., 2017). Contour levels start at five times the rms noise level (4.1 mJy/beam) and double in value up to the peak value. The solid circle shows the aperture ($11'' \times 11''$) from which the spectra was extracted from to examine the velocity components of the three isomers. The triangle marker shows the LMH region.

The average systemic $V_{\rm lsr}$ of the N1 core is ~64 km s^{-1} while that for N2 and N3 is $V_{\rm lsr}$ ~ 73 km s^{-1}.

In the most unblended spectral transitions within an aperture comparable to the size of the major continuum emission region, MF has two emission features at two different systemic velocities, $V_{\rm lsr}$ ~ 64 and 73 km s^{-1}. The velocity constitution of MF is consistent with the findings in Belloche et al. (2016) and Bonfand et al. (2017). In contrast to Belloche et al. (2013), who did not detect the high-velocity component of

GLA toward Sgr B2(N) with the IRAM 30 m line survey, two velocity components of GLA are also identified in our study. This difference from our result could be explained by the low sensitivity of the IRAM telescope due to beam dilution and smaller total collecting area. ALMA's high angular resolution and sensitivity give us a better understanding of the velocity components of these LAMs. In contrast to MF and GLA, however, AcA had only a single velocity component near 64 km s^{-1} resolved. There is no AcA emission above 1σ around the N2 or N3 regions for any AcA transitions.

4.4.1 Transition Maps

We carried out an intensive study on the spatial mapping of the $C_2H_4O_2$ isomeric family with the most uncontaminated transitions that were discussed in Sec 4.3.2. We generated peak intensity images (i.e. moment-8 map) for the least contaminated transitions of the $C_2H_4O_2$ isomeric species and refer to them as transition maps. For MF and GLA, we imaged each of the transitions near the two systemic velocity components separately. For the low-velocity component, the integrated velocity range is $59 - 68$ km s^{-1} while for the high-velocity component, the range is $70 - 75$ km s^{-1}. For AcA, only the one velocity range, $59 - 67$ km s^{-1}, was imaged.

$HCOOCH_3$ For MF, we imaged the emission from the 10 most uncontaminated transitions with P factor >95 and D factor >60, over a range of upper-state energies from 23 K to 221 K. The peak intensity images of the low-velocity component and high-velocity component are shown in Figure 4.10 and 4.11 respectively. In Figure 4.10 and 4.11, the background color images are the 85.9 GHz continuum of the Sgr B2(N) region. The contours indicate the location of the MF emission of each transition. As the most uncontaminated transitions are selected based on the spectrum

toward LMH only, some of these MF lines still suffer from spatial contamination, as summarized in the captions of Figure 4.10 and 4.11.

Despite the spatial contamination, based on the peak intensity images of MF, it is clear that different transition maps of MF show nearly identical spatial distributions to each other at each characteristic velocity over a range of excitation levels. We identified two cores of emission of the low-velocity component and two of the high-velocity component among all the transition maps in Figure 4.10 and 4.11. The low-velocity component has a extended distribution which is offset from the continuum emission peak. The distribution of the emission cores of MF is described more completely in Section 4.4.2 in a quantitative way using its chemical map, which is, in short, a weighted composite transition map.

As outlined in Brouillet et al. (2015), the spatial distributions from interferometric observations were suggested to be similar among transitions with similar excitation conditions. However, we find that the morphology of MF is consistent across a wide range of upper-state energy levels; i.e., the intensity maps obtained from v = 0 and v = 1 of MF are similar.

CH_2OHCHO We generated the interferometric images of the 10 least blended GLA transitions with upper-state energy levels ranging from 22 to 64 K for both the low-velocity and high-velocity components, as shown in Figures 4.12 and 4.13, respectively. In contrast to MF, there is substantial contamination among the spatial distributions of GLA. While the LMH region line profiles are relatively clean, the N2 region suffers much more significantly from this.

Despite the contamination mentioned above, the remaining peak intensity images of GLA are consistent with each other, including the low-velocity components of seven transitions which are marked with "l" in Table 4.3 and the high-velocity components of

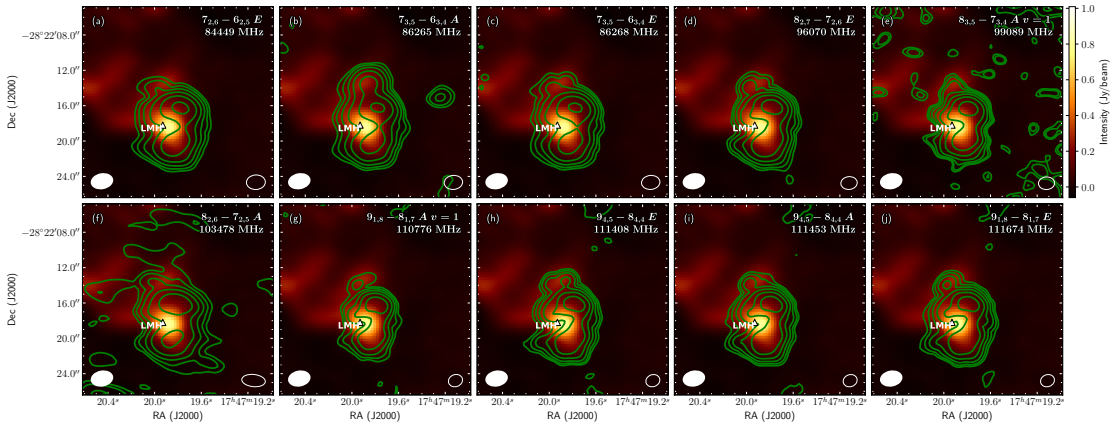

Figure 4.10: Peak intensity images of the low-velocity component ($64\,\mathrm{km\,s^{-1}}$) of the 10 MF transitions overlaid on the continuum emission at 85.9 GHz (background color image). The integrated velocity range of the low-velocity component ranges from 59 to $68\,\mathrm{km\,s^{-1}}$. The MF contours start at $3\,\sigma$ and double in value up to the peak value. Most of transitions of MF show consistent morphology. Spatial contamination source: panel (b) is contaminated with the high-velocity component of the MF $7(3,5)-6(3,4)$ E transition at 86265 MHz.

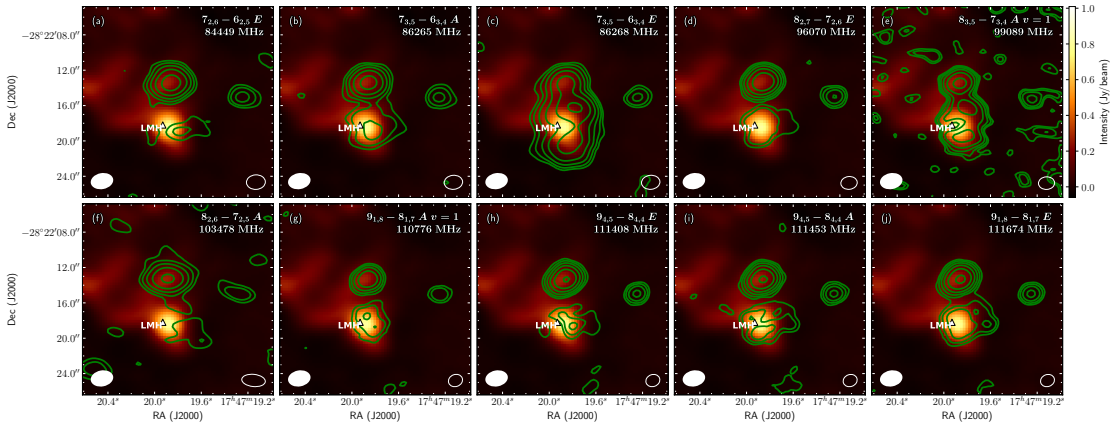

Figure 4.11: Peak intensity images of the high-velocity component ($73\,\mathrm{km\,s^{-1}}$) of the 10 MF transitions overlaid on the continuum emission at 85.9 GHz (background color image). The integrated velocity range of the high-velocity component ranges from 70 to $75\,\mathrm{km\,s^{-1}}$. The MF contours start at $3\,\sigma$ and double in value up to the peak value. We resolve the high-velocity component as the second velocity-component of MF. Spatial contamination sources: panel (c): the low-velocity component of the MF $7(3,5)-6(3,4)$ A transition at 86265 MHz; panel (e): the thioformaldehyde ($H_2{}^{13}CS$) $3(2,1)-2(2,0)$ transition at 99086 MHz.

four transitions marked with "h" in Table 4.3 respectively. From the uncontaminated transitions, as evident in Figures 4.12 and 4.13, we resolved one emission core from the low-velocity component of GLA with a source size smaller than $7''$ and one from the high-velocity component with a source size $\sim 4''$. The emission regions of GLA are more compact that those of MF. A detailed comparison of the distributions of the isomers is discussed in Section 4.4.2.

The result of a compact emission region of GLA is in contradiction with previous research on the spatial distribution of GLA. Hollis et al. (2001) mapped the $8(0,8) - 7(1,7)$ transition of GLA at 82470.67 MHz with the BIMA array and suggested an extended distribution of GLA toward Sgr B2(N) with a source size of around $60''$. The difference found between the distributions from our study may be due to the contamination of the transition detected by Hollis et al. (2001). In their study, only one transition was mapped. Therefore, they could not distinguish if the transition was contaminated by comparing maps from different transitions which is what we do in the present study. In addition, the broad line width of the GLA $8(0,8) - 7(1,7)$ transition imaged by Hollis et al. (2001), $24.3\,\mathrm{km\,s^{-1}}$, compared with $8.2\,\mathrm{km\,s^{-1}}$ for the MF line in their observations is also consistent with the existence of contamination. Thus, the conclusions reached by Hollis et al. (2001) are most likely inaccurate given the fact that it is probably based on a blended transition of GLA.

CH_3COOH Figure 4.14 shows the peak intensity images of AcA for the five transitions listed in Table 4.4. The upper-state energy levels range from 26 to 266 K. Because there is no emission with S/N > 1 in the $\sim 73\,\mathrm{km\,s^{-1}}$ regions, we only resolve one low-velocity component of AcA ($64\,\mathrm{km\,s^{-1}}$). In addition to the limited number of clean emission transitions, AcA also suffers from severe spatial contamination. The least contaminated three transitions are marked with "l" in Table 4.4.

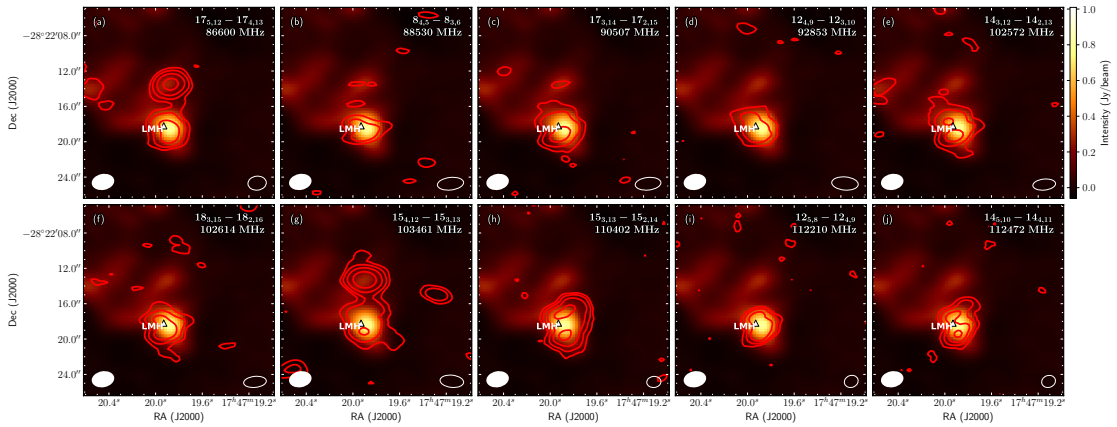

Figure 4.12: Peak intensity images of the low-velocity component ($64\,\mathrm{km\,s^{-1}}$) of the 10 GLA transitions overlaid on the continuum emission at 85.9 GHz (background color image). The integrated velocity range of the high-velocity component ranges from 59 to 68 $\mathrm{km\,s^{-1}}$. The GLA contours start at $3\,\sigma$ and double in value up to the peak value. Despite the transitions suffering from spatial contamination, GLA shows consistent distribution among different transitions. Spatial contamination sources: panel (a): the high-velocity components of the acetone ($(CH_3)_2CO$) $19(10,10) - 19(9,11)$ AA transition at 86604.63 MHz, and the gauche-ethanol (g$-CH_3CH_2OH$) $5(3,3) - 4(3,2)$ transition at 86604.34 MHz; panel (g): the high-velocity component of MF $8(2,6) - 7(2,5)$ E at 103466 MHz; panel (h): the $(CH_3)_2CO$ $6(5,2) - 5(4,1)$ EE transition at 110401 MHz.

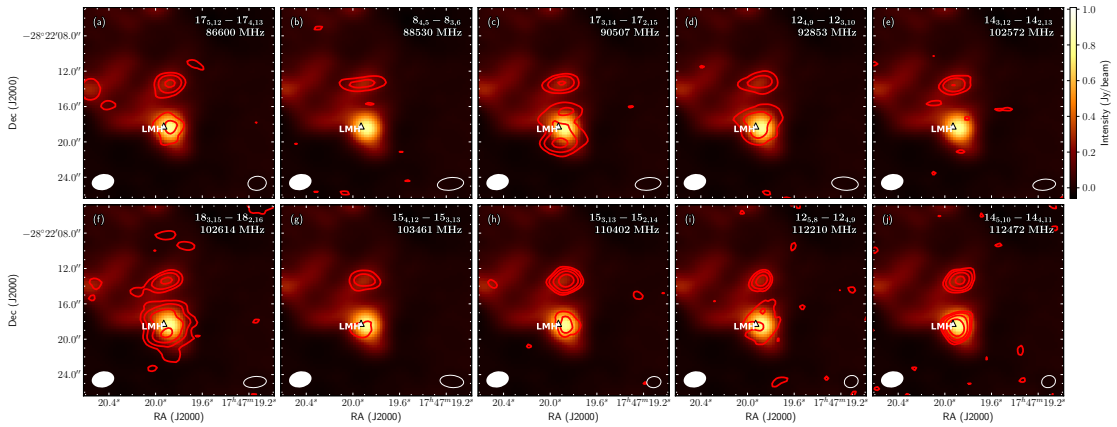

Figure 4.13: Peak intensity images of the high-velocity component ($73\,\mathrm{km\,s^{-1}}$) of the 10 GLA transitions overlaid on the continuum emission at 85.9 GHz (background color image). The integrated velocity range of the high-velocity component ranges from 70 to 75 $\mathrm{km\,s^{-1}}$. The GLA contours start at $3\,\sigma$ and double in value up to the peak value. We resolve the high-velocity component near the N2 region as the second velocity-component of GLA. Spatial contamination sources: panel (a): a weak and unidentified emission feature; panel (c): a strong emission from g$-CH_3CH_2OH$ $6(2,5) - 5(1,5)$ at 90503 MHz; panel (d): unidentified; panel (f): unidentified; panel (j): the low-velocity component of the strong emission feature from the formic acid (HCOOH) $5(3,2) - 4(3,1)$ transition at 112467 MHz.

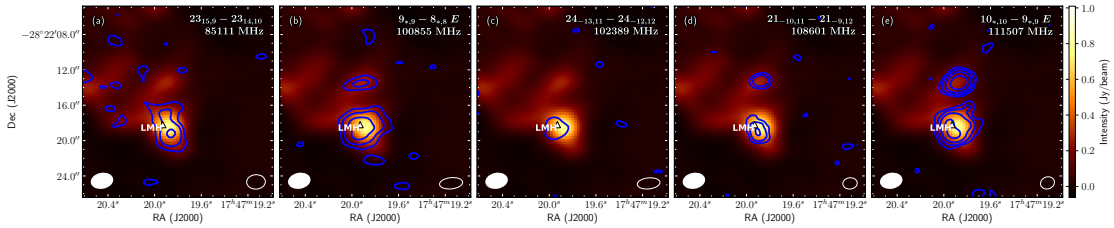

Figure 4.14: Peak intensity images of the five AcA transitions overlaid on the continuum emission at 85.9 GHz (background color image). The integrated velocity range of the high-velocity component ranges from 59 to 67 $\mathrm{km\,s^{-1}}$. The AcA contours start at $3\,\sigma$ and double in value up to the peak value. We only resolved one velocity component of AcA (~64 $\mathrm{km\,s^{-1}}$) and have limited number of the transition maps of AcA. Spatial contamination sources: panel (b) is contaminated by a weak emission feature toward the N2 region contributed by the high-velocity component of the GLA transition $24(7,18) - 23(8,15)$ at 100859 MHz; panel (d) is probably contaminated by the high-velocity component of a transition with a rest frequency of ~108606 MHz, of which the low-velocity component was also observed toward LMH as a strong emission line. However, this transition is not found in any public database and, as such, remains unidentified; panel (e) is contaminated by the high-velocity component of the overlapping transitions of trans-ethanol (t$-CH_3CH_2OH$)-$12(7,6) - 13(6,7)$ and $12(7,5) - 13(6,8)$)-at 111510 MHz in the north region.

Given these limitations, the morphology of AcA cannot be accurately determined based on the limited number and the spatial contamination of the transition maps. But we can still see that the emission peaks are co-spatial among all the transition maps. Besides, Mehringer et al. (1997) mapped Sgr B2(N) with the OVRO array in two transitions of AcA at 90246 MHz and 100855 MHz and Remijan et al. (2002) did the same at 111507 MHz and 111547 MHz. Although the two transitions, 90246 MHz and 111547 MHz, are are known to be contaminated toward LMH and the distribution of the transition at 111507 MHz is spatially contaminated toward the N2 region, the AcA emission peak resolved with the previous observations is consistent with our study. The peak positions are all at $\alpha_{\mathrm{J2000}} = 17^{\mathrm{h}}47^{\mathrm{m}}19.9(0.1)^{\mathrm{s}}$, $\delta_{\mathrm{J2000}} = -28^{\circ}22^{\prime}19(1)^{\prime\prime}$ within $1^{\prime\prime}$ which confirms the assertion that the AcA lines are coming from a common source (Remijan et al., 2002).

4.4.2 Chemical Maps of $C_2H_4O_2$

Because the uncontaminated transitions covering an extensive range of upper-state energies show similar morphology, the effect of excitation conditions is ruled out and the morphology of these transition maps is determined by the true distribution of molecules. For this reason, with an increased number of unblended transitions with similar morphologies, we can combine the transition maps to achieve mm chemical maps for the $C_2H_4O_2$ isomers. A chemical map is obtained by stacking the peak intensity images of transitions which are mostly free of contamination. In the stacking process, we used the inverse-variance weighting for each transition, where the variance is the square of the noise of each data cube. Compared with a single transition map, the chemical map allows us to infer molecular distributions at a high S/N. It is worthwhile noting that the intensities in a chemical map represent the joint properties of both the detected emission and the sensitivity of the observation. Nonetheless, the S/N value at each location indicates the detection significance and, hence, provides the relative molecular abundance. In order to obtain information about the absolute abundance, spectral fittings at each location need to be performed individually.

For MF, we stacked the peak intensity images of the nine least contaminated transitions marked with "l" in Table 4.2 to obtain the low-velocity component and the eight transitions marked with "h" in Table 4.2 for the high-velocity component of the chemical map of MF. Figure 4.15 (left panel) shows the chemical maps of MF in green with solid lines representing the low-velocity component and dashed lines the high-velocity component over the 85.9 GHz continuum emission. Compared with transition maps, we can better quantify the distribution of the emission cores with the chemical map. In the chemical map of MF, four distinct emission cores of MF are resolved. The low-velocity component contains two emission cores marked as MF1

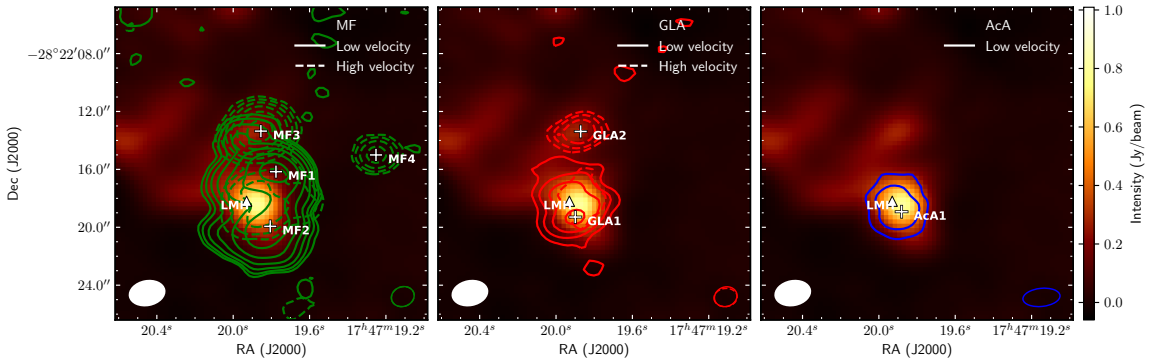

Figure 4.15: Emission contours from the chemical maps of MF (left), GLA (middle) and AcA (right) overlaid on the continuum emission at 85.9 GHz (background color image) toward Sgr B2(N). The solid lines represent the low-velocity component, while the dashed lines correspond to the high-velocity component. The contour levels start at $5\,\sigma$ and double in value up to the peak value, with $\sigma \sim 1.7\,\mathrm{mJy\,beam^{-1}}$ for MF, $\sim$2.0 mJy beam^{-1} for GLA and $\sim$2.5 mJy beam^{-1} for AcA. The emission cores of each molecule are marked by a cross and labeled $\mathrm{MF_{NUMBER}}$, $\mathrm{GLA_{NUMBER}}$ and $\mathrm{AcA_{NUMBER}}$ correspondingly.

and MF2, which are connected with each other over a distance of 3.8″ and located within the cloud. The other two emission cores, MF3 and MF4, with high velocity, are separated by around 8.1″. The coordinates of the four cores are summarized in Table 4.5. The overall distribution of MF is offset from the continuum emission and more extended than that of GLA and AcA. The two emission peaks of MF with low velocity are offset from LMH by $\sim$2.9″ for MF1 and $\sim$2.4″ for MF2 respectively, while MF3 and MF4 are spatially coincident with the N2 core and N3 core defined in Bonfand et al. (2017), respectively.

The chemical map of GLA is represented in Figure 4.15 (middle panel), which is stacked with the transition maps of the seven transitions marked with "l" in Table 4.3 for the low-velocity component and the four transitions marked with "h" in Table 4.3 for the high-velocity component. With the chemical map of GLA, we can better examine the spatial distribution features of GLA that are not clearly resolved in its transition maps. GLA also has distinct high- and low-velocity components. For

the low-velocity component, we locate the major emission core (GLA1) at $\alpha_{\rm J2000}$ = $17^{\rm h}47^{\rm m}19.9^{\rm s}$, $\delta_{\rm J2000}$ = $-28^{\circ}22'19.3''$ and resolve an extended feature to the north-east. An emission core with high velocity (GLA2) is resolved and co-spatial with the MF3 core. GLA2 is ~$5.9''$ north of GLA1. Compared with MF, the distribution of GLA is more compact and spatially consistent with the continuum emission. The GLA1 core is offset from the LMH peaks by only ~$1.2''$ while the GLA2 core is co-spatial with the N2 continuum emission core (Bonfand et al., 2017).

Each of the transition maps of AcA are quite different from each another, perhaps due to the low S/N of the most uncontaminated lines. The difference, as well as the limited number of the unblended transitions, 5 in total, make the morphology of AcA difficult to characterise. But, we can gain insight as to its distribution by looking at its chemical map with increased S/N. In the chemical map of AcA as shown in Figure 4.15 (right), AcA only emits from the region within the low-velocity cloud and has one emission core (AcA1). We do not resolve any high-velocity component for AcA. In addition, the emission region of AcA appeared to be, interestingly, coincident with the distribution of the low-velocity component of GLA, and the spatial separation of AcA1 and GLA1 is smaller than $0.5''$. As with GLA, we find the emission region of AcA to be compact and spatial coincident with the continuum emission. AcA1 is offset from the LMH peaks by only ~$1.0''$.

4.5 Discussion

Our observations indicate that the three isomers of $C_2H_4O_2$ have distinct morphologies, as shown in Figure 4.15. The question remains as to why the three isomers have such different distributions compared to each other despite their identical atomic composition. Here, we discuss the possible mechanisms that could contribute to this difference.

Table 4.5: Positions of the LMH Region and the Molecular Emission Peaks of the $C_2H_4O_2$ isomers

Source	Coordinate		$V_{\rm lsr}$
	17^h47^m	$-28^\circ22'$	km s^{-1}
LMH(centroid)	19.930^s	$18.200''$	64
MF1	19.776^s	$16.158''$	64
MF2	19.806^s	$19.934''$	64
MF3	19.855^s	$13.357''$	73
MF4	19.252^s	$15.002''$	73
GLA1	19.899^s	$19.294''$	64
GLA2	19.871^s	$13.379''$	73
AcA1	19.881^s	$18.926''$	64

Although different observations could bias the result of imaging and contribute to spatial difference, this is not the case in our study. Because we self-consistently analyzed these three isomers in the same observations, we can rule out any differences caused by observations with different facilities, techniques, or frequency regimes. Instead, there are both physical and chemical causes, which could be interwoven, to explain the spatial difference.

Different physical conditions and therefore different excitation conditions inside the source might lead to the diversity in morphology. While our best fit to the observed data suggests the $T_{\rm ex}$ of MF toward LMH to be ~200 K, Bonfand et al. (2017) derived a similar $T_{\rm ex}$, ~150 K, toward both N2 and N3, the two high-velocity cores. Because the transition maps of each molecule are spatially similar across a large range of upper-state energy levels, we can largely rule out the excitation temperatures of the multiple components of Sgr B2(N) as the source of the distinct distributions. In addition, the three species are similar in terms of both photo-absorption cross-sections and ionization potentials (Puletti et al., 2010). Therefore, selective photo-destruction

fails to account for the differentiation in these morphologies. Regarding cloud density, Sánchez-Monge et al. (2017) characterized the small scale structures of Sgr B2(N), which include the cores associated with the seven molecular emission peaks of the three isomers, with various hydrogen densities in a range of $10^7 - 10^9\,\mathrm{cm}^{-3}$. To estimate n_{crit}, we adopted a typical H_2 collisional cross section $\sim 10^{-15}\,\mathrm{cm}^2$ (Condon & Ransom, 2016). Compared with n_{crit} of the $C_2H_4O_2$ transitions listed in Table 4.2, 4.3 and 4.4, we indeed find $n_{\mathrm{H_2}} > n_{\mathrm{crit}} \sim 10^3\,\mathrm{cm}^{-3}$ for the detected lines so that the transitions are probably all thermalized. We also noticed that absorption by the extended material in the cold envelope can cause the offset of MF from the continuum emission peak and should not be neglected. Finally, evolving source properties with time may contribute to the differences in their spatial distributions. A more thorough analysis of other physical properties of the sources would provide further insights into addressing this point.

The morphological differences among the $C_2H_4O_2$ isomeric family could be explained in part by the difference in their production mechanisms and the large energy barriers for the isomerization among them. The grain surface formation routes originally suggested by Garrod & Herbst (2006) and Garrod et al. (2008) are accepted as the most likely mechanisms to efficiently form LAMs during the warm-up phase of the hot cores. Because thermal desorption is efficient in a warm region, a compact distribution of warm molecules toward hot cores is usually associated with a grain-surface formation scheme followed by thermal desorption, although, as discussed below, gas-phase synthesis cannot be ruled out. In this scenario, the HCO radical becomes mobile on grain surfaces and then reacts with the CH_3O radical to form $HCOOCH_3$ or with the CH_2OH radical to form CH_2OHCHO. Recent laboratory studies show that H-atom addition and abstraction reactions in ice mantles can lead to more reactive intermediates, which enhance the probability to form MF and GLA through radical-

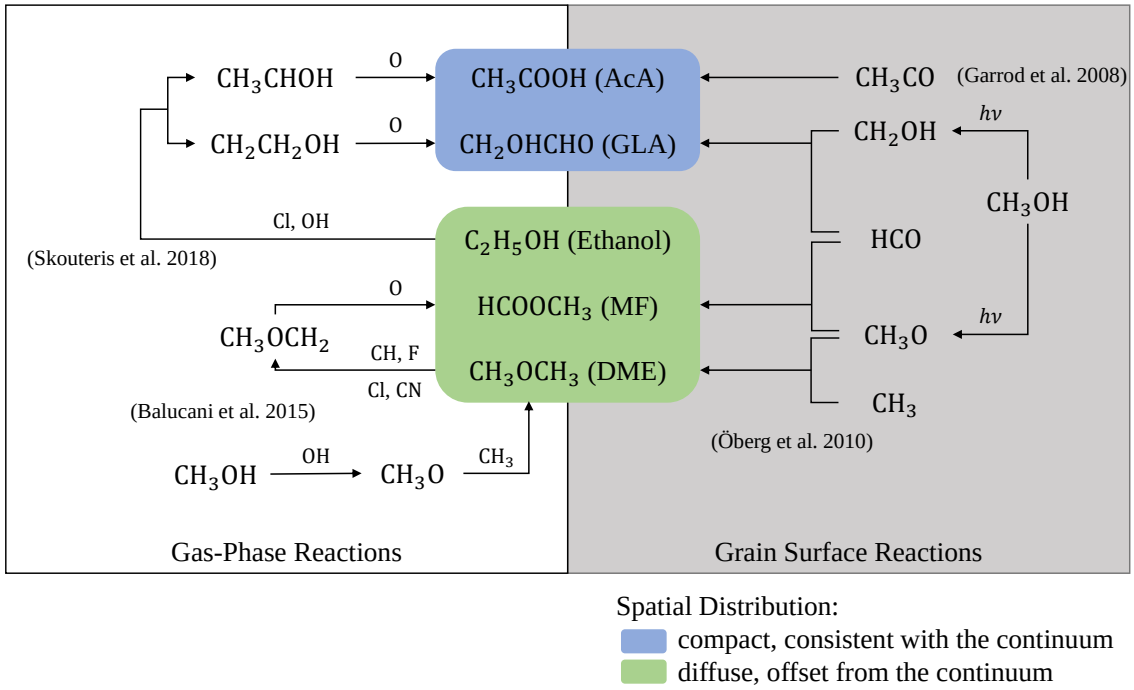

Figure 4.16: Schematic diagram of the prevalent formation mechanisms related to the $C_2H_4O_2$ isomers.

radical recombination (Chuang et al., 2016). Although the grain-surface formation routes of MF and GLA are similar, as both involve HCO, the observed abundances of MF and GLA may be influenced by the abundance difference of the CH_3O and CH_2OH radicals on grain surfaces, which, as of yet, have not been measured. Although direct measurements of the abundances of CH_3O and CH_2OH on grain by IR absorption lines will be difficult to achieve, indirect determinations could be based on possible future observation of gaseous CH_2OH and chemical models.

While the radical-radical reactions of MF and GLA only involve primary radicals, Garrod et al. (2008) suggested that AcA is assembled from the OH radical and the CH_3CO radical. Different from the dominant primary radicals, the CH_3CO radical, which is a secondary radical, is weakly produced and becomes mobile at higher temperatures than primary radicals due to its complexity (Garrod et al., 2008). The

involvement of the CH_3CO radical makes the AcA formation route different from its structural isomers.

If the scenario of radical-radical reactions on grain surfaces (Garrod et al., 2008) is the main formation mechanism of the three isomers, it is reasonable to expect that the spatial distribution of MF and GLA would be similar to each other, since their precursors are HCO and the isomeric radicals that both form from methanol photolysis (Laas et al., 2011), but different from that of AcA. However, the spatial separation of gaseous MF from its isomers and the spatial coincidence of gaseous GLA and AcA make this scenario insufficient for an overall explanation of the observational result. Additionally, there are other pathways involving other surface radicals to form GLA and AcA. GLA could also be formed from the reactions of the HCO radical with the H_2CO and H on grain surfaces (Beltrán et al., 2009), which was suggested to be the most probable formation mechanism of GLA at low temperature (Woods et al., 2012). Bennett & Kaiser (2007) also proposed that AcA could form via the association reaction of the HOCO radical and the CH_3 radical on grains. But the effectiveness of these proposed pathways is still not fully understood and requires further studies.

In addition to grain chemistry, it was suggested that MF could be also formed via gas-phase processes (Laas et al., 2011; Balucani et al., 2015). Balucani et al. (2015) outlined a possible mechanism for the synthesis of MF with gas-phase reactions in cold environments. Therefore, it is a natural outcome that molecules formed in the gas possess extended distributions (Hollis et al., 2001) but there remains the exception that non-thermal desorption can eject molecules formed on cold grain surfaces into a cold gas, as for the case of methanol formation (Watanabe & Kouchi, 2002). Nevertheless, in the gas-phase model, dimethyl ether (CH_3OCH_3, DME) works as the precursor of MF via the loss of a hydrogen atom to form the CH_3OCH_2 radical followed by reaction with atomic oxygen. In addition, an up-to-date scheme for

the gas-phase synthesis of GLA and AcA was proposed, where GLA and AcA were both formed from ethanol (CH_3CH_2OH) (Skouteris et al., 2018). With H-abstraction from ethanol, two different reactive radicals, CH_2CH_2OH and CH_3CHOH, form and further react with atomic oxygen to produce GLA and AcA respectively. Based on this formation scheme involving ethanol, Skouteris et al. (2018) predicted a higher abundance of AcA than GLA, which agrees well with our findings.

As a test of the different gas-phase formation pathways, the distributions of the chemical precursors could work as proxies to interpret the different morphology of these isomeric and related interstellar molecules. If there are either correlations or anti-correlations between the spatial distributions of the precursors and those of the corresponding products, that could be evidence to support the related chemistry. Therefore, we further imaged the chemical maps of the two proposed precursors, DME and ethanol, involved in the gas-phase reactions. We find that DME is co-spatial with MF, which is consistent with their distributions toward another star formation region, Orion KL (Brouillet et al., 2013). The correlation of MF and DME could also be explained with the common precursor, the surface CH_3O radical, in their grain-surface formation pathways (Öberg et al., 2010). We also suspect that ethanol, the precursor of GLA and AcA, should have a similar distribution to GLA and AcA. However, the distribution of ethanol is co-spatial to MF and DME proving that no relationship between the triplet of $C_2H_4O_2$ and the proposed gas-phase precursors could be determined.

Different desorption behaviors of the three isomers could also contribute to the spatial separation between MF and the other isomers. In the warm-up model, desorption begins at different temperatures (Garrod et al., 2008). Thus, temperature, which can be a substitute for time in the model, could be related to differing distributions. Burke et al. (2015) found via a Temperature Programmed Desorption (TPD) analysis

that MF desorption starts at a lower temperature, ~70 K, compared with the desorption of the other two isomers, ~110 K. This different behavior during the thermal processing could account for the extended distribution of MF compared with GLA and AcA. A neglected drawback with the analysis presented in Burke et al. (2015), however, is that they assumed identical grain-surface abundances of the isomers. To connect the effect of the desorption property to the morphological features, taking into account a chemical model, with which the abundances of the isomers could be constrained, seems to be required.

Future research is essential to understand the relative role of the gas-grain chemistry of these three isomers of $C_2H_4O_2$. By carrying out detailed model calculations, involving both grain-surface reactions and the newly proposed gas phase pathways of these three molecules (Balucani et al., 2015; Skouteris et al., 2018), we hope to constrain the formation mechanisms of the isomers. Observations of the $C_2H_4O_2$ and other isomers toward a large sample of interstellar sources could help to constrain the relative importance of their formation pathways and explain the spatial distribution of different molecular isomers.

4.6 Summary

In this paper, we report an intensive spectral and morphological analysis of the $C_2H_4O_2$ isomers towards Sgr B2(N) with sensitive ALMA Band 3 observations (Belloche et al., 2016).

We developed quantitative methods to identify weak and mostly uncontaminated transitions which are critical to automatically detect interstellar molecules within a source that has a dense spectrum and a high level of spectral confusion. From these methods, we identified the 26 least contaminated transitions for MF, 10 for GLA and 5 for AcA and further imaged the peak emission maps of these clean transitions. We

stacked all of the consistent transition maps of each molecule to obtain their chemical maps, which show more reliable distributions of the molecules with higher S/N ratios.

From the high spatial resolution millimeter chemical maps of the three isomers, we find that they have distinct morphologies. Four emission cores of MF are resolved, in which two of them, MF1 and MF2, are connected to each other and located within the portion of the cloud with the low $V_{\rm lsr}$ of ~64 km s^{-1}. For this velocity component, the distribution of MF is extended and offset from the continuum emission. The other two emission cores of MF, MF3 and MF4, with the high $V_{\rm lsr}$, ~73 km s^{-1}, are separated by around 8.1″ from each other. GLA also displays two velocity components, while the $V_{\rm lsr}$ of GLA1 is ~64 km s^{-1} and of GLA2 is ~73 km s^{-1}. Only one velocity component of AcA, AcA1 at ~64 km s^{-1}, is resolved. In contrast to MF, the overall distribution of GLA and AcA are more compact and co-spatial with the continuum emission.

Because the distributions in the transition maps of each isomer are spatially consistent across a wide range of upper level energies, we rule out excitation conditions as the source of the distinct distributions of the $C_2H_4O_2$ isomers. The dissimilar morphology of MF compared with GLA and AcA suggests that MF has a different formation mechanism than do GLA and AcA. Through a thorough investigation into the prevalent formation mechanisms involving both grain-surface and gas-phase routes, however, we find that the current existing chemical theory as summarized in Figure 4.16 can not explain the observed spatial distribution of the $C_2H_4O_2$ isomers. In addition, different desorption behaviors of the three isomers could contribute to the spatial distributions of the $C_2H_4O_2$ isomeric family. Therefore, more observations of the three isomers toward a larger sample of astronomical objects might help to constrain the morphological features and to probe the chemical formation mechanisms in these environments.

4.7 Acknowledgments

We acknowledge funding from the National Science Foundation for support of the astrochemistry program of E. H. Also special thanks go to K. H. Lam for helpful discussions on the quantification of the degree of consistency. We are indebted to B.A. McGuire for providing a Python program for simulating and visualizing molecular emission spectra, and to T. Hunter for providing codes to identify the continuum channels. A.M.B. was a Grote Reber Fellow for a portion of this project, and support for this work was provided by the NSF through the Grote Reber Fellowship Program administered by Associated Universities, Inc./National Radio Astronomy Observatory and the Virginia Space Grant Consortium. A.M.B. also acknowledges support from the Smithsonian Institution as a current Submillimeter Array (SMA) Fellow. This paper makes use of the following ALMA data: ADS/JAO.ALMA#2011.0.00017.S, ADS/JAO.ALMA#2012.1.00012.S. ALMA is a partnership of ESO (representing its member states), NSF (USA) and NINS (Japan), together with NRC (Canada), NSC and ASIAA (Taiwan), and KASI (Republic of Korea), in cooperation with the Republic of Chile. The Joint ALMA Observatory is operated by ESO, AUI/NRAO and NAOJ.

4.8 Tables of the $C_2H_4O_2$ transitions above the $3\,\sigma$ level

Tables 4.6, 4.7 and 4.8 list the transitions of the $C_2H_4O_2$ isomers that are detected above the $3\,\sigma$ level toward Sgr B2(N). P and D factors are calculated based on the observed spectra toward LMH and the simulated spectra assuming an excited temperature of 190 K. Comments in these tables acknowledge the reference observations.

Table 4.6: Transitions of MF with S/N > 3 covered by the EMoCA survey.

Rest Frequency (MHz)	Transition	E_u (K)	$\log_{10} \frac{A_{ul}}{s^{-1}}$	$S_{ij}\mu^2$ (D^2)	P Factor (%)	D Factor (%)	Obs Ref
84449.1690(100)	$7(2,6) - 6(2,5)E$	19.00	-5.0992	17.0	97.6	79.9	
84454.7540(100)	$7(2,6) - 6(2,5)A$	18.98	-5.0990	17.0	95.5	58.1	
85185.4660(100)	$7(5,3) - 6(5,2)A$ $v = 1$	220.90	-5.3602	9.1	97.4	63.4	
85186.0630(100)	$7(5,2) - 6(5,1)A$ $v = 1$	220.90	-5.3602	9.1	"	"	
85327.0290(100)	$7(4,4) - 6(4,3)A$ $v = 1$	214.91	-5.2200	12.5	79.2	6.4	
85360.7640(100)	$7(4,3) - 6(4,2)A$ $v = 1$	214.91	-5.2195	12.5	88.5	7.0	
85371.7300(100)	$7(3,5) - 6(3,4)A$ $v = 1$	210.26	-5.1362	15.1	79.9	11.8	
85506.2190(100)	$7(4,3) - 6(4,2)E$ $v = 1$	214.56	-5.2143	12.6	91.3	17.3	
85743.9760(100)	$7(4,4) - 6(4,3)E$ $v = 1$	214.03	-5.2119	12.5	87.7	54.0	
85761.8760(100)	$21(5,16) - 21(4,17)E$	155.82	-5.8778	7.8	76.6	9.3	
85773.3990(100)	$21(5,16) - 21(4,17)A$	155.82	-5.8778	7.8	83.3	4.7	
85780.6730(100)	$20(5,15) - 20(4,16)E$	142.79	-5.8864	7.2	73.6	24.5	
85785.3420(100)	$20(5,15) - 20(4,16)A$	142.79	-5.8865	7.2	93.9	2.8	
85919.2090(100)	$7(6,1) - 6(6,0)E$	40.44	-5.6139	4.9	71.1	7.2	
85926.5530(100)	$7(6,2) - 6(6,1)E$	40.42	-5.6137	4.9	94.6	8.6	
85927.2270(100)	$7(6,2) - 6(6,1)A$	40.42	-5.6136	4.9	"	"	
85927.2270(100)	$7(6,2) - 6(6,1)A$	40.42	-5.6136	4.9	"	"	
86021.1240(100)	$7(5,2) - 6(5,1)E$	33.13	-5.3461	9.1	89.7	21.9	(Hollis et al., 2001)
86027.7230(100)	$7(5,3) - 6(5,2)E$	33.12	-5.3461	9.1	99.6	70.8	(Hollis et al., 2001)
86029.4420(100)	$7(5,3) - 6(5,2)A$	33.11	-5.3459	9.1	"	"	(Hollis et al., 2001)
86030.1860(100)	$7(5,2) - 6(5,1)A$	33.11	-5.3459	9.1	"	"	(Hollis et al., 2001)
86034.0130(100)	$7(3,4) - 6(3,3)E$ $v = 1$	209.82	-5.1231	15.2	97.5	34.6	
86155.0780(100)	$7(3,4) - 6(3,3)A$ $v = 1$	210.32	-5.1242	15.1	92.2	12.8	
86172.7060(100)	$7(3,5) - 6(3,4)E$ $v = 1$	209.41	-5.1242	15.1	99.3	23.7	
86210.0570(100)	$7(4,4) - 6(4,3)A$	27.15	-5.2050	12.5	84.7	23.3	
86223.6550(100)	$7(4,3) - 6(4,2)E$	27.17	-5.2074	12.5	99.3	65.2	
86224.1600(100)	$7(4,4) - 6(4,3)E$	27.16	-5.2075	12.5	"	"	
86250.5520(100)	$7(4,3) - 6(4,2)A$	27.15	-5.2044	12.5	91.0	33.0	(Hollis et al., 2001)

Table 4.6 continued

Table 4.6: Transitions of MF with S/N > 3 covered by the EMoCA survey. (continued)

Rest Frequency (MHz)	Transition	E_u (K)	$\log_{10} \frac{A_{ul}}{s^{-1}}$	$S_{ij}\mu^2$ (D^2)	P Factor (%)	D Factor (%)	Obs Ref
86265.7960(100)	$7(3,5) - 6(3,4)A$	22.51	-5.1210	15.2	99.7	63.2	(Hollis et al., 2001)
86268.7390(100)	$7(3,5) - 6(3,4)E$	22.53	-5.1248	15.1	99.7	69.3	(Hollis et al., 2001)
87143.2820(100)	$7(3,4) - 6(3,3)E$	22.60	-5.1116	15.1	95.1	51.1	
87160.8350(100)	$8(0,8) - 7(1,7)E$ $v = 1$	207.04	-5.8948	2.8	99.2	33.9	
87161.2850(100)	$7(3,4) - 6(3,3)A$	22.58	-5.1074	15.2	"	"	
87766.3820(100)	$8(0,8) - 7(1,7)E$	20.08	-5.8757	2.9	98.7	19.6	
87960.0490(100)	$7(1,6) - 6(1,5)A$ $v = 1$	205.65	-5.0223	18.0	93.9	11.5	
88053.9730(100)	$19(5,14) - 19(4,15)E$	130.44	-5.8713	6.6	99.4	31.3	
88054.4610(100)	$19(5,14) - 19(4,15)A$	130.44	-5.8716	6.6	"	"	
88220.7530(100)	$7(1,6) - 6(1,5)E$ $v = 1$	204.91	-5.0168	18.1	93.9	12.3	
88337.8140(100)	$22(5,17) - 22(4,18)E$	169.52	-5.8423	8.1	70.6	4.0	
88358.4870(100)	$22(5,17) - 22(4,18)A$	169.52	-5.8422	8.1	99.4	28.7	
88770.8680(100)	$8(1,8) - 7(1,7)A$ $v = 1$	207.91	-5.0025	20.8	97.9	32.1	
88843.1870(100)	$7(1,6) - 6(1,5)E$	17.96	-5.0081	18.0	89.1	25.0	
88851.6070(100)	$7(1,6) - 6(1,5)A$	17.94	-5.0079	18.0	95.0	35.8	
88998.3650(100)	$7(2,5) - 6(2,4)A$ $v = 1$	207.37	-5.0298	17.1	97.4	40.9	
89140.3750(100)	$7(2,5) - 6(2,4)E$ $v = 1$	206.70	-5.0277	17.1	96.2	6.2	
89314.6570(100)	$8(1,8) - 7(1,7)E$	20.15	-4.9931	20.8	99.2	15.2	
89316.6420(100)	$8(1,8) - 7(1,7)A$	20.14	-4.9929	20.8	100.0	8.1	
89731.6950(100)	$8(0,8) - 7(0,7)A$ $v = 1$	207.83	-4.9870	20.8	91.8	10.1	
89829.7040(100)	$8(0,8) - 7(0,7)E$ $v = 1$	207.04	-4.9832	20.9	98.4	21.9	
90145.7230(100)	$7(2,5) - 6(2,4)E$	19.68	-5.0114	17.1	99.8	25.4	(Remijan et al., 2003) (Requena-Torres et al., 2006)
90156.4730(100)	$7(2,5) - 6(2,4)A$	19.67	-5.0111	17.1	98.7	28.2	(Remijan et al., 2003) (Requena-Torres et al., 2006)
90227.6590(100)	$8(0,8) - 7(0,7)E$	20.08	-4.9785	20.9	100.0	50.4	(Remijan et al., 2003) (Requena-Torres et al., 2006)
90229.6240(100)	$8(0,8) - 7(0,7)A$	20.06	-4.9783	20.9	99.5	45.1	(Remijan et al., 2003) (Requena-Torres et al., 2006)

Table 4.6 continued

Table 4.6: Transitions of MF with S/N > 3 covered by the EMoCA survey. (continued)

Rest Frequency (MHz)	Transition	E_u (K)	$\log_{10} \frac{A_{ul}}{s^{-1}}$	$S_{ij}\mu^2$ (D^2)	P Factor (%)	D Factor (%)	Obs Ref
91775.9350(100)	$8(1,8) - 7(0,7)E$	20.15	-5.8125	2.9	99.5	29.1	
91776.8860(100)	$20(4,16) - 20(3,17)E$	138.67	-5.8587	6.3	"	"	
91777.2300(100)	$8(1,8) - 7(0,7)A$	20.14	-5.8128	2.9	"	"	
92073.1010(100)	$18(5,13) - 18(4,14)A$	118.78	-5.8392	5.9	87.8	10.7	
92074.0200(100)	$18(5,13) - 18(4,14)E$	118.79	-5.8391	5.9	"	"	
95242.0050(100)	$8(2,7) - 7(2,6)A$ $v = 1$	211.31	-4.9318	19.8	94.9	37.5	
95689.3990(100)	$8(2,7) - 7(2,6)E$ $v = 1$	210.57	-4.9247	19.8	83.2	18.4	
96070.7250(100)	$8(2,7) - 7(2,6)E$	23.61	-4.9191	19.8	97.7	97.6	
96076.8450(100)	$8(2,7) - 7(2,6)A$	23.59	-4.9189	19.8	99.4	51.8	
97199.1110(100)	$17(5,12) - 17(4,13)E$	107.82	-5.7969	5.2	"	"	
97199.2220(100)	$17(5,12) - 17(4,13)A$	107.81	-5.7970	5.2	"	"	
97304.7110(100)	$8(7,1) - 7(7,0)A$ $v = 1$	241.56	-5.5029	5.0	93.2	0.8	
97304.7110(100)	$8(7,1) - 7(7,0)A$ $v = 1$	241.56	-5.5029	5.0	"	"	
97350.4170(300)	$8(6,2) - 7(6,1)A$ $v = 1$	232.90	-5.2315	9.3	96.8	56.8	
97350.4170(300)	$8(6,2) - 7(6,1)A$ $v = 1$	232.90	-5.2315	9.3	"	"	
97395.3420(100)	$8(6,2) - 7(6,1)E$ $v = 1$	232.82	-5.2291	9.3	94.3	15.3	
97457.9670(100)	$8(5,4) - 7(5,3)A$ $v = 1$	225.57	-5.0864	12.9	89.1	17.6	
97460.3950(100)	$8(5,3) - 7(5,2)A$ $v = 1$	225.57	-5.0863	12.9	93.3	26.3	
97577.3030(100)	$8(5,3) - 7(5,2)E$ $v = 1$	225.36	-5.0824	13.0	72.9	43.2	
97597.1610(100)	$8(3,6) - 7(3,5)A$ $v = 1$	214.94	-4.9360	18.2	79.2	14.5	
97651.2700(300)	$10(4,7) - 10(3,8)E$	43.17	-5.9016	2.4	80.6	10.1	
97651.2700(300)	$10(4,7) - 10(3,8)E$	43.17	-5.9016	2.4	"	"	
97661.4010(100)	$8(4,5) - 7(4,4)A$ $v = 1$	219.60	-4.9937	15.9	93.4	24.8	
97738.7380(100)	$8(6,3) - 7(6,2)E$ $v = 1$	232.09	-5.2243	9.3	"	"	
97752.8850(100)	$8(4,4) - 7(4,3)A$ $v = 1$	219.60	-4.9924	15.9	80.4	58.4	
97885.6630(100)	$8(5,4) - 7(5,3)E$ $v = 1$	224.73	-5.0787	13.0	91.4	20.6	
97897.1180(100)	$8(4,4) - 7(4,3)E$ $v = 1$	219.26	-4.9875	16.0	99.3	42.5	
98176.2930(100)	$8(4,5) - 7(4,4)E$ $v = 1$	218.74	-4.9853	16.0	82.3	1.8	
98182.3360(100)	$8(7,1) - 7(7,0)E$	53.78	-5.4902	5.0	80.2	2.7	

Table 4.6 continued

Table 4.6: Transitions of MF with S/N > 3 covered by the EMoCA survey. (continued)

Rest Frequency (MHz)	Transition	E_u (K)	$\log_{10} \frac{A_{ul}}{s^{-1}}$	$S_{ij}\mu^2$ (D^2)	P Factor (%)	D Factor (%)	Obs Ref
98190.6580(100)	$8(7,2) - 7(7,1)A$	53.76	-5.4900	5.0	99.7	34.8	
98190.6580(100)	$8(7,2) - 7(7,1)A$	53.76	-5.4900	5.0	"	"	
98191.4600(100)	$8(7,2) - 7(7,1)E$	53.76	-5.4901	5.0	"	"	
98270.5010(100)	$8(6,2) - 7(6,1)E$	45.15	-5.2180	9.3	79.0	15.2	
98278.9210(100)	$8(6,3) - 7(6,2)E$	45.13	-5.2179	9.3	96.4	65.3	
98279.7620(100)	$8(6,3) - 7(6,2)A$	45.13	-5.2178	9.3	"	"	
98279.7620(100)	$8(6,3) - 7(6,2)A$	45.13	-5.2178	9.3	"	"	
98423.1650(100)	$9(0,9) - 8(1,8)A$ $v = 1$	212.63	-5.7011	3.4	91.4	36.1	
98424.2070(100)	$8(5,3) - 7(5,2)E$	37.86	-5.0722	13.0	"	"	
98431.8030(100)	$8(5,4) - 7(5,3)E$	37.84	-5.0721	13.0	98.9	38.8	
98432.7600(100)	$8(5,4) - 7(5,3)A$	37.84	-5.0720	13.0	"	"	
98435.8020(100)	$8(5,3) - 7(5,2)A$	37.84	-5.0720	13.0	99.7	33.3	
98606.8560(100)	$8(3,6) - 7(3,5)E$	27.26	-4.9216	18.2	82.3	9.4	
98611.1630(100)	$8(3,6) - 7(3,5)A$	27.24	-4.9209	18.3	97.9	4.0	
98682.4210(100)	$8(3,6) - 7(3,5)E$ $v = 1$	214.15	-4.9245	18.1	99.7	54.8	
98682.6150(100)	$8(4,5) - 7(4,4)A$	31.89	-4.9786	16.0	"	"	
98712.0010(100)	$8(4,5) - 7(4,4)E$	31.90	-4.9928	15.4	89.5	6.6	
98713.6550(100)	$26(8,18) - 25(9,17)E$	250.95	-6.7530	0.8	"	"	
98747.9060(100)	$8(4,4) - 7(4,3)E$	31.91	-4.9923	15.4	93.0	8.8	
98792.2890(100)	$8(4,4) - 7(4,3)A$	31.89	-4.9772	16.0	91.5	11.1	
98815.2900(100)	$8(3,5) - 7(3,4)E$ $v = 1$	214.56	-4.9193	18.2	95.6	36.2	
99089.5180(100)	$8(3,5) - 7(3,4)A$ $v = 1$	215.08	-4.9159	18.2	98.7	64.8	
99133.2720(100)	$9(0,9) - 8(1,8)E$	24.91	-5.6979	3.4	98.8	22.3	
99135.7620(100)	$9(0,9) - 8(1,8)A$	24.89	-5.6982	3.4	100.0	13.0	
99489.0570(100)	$9(1,9) - 8(1,8)A$ $v = 1$	212.69	-4.8499	23.4	99.1	39.4	
99575.5480(100)	$8(1,7) - 7(1,6)A$ $v = 1$	210.43	-4.8565	20.6	98.1	31.1	
99577.4190(100)	$9(1,9) - 8(1,8)E$ $v = 1$	211.90	-4.8461	23.6	"	"	
99869.1020(100)	$8(1,7) - 7(1,6)E$ $v = 1$	209.71	-4.8509	20.7	94.0	10.4	
100078.6080(100)	$9(1,9) - 8(1,8)E$	24.96	-4.8407	23.5	96.9	9.7	

Table 4.6 continued

Table 4.6: Transitions of MF with S/N > 3 covered by the EMoCA survey. (continued)

Rest Frequency (MHz)	Transition	E_u (K)	$\log_{10} \frac{A_{ul}}{s^{-1}}$	$S_{ij}\mu^2$ (D^2)	P Factor (%)	D Factor (%)	Obs Ref
100080.5420(100)	$9(1,9) - 8(1,8)A$	24.94	-4.8406	23.5	94.7	6.8	
100136.9130(100)	$9(0,9) - 8(0,8)A$ v = 1	212.63	-4.8407	23.5	73.1	13.2	
100226.6840(100)	$9(0,9) - 8(0,8)E$ v = 1	211.85	-4.8370	23.6	81.9	31.9	
100294.6040(100)	$8(3,5) - 7(3,4)E$	27.41	-4.8992	18.3	99.7	32.3	
100308.1790(100)	$8(3,5) - 7(3,4)A$	27.40	-4.8985	18.3	99.3	37.7	
100482.2410(100)	$8(1,7) - 7(1,6)E$	22.78	-4.8437	20.6	99.8	13.5	
100490.6820(100)	$8(1,7) - 7(1,6)A$	22.76	-4.8435	20.6	87.5	20.6	
100681.5450(100)	$9(0,9) - 8(0,8)E$	24.91	-4.8323	23.5	98.2	34.9	
100683.3680(100)	$9(0,9) - 8(0,8)A$	24.89	-4.8322	23.5	"	"	
101626.8840(100)	$9(1,9) - 8(0,8)E$	24.96	-5.6633	3.4	90.9	24.9	
101628.1490(100)	$9(1,9) - 8(0,8)A$	24.94	-5.6636	3.4	"	"	
102179.5100(100)	$8(2,6) - 7(2,5)A$ v = 1	212.27	-4.8370	19.9	96.5	8.8	
102503.1050(100)	$8(2,6) - 7(2,5)E$ v = 1	211.62	-4.8307	20.0	92.3	25.2	
102734.2120(100)	$16(5,11) - 16(4,12)E$	97.52	-5.7520	4.6	99.6	18.0	
102736.8690(100)	$16(5,11) - 16(4,12)A$	97.51	-5.7519	4.6	99.3	16.2	
103376.8420(100)	$24(6,18) - 24(5,19)A$	203.82	-5.6555	8.4	70.8	11.7	
103387.2000(100)	$24(6,18) - 24(5,19)E$	203.82	-5.6553	8.4	91.0	2.5	
103466.5720(100)	$8(2,6) - 7(2,5)E$	24.65	-4.8190	20.0	98.3	42.2	
103478.6630(100)	$8(2,6) - 7(2,5)A$	24.63	-4.8187	20.0	98.9	63.4	
106648.7540(100)	$9(2,8) - 8(2,7)A$ v = 1	216.42	-4.7760	22.5	95.6	8.8	
107022.1590(100)	$9(2,8) - 8(2,7)E$ v = 1	215.71	-4.7693	22.6	79.3	6.5	
107537.2580(100)	$9(2,8) - 8(2,7)E$	28.77	-4.7639	22.6	75.8	20.4	(Remijan et al., 2003)
107543.7110(100)	$9(2,8) - 8(2,7)A$	28.75	-4.7637	22.6	98.3	5.9	(Remijan et al., 2003)
107590.3890(100)	$23(6,17) - 23(5,18)A$	189.04	-5.6251	7.7	91.8	1.0	
107604.3660(100)	$23(6,17) - 23(5,18)E$	189.04	-5.6248	7.7	93.9	1.1	
108045.9590(100)	$15(5,10) - 15(4,11)E$	87.87	-5.7107	4.1	94.6	25.3	
108050.9390(100)	$15(5,10) - 15(4,11)A$	87.86	-5.7099	4.1	88.1	25.4	
109501.2460(100)	$9(8,1) - 8(8,0)A$ v = 1	256.83	-5.3939	5.0	84.9	2.5	
109501.2460(100)	$9(8,1) - 8(8,0)A$ v = 1	256.83	-5.3939	5.0	"	"	

Table 4.6 continued

Table 4.6: Transitions of MF with S/N > 3 covered by the EMoCA survey. (continued)

Rest Frequency (MHz)	Transition	E_u (K)	$\log_{10} \frac{A_{ul}}{s^{-1}}$	$S_{ij}\mu^2$ (D^2)	P Factor (%)	D Factor (%)	Obs Ref
109502.6550(100)	$9(7,2) - 8(7,1)E$ $v = 1$	246.89	-5.1181	9.5	"	"	
109531.4130(100)	$9(7,2) - 8(7,1)A$ $v = 1$	246.82	-5.1190	9.4	99.5	34.9	
109531.4130(100)	$9(7,2) - 8(7,1)A$ $v = 1$	246.82	-5.1190	9.4	"	"	
109608.5400(300)	$9(6,3) - 8(6,2)A$ $v = 1$	238.16	-4.9703	13.3	64.0	11.3	
109608.5400(300)	$9(6,3) - 8(6,2)A$ $v = 1$	238.16	-4.9703	13.3	"	"	
109662.9440(100)	$9(6,3) - 8(6,2)E$ $v = 1$	238.08	-4.9679	13.3	90.5	66.7	
109763.7370(100)	$9(3,7) - 8(3,6)A$ $v = 1$	220.21	-4.7655	21.2	91.3	12.2	
109770.9950(100)	$9(5,5) - 8(5,4)A$ $v = 1$	230.84	-4.8736	16.5	89.0	11.5	
109778.8350(100)	$9(5,4) - 8(5,3)A$ $v = 1$	230.84	-4.8735	16.5	94.7	3.0	
109912.1680(100)	$9(5,4) - 8(5,3)E$ $v = 1$	230.63	-4.8697	16.6	80.5	3.2	
109924.8170(100)	$9(7,3) - 8(7,2)E$ $v = 1$	246.10	-5.1124	9.5	87.8	70.9	
110035.2690(100)	$9(4,6) - 8(4,5)A$ $v = 1$	224.88	-4.8060	19.2	97.6	7.2	
110050.3320(100)	$9(6,4) - 8(6,3)E$ $v = 1$	237.38	-4.9631	13.3	96.4	1.8	
110153.6520(100)	$10(1,10) - 9(1,9)A$ $v = 1$	217.97	-4.7139	26.1	94.6	14.8	
110364.5200(100)	$9(4,5) - 8(4,4)E$ $v = 1$	224.55	-4.7991	19.3	99.4	2.6	
110447.1800(100)	$9(8,1) - 8(8,0)E$	69.04	-5.3818	5.0	93.3	6.3	
110455.3720(100)	$9(8,2) - 8(8,1)A$	69.03	-5.3817	5.0	89.4	43.3	
110455.3720(100)	$9(8,2) - 8(8,1)A$	69.03	-5.3817	5.0	"	"	
110458.0140(100)	$9(8,2) - 8(8,1)E$	69.02	-5.3817	5.0	"	"	
110525.7410(100)	$9(7,2) - 8(7,1)E$	59.09	-5.1063	9.5	83.0	60.7	
110526.1900(100)	$7(2,6) - 6(1,5)A$ $v = 1$	206.74	-5.8286	1.4	"	"	
110535.1860(100)	$9(7,3) - 8(7,2)A$	59.07	-5.1061	9.5	91.3	67.5	
110535.1860(100)	$9(7,3) - 8(7,2)A$	59.07	-5.1061	9.5	"	"	
110536.0030(100)	$9(7,3) - 8(7,2)E$	59.07	-5.1061	9.5	"	"	
110571.6320(100)	$10(0,10) - 9(0,9)A$ $v = 1$	217.94	-4.7086	26.1	93.4	28.8	
110652.8130(100)	$9(6,3) - 8(6,2)E$	50.46	-4.9568	13.3	98.5	30.4	
110655.3100(100)	$10(0,10) - 9(0,9)E$ $v = 1$	217.16	-4.7051	26.3	98.6	16.3	
110662.3150(100)	$9(6,4) - 8(6,3)E$	50.45	-4.9567	13.3	77.1	19.0	
110663.2730(100)	$9(6,4) - 8(6,3)A$	50.44	-4.9566	13.3	"	"	

Table 4.6 continued

Table 4.6: Transitions of MF with S/N > 3 covered by the EMoCA survey. (continued)

Rest Frequency (MHz)	Transition	E_u (K)	$\log_{10} \frac{A_{ul}}{s^{-1}}$	$S_{ij}\mu^2$ (D^2)	P Factor (%)	D Factor (%)	Obs Ref
110663.4290(100)	$9(6,3) - 8(6,2)A$	50.44	-4.9566	13.3	"	"	
110684.1230(100)	$9(4,6) - 8(4,5)E$ v = 1	224.06	-4.7970	19.2	92.6	2.9	
110776.4990(100)	$9(1,8) - 8(1,7)A$ v = 1	215.75	-4.7150	23.1	96.9	68.0	
110788.6640(100)	$10(1,10) - 9(1,9)E$	30.27	-4.7051	26.2	96.6	62.5	
110790.5260(100)	$10(1,10) - 9(1,9)A$	30.26	-4.7049	26.2	"	"	
110873.9550(100)	$9(5,4) - 8(5,3)E$	43.18	-4.8594	16.6	96.8	57.9	
110879.7660(100)	$9(3,7) - 8(3,6)E$	32.58	-4.7510	21.2	97.1	89.6	
110880.4470(100)	$9(5,5) - 8(5,4)A$	43.16	-4.8592	16.6	"	"	
110882.3310(100)	$9(5,5) - 8(5,4)E$	43.16	-4.8594	16.6	"	"	
110887.0920(100)	$9(3,7) - 8(3,6)A$	32.57	-4.7507	21.3	99.8	52.7	
110890.2560(100)	$9(5,4) - 8(5,3)A$	43.16	-4.8590	16.6	99.4	39.2	
111005.6720(100)	$9(3,7) - 8(3,6)E$ v = 1	219.48	-4.7583	20.8	70.7	13.4	
111094.1240(100)	$9(1,8) - 8(1,7)E$ v = 1	215.04	-4.7094	23.2	71.8	14.7	
111169.9030(100)	$10(0,10) - 9(0,9)E$	30.25	-4.7002	26.2	99.6	82.7	
111171.6340(100)	$10(0,10) - 9(0,9)A$	30.23	-4.7001	26.2	"	"	
111195.9620(100)	$9(4,6) - 8(4,5)A$	37.22	-4.7909	19.2	93.9	55.9	
111223.4910(100)	$9(4,6) - 8(4,5)E$	37.23	-4.8145	18.2	98.7	53.0	
111224.9860(100)	$14(3,11) - 13(4,10)E$ v = 1	256.70	-6.3187	0.9	"	"	
111408.4120(100)	$9(4,5) - 8(4,4)E$	37.26	-4.8123	18.2	94.9	86.1	(Requena-Torres et al., 2006)
111453.3000(100)	$9(4,5) - 8(4,4)A$	37.24	-4.7878	19.2	99.9	75.0	(Remijan et al., 2003)
111674.1310(100)	$9(1,8) - 8(1,7)E$	28.14	-4.7037	23.2	99.6	78.7	(Requena-Torres et al., 2006)
111682.1890(100)	$9(1,8) - 8(1,7)A$	28.12	-4.7035	23.2	99.6	58.9	(Requena-Torres et al., 2006)
111734.0020(100)	$10(1,10) - 9(0,9)E$	30.27	-5.5269	3.8	95.9	36.0	
111735.3070(100)	$10(1,10) - 9(0,9)A$	30.26	-5.5271	3.8	"	"	
112011.9660(100)	$9(3,6) - 8(3,5)E$ v = 1	219.94	-4.7426	21.0	"	"	
112306.9410(100)	$9(3,6) - 8(3,5)A$ v = 1	220.47	-4.7352	21.2	96.7	18.8	
113743.1070(100)	$9(3,6) - 8(3,5)E$	32.87	-4.7171	21.3	98.1	14.4	
113756.6100(100)	$9(3,6) - 8(3,5)A$	32.86	-4.7168	21.3	99.1	30.5	

NOTE — Pertinent parameters of the detected transitions of MF taken from JPL catalog. The transitions with ditto marks in the column of P and D factors are blended with the transitions in the previous row.

Table 4.7: Transitions of GLA with S/N > 3 covered by the EMoCA survey.

Rest Frequency (MHz)	Transition	E_u (K)	$\log_{10} \frac{A_{ul}}{s^{-1}}$	$S_{ij}\mu^2$ (D^2)	P Factor (%)	D Factor (%)	Obs Ref
85288.3467(47)	$8(4,4) - 8(3,5)$	29.74	-5.0287	22.0	73.0	63.8	
85476.6666(92)	$11(1,10) - 11(0,11)$	37.91	-5.3021	15.8	97.9	41.4	
85782.2440(55)	$8(1,8) - 7(0,7)$	18.87	-4.8264	34.5	73.6	31.2	(Halfen et al., 2006)
86600.5997(67)	$17(5,12) - 17(4,13)$	101.14	-4.8624	63.6	91.0	86.6	
87764.5007(47)	$5(2,4) - 4(1,3)$	10.69	-5.0665	12.0	84.5	27.8	
87812.2080(47)	$6(4,2) - 6(3,3)$	21.38	-5.0745	13.9	94.3	8.9	
88425.7474(47)	$7(4,4) - 7(3,5)$	25.27	-5.0198	17.8	99.0	20.7	
88463.7084(47)	$6(4,3) - 6(3,4)$	21.38	-5.0662	13.9	90.7	15.9	
88530.4001(46)	$8(4,5) - 8(3,6)$	29.73	-4.9874	21.7	94.9	68.9	
88691.2605(68)	$12(3,10) - 12(2,11)$	48.77	-5.0203	29.4	92.2	58.9	
88892.4467(45)	$9(4,6) - 9(3,7)$	34.76	-4.9607	25.4	85.0	14.1	
89616.3982(132)	$20(4,16) - 20(3,17)$	130.44	-4.8374	71.2	98.4	29.8	
89644.1477(45)	$10(4,7) - 10(3,8)$	40.35	-4.9352	29.1	89.7	2.2	
89832.2856(115)	$14(2,12) - 14(1,13)$	62.93	-5.0296	32.1	91.8	39.5	
89868.6318(54)	$9(1,8) - 8(2,7)$	26.42	-5.0389	20.6	94.0	16.8	(Halfen et al., 2006)
90187.0697(109)	$23(5,18) - 23(4,19)$	172.97	-4.7716	93.1	95.7	28.2	
90507.2610(133)	$17(3,14) - 17(2,15)$	93.78	-4.9064	50.3	98.1	80.4	
90591.3442(78)	$11(2,10) - 11(1,11)$	38.17	-5.2329	15.5	86.6	1.8	
90922.2144(46)	$11(4,8) - 11(3,9)$	46.51	-4.9075	32.5	58.2	22.1	
91712.9604(71)	$16(5,11) - 16(4,12)$	91.41	-4.8169	56.0	74.2	7.9	
92738.2867(52)	$25(6,19) - 25(5,20)$	206.18	-4.7044	108.5	85.7	27.2	
92853.9487(49)	$12(4,9) - 12(3,10)$	53.23	-4.8762	35.7	97.2	79.2	
93048.5007(46)	$24(6,18) - 24(5,19)$	191.55	-4.7088	102.2	94.2	27.1	
93052.6745(56)	$9(0,9) - 8(1,8)$	23.34	-4.7062	39.8	95.7	44.1	(Hollis et al., 2000)

Table 4.7 continued

Table 4.7: Transitions of GLA with S/N > 3 covered by the EMoCA survey. (continued)

Rest Frequency (MHz)	Transition	E_u (K)	$\log_{10} \frac{A_{ul}}{s^{-1}}$	$S_{ij}\mu^2$ (D^2)	P Factor (%)	D Factor (%)	Obs Ref
							(Halfen et al., 2006)
95070.0983(60)	$9(1,9) - 8(0,8)$	23.37	-4.6763	40.0	78.9	10.5	(Halfen et al., 2006)
95175.1800(76)	$26(6,20) - 26(5,21)$	221.45	-4.6731	112.1	84.4	31.5	
95300.4082(75)	$13(3,11) - 13(2,12)$	55.93	-4.9488	30.2	84.9	26.7	
95443.0896(53)	$6(2,5) - 5(1,4)$	13.97	-4.9612	14.0	99.5	1.2	
95544.7538(53)	$13(4,10) - 13(3,11)$	60.52	-4.8397	38.5	82.6	18.2	
95741.7260(94)	$12(1,11) - 12(0,12)$	44.35	-5.1911	15.8	79.9	4.6	
95756.2369(57)	$23(6,17) - 23(5,18)$	177.57	-4.6897	94.0	83.9	58.9	
96078.4307(75)	$11(2,9) - 10(3,8)$	40.66	-5.1981	14.1	75.8	13.6	
96870.7828(70)	$15(5,10) - 15(4,11)$	82.31	-4.7720	49.5	89.6	67.1	
97919.5791(49)	$3(3,1) - 2(2,0)$	8.80	-4.6806	13.4	7.1	49.1	
98070.5113(49)	$3(3,0) - 2(2,1)$	8.80	-4.6793	13.3	87.8	12.2	
99068.4727(59)	$14(4,11) - 14(3,12)$	68.36	-4.7976	40.8	71.4	20.6	
99109.9990(83)	$12(2,11) - 12(1,12)$	44.52	-5.1491	15.7	99.6	41.8	
99346.4488(133)	$24(5,19) - 24(4,20)$	187.08	-4.6741	90.9	93.1	11.8	
100323.8733(73)	$22(6,16) - 22(5,17)$	164.25	-4.6532	85.1	92.8	2.2	
100506.6546(103)	$27(6,21) - 27(5,22)$	237.35	-4.6155	112.8	92.7	21.8	
101116.3124(145)	$21(4,17) - 21(3,18)$	142.69	-4.7161	68.7	99.6	39.5	
101232.1720(115)	$15(2,13) - 15(1,14)$	71.31	-4.9076	31.8	79.8	21.7	
101527.8515(65)	$14(5,9) - 14(4,10)$	73.82	-4.7334	44.0	93.9	15.0	
102549.7240(60)	$7(2,6) - 6(1,5)$	17.78	-4.8570	16.6	76.3	8.1	(Halfen et al., 2006)
102572.9391(82)	$14(3,12) - 14(2,13)$	63.60	-4.8764	30.7	99.0	62.2	
102614.3429(137)	$18(3,15) - 18(2,16)$	104.10	-4.7784	49.0	97.9	64.4	
103391.2854(62)	$10(0,10) - 9(1,9)$	28.34	-4.5552	45.5	93.5	26.3	(Hollis et al., 2000)
							(Halfen et al., 2006)

Table 4.7 continued

Table 4.7: Transitions of GLA with S/N > 3 covered by the EMoCA survey. (continued)

Rest Frequency (MHz)	Transition	E_u (K)	$\log_{10} \frac{A_{ul}}{s^{-1}}$	$S_{ij}\mu^2$ (D^2)	P Factor (%)	D Factor (%)	Obs Ref
103461.3106(66)	$15(4,12) - 15(3,13)$	76.75	-4.7501	42.8	95.0	77.7	
103667.9094(57)	$10(1,9) - 9(2,8)$	31.93	-4.7910	26.2	91.3	58.6	(Hollis et al., 2000) (Halfen et al., 2006)
104587.7032(64)	$10(1,10) - 9(0,9)$	28.36	-4.5394	45.5	88.2	6.9	(Halfen et al., 2006)
105355.6639(59)	$13(5,8) - 13(4,9)$	65.93	-4.7051	39.1	99.2	16.0	
106067.4262(84)	$21(6,15) - 21(5,16)$	151.60	-4.6068	76.6	87.7	21.6	
106710.9951(60)	$29(7,22) - 29(6,23)$	275.99	-4.5255	124.4	87.1	22.4	
107380.1425(74)	$30(7,23) - 30(6,24)$	293.59	-4.5135	129.8	81.9	21.5	
107663.7353(115)	$19(5,14) - 18(6,13)$	122.53	-5.3224	12.8	88.9	13.9	
107874.8614(87)	$13(2,12) - 13(1,13)$	51.36	-5.0703	15.7	99.4	13.3	
108261.4557(56)	$12(5,7) - 12(4,8)$	58.63	-4.6885	34.7	94.7	40.1	
108719.6747(73)	$16(4,13) - 16(3,14)$	85.69	-4.6979	44.2	94.6	3.8	
108824.4021(62)	$28(7,21) - 28(6,22)$	259.05	-4.5133	116.5	98.2	59.3	
109114.1722(53)	$4(3,2) - 3(2,1)$	11.02	-4.6411	13.6	79.0	18.3	
109280.0092(66)	$8(2,7) - 7(1,6)$	22.11	-4.7522	19.8	87.7	60.2	(Halfen et al., 2006)
109877.1408(54)	$4(3,1) - 3(2,2)$	11.02	-4.6354	13.5	77.9	1.9	
110330.6028(55)	$11(5,6) - 11(4,7)$	51.91	-4.6836	30.5	99.2	3.3	
110402.5367(87)	$15(3,13) - 15(2,14)$	71.79	-4.8048	31.0	99.4	80.3	
110608.5089(148)	$25(5,20) - 25(4,21)$	201.73	-4.5659	88.0	84.5	3.9	
110845.1604(102)	$14(3,11) - 13(4,10)$	65.84	-5.1366	13.4	74.9	2.8	
111098.2681(97)	$31(7,24) - 31(6,25)$	311.83	-4.4755	132.1	97.6	53.3	
111734.8569(55)	$10(5,5) - 10(4,6)$	45.76	-4.6897	26.4	98.5	47.0	
112177.7128(51)	$13(5,9) - 13(4,10)$	65.90	-4.6338	38.2	75.4	27.1	
112210.4422(52)	$12(5,8) - 12(4,9)$	58.62	-4.6471	34.3	92.2	70.7	
112247.9894(87)	$20(6,14) - 20(5,15)$	139.58	-4.5575	69.0	81.7	25.9	

Table 4.7 continued

Table 4.7: Transitions of GLA with S/N > 3 covered by the EMoCA survey. (continued)

Rest Frequency (MHz)	Transition	$E_{\rm u}$ (K)	$\log_{10} \frac{A_{ul}}{\rm s^{-1}}$	$S_{ij}\mu^2$ ($\rm D^2$)	P Factor (%)	D Factor (%)	Obs Ref
112341.6773(114)	$16(2,14) - 16(1,15)$	80.14	-4.8011	31.6	94.4	22.8	
112444.3079(53)	$11(5,7) - 11(4,8)$	51.90	-4.6614	30.3	86.6	31.1	
112472.7946(50)	$14(5,10) - 14(4,11)$	73.76	-4.6197	42.0	98.6	98.4	
112656.0535(56)	$9(5,4) - 9(4,5)$	40.19	-4.7071	22.4	69.6	8.7	
112773.4455(55)	$10(5,6) - 10(4,7)$	45.76	-4.6788	26.4	81.6	9.2	
113326.8996(77)	$12(2,10) - 11(3,9)$	47.58	-4.9081	18.2	88.5	14.4	(Halfen et al., 2006)
113429.3652(57)	$8(5,4) - 8(4,5)$	35.18	-4.7360	18.4	95.7	5.9	
113569.5317(66)	$11(0,11) - 10(1,10)$	33.81	-4.4222	51.0	75.3	42.3	(Halfen et al., 2006)
113616.7028(57)	$7(5,2) - 7(4,3)$	30.73	-4.7891	14.3	83.5	5.3	
113679.1292(57)	$7(5,3) - 7(4,4)$	30.73	-4.7884	14.3	95.8	7.9	
113694.9880(150)	$22(4,18) - 22(3,19)$	155.43	-4.5962	66.7	95.6	10.1	
114264.4356(67)	$11(1,11) - 10(0,10)$	33.82	-4.4139	51.1	95.8	29.3	(Halfen et al., 2006)

NOTE — Pertinent parameters of the detected transitions of GLA taken from CDMS catalog. The transitions with ditto marks in the column of P and D factors are blended with the transitions in the previous row.

Table 4.8: Transitions of AcA with S/N > 3 covered by the EMoCA survey.

Rest Frequency (MHz)	Transition	E_u (K)	$\log_{10} \frac{A_{ul}}{s^{-1}}$	$S_{ij}\mu^2$ (D^2)	P Factor (%)	D Factor (%)	Obs Ref
84857.3100(10)	$10(2,8) - 10(2,9)$ + −	39.18	-6.4449	1.1	89.4	62.3	
84857.3200(10)	$10(2,8) - 10(1,9)$ + −	39.18	-5.7818	4.9	"	"	
84857.8300(10)	$10(3,8) - 10(2,9)$ + −	39.18	-5.7818	4.9	"	"	
84857.8300(10)	$10(3,8) - 10(2,9)$ + −	39.18	-5.7818	4.9	"	"	
85399.0300(10)	$19(10,9) - 19(9,10)$ + −	167.72	-5.3809	22.4	89.8	50.3	
85981.5900(10)	$19(-10,9) - 19(-9,10)$	167.84	-5.3722	22.4	81.1	22.7	
86473.4400(20)	$23(15,9) - 23(14,10)$ + −	251.63	-5.3148	30.2	95.1	4.7	
86569.9100(10)	$20(12,9) - 20(11,10)$ − +	187.34	-5.3465	24.4	80.8	86.5	
86879.0100(20)	$23(13,10) - 23(12,11)$ − +	247.08	-5.3194	29.5	96.5	6.0	
87631.1000(40)	$15(-11,4) - 15(-9,6)$	113.06	-7.0292	0.4	95.5	5.6	
87632.9100(10)	$19(11,9) - 19(10,10)$	167.92	-5.3486	22.3	"	"	
87759.3100(30)	$14(-14,0) - 14(-13,1)$	112.51	-5.9766	3.9	91.1	14.8	
87761.2200(10)	$19(11,9) - 19(10,10)$ + −	167.84	-5.3475	22.3	"	"	
87822.7200(10)	$4(-4,0) - 3(-3,0)$	10.91	-5.2581	6.3	84.7	3.6	
87823.6800(10)	$6(2,4) - 5(3,3)$ + +	16.93	-5.4130	6.4	"	"	
89516.9600(10)	$7(-1,6) - 6(2,5)$	19.59	-5.1941	11.5	93.2	9.2	
89518.9500(10)	$7(2,6) - 6(2,5)$	19.59	-5.6395	4.1	"	"	
89531.1900(10)	$7(-1,6) - 6(-1,5)$	19.59	-5.6393	4.1	88.9	55.7	
89533.1800(10)	$7(2,6) - 6(-1,5)$	19.59	-5.1939	11.5	"	"	
89653.2800(10)	$7(1,6) - 6(2,5)$ − −	19.12	-5.1974	11.3	92.7	3.4	
89677.4100(10)	$7(2,6) - 6(1,5)$ − −	19.12	-5.1971	11.3	90.3	3.2	
90203.4400(10)	$8(*,8) - 7(1,7)$	20.83	-4.9646	21.6	99.0	23.3	(Mehringer et al., 1997) (Remijan et al., 2003)
90203.4600(10)	$8(*,8) - 7(0,7)$	20.83	-4.9646	21.6	"	"	(Mehringer et al., 1997)

Table 4.8 continued

Table 4.8: Transitions of AcA with S/N > 3 covered by the EMoCA survey. (continued)

Rest Frequency (MHz)	Transition	E_u (K)	$\log_{10} \frac{A_{ul}}{s^{-1}}$	$S_{ij}\mu^2$ (D^2)	P Factor (%)	D Factor (%)	Obs Ref
90246.2400(10)	$8(*,8) - 7(1,7) + +$	20.33	-4.9642	21.6	96.8	47.1	(Remijan et al., 2003) (Mehringer et al., 1997)
90246.2700(10)	$8(*,8) - 7(0,7) + +$	20.33	-4.9642	21.6	"	"	(Remijan et al., 2003) (Mehringer et al., 1997)
93760.4300(10)	$12(-3,9) - 12(*,10)$	58.24	-5.4784	8.7	66.9	16.1	(Remijan et al., 2003)
93760.6900(10)	$12(4,9) - 12(3,10)$	58.24	-5.5568	7.2	"	"	
93760.6900(10)	$12(4,9) - 12(3,10)$	58.24	-5.5568	7.2	"	"	
94499.3200(10)	$12(3,9) - 12(3,10) - +$	57.87	-6.2182	1.5	76.9	33.9	
94499.3300(10)	$12(3,9) - 12(2,10) - +$	57.87	-5.5502	7.2	"	"	
94499.8200(10)	$12(4,9) - 12(3,10) - +$	57.87	-5.5502	7.2	"	"	
94499.8300(10)	$12(4,9) - 12(2,10) - +$	57.87	-6.2182	1.5	"	"	
95199.7500(10)	$22(13,10) - 22(12,11)$	225.12	-5.2227	26.8	75.9	1.8	
95243.0100(10)	$22(13,10) - 22(12,11) + -$	225.11	-5.2236	26.7	84.1	18.5	
95568.4100(10)	$21(-11,10) - 21(-10,11)$	203.65	-5.2349	24.6	72.9	23.6	
96694.7700(10)	$21(12,10) - 21(11,11)$	203.71	-5.2204	24.6	98.5	19.2	
96707.2300(10)	$21(12,10) - 21(11,11) - +$	203.68	-5.2216	24.5	80.5	17.0	
97347.3100(20)	$25(14,11) - 25(13,12) + -$	290.34	-5.1772	31.6	82.6	37.2	
97508.8900(10)	$20(10,10) - 20(9,11) + -$	183.14	-5.2308	22.3	72.8	22.7	
97685.6600(10)	$20(-10,10) - 20(-9,11)$	183.22	-5.2269	22.4	70.2	20.6	
98134.2400(10)	$20(11,10) - 20(10,11)$	183.25	-5.2211	22.4	96.5	4.3	
98194.4400(10)	$20(11,10) - 20(10,11) + -$	183.18	-5.2221	22.3	96.0	13.6	
99262.3700(10)	$19(-9,10) - 19(-8,11)$	163.72	-5.2288	20.2	98.6	27.4	
99341.5700(10)	$7(-2,5) - 6(3,4)$	22.19	-5.1689	8.9	80.3	18.1	
99424.7200(10)	$7(3,5) - 6(3,4)$	22.20	-5.5518	3.7	77.5	67.2	

Table 4.8 continued

Table 4.8: Transitions of AcA with S/N > 3 covered by the EMoCA survey. (continued)

Rest Frequency (MHz)	Transition	E_u (K)	$\log_{10} \frac{A_{ul}}{s^{-1}}$	$S_{ij}\mu^2$ (D^2)	P Factor (%)	D Factor (%)	Obs Ref
99425.9200(10)	$19(10,10) - 19(9,11)$	163.73	-5.2266	20.2	"	"	
99487.5000(10)	$7(2,5) - 6(3,4) + +$	21.74	-5.1743	8.8	86.7	15.5	
99579.4600(10)	$19(10,10) - 19(9,11) - +$	163.63	-5.2268	20.1	65.9	12.3	
99862.2800(10)	$7(3,5) - 6(-2,4)$	22.19	-5.1601	8.9	79.9	13.5	
100168.7100(10)	$8(-1,7) - 7(2,6)$	24.40	-5.0256	13.7	100.0	10.4	
100168.9700(10)	$8(2,7) - 7(2,6)$	24.40	-5.4811	4.8	"	"	
100170.7000(10)	$8(-1,7) - 7(-1,6)$	24.40	-5.4810	4.8	99.8	18.4	
100170.9600(10)	$8(2,7) - 7(-1,6)$	24.40	-5.0256	13.7	"	"	
100202.9200(10)	$7(3,5) - 6(2,4) + +$	21.74	-5.1625	8.8	92.4	13.2	
100306.5300(10)	$8(1,7) - 7(2,6) - -$	23.94	-5.0295	13.5	87.4	23.4	
100306.9800(10)	$8(2,7) - 7(2,6) - -$	23.94	-5.4650	5.0	"	"	
100309.1100(40)	$14(11,4) - 14(9,5) + -$	100.77	-6.8014	0.4	92.0	15.3	
100309.6900(10)	$8(1,7) - 7(1,6) - -$	23.94	-5.4650	5.0	"	"	
100310.1300(10)	$8(2,7) - 7(1,6) - -$	23.94	-5.0295	13.5	"	"	
100481.8000(10)	$18(-8,10) - 18(-7,11)$	145.13	-5.2386	18.1	96.9	2.1	
100536.1900(10)	$18(9,10) - 18(8,11)$	145.15	-5.2378	18.1	73.8	40.3	
100855.4300(10)	$9(*,9) - 8(*,8)$	25.67	-4.5117	49.0	94.7	70.7	(Mehringer et al., 1997) (Remijan et al., 2003)
100897.4500(10)	$9(*,9) - 8(*,8) + +$	25.17	-4.5113	49.0	92.0	40.8	(Mehringer et al., 1997) (Remijan et al., 2003)
101448.7200(10)	$17(-7,10) - 17(7,11)$	127.51	-6.0030	2.9	65.9	10.4	
101449.4900(10)	$17(-7,10) - 17(-6,11)$	127.51	-5.2563	16.0	"	"	
101465.8700(10)	$17(8,10) - 17(7,11)$	127.51	-5.2561	16.0	80.3	49.9	
101466.6400(10)	$17(8,10) - 17(-6,11)$	127.51	-6.0028	2.9	"	"	
102227.0100(10)	$16(-6,10) - 16(6,11)$	110.83	-6.0173	2.5	90.0	2.1	

Table 4.8 continued

Table 4.8: Transitions of AcA with S/N > 3 covered by the EMoCA survey. (continued)

Rest Frequency (MHz)	Transition	E_u (K)	$\log_{10} \frac{A_{ul}}{s^{-1}}$	$S_{ij}\mu^2$ (D^2)	P Factor (%)	D Factor (%)	Obs Ref
102227.1700(10)	$16(-6,10) - 16(-5,11)$	110.83	-5.2827	13.8	"	"	
102231.5800(10)	$16(7,10) - 16(6,11)$	110.83	-5.2827	13.8	73.9	4.6	
102231.7500(10)	$16(7,10) - 16(-5,11)$	110.83	-6.0173	2.5	"	"	
102728.0300(10)	$16(6,10) - 16(6,11) + -$	110.62	-5.9798	2.7	93.9	23.0	
102728.3900(10)	$16(6,10) - 16(5,11) + -$	110.62	-5.2801	13.7	"	"	
102736.4900(10)	$16(7,10) - 16(6,11) + -$	110.62	-5.2800	13.7	97.0	13.6	
102736.8400(10)	$16(7,10) - 16(5,11) + -$	110.62	-5.9796	2.7	"	"	
102853.7400(10)	$15(-5,10) - 15(5,11)$	95.10	-6.0463	2.2	94.8	54.1	
102853.7700(10)	$15(-5,10) - 15(-4,11)$	95.10	-5.3206	11.7	"	"	
102854.8100(10)	$15(6,10) - 15(5,11)$	95.10	-5.3206	11.7	"	"	
102854.8400(10)	$15(6,10) - 15(-4,11)$	95.10	-6.0463	2.2	"	"	
103356.4500(10)	$14(-4,10) - 14(4,11)$	80.35	-6.0910	1.8	94.6	21.3	
103356.4600(10)	$14(-4,10) - 14(-3,11)$	80.35	-5.3743	9.5	"	"	
103356.6700(10)	$14(5,10) - 14(4,11)$	80.35	-5.3743	9.5	"	"	
103356.6800(10)	$14(5,10) - 14(-3,11)$	80.35	-6.0910	1.8	"	"	
104077.7400(10)	$14(4,10) - 14(4,11) + -$	80.06	-6.0455	2.0	77.5	8.2	
104077.7500(10)	$14(4,10) - 14(3,11) + -$	80.06	-5.3703	9.4	"	"	
104078.1700(10)	$14(5,10) - 14(4,11) + -$	80.06	-5.3703	9.4	"	"	
104078.1900(10)	$14(5,10) - 14(3,11) + -$	80.06	-6.0455	2.0	"	"	
104078.5800(10)	$24(14,11) - 24(13,12) - +$	266.33	-5.1099	29.0	"	"	
104574.9600(10)	$13(3,10) - 13(*,11) - +$	66.21	-5.3636	8.8	92.2	5.9	
104575.0300(10)	$13(4,10) - 13(*,11) - +$	66.21	-5.3636	8.8	"	"	
107339.7000(10)	$22(12,11) - 22(11,12) - +$	220.54	-5.1055	24.5	69.8	4.0	
107353.9100(10)	$22(12,11) - 22(11,12)$	220.55	-5.1025	24.7	98.8	11.9	
108601.4600(10)	$21(-10,11) - 21(-9,12)$	199.07	-5.1076	22.5	90.1	82.6	

Table 4.8 continued

Table 4.8: Transitions of AcA with S/N > 3 covered by the EMoCA survey. (continued)

Rest Frequency (MHz)	Transition	E_u (K)	$\log_{10} \frac{A_{ul}}{s^{-1}}$	$S_{ij}\mu^2$ (D^2)	P Factor (%)	D Factor (%)	Obs Ref
108621.1100(10)	$21(10,11) - 21(9,12) + -$	199.03	-5.1107	22.3	96.2	43.9	
108709.3300(10)	$21(11,11) - 21(10,12)$	199.08	-5.1065	22.5	88.2	1.3	
108797.3900(10)	$21(11,11) - 21(10,12) + -$	199.04	-5.1086	22.3	76.9	6.8	
108912.9900(10)	$5(5,1) - 4(4,1)$	15.80	-4.9257	8.7	75.7	27.9	
109835.4100(10)	$20(-9,11) - 20(9,12)$	178.54	-5.8830	3.5	59.3	1.6	
109837.5600(10)	$20(-9,11) - 20(-8,12)$	178.54	-5.1158	20.4	"	"	
109873.5600(10)	$20(10,11) - 20(9,12)$	178.54	-5.1154	20.4	94.2	0.5	
109875.7100(10)	$20(10,11) - 20(-8,12)$	178.54	-5.8826	3.5	"	"	
110079.5700(10)	$20(10,11) - 20(9,12) - +$	178.47	-5.1168	20.2	95.3	4.2	
110145.1600(10)	$8(-2,6) - 7(3,5)$	27.47	-4.9909	11.2	92.7	4.1	
110179.7400(10)	$5(5,1) - 4(4,0) + +$	15.62	-4.9042	8.8	75.8	6.7	
110358.1900(10)	$8(2,6) - 7(3,5) + +$	27.04	-4.9951	11.0	88.8	5.1	
110393.5000(10)	$5(-5,0) - 4(-4,0)$	16.20	-4.9056	8.7	64.7	9.8	
110499.9800(10)	$8(3,6) - 7(2,5) + +$	27.04	-4.9934	11.0	88.6	81.4	
110817.2500(10)	$9(-1,8) - 8(2,7)$	29.72	-4.8768	15.9	73.4	40.0	
110817.2800(10)	$9(2,8) - 8(2,7)$	29.72	-5.3410	5.5	"	"	
110817.5000(10)	$9(-1,8) - 8(-1,7)$	29.72	-5.3410	5.5	"	"	
110817.5400(10)	$9(2,8) - 8(-1,7)$	29.72	-4.8768	15.9	"	"	
110954.1100(10)	$9(1,8) - 8(2,7) - -$	29.27	-4.8820	15.7	99.0	39.3	
110954.1700(10)	$9(2,8) - 8(2,7) - -$	29.27	-5.3223	5.7	"	"	
110954.5500(10)	$9(1,8) - 8(1,7) - -$	29.27	-5.3223	5.7	"	"	
110954.6100(10)	$9(2,8) - 8(1,7) - -$	29.27	-4.8820	15.7	"	"	
111507.2800(10)	$10(*,10) - 9(*,9)$	31.02	-4.3757	54.8	99.4	86.7	(Remijan et al., 2003)
111548.5300(10)	$10(*,10) - 9(*,9) + +$	30.53	-4.3753	54.8	99.5	38.4	(Remijan et al., 2003)
112357.4100(10)	$17(-6,11) - 17(6,12)$	122.64	-5.9181	2.6	83.0	25.5	

Table 4.8 continued

Table 4.8: Transitions of AcA with S/N > 3 covered by the EMoCA survey. (continued)

Rest Frequency (MHz)	Transition	E_u (K)	$\log_{10} \frac{A_{ul}}{s^{-1}}$	$S_{ij}\mu^2$ (D^2)	P Factor (%)	D Factor (%)	Obs Ref
112357.4400(10)	$17(-6,11) - 17(-5,12)$	122.64	-5.1808	14.0	"	"	
112358.1900(10)	$17(7,11) - 17(6,12)$	122.64	-5.1808	14.0	"	"	
112358.2200(10)	$17(7,11) - 17(-5,12)$	122.64	-5.9181	2.6	"	"	
112917.6300(10)	$16(-5,11) - 16(*,12)$	105.92	-5.1475	14.0	86.4	19.8	
112917.8000(10)	$16(6,11) - 16(*,12)$	105.92	-5.1475	14.0	"	"	
112925.8100(10)	$17(6,11) - 17(6,12) + -$	122.46	-5.8710	2.8	99.6	9.4	
112925.8700(10)	$17(6,11) - 17(5,12) + -$	122.46	-5.1802	13.8	"	"	
112927.3800(10)	$17(7,11) - 17(6,12) + -$	122.46	-5.1802	13.8	"	"	
112927.4400(10)	$17(7,11) - 17(5,12) + -$	122.46	-5.8710	2.8	"	"	
113374.0500(10)	$15(-4,11) - 15(*,12)$	90.17	-5.2031	11.4	96.8	2.9	
113374.0800(10)	$15(5,11) - 15(*,12)$	90.17	-5.2031	11.4	"	"	
113600.7200(10)	$16(5,11) - 16(5,12) - +$	105.69	-5.8990	2.4	96.0	8.8	
113600.7300(10)	$16(5,11) - 16(4,12) - +$	105.69	-5.2201	11.7	"	"	
113601.0800(10)	$16(6,11) - 16(5,12) - +$	105.69	-5.2201	11.7	"	"	
113601.0900(10)	$16(6,11) - 16(4,12) - +$	105.69	-5.8990	2.4	"	"	
113742.2700(20)	$14(*,11) - 14(*,12)$	75.38	-4.9837	17.6	99.0	3.1	
114166.3000(10)	$15(4,11) - 15(*,12) + -$	89.89	-5.1921	11.5	96.1	8.0	
114166.3700(10)	$15(5,11) - 15(*,12) + -$	89.89	-5.1921	11.5	"	"	

NOTE — Pertinent parameters of the detected transitions of AcA taken from SLAIM catalog. The transitions with ditto marks in the column of P and D factors are blended with the transitions in the previous row.

Chapter 5

Molecule in Different Energy Levels - Vibrationally Excited (v_t = 1, 2) Acetic Acid toward NGC 6334I

Vibrationally excited states of detected interstellar molecules have been shown to account for a large portion of unidentified spectral lines in observed interstellar spectra toward chemically rich sources. Here, we present the first interstellar detection of the first and second vibrationally excited torsional states of acetic acid (v_t = 1, 2) toward the high-mass star-forming region NGC 6334I. The observations presented were taken with the Atacama Large Millimeter/submillimeter Array in bands 4, 6, and 7 covering a frequency range of 130 – 352 GHz. By comparing a single excitation temperature model to the observations, the best-fit excitation temperature and column density are obtained to be 142(25) K and $1.12(7) \times 10^{17}$cm^{-2} respectively. Based on the intensity maps of the vibrationally excited CH_3COOH transitions, we

found that the CH_3COOH emissions are compact and concentrated toward the MM1 and MM2 regions with a source size smaller than $2''$. After locating the emission from different CH_3COOH transitions, which cover a large range of excitation energies, we are able to explain the variation of the CH_3COOH emission peak within the MM2 core by invoking continuum absorption or outflows. *The following chapter is primarily reproduced from Xue, C.; Remijan A. J.; Brogan, C. L.; Hunter, T. R., Herbst E., McGuire, B. A. Astrophysical Journal* ***2019****, 882, 118.*

5.1 Introduction

Although more than 200 individual molecular species have been detected in both galactic and extragalactic interstellar and circumstellar environments to date (McGuire, 2018), a substantial number of unidentified spectral lines in the observed spectra toward a host of molecule-rich regions continue to plague observational astrochemistry. While many of these features are certainly due to as of yet unidentified new species, the carriers of these unidentified lines could also be isotopologues or vibrationally excited states of already known molecules (Daly et al., 2013; López et al., 2014; Müller et al., 2016). As such, studying the vibrationally excited states of known molecules is essential to characterizing the observed spectra and interstellar chemical inventories (Sakai et al., 2015).

Acetic acid (CH_3COOH) is a LAM and of increasing interest to study from both an astrochemical and an astrobiological point of view (Remijan et al., 2003). The first detection of interstellar CH_3COOH was toward Sgr B2(N) as reported by Mehringer et al. (1997) and later confirmed by Remijan et al. (2002). To date, CH_3COOH has been detected in its vibrational ground state toward a variety of high- and low-mass star forming regions (Cazaux et al., 2003; Remijan et al., 2003; Shiao et al., 2010). Since this initial detection, additional theoretical and experimental spectro-

scopic studies of the excited torsional states of CH_3COOH have provided the data needed to search for CH_3COOH in its first three torsional states ($v_t = 0, 1, 2$) up to 400 GHz (Ilyushin et al., 2001, 2003, 2013). Here, we present a search for the vibrationally excited rotational transitions ($v_t = 1, 2$) in an appealing target: NGC 6334I.

NGC 6334I is a massive star-forming core located at the northeastern end of the NGC 6334 molecular cloud (Beuther et al., 2008) with a distance of ~1.3 kpc (Reid et al., 2014). The millimeter continuum emission maps have spatially resolved NGC 6334I into nine distinct sources, with most of the hot core molecular line emission originating from the two brightest continuum sources, MM1 and MM2 (Hunter et al., 2006; Brogan et al., 2016). MM1 is furthered characterized as a hot multi-core which comprises seven components and exhibits a high-velocity bipolar outflow (Brogan et al., 2016, 2018). NGC 6334I is complex not only in physical structure but also in chemical composition (Bøgelund et al., 2018). Rich spectral line emission originates from this region (McCutcheon et al., 2000; Schilke et al., 2006), as exemplified by interferometric line surveys with the Submillimeter Array (SMA) (Zernickel et al., 2012), and the Atacama Large Millimeter/submillimeter Array (ALMA), the latter of which led to the first interstellar detection of methoxymethanol (CH_3OCH_2OH) (McGuire et al., 2017b, 2018b).

Recent observations of glycolaldehyde at ALMA Band 10 in this source showed bright emission lines from rotational states with upper state energies (E_u) in the range of $530 - 631$ K (McGuire et al., 2018b). Combined with the high dust temperatures of MM1 (up to 450 K; Brogan et al., 2016), sufficient energy may be available to populate energetic low-lying vibrational states of LAMs that can then be detected through their rotational transitions within these excited states. Following the detection of CH_3COOH in the vibrational ground state toward NGC 6334I (El-Abd et al.

2019, under revision), NGC 6334I is clearly an ideal region to search for emission features of the vibrationally excited transitions of CH_3COOH, particularly because of its relatively narrow lines.

In this paper, we report the first interstellar detection of vibrationally excited CH_3COOH ($v_t = 1, 2$) toward NGC 6334I with ALMA in Bands 4, 6 and 7. The observations are described in Section 5.2. The process of line identification and spatial imaging is presented in Section 5.3. In Section 5.4, the spatial distribution is discussed with respect to the complicated structure of the dust emission cores, MM1 and MM2. The results are summarized in Section 5.5.

5.2 Observations

The detection of the first and second vibrationally excited states of CH_3COOH was achieved with three data sets involving ALMA Bands 4, 6, and 7 ranging from 130 to 352 GHz. The Band 6 data are first presented in this paper, while a detailed description of the Band 4 and 7 data have been presented elsewhere (McGuire et al., 2018b; Hunter et al., 2017; McGuire et al., 2017b). The Band 6 observation was performed on 2017 December 28 (project code 2017.1.00370.S). A synthesized beam size of $0.18'' \times 0.15''$ was achieved with a baseline range from 15 m to 2.5 km. The salient observational parameters for the Band 6 data are summarized in Table 5.1. The Band 4 data (project code 2017.1.00661.S) were taken in Cycle 5 with a spectral resolution of 0.488 MHz and an rms noise of ~0.8 mJy beam^{-1} (McGuire et al., 2018b). The Band 7 data (project code 2015.A.00022.T) were taken in Cycle 3 with a spectral resolution of 0.977 MHz and an rms noise of ~2.0 mJy beam^{-1} at 1.1 mm and 3.3 mJy beam^{-1} at 0.87 mm (Hunter et al., 2017; McGuire et al., 2017b).

The data have been analyzed with the `CASA`. The relatively line-free continuum channels were selected with the techniques described in Brogan et al. (2018) and used

Table 5.1: Observational Parameters for the Band 6 ALMA Data

Parameter	Band 6 (259 GHz)
Observation Date	28th Dec 2017
Cycle	5
Project Code	2017.1.00370.S
Configuration	C43-5/C43-6
Time on Source (minutes)	48
Phase Center (J2000 RA, DEC)	17:20:53.35, -35:47:01.5
SPW Center Frequency (GHz)	251.4, 251.8, 266.3, 270.7
SPW Bandwidth (MHz)	468.75
HPBW Primary Beam ($'$)	0.37
Gain Calibrator	J1713-3418
Bandpass and Flux Calibrator	J1517-2422
Phase Calibrator	J1733-3722
Spectral Resolution (MHz)	0.244
Angular resolution [a] ($'' \times ''$)	0.18×0.15
RMS per Channel (mJy beam^{-1})	4.0

[a] The angular resolution is achieved with a Robust weighting parameter of 0.5. The images are further smoothed to $0.26'' \times 0.26''$ for consistency between all observations.

to subtract the continuum emission in the UV-plane. The Briggs weighting scheme and a Robust parameter of 0.5 for the Band 4 and 6 data and 0.0 for the Band 7 data were used in the `TCLEAN` task of `CASA` for imaging, which resulted in elliptical beam shapes. The images were smoothed to a $0.26''$ uniform, circular beam size from the image plane for consistency among the 3 datasets. The spectra presented in this paper were extracted toward MM1 from a single pixel centered at $\alpha_{\rm J2000} = 17^{\rm h}20^{\rm m}53.374^{\rm s}$, $\delta_{\rm J2000} = -35^{\circ}46'58.34''$.

5.3 Analysis and Results

5.3.1 Line Identification

The dense molecular spectra of NGC 6334I as described by Zernickel et al. (2012) indicate a high degree of spectral contamination, i.e., a substantial proportion of spectral lines are overlapped and blended with adjacent lines of either the same or another species. To positively identify a vibrationally excited CH_3COOH line from this highly contaminated spectra, we adopt the five criteria for line identification proposed in Snyder et al. (2005) (hereafter, the Snyder criteria): (1) accurate rest frequencies, (2) take into account beam dilution effect, (3) frequency agreement, (4) intensity agreement, and (5) presence of transitions with detectable intensity. Because the processes for analyzing following the Snyder criteria in this study are similar with those in Xue et al. (2019b), we will highlight the main points here, and refer the reader to Section 3.1 in Xue et al. (2019b) for more detail.

The emitting area of most LAMs toward NGC 6334I is over an extent of $\sim 5''$ (McGuire et al., 2017b), while that of glycolaldehyde (CH_2OHCHO), a structural isomer of CH_3COOH, has a source size $\sim 2.5'' \times 0.8''$ (McGuire et al., 2018b). Accordingly, it is reasonable to assume that the spatial distribution of the CH_3COOH emission is more extended than the angular resolution used in this study ($0.26''$), and therefore, the beam dilution effect is negligible. On the other hand, it is very unlikely that the source size of CH_3COOH would exceed the maximum recoverable scale of the ALMA observations presented in this study ($\sim 3''$). If there is a large-scale emission of CH_3COOH, it should be observable with single dishes but CH_3COOH has never been detected toward NGC 6334I with single-dish observations. Moreover, the CH_3COOH emission display a compact morphology in many other hot molecular cores (Remijan

et al., 2003), which further support our assumptions.

McGuire et al. (2018b) showed that a single-excitation temperature can well describe the spectra of most LAMs across the full range of ALMA wavelengths (Bands 3-10) toward the MM1 region, in which $n_{\mathrm{H_2}} > 10^9\,\mathrm{cm}^{-3}$ (Brogan et al., 2016). After estimating the critical density for the CH_3COOH transitions in the vibrationally excited states, we found that n_{crit} of the $v_{\mathrm{t}} = 1$ and $v_{\mathrm{t}} = 2$ transitions are at most $\sim 10^5\,\mathrm{cm}^{-3}$. The upper limit of n_{crit} is given by a lower limit of the collisional cross section, which is $\sim 10^{-15}\,\mathrm{cm}^2$, the cross section of H_2. It is noted that the cross section of $HCOOCH_3$, a molecule that has similar complexity with CH_3COOH, is significantly larger than that of H_2 (Faure et al., 2014). Hence, while being conservative, the upper limit of n_{crit} estimated here is well-grounded. As $n_{\mathrm{H_2}} \gg n_{\mathrm{crit}}$, it is reasonable to assume that these CH_3COOH transitions are thermalized toward MM1.

Following the convention of Turner (1991), we simulated the spectrum of CH_3COOH in each state with the assumption that the transitions of CH_3COOH are thermalized, as in McGuire et al. (2018b). Constant background continuum temperature (T_{bg}) is considered in each frequency range covered by the datasets. In particular, based on brightness temperature measurements, T_{bg} is estimated to be 11.5 K, 27.4 K, 33.9 K and 43.1 K for the Band 4, Band 6, Band 7 1.1 mm and Band 7 0.87 mm datasets respectively. The spectroscopic data of the vibrationally excited states in the $130 - 352$ GHz frequency range are taken from Ilyushin et al. (2013). The torsional vibrational states of CH_3COOH have the following excitation energies: the $v_{\mathrm{t}} = 1$ state lies at around $74\,\mathrm{cm}^{-1}$ (or 107 K) while the $v_{\mathrm{t}} = 2$ state lies at $127\,\mathrm{cm}^{-1}$ (or 184 K) above the ground state (Ilyushin et al., 2001). Within the observed spectral range, the criterion of accurate rest frequencies is fulfilled by the small uncertainties associated with the transitions, which are smaller than $0.2\,\mathrm{km\,s}^{-1}$, compared with the observed linewidth ($\sim 3\,\mathrm{km\,s}^{-1}$). The torsional-rotational partition function Q_{rv} is ap-

proximated by fitting the total internal partition function as a function of temperature (T) using a sixth order polynomial (Ilyushin et al., 2013):

$$\begin{aligned} Q_{\rm rv}(T) = &- 8.88 \times 10^{-11}\, T^6 + 1.03 \times 10^{-7}\, T^5 \\ &- 5.02 \times 10^{-5}\, T^4 + 1.34 \times 10^{-2}\, T^3 \\ &+ 7.83 \times 10^{-1}\, T^2 + 49.0\, T - 139. \end{aligned} \tag{5.1}$$

By assuming $T_{\rm ex}$ to be 135 K (McGuire et al., 2018b), 40 spectral emission features for $v_{\rm t}$ = 1 and 17 spectral emission features for $v_{\rm t}$ = 2 are expected to be over the detection threshold, i.e, with $S/N > 3$, in this study. Only a few of these line features are individual transitions, while the others are an ensemble of multiple transitions. We find all these emission lines to be present and no lines to be missing in the observed spectra if we take into account the contaminated lines, as shown in Section 5.8.

Xue et al. (2019b) describe a way to quantitatively measure the agreement between the modeled spectra and the observations by, first, selecting an appropriate spectral range for comparing line profiles from the observation and simulation and, second, computing the P (Product) and D (Difference) factors (see equations (1)-(2) of Xue et al., 2019b). The P factor is based on the product of the observed and modeled line profiles to characterize how close the observed line is located to the expected rest frequency. The D factor is based on the difference of the integrated intensities between the spectra, which compares the modeled line intensities to the astronomically observed values. Instead of setting an absolute threshold for the P and D factors, it is more relevant to compare the derived factors among each emission feature; overall, features with higher P and D factors are more likely to be "clean". Therefore, the two factors serve as tools to assist and accelerate the line identification process by eliminating features that are buried under or strongly contaminated by

other emission features. This greatly reduces the number of emission features to be visually examined and provides a feasible and crucial strategy for line identification over large bandwidth. Due to the success of uniquely identifying lines in Xue et al. (2019b), the same approach is adopted here.

We identify a total of six $v_t = 1$ features and three $v_t = 2$ features, as shown in Figure 5.1. All of these CH_3COOH features are a collection of four transitions. The observational results of the clean emission features are summarized in Table 5.2, while the detailed spectroscopic parameters of the pertaining transitions are listed in Section 5.7. Note that the 281789 MHz line complex has a broader line width than the others, which may be due to the presence of a weak blended emission feature located near the wing of the 281789 MHz feature, as will be discussed in Section 5.3.2.

The excitation temperature (T_{ex}) and the column density (N_T) are determined by fitting a single excitation temperature model to the observed data. The observed results of the clean emission features are used to constrain the line width (ΔV) and source velocity (V_{lsr}), which are in good agreement among all the clean features. Therefore, ΔV is fixed to the median of the FWHM of the clean line complexes and V_{lsr} is fixed to the median value. χ^2 fitting is performed to statistically optimize the model and determine T_{ex} and N_T. Rather than considering all of the detectable emission features, the fitting procedures are performed with the clean features only. The process is also described in Xue et al. (2019b, see section 3.3).

The ΔV is fixed to $2.72\,\mathrm{km\,s^{-1}}$ and the V_{lsr} is fixed to $-6.90\,\mathrm{km\,s^{-1}}$. A T_{ex} of $142(25)\,\mathrm{K}$ and an N_T of $1.12(7) \times 10^{17}\,\mathrm{cm^{-2}}$ minimize the χ^2 value and best fit the observations. The values of ΔV and V_{lsr} characterized here are consistent with the values obtained from the spectrum of glycolaldehyde emission, $\Delta V = 3.2\,\mathrm{km\,s^{-1}}$ and $V_{lsr} = -7\,\mathrm{km\,s^{-1}}$ (McGuire et al., 2018b). The N_T and T_{ex} also correlate fairly well with El-Abd et al. (2019), who measure an N_T of $1.24 \times 10^{17}\,\mathrm{cm^{-2}}$ and a T_{ex} of

135 K derived from the CH_3COOH transitions in the ground state toward the MM1 region. The uncertainties quoted here are the standard deviations ($1\,\sigma$) of the best-fit model, which include the fitting error derived from the inverse of the Hessian matrix and the error propagation from the rms noise of the observed spectra. We want to emphasize that the uncertainties listed here might be underestimated as we have not incorporated the systematic uncertainties introduced by continuum subtraction.

Table 5.2: Ensemble of Spectral Line Transitions of Vibrationally Excited CH_3COOH

Emission Features (MHz)	v_t	I_{peak} (mJy beam^{-1})	FWHM (km s^{-1})	V_{lsr} (km s^{-1})	P Factor	D Factor	Channel rms (mJy beam^{-1})
130306	1	6.605	3.33	-6.90	98.7	93.5	0.8
144791	2	9.134	2.59	-6.96	99.3	58.1	0.8
144975	2	11.697	2.72	-6.48	95.6	61.1	0.8
251599	2	34.337	2.36	-6.95	99.4	90.7	4.0
266285	1	26.868	2.27	-6.98	98.9	62.8	4.0
270849	1	56.095	3.07	-7.10	98.6	68.4	4.0
281447	1	45.838	2.00	-6.76	98.3	88.1	2.0
281789[a]	1	58.785	4.05	-6.43	97.7	68.1	2.0
282044[b]	1	65.64	2.91	-6.64	98.3	77.0	2.0

NOTE — Observed and fitted parameters of the clean emission features pertaining to vibrationally excited CH_3COOH (v_t = 1 and v_t = 2). The approximate frequencies listed here are used to represent the emission features, of which the accurate rest frequencies are presented in Section 5.7. FWHM and V_{lsr} were obtained by the Gaussian fitting function. P and D Factors were calculated based on the observed spectra toward the MM1 region and the simulated spectra with a T_{ex} of 142 K.

[a] The 281789 MHz feature suffers from spatial contamination due to the weak blended emission feature at the line wing.

[b] The 282044 MHz feature suffers from spatial contamination due to the adjacent line.

5.3.2 Spatial Distribution

We can only be confident in the spatial extent and morphology for those spectral regions where the extracted spectra fulfill the Snyder criteria. Thus, there remains the possibility of a problem of spatial contamination toward other regions of the same source, i.e., contamination from other molecules may be present in the regions where the spectra are not examined. Nonetheless, the chance of the maps being contaminated by molecules with a similar spatial distribution pattern is unlikely. If a similar morphology is displayed among most of the transitions of a given molecule, odds are that it represents the intrinsic spatial distribution of that molecule. Therefore, the spatial distribution coherence can serve as an additional criterion for securing the morphology determination (Brouillet et al., 2015).

The continuum emission features at Bands 4, 6, and 7 have different flux densities but display consistent morphology toward MM1 and MM2. In this study, we use the continuum emission map at 287 GHz from the Band 7 observations as representative, which is shown in contours in Figure 5.2. All the 9 peak intensity maps of vibrationally excited CH_3COOH within the $V_{\rm lsr}$ range of -3 to $-9\,{\rm km\,s^{-1}}$ are presented in color. However, the right two maps in the bottom row are discarded from the following analysis because of spatial inconsistencies and possible contamination as described below. The broad line width and relatively extended distribution of the 281789 MHz feature suggest the existence of contamination, which might be attributed to the propanal 26(7,19)-25(7,18) transition at 281787 MHz. The 282044 MHz map is spatially contaminated by the emission of the nearby line complex peaked at 282039 MHz (assuming a $V_{\rm lsr}$ at $-6.8\,{\rm km\,s^{-1}}$), which is the superposition of $S^{18}O$, c$-$HCCCH and SO_2 lines. Apart from the two contaminated maps, the seven remaining peak intensity maps of vibrationally excited CH_3COOH present a coherent distribution with

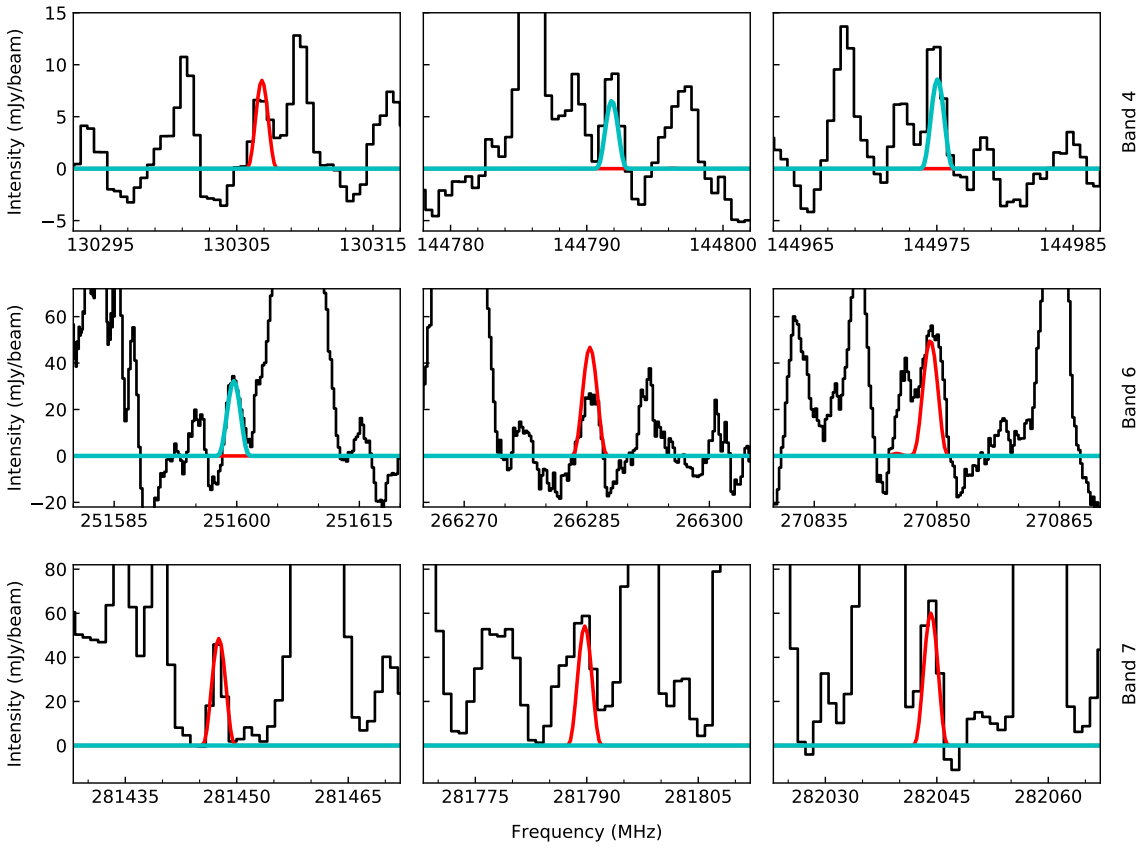

Figure 5.1: Band 4, 6, 7 spectra of NGC 6334I extracted toward the MM1 region are shown in black. The best-fit simulated spectra are overlaid in red and cyan for $v_{\rm t}$ = 1 and $v_{\rm t}$ = 2 respectively. The best-fit parameters are $T_{\rm ex}$ = 142 K, $N_{\rm T}$ = 1.12×10^{17} cm^{-2}, and ΔV = 2.72 km s^{-1}. The horizontal axes are the rest frequency with respect to a radial velocity of -6.9 km s^{-1}. Only the 9 identified emission features are shown in this figure. Refer to Section 5.8 for the other transitions with detectable expected intensities.

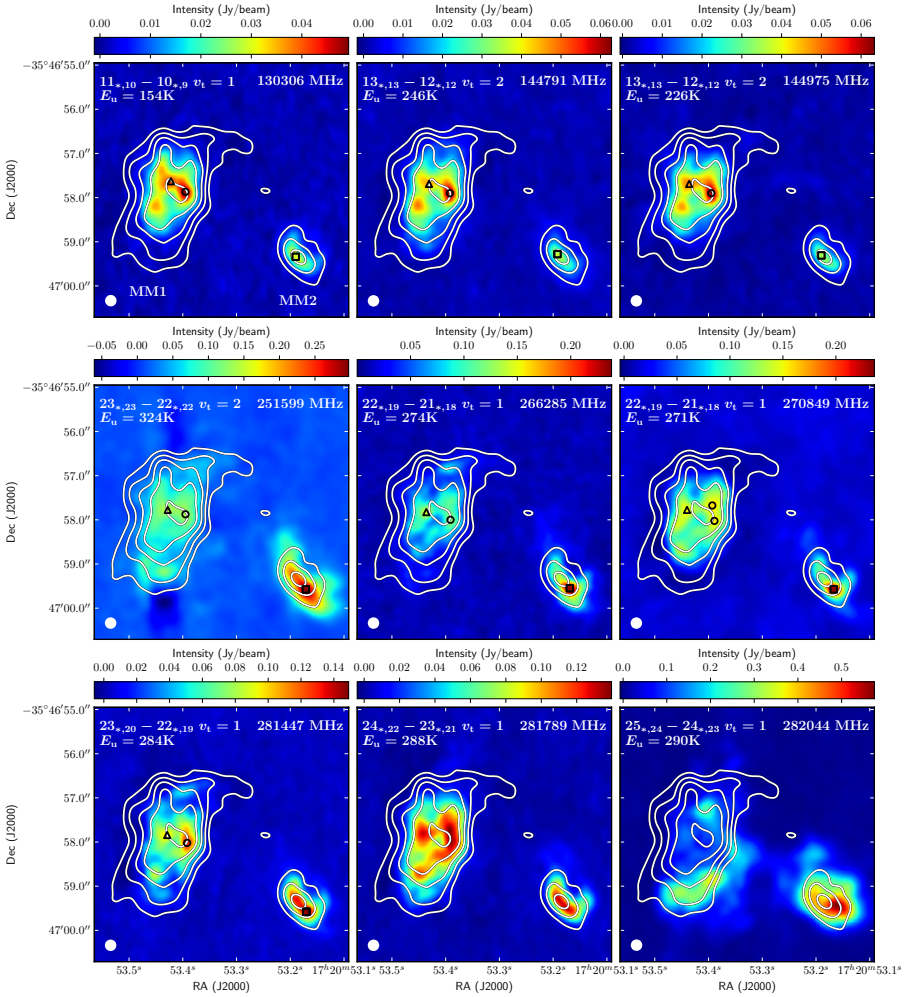

Figure 5.2: The peak intensity maps over the velocity range of -3 to $-9\,\mathrm{km\,s^{-1}}$ of the clean lines of vibrationally excited CH_3COOH overlaid with the 287 GHz continuum emission in contours. The resolved quantum numbers represented by asterisks in the legends are listed in Section 5.7. The contour levels correspond to 46, 92, 184, 368 and $736\,\mathrm{mJy\,beam^{-1}}$. The images are smoothed with uniform circular beam size of $0.26'' \times 0.26''$, as shown in the bottom left corner. The open circle, triangle, and square markers denote the CH_3COOH molecular emission peaks. The inconsistency seen in the morphology of the 281789 MHz and 282044 MHz maps compared with the others suggest the two maps suffer from spatial contamination from other molecular emission.

each other over a range of energy levels.

As is clear from the seven remaining maps, the emission from CH_3COOH is mainly distributed over both MM1 and MM2. The reported coordinates of MM1 and MM2 are (α_{J2000} = $17^h20^m53.412^s$, δ_{J2000} = $-35^\circ46'57.90''$) and (α_{J2000} = $17^h20^m53.185^s$, δ_{J2000} = $-35^\circ46'59.34''$), respectively. The source size of vibrationally excited CH_3COOH, estimated at half peak flux density, is resolved to be $\sim 2'' \times 1.2''$ toward MM1 and $\sim 1'' \times 0.4''$ toward MM2. Although its compact distribution is consistent with the continuum emission on a larger scale, they do not exactly coincide. There is an offset between the molecular emission and 287 GHz continuum emission peaks with a closest distance $<0.36''$. We resolved three prominent CH_3COOH emission peaks throughout all the clean line complexes. The AcA1 and AcA2 emission peaks, denoted by an open circle and triangle markers in Figures 5.2 and 5.3, are within MM1, whereas the AcA3 emission peak marked with an open square is located toward MM2. The observed parameters, including the coordinates, intensity, and the distance between the molecular and continuum emission, of all the CH_3COOH emission features are listed in Table 5.3. The individual CH_3COOH peak positions can vary by at most $0.3''$ from one transition to another.

5.4 Discussion

The multiple hot cores revealed toward NGC 6334I themselves exhibit complex structures and heterogeneous temperature distributions (Brogan et al., 2016). Considering that the compact CH_3COOH emission is concentrated toward the MM1 and MM2 regions, we will discuss below the locations of the CH_3COOH emission peaks with regard to the sub-components of the two hot cores, MM1 and MM2.

Seven dust clumps were resolved toward the hot core MM1, namely MM1A–G, with associated dust temperatures ranging from 116 to 450 K (Brogan et al., 2016).

Table 5.3: Vibrationally Excited CH_3COOH Emission Peaks

Emission Features (MHz)	Peaks	Coordinate 17^h20^m	Coordinate $-35^\circ46'$	Dist [a] ($''$)	Intensity (Jy beam^{-1})	Markers [b]
130306	AcA1	53.395^s	$57.870'$	0.21	0.0493	○
	AcA2	53.422^s	$57.630'$	0.30	0.0405	△
	AcA3	53.190^s	$59.340'$	0.06	0.0303	□
144791	AcA1	53.392^s	$57.900'$	0.24	0.0628	○
	AcA2	53.431^s	$57.690'$	0.31	0.0455	△
	AcA3	53.192^s	$59.280'$	0.10	0.0371	□
144975	AcA1	53.395^s	$57.900'$	0.21	0.0633	○
	AcA2	53.436^s	$57.690'$	0.36	0.0490	△
	AcA3	53.190^s	$59.310'$	0.07	0.0353	□
251599	AcA1	53.395^s	$57.875'$	0.21	0.1374	○
	AcA2	53.428^s	$57.775'$	0.23	0.1382	△
	AcA3	53.171^s	$59.575'$	0.29	0.2974	□
266285	AcA1	53.391^s	$58.000'$	0.27	0.1255	○
	AcA2	53.436^s	$57.825'$	0.30	0.1452	△
	AcA3	53.169^s	$59.550'$	0.29	0.2382	□
270849[c]	AcA1	53.389^s	$58.025'$	0.31	0.1545	○
	AcA1	53.393^s	$57.675'$	0.32	0.1584	○
	AcA2	53.440^s	$57.775'$	0.36	0.1513	△
	AcA3	53.167^s	$59.575'$	0.32	0.2364	□
281447	AcA1	53.392^s	$58.020'$	0.27	0.1298	○
	AcA2	53.429^s	$57.840'$	0.22	0.0997	△
	AcA3	53.170^s	$59.580'$	0.30	0.1490	□

[a] The distance to the nearest 287 GHz continuum emission peaks, $\alpha_{J2000} = 17^h20^m53.412^s$, $\delta_{J2000} = -35^\circ46'57.90''$ at MM1 and $\alpha_{J2000} = 17^h20^m53.185^s$, $\delta_{J2000} = -35^\circ46'59.34''$ at MM2.

[b] The open circle, triangle, and square markers refer to the markers used in Figure 5.2 and Figure 5.3.

[c] The 270849 MHz image has two emission peaks close to the AcA1 position.

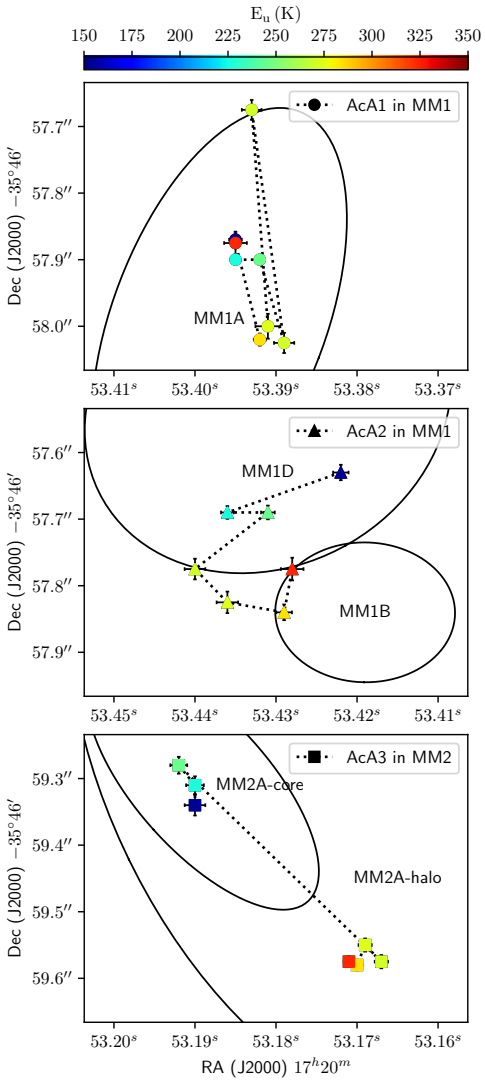

Figure 5.3: The peak emission positions for each of the seven spatially consistent transitions and the associated continuum emission cores. The peak emission positions close to AcA1, AcA2, and AcA3 are marked by circles, triangles, and squares, respectively. The colors of the markers represent the upper state energy of each transition. The error bars are the $5\,\sigma$ position uncertainties estimated by equation (1) in Reid et al. (1988). The dotted lines connect the markers in ascending $E_{\rm u}$. The ellipses mark the extent of the dust cores MM1A, MM1B, MM1D and MM2A-core and -halo taken from Brogan et al. (2016). Note that the 270849 MHz map has two emission peaks close to the AcA1 position.

As illustrated in Figure 5.3, all the AcA1 emission peaks are associated with the densest core MM1A, which has $n_{\mathrm{H_2}} \sim 7.2 \times 10^9\,\mathrm{cm}^{-3}$. The individual positions of the AcA1 peaks among different rotational states are scattered in a region the size of a synthetic beam. While the AcA2 emission peaks also show a dispersed distribution, they lie between the MM1B and MM1D compact components, which are the hottest dust sources of MM1 with T_{dust} at 442 K for MM1B and 305 K for MM1D (Brogan et al., 2016). A distribution that lies in between cores is an atypical phenomenon of LAMs. Another example of a molecule with this kind of distribution is acetone ($(CH_3)_2CO$), which is located between the hot cores and compact regions in Orion KL (Peng et al., 2013). While the different peak positions versus E_{u} may indicate additional unresolved structures that are smaller than the beam, the complexity of the MM1 core makes the explanation and generalization of the positions of the CH_3COOH emission peaks difficult.

In contrast, a core-halo structure was suggested for MM2, within which the dust temperature of the core was estimated to be ~152 K (Brogan et al., 2016). Different from AcA1 and AcA2, which show dispersed distributions, the AcA3 peaks toward the MM2 cluster into two groups depending on their energy levels, which are separated by $0.3''$. In particular, whereas the AcA3 emission peaks pertaining to the lower excited states of CH_3COOH are located toward the core region, the higher energy transitions peaks are located in the MM2 halo toward the south-west. This offset could be explained in part by the dust opacity. We have noticed that there is deep contaminating absorption from continuum emission at the high frequency bands (i.e., Bands 6 and 7). With the absorption toward the continuum peak becoming strong, the observable molecular emission toward the continuum peak would decrease and, consequently, the molecular emission peaks would deviate from the continuum peak. The effect of the strong contaminating absorption from continuum emission on our

study is that the AcA3 emission peaks of the Band 6 and 7 transitions, with $\nu >$ 250 GHz, would be offset from the continuum peak, whereas the AcA3 peaks of the Band 4 transitions, where there is almost no continuum absorption, are located toward the core region. Additional support for this explanation is provided by the existence of another CH_3COOH emission peak located to the southeast of the AcA2 peaks and close to the MM1C continuum core, which is only seen in the three Band 4 images. The disappearance of the emission peak from the higher frequency images could be explained well by the dust opacity in a similar fashion to the case of the AcA3 position shift.

Only a few studies have focused on spatially mapping vibrationally excited molecules and comparing the morphological differentiation of a molecule in different energy levels. The $HCOOCH_3$ observation toward Orion KL made with ALMA indicated that the distributions of different vibrationally excited $HCOOCH_3$ states resemble each other with a consistency of peak positions (Sakai et al., 2015). In contrast, the work by Peng et al. (2017) with the same set of data showed a trend of the displacements among the HC_3N emission peaks. The HC_3N observation revealed that the emission peaks of its vibrationally excited lines are displaced from the south of the hot core region to the northeast as the E_u increases, which is coincident with the major axis of the SiO outflow (Peng et al., 2017). Accordingly, the variation of the positions of the AcA3 peaks might also hint at an outflow structure proceeding in the southwest direction within MM2. Indeed, based on the ALMA CS $6-5$ observation, Brogan et al. (2018) found a one-sided blueshifted component from MM2 extending in the southwest direction. However, there is also a northeast–southwest outflow originating from MM1, and both the MM2 core and the one-sided outflow from MM2 are projected onto the large-scale blueshifted lobe of the MM1 outflow (Brogan et al., 2018). Even though it is hard to constrain which one, or both, of the

outflows is causing the shift of the AcA3 peaks, we can not rule out the role that $E_{\rm u}$ might have on the change in the AcA3 positions caused by outflows.

Although both of the mechanisms could account for the change in the AcA3 peak positions, the one that invokes dust opacity would lead to a correlation between positions and line frequencies, while the one that invokes outflows would lead to a correlation between positions and $E_{\rm u}$. With the current data, we are not able to constrain which one of the two is the dominant mechanism that causes the peak-position variations due to the limited number of clean lines and the coincidence that all the high $E_{\rm u}$ lines happen to be found at high frequencies. Nonetheless, the degeneracy could be resolved by imaging lines with low $E_{\rm u}$ and high frequencies, or vice versa. Moreover, our analysis is limited to the range of energy levels ($154-324$ K). Therefore, our data are probably not sufficient to exactly determine the dependence of peak positions on $E_{\rm u}$. Future work touching on precisely locating the emission region of more LAMs with a wider range of excitation energy is necessary, which could advance our knowledge to verify and understand this trend.

5.5 Summary

Based on ALMA observations of NGC 6334I, we have identified and imaged the first and second vibrationally excited states of CH_3COOH for the first time in the interstellar medium. More than 100 transitions attributed to vibrationally excited CH_3COOH contribute to the emission features in the $130-352$ GHz spectra, although the majority of them are blended. It appears that vibrationally excited states of the detected interstellar molecules certainly account for a significant number of unidentified lines in the observed spectra toward hot core regions in molecular clouds.

The observed spectrum was well-fit with the single excitation temperature model of CH_3COOH at the $v_{\rm t}$ = 1 and $v_{\rm t}$ = 2 states. Through comparing the observed and

modeled spectra, six features were assigned to the v_t = 1 state while three features were assigned to the v_t = 2 state. The best fit yields an excitation temperature of $142(25)$ K and a resulting column density of $1.12(7) \times 10^{17}$ cm^{-2}.

We further imaged the peak intensity images of the 9 features that suffer least from contamination by other species. Through imaging multiple transitions, we eliminated spatial contamination in our analysis of the distribution of vibrationally excited CH_3COOH. Based on the intensity maps that show consistent morphology, we found that the CH_3COOH emissions are compact and concentrated toward the MM1 and MM2 regions. There is a global overlap of the CH_3COOH emission with the continuum emission, but, with a displacement between the molecular emission peaks and the continuum emission peaks. Three emission peaks of CH_3COOH were resolved. The AcA1 peaks are located toward the MM1A clump, and the AcA2 peaks lie between the MM1B and MM1D cores, while the AcA3 peaks are located toward the MM2 region. By locating the CH_3COOH emission from different values of E_u, we found that there is not an obvious dependence of the positions of the AcA1 and AcA2 peak on excited energy levels, while the change of the AcA3 peak positions could be explained either by the effect of dust opacity or outflows. Our study does reveal the importance of the observation of a sufficient number of uncontaminated lines, which prevent our analysis from being biased by spatial contamination.

5.6 Acknowledgments

We acknowledge the support of the National Science Foundation (US) for the astrochemistry program of E. H. (grant number AST-1514844). This paper makes use of the following ALMA data: ADS/JAO.ALMA#2015.A.00022.T, ADS/JAO.ALMA#2017.1.00370.S and ADS/JAO.ALMA#2017.1.00661.S. ALMA is a partnership of ESO (representing its member states), NSF (USA) and NINS (Japan),

together with NRC (Canada), MOST and ASIAA (Taiwan), and KASI (Republic of Korea), in cooperation with the Republic of Chile. The Joint ALMA Observatory is operated by ESO, AUI/NRAO and NAOJ. The National Radio Astronomy Observatory is a facility of the National Science Foundation operated under cooperative agreement by the Associated Universities, Inc. Support for B.A.M. was provided by NASA through Hubble Fellowship grant #HST-HF2-51396 awarded by the Space Telescope Science Institute, which is operated by the Association of Universities for Research in Astronomy, Inc., for NASA, under contract NAS5-26555.

5.7 Spectroscopic Parameters of the Related Transitions

Table 5.4: Spectroscopic Properties of the Most Uncontaminated Transitions for Vibrationally Excited CH_3COOH

Rest Frequency (MHz)	Quantum Number	$E_{\rm u}$ (K)	$\log_{10} \frac{A_{ul}}{\rm s^{-1}}$
130306.8457	$v_{\rm t}$ = 1 $11(1,10) - 10(2,9)$ A	154.261	-4.52
130306.8458	$v_{\rm t}$ = 1 $11(2,10) - 10(2,9)$ A	"	-5.82
130306.8462	$v_{\rm t}$ = 1 $11(1,10) - 10(1,9)$ A	"	-5.82
130306.8462	$v_{\rm t}$ = 1 $11(2,10) - 10(1,9)$ A	"	-4.52
144791.7911	$v_{\rm t}$ = 2 $13(0,13) - 12(1,12)$ E	246.132	-4.41
144791.8037	$v_{\rm t}$ = 2 $13(1,13) - 12(1,12)$ E	"	-5.19
144791.8596	$v_{\rm t}$ = 2 $13(0,13) - 12(0,12)$ E	"	-5.19
144791.8722	$v_{\rm t}$ = 2 $13(1,13) - 12(0,12)$ E	"	-4.41
144975.0345	$v_{\rm t}$ = 2 $13(0,13) - 12(1,12)$ A	226.084	-4.48
144975.0422	$v_{\rm t}$ = 2 $13(1,13) - 12(1,12)$ A	"	-4.82
144975.0594	$v_{\rm t}$ = 2 $13(0,13) - 12(0,12)$ A	"	-4.82
144975.0672	$v_{\rm t}$ = 2 $13(1,13) - 12(0,12)$ A	"	-4.48
251599.6383	$v_{\rm t}$ = 2 $23(0,23) - 22(0,22)$ A	323.807	-3.77
"	$v_{\rm t}$ = 2 $23(1,23) - 22(1,22)$ A	"	-3.77

Table 5.4 continued

Table 5.4: Spectroscopic Properties of the Most Uncontaminated Transitions for Vibrationally Excited CH_3COOH (continued)

Rest Frequency (MHz)	Quantum Number	E_u (K)	$\log_{10} \frac{A_{ul}}{s^{-1}}$
"	v_t = 2 $23(0,23) - 22(1,22)$ A	"	-4.04
"	v_t = 2 $23(1,23) - 22(0,22)$ A	"	-4.04
266285.3833	v_t = 1 $22(3,19) - 21(4,18)$ A	274.159	-3.79
"	v_t = 1 $22(4,19) - 21(3,18)$ A	"	-3.79
"	v_t = 1 $22(3,19) - 21(3,18)$ A	"	-3.99
"	v_t = 1 $22(4,19) - 21(4,18)$ A	"	-3.99
270849.2061	v_t = 1 $22(3,19) - 21(4,18)$ E	270.833	-3.71
"	v_t = 1 $22(4,19) - 21(3,18)$ E	"	-3.71
"	v_t = 1 $22(3,19) - 21(3,18)$ E	"	-4.09
"	v_t = 1 $22(4,19) - 21(4,18)$ E	"	-4.09
281447.5805	v_t = 1 $23(3,20) - 22(4,19)$ E	284.341	-3.63
"	v_t = 1 $23(4,20) - 22(3,19)$ E	"	-3.63
"	v_t = 1 $23(3,20) - 22(3,19)$ E	"	-4.10
"	v_t = 1 $23(4,20) - 22(4,19)$ E	"	-4.10
281789.7257	v_t = 1 $24(2,22) - 23(2,21)$ E	287.659	-3.59
"	v_t = 1 $24(3,22) - 23(3,21)$ E	"	-3.59
"	v_t = 1 $24(2,22) - 23(3,21)$ E	"	-4.11
"	v_t = 1 $24(3,22) - 23(2,21)$ E	"	-4.11
282044.2002	v_t = 1 $25(1,24) - 24(2,23)$ E	289.904	-3.61
"	v_t = 1 $25(2,24) - 24(1,23)$ E	"	-3.61
"	v_t = 1 $25(1,24) - 24(1,23)$ E	"	-3.97
"	v_t = 1 $25(2,24) - 24(2,23)$ E	"	-3.97

NOTE — Relevant spectroscopic data of the transitions corresponding to the nine clean emission features in Table 5.2 taken from Ilyushin et al. (2013).

5.8 Spectra of All Detected Emission

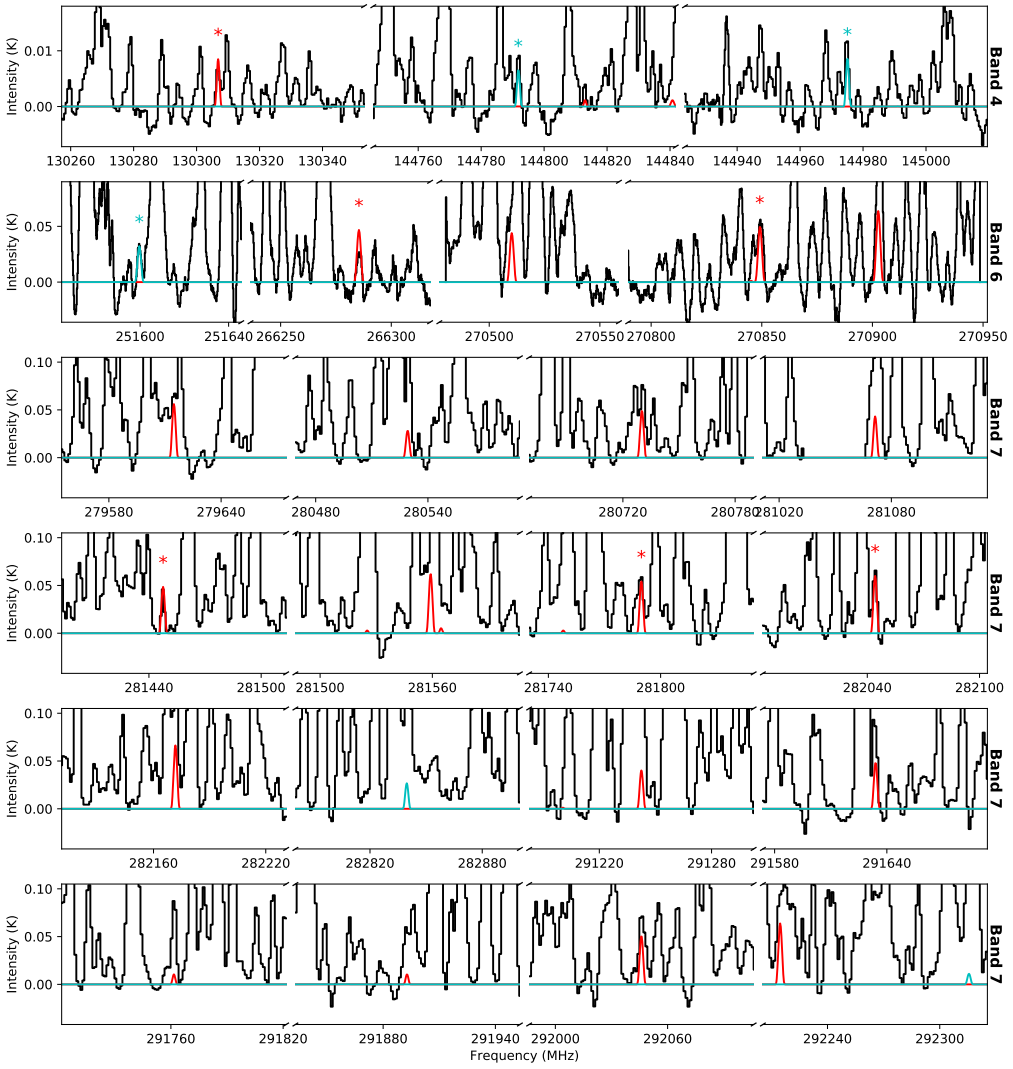

Figure 5.4: The observed spectra of NGC 6334I extracted toward the MM1 region are plotted in black with the single-excitation temperature model spectra of vibrationally excited CH_3COOH in red for $v_t = 1$ and cyan for $v_t = 2$. Asterisk makers mark the clean spectral features, of which the blowups are shown in Figure 5.1. The best-fit parameters are $T_{ex} = 142\,\mathrm{K}$, $N_T = 1.12 \times 10^{17}\,\mathrm{cm}^{-2}$, and $\Delta V = 2.72\,\mathrm{km\,s}^{-1}$. The horizontal axes are the rest frequency with respect to a radial velocity of $-6.9\,\mathrm{km\,s}^{-1}$.

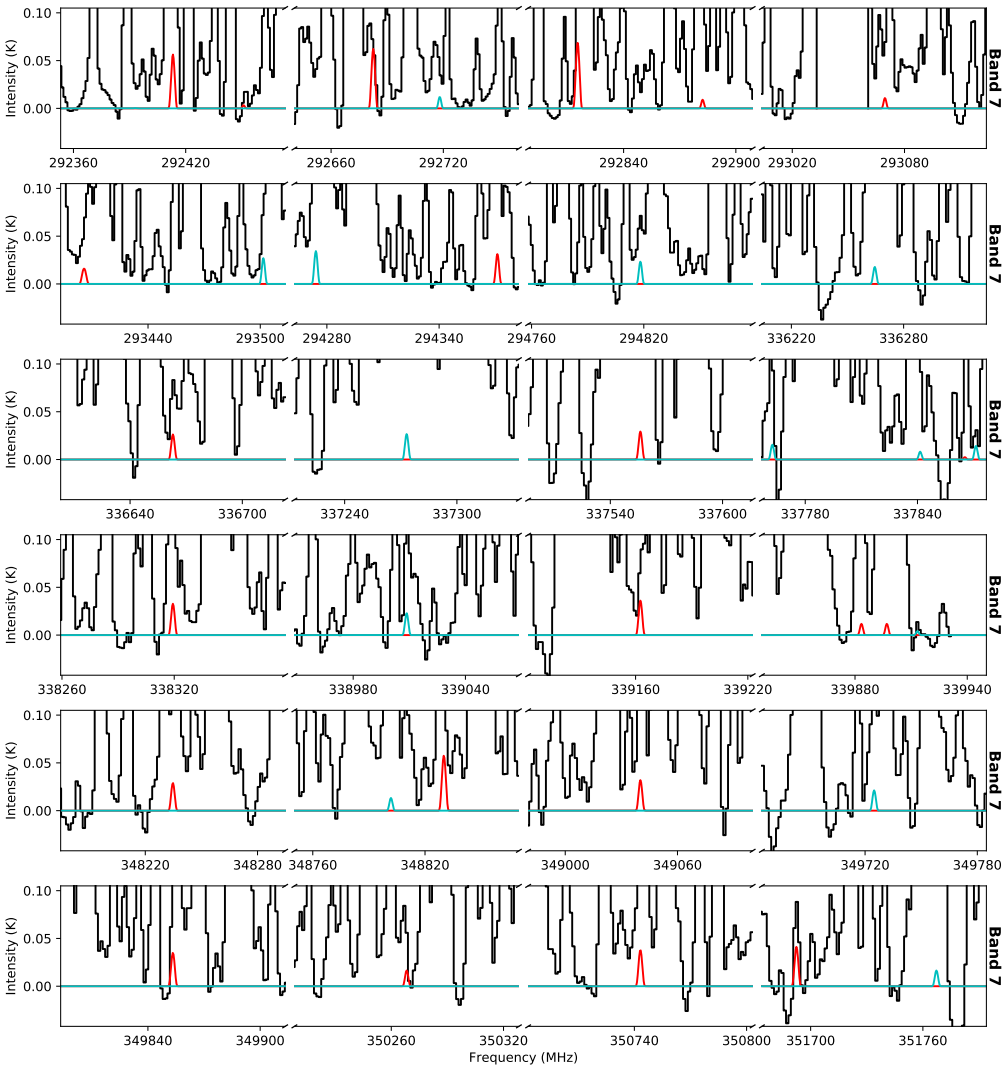

Figure 5.5: Continue to Figure 5.4

Chapter 6

Multi-wavelength Investigation on Molecular Masers

This chapter presents a detailed mapping of maser signals from CH_2NH, CH_3NH_2, and CH_3OH Class I masers toward the Sagittarius B2(N) massive star-forming region. At the centimeter wavelength, the single-dish observation, PRIMOS survey, has suggested that Sgr B2 hosts weak maser emission from complex molecules, including CH_2NH, HNCNH, and $HCOOCH_3$ (McGuire et al., 2012; Faure et al., 2014, 2018). Following these studies, the interferometric observations performed with the Very Large Array (VLA) now enable us to resolve the region where the maser emission originates and constrain the pumping mechanisms. While the detection of CH_3OH Class I masers has been previously reported in the 44 GHz transition, the relatively rare 84-GHz maser are observed toward SgrB2(N) for the first time. Alongside the discoveries of two CH_3OH Class I maser transitions, we also characterized their distribution at millimeter wavelength. By comparing the distribution of several maser emissions, it is revealed that the new maser species, CH_2NH and CH_3NH_2, have a close spatial relationship with the CH_3OH Class I masers. This relationship serves as

observational evidence to suggest a similar collisional pumping mechanism for these maser transitions. Benefited by the information of source size of maser emission and the calculated collisional rate coefficients, we also perform a detailed spectral analysis to model the maser spectra and assess the quantitative characteristics of the observed spectral profiles. Because masers often trace specific conditions within the massive star-forming regions, finding new maser transitions and species provides critical insights into the physical structures hidden behind the thick dust.

6.1 Introduction

Molecular masers have been shown with compelling roles in anchoring complex dynamics in both the start and end stages of stellar evolution. While molecular masers can arise in the winds and outflows of evolved stars interacting with the molecule-rich circumstellar atmospheres in the late stage of stellar evolution (e.g Yates et al., 1995; Richards et al., 2014; Menten et al., 2018), masers also offer a mean to discover stars in their embryonic stage, which are embedded in the dust of surrounding molecular clouds (e.g., Minier et al., 2001; Hunter et al., 2004; Minier et al., 2005; Brogan et al., 2019). The energetic events (e.g., outflows and collimated jets) and infrared radiation surrounding massive protostars provide energies to overpopulate the upper energy level of specific molecular transitions and amplify the molecular emission intensities (Moscadelli et al., 2016; Sanna et al., 2016). The common molecular species exhibiting maser emission include but not limit to OH, SiO, H_2O, H_2CO, NH_3, and CH_3OH. Maser emissions from these species have supplied critical insights into the kinetic properties of young stars and even monitored the accretion process (Hunter et al., 2018, and reference therein). Recently, a new maser species HNCO was found to be associated with accretion flows and helped build an arm-spiral-structure model of high-mass young stellar objects (Chen et al., 2020). An empirical taxonomy based

on pumping mechanisms classifies molecular masers into two categories (Batrla et al., 1987; Cyganowski et al., 2009); the Class I CH_3OH and H_2O masers are excited via collisions and tend to reside in shocked materials around outflows and expanding H II regions (e.g. Baudry et al., 1974; Elitzur & Fuqua, 1989; Voronkov et al., 2014; Towner et al., 2017), while the Class II CH_3OH and OH masers are excited via radiation and are generally close to the exciting young stellar objects and infrared sources (e.g., Sobolev & Deguchi, 1994; Sobolev et al., 1997; Cragg et al., 2002, 2005).

Maser emission also provides a tremendous role in probing the evolutionary phases of massive star formation by comparing emissions from diverse species and pumping mechanisms. A survey toward 74 star-forming regions statistically found that the H_2O and OH masers appear in the evolutionary sequence with the isolated H_2O masers representing the earliest stages of star formation (Forster & Caswell, 1989). While Class II CH_3OH masers share a similar radiative pumping characteristic to OH masers, they typically arise before the OH masers and ultra-compact H II (UC H II) regions turn on but have a significant overlap with H_2O masers (Walsh et al., 2003; Szymczak et al., 2005).

However, within the picture of massive star formation, the position for Class I CH_3OH masers in this evolutionary sequence is less clear. In comparison with the mid-infrared properties of the sample sources, Ellingsen (2006) suggested that the Class I CH_3OH masers signpost the earliest stage of massive star formation, even prior to the H_2O masers. In contrast, a detailed mapping of multiple Class I CH_3OH maser transitions toward a luminous young stellar object, IRAS16547-4247, led Voronkov et al. (2006) to argue that Class I CH_3OH masers may appear earlier than the Class II masers and last long enough to coexist with the OH masers. Later, observations toward a massive protocluster G18.67+0.03 further suggested that the Class I CH_3OH masers might associate with both young sites and relatively evolved UC H II regions

within the same protocluster (Cyganowski et al., 2012).

The high mass star-forming region, Sgr B2(N), is the richest known source for molecular detections, contributing 69 new species (~30%) to the known interstellar molecular inventory (McGuire, 2021). In addition to the chemical richness, Sgr B2 displays interesting maser activities from diverse complex molecules. The single-dish spectral survey, the PRebiotic Interstellar MOlecular Survey (PRIMOS), has identified numerous species masering at centimeter wavelengths. The discovery of interstellar carbodiimide (HNCNH) was achieved with its maser emission (McGuire et al., 2013). The radiative transfer calculations also revealed that most emission lines of both methyl formate ($HCOOCH_3$) and methanimine CH_2NH detected in PRIMOS were weak maser emission amplifying the background continuum radiation of Sgr B2(N) at cm wavelengths (Faure et al., 2014, 2018). However, the large $\sim 2.5' \times 2.5'$ observation field of PRIMOS accommodated both the North and Main clumps of Sgr B2, complicating the interpretation of the spectral profiles. Therefore, it is crucial to have interferometric observations to disentangle in detail the various components of maser emission.

In this chapter, we present a rigorous mapping study of maser emission from CH_2NH, CH_3NH_2, and CH_3OH Class I masers toward Sgr B2(N) leveraging the interferometric observations at both centimeter (cm) and millimeter (mm) wavelength regime. We described the observations in Section 6.2. Section 6.3 presents both the spectra and distribution per maser species. The spatial correlation and pumping mechanisms for the new maser emission were discussed in Section 6.4. Lastly, the single-dish measurement of the centimeter maser was compared against the interferometric observations using morphological information.

6.2 Observations

The interferometric data used here were acquired from two data sets involving VLA C-band observation and ALMA Bands 3 observation, wavelength coverage ranging between 6 cm and 3 mm. The VLA observations were performed on 2016 May 27 (project code: 16A-076) with the C-band receiver. The correlator was configured to observe 15 spectral windows with channel width ranging between $0.485\,\mathrm{km\,s^{-1}}$ and $2.31\,\mathrm{km\,s^{-1}}$ depending on the corresponding bandwidth and observed frequency. Detailed observation parameters of each spectral window are presented in Table 6.1. The phase center of the observation was targeted toward Sgr B2 (N), with the field center at $\alpha_{\mathrm{J2000}} = 17^{\mathrm{h}}47^{\mathrm{m}}19.80^{\mathrm{s}}$, $\delta_{\mathrm{J2000}} = -28^{\circ}22'17.00''$. The bandpass and absolute flux calibrator were 3C286, while the phase and amplitude calibrator were J1744-3116. The array was in the B configuration with 27 antennas, which covered baselines from 250 m up to 11 km and resulted in the largest angular scale structure of $25''$ at 6 GHz and $37''$ at 4 GHz.

The CASA software (version 5.6.1) was used for data reduction and imaging analysis of the VLA observation. For each spectral window, the continuum emission was subtracted in the UV-plane before imaging the spectral cubes. For all VLA data sets, we used the `tclean` task for imaging with the Natural weighting scheme and a cell size of $0.27''$. The resulting size of the synthesized beam (HPBW) of each data cube has a median value of $\sim 3.8'' \times 1.5''$. The median of resultant typical RMS noise levels is $\sim 0.9\,\mathrm{mJy\,beam^{-1}}$.

Table 6.1: Summary of Observation Parameters

SPW	Frequency Range (MHz)	Channel Number	Spectral Resolution (kHz | $km\,s^{-1}$)	BWs (MHz)	Synthesized Beam [a] $'' \times ''$	Targeted Species
3	5172.8 – 5180.8	512	15.625 | 0.905	8		H_2COH^+
5	5282.8 – 5298.8	1024	15.625 | 0.885	16	3.351×1.292	CH_2NH
7	5556.8 – 5560.8	256	15.625 | 0.843	4		t$-CH_3CH_2OH$
9	6023.8 – 6039.8	1024	15.625 | 0.777	16		OH
10	6046.8 – 6050.8	256	15.625 | 0.774	4		OH
12	4049.8 – 4057.8	256	31.250 | 2.31	8	4.350×1.687	H_2CCNH
14	4337.8 – 4345.8	512	15.625 | 1.08	8	4.071×1.575	HNCNH
15	4360.8 – 4368.8	256	31.250 | 2.15	8	4.052×1.568	CH_3NH_2
17	4439.8 – 4443.8	256	15.625 | 1.05	4	3.983×1.542	CH_2NH
18	4584.8 – 4600.8	512	31.250 | 2.04	16		$H_2{}^{13}CO$
19	4609.8 – 4625.8	512	31.250 | 2.03	16	3.841×1.483	NH_2CHO
21	4799.8 – 4807.8	512	15.625 | 0.975	8	3.693×1.424	HNCNH
22	4823.8 – 4839.8	2048	7.812 | 0.485	16	3.672×1.416	H_2CO
24	4915.8 – 4919.8	128	31.250 | 1.90	4		t$-H_2COOH$
25	4927.8 – 4935.8	256	31.250 | 1.90	8	3.597×1.389	H_2CCCNH

[a] The synthesized beam size obtained with `Natural` weighting.

The ALMA observation data were acquired from the ALMA Science Archive of the EMoCA survey. A detailed description of the EMoCA data has been presented in Section 4.2. In this study, two measurement sets, spectral window 0 of setup S1 and spectral window 0 of setup S4 (Table 4.1), were used for imaging the 84-GHz and 95-GHz CH_3OH transitions. The resultant synthesized beam size is $2.14'' \times 1.56''$ at 84 GHz and $1.82'' \times 1.40''$ at 95 GHz with a median RMS value of 4 mJy beam^{-1}. Different from Chapter 4, we used the `tclean` task with the auto-masking algorithm for the imaging analysis, consistent with the VLA imaging process.

6.3 Results

Multi-wavelength observations are leveraged to provide a complete picture of the physical and chemical environment of Sgr B2; the ALMA observation at the mm wavelength regime characterizing the hot and compact emission while the VLA observation at the cm regime characterizing cold and extended regions. Figure 6.1 shows the continuum emission of Sgr B2(N) observed at 6.8 cm and 3.5 mm. The free-free continuum emission concentrations at cm include four arcsecond cores, K1 - K4, and the two 10-arcsec bow-shaped H II regions, K5 and K6 (Corby et al., 2015, marked in green in Figure 6.1). At mm, dust continuum emission were resolved into three main cores, N1 - N3 (Bonfand et al., 2017, marked in orange in Figure 6.1). In addition, the reported maser locations in this region were shown with + symbols. The Class II CH_3OH maser spot at 6.6 GHz spatially associated with the N3 mm core (Caswell, 1996; Caswell et al., 2010). Six OH maser spots have been identified with a VLA survey of hydroxyl masers with the brightest spot being associated with the K3 cm core (Argon et al., 2000; Qiao et al., 2014). Another survey performed with the Australia Telescope Compact Array (ATCA) characterized 30 H_2O maser spots where the majority of them located within the N1-K2-K3 region (Walsh et al., 2014).

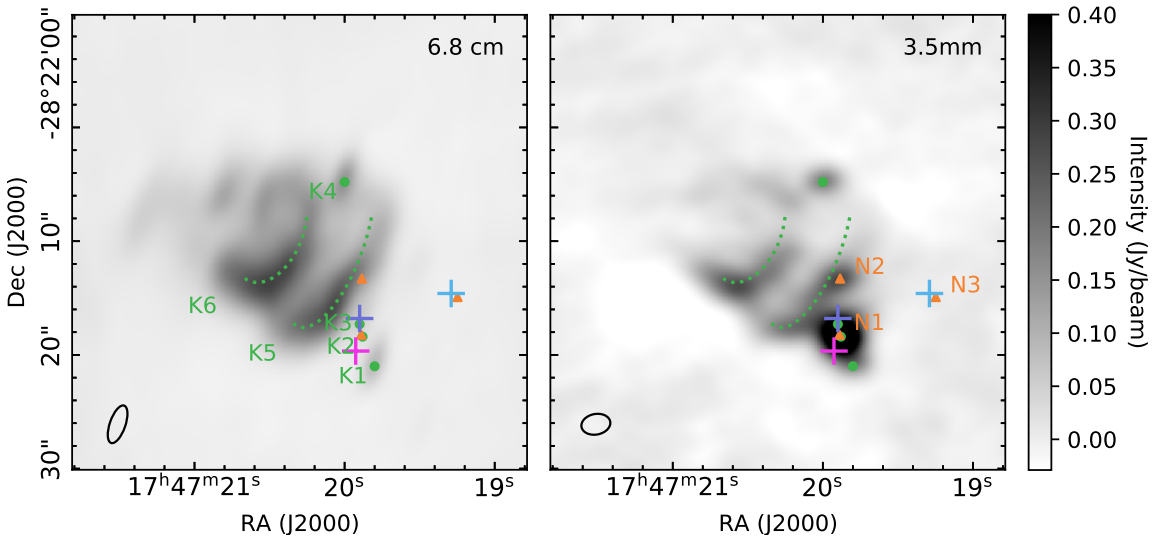

Figure 6.1: Continuum emission toward the Sgr B2(N) region obtained with VLA at 6.8 cm and ALMA at 3.5 mm. The centimeter emission concentrations are indicated by green dashed lines and circle markers whereas the millimeter emission cores are indicated by organ triangle markers. The + symbols mark the location of Class II CH_3OH masers in blue, the brightest OH maser spot in purple (Argon et al., 2000), and the brightest H_2O maser spot in magenta (Walsh et al., 2014).

Table 6.2: Searched Maser Transitions

Molecule	Rest Frequency (MHz)	Transition	$E_{\rm u}$ (K)	$S_{ij}\mu^2$ (D^2)	$T_{\rm B,peak}$ (K)
CH_2NH	5288.962(3)	$1(1,0) - 1(1,1),\ F = 0 - 1$	11.1	0.897	121.7 ± 9.4
	5289.712(3)	$F = 1 - 0$		0.897	
	5289.815(3)	$F = 2 - 2$		3.365	
	5290.671(3)	$F = 2 - 1$		1.121	
	5290.828(3)	$F = 1 - 2$		1.122	
	5291.682(3)	$F = 1 - 1$		0.673	
CH_3NH_2	4362.872(5)	$2(0) - 1(1)\ E,\ F = 1 - 0$	6.8	0.051	75.8 ± 9.3
	4364.087(5)	$F = 3 - 2$		0.213	
	4364.169(5)	$F = 1 - 1$		0.038	
	4364.873(5)	$F = 2 - 2$		0.038	
	4365.392(5)	$F = 2 - 1$		0.114	
CH_3OH	84521.172(12)	$5(-1) - 4(0)\ E$	40.4	12.332	407.5 ± 0.2
CH_3OH	95169.391(11)	$8(0) - 7(1)\ A$	83.5	28.885	109.1 ± 0.2

6.3.1 Class I CH_3OH Masers

Class I CH_3OH masers are prevailing in massive star formation regions and the most extensively studied maser lines are the $4(-1) - 3(0)$ E transition at 36 GHz, the $7(0) - 6(1)$ A transition at 44 GHz, and the $8(0) - 7(1)$ A transition at 95 GHz (e.g. Plambeck & Menten, 1990; Liechti & Wilson, 1996; Voronkov et al., 2014; Yang et al., 2017). In particular, the 44-GHz maser line were observed toward Sgr B2 at $3''$ resolution (Mehringer & Menten, 1997). In contrast, there is limited information about the $5(-1) - 4(0)$ E Class I CH_3OH maser at 84 GHz, a member of the same $J + 1(-1) - J(0)$ E-type transition family with the 36-GHz line (Breen et al., 2019, and references therein). Even rarer are the interferometric observation of the 84-GHz line.

Here, we present the first interferometric observation of the rare 84-GHz CH_3OH masers at a resolution of $1.5''$ with ALMA as well as the first detection of the 84-GHz maser toward Sgr B2. The spread of 84-GHz maser spots is manifest in the channel images shown in Figure 6.2. In total, eight maser knots with velocities ranging from 50 to 86 $\mathrm{km\,s^{-1}}$ were resolved for the 84-GHz maser. The brightest maser spot is located ~$3.6''$ west of the K4 core with a brightness temperature (T_B) of 407.5 ± 0.2 K. In addition to the brightest 58-$\mathrm{km\,s^{-1}}$ spot, another maser knot associated with the K6 H II region is also identified with a V_lsr of 84 $\mathrm{km\,s^{-1}}$, which will be discussed along with other masers in Section 6.4.

Alongside our observation of the Class I 84-GHz CH_3OH maser, we were also able to observe another CH_3OH transition at 95 GHz (Figure 6.3). The channel maps revealed the brightest 95-GHz emission peak being co-spatial with the N1 core with a peak T_B of 109.1 ± 0.2 K. In light of the similar spatial distribution for the 95-GHz line to that for other thermal molecular lines, as well as the fact that the $T_\mathrm{B,peak}$ is

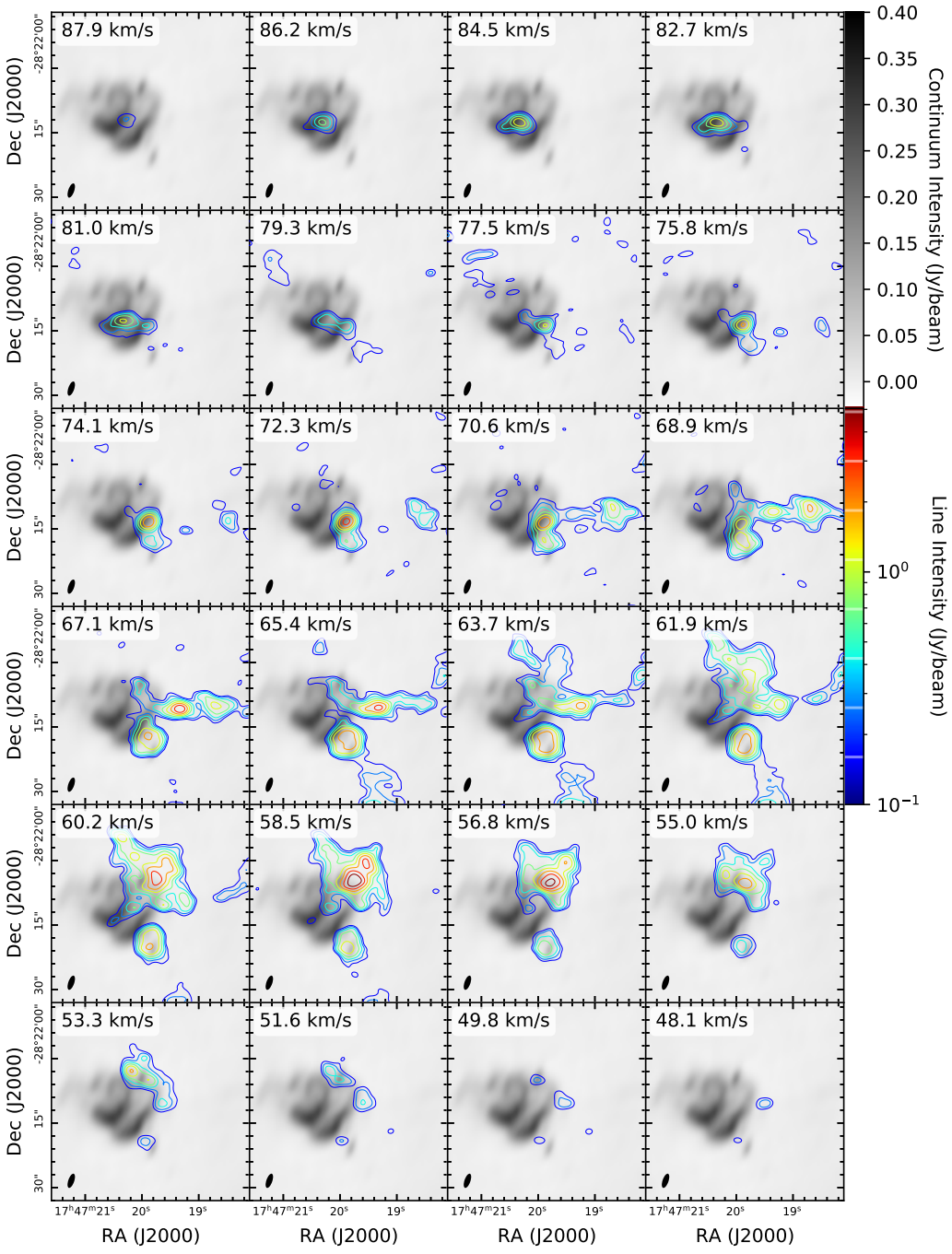

Figure 6.2: Channel maps of the Class I CH_3OH maser at 84 GHz overlaid on the continuum emission observed at 6.8 cm. The contours levels are 40, 65, 106, 173, 282, 459, 749, 1220 σ. The peak value is 7.95 Jy beam^{-1}.

comparable with N1's source temperature (150 K), it is challenging to determine the excitation mechanism for each 95-GHz emission spot toward Sgr B2(N). This emission could be either weak maser, thermal, or a combination of both. While the 95-GHz line exhibits maser activity toward several famous star-forming regions (e.g., Orion–KL (Plambeck & Wright, 1988), DR 21 (Plambeck & Menten, 1990), and W51 (Pratap & Menten, 1993)), it is noteworthy that Mehringer & Menten (1997) attributed the 44-GHz emission, a consecutive transition of the $J + 1(0) - J(1)$ A series with the 95-GHz transition, to both masers and quasi-thermal emission component in Sgr B2.

6.3.2 CH_2NH Masers

The maser activity of the $1(1,0)-1(1,1)$ CH_2NH transitions has been revealed toward both galactic center and extra galaxies, although with no position measurement (Faure et al., 2018; Gorski et al., 2021). The VLA observation enabled us to resolved the CH_2NH maser emission at 5.29 GHz into three velocity components with a $V_{\rm lsr}$ of 64, 73, and 84 km s^{-1}. For the illustration of the multiple velocity components, Figure 6.4 shows a spectrum extracted from an aperture of $10''$, which is large enough to accommodate the majority of the 5.29-GHz CH_2NH emission. In addition to the three velocity components, we also simultaneously fitted six hyperfine components of the $1(1,0) - 1(1,1)$ transitions, with the $F = 1 - 0$ and $F = 2 - 2$ blending together.

The emission region for each component is shown in Figure 6.5 respectively. The 84-km s^{-1} and 64-km s^{-1} components are both associated with the K6 H II region. While the brightest 84-km s^{-1} component displays a more compact distribution, the 64-km s^{-1} component consists of a cluster of spots distributed along K6. The 73-km s^{-1} component is concentrated toward the K5 region. The $T_{\rm B}$ of the 5.29-GHz CH_2NH maser is 66.6 ± 9.4, 89.3 ± 9.4, and 121.7 ± 9.4 K associated with the 64-, 73-, and 84-km s^{-1} components, respectively.

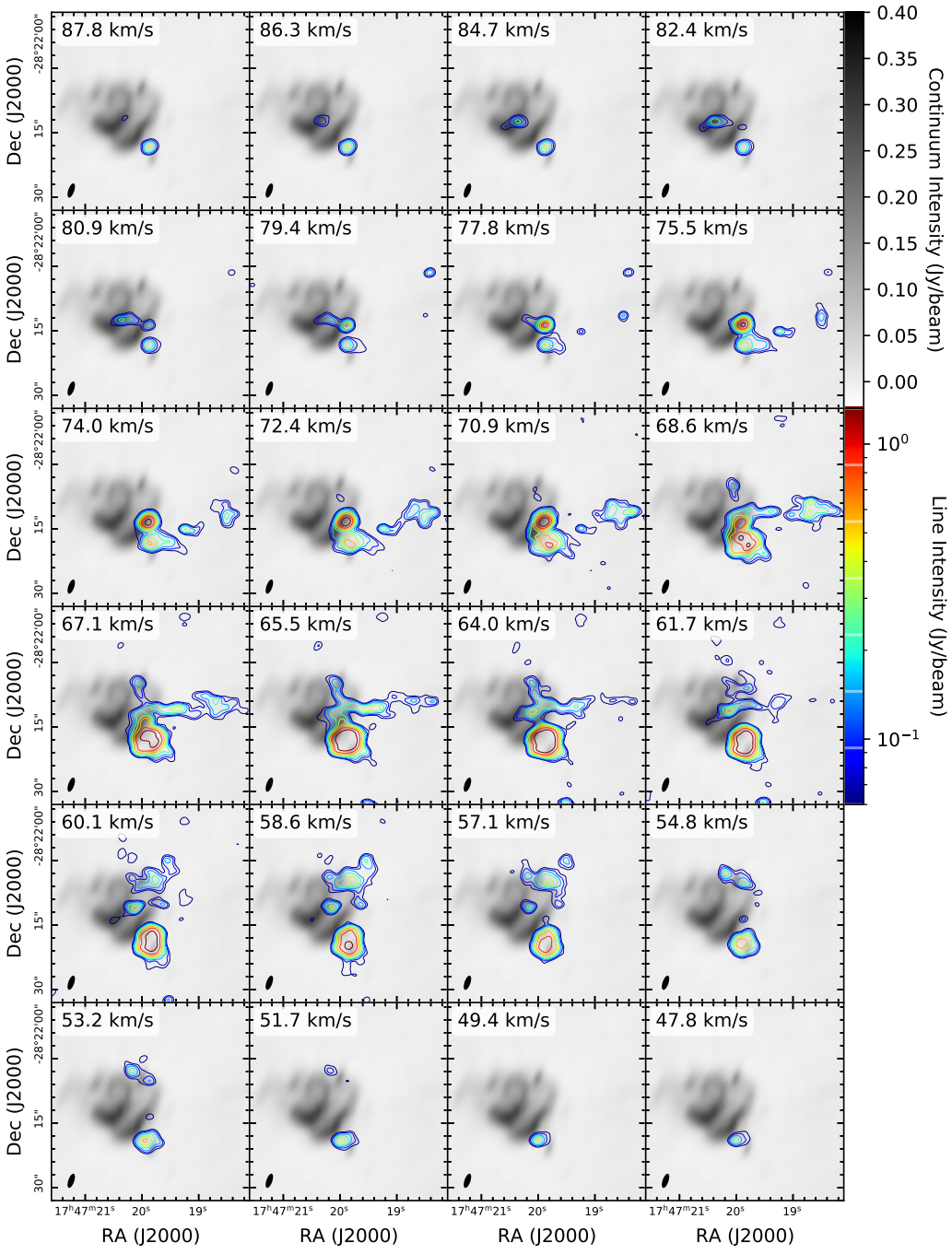

Figure 6.3: Channel maps of the Class I CH_3OH maser at 95 GHz overlaid on the continuum emission observed at 6.8 cm. The contours levels are 15, 23, 36, 56, 88, 137, 212, 330 σ. The peak value is 2.06 Jy beam^{-1}.

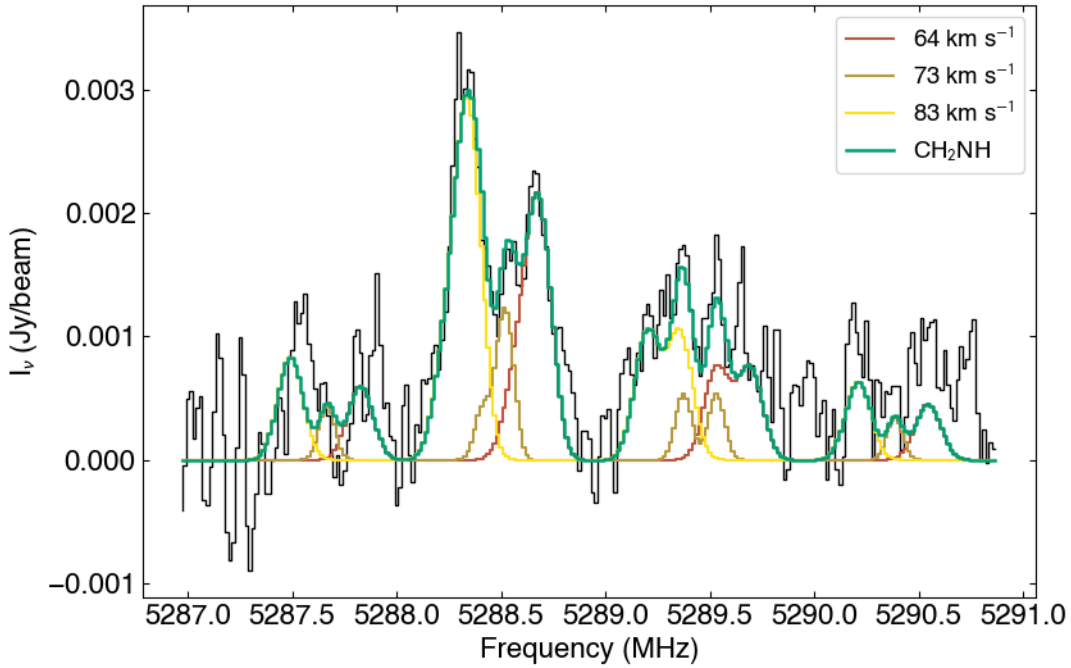

Figure 6.4: VLA spectrum extracted from an aperture with a diameter of 10″ shown in black. The best-fit simulated spectra of CH_2NH with hyperfine splitting are overlaid in red, brown, and yellow for the 64-, 73-, and 84-km s^{-1} components, respectively. The sum of all three velocity components is overlaid in green.

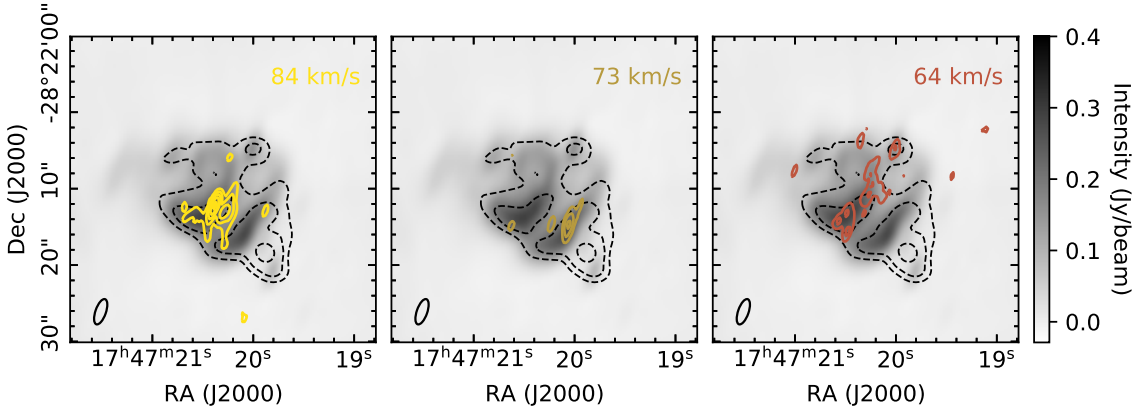

Figure 6.5: Peak intensity maps for each velocity component of the CH_2NH maser at 5.29 GHz superimposed on the continuum emission observed at 6.8 cm. The contours levels start at 4 σ and up to the peak value with a step size of 2 σ. The peak value is 12.1, 8.86, 6.60 mJy beam^{-1} for the 84-, 73-, and 64-km s^{-1} components, respectively.

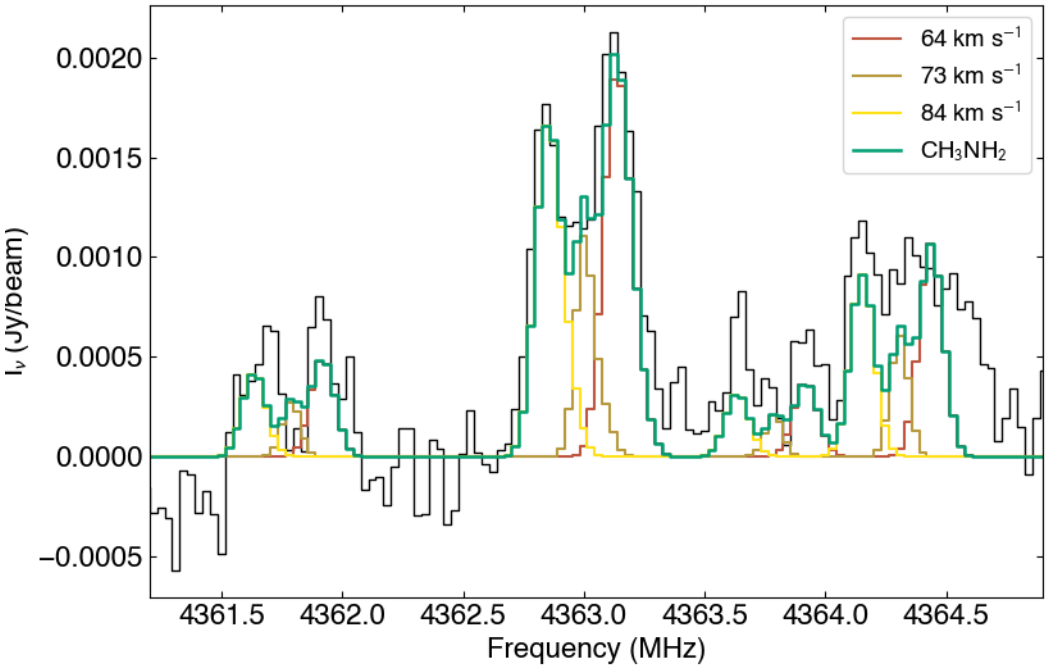

Figure 6.6: Spectra of the CH_3NH_2 maser at 4363 MHz. See Figure 6.4 caption for details.

6.3.3 CH_3NH_2 Masers

The $2(0) - 1(1)$ E CH_3NH_2 transition displays analogous maser emission with the 5.29-GHz CH_2NH transition. Three velocity components were resolved for the CH_3NH_2 maser emission at 4.36 GHz, with a high degree of morphological consistency with the CH_2NH maser. However, the intensity ratios between the 4.36-GHz-CH_3NH_2 and 5.29-GHz-CH_2NH line vary among the three velocity components. The brightest component for the 4.36 CH_3NH_2 maser is the 64-km s^{-1} component, displaying an elongated distribution along the K6 shell with a length of 15″ in extent (Figure 6.7). A T_B of 75.8 ± 9.3, 49.3 ± 9.3, 59.1 ± 9.3 K was reported for the 64-, 73-, and 84-km s^{-1} components, respectively.

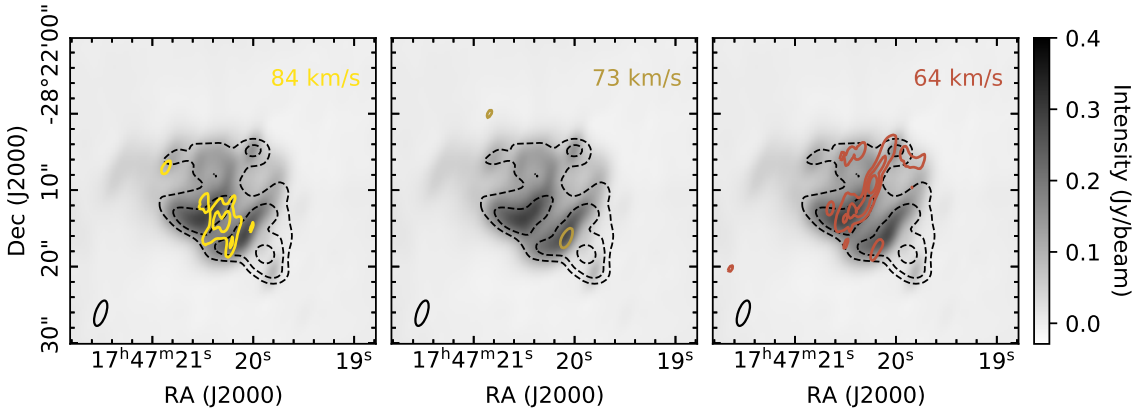

Figure 6.7: Peak intensity maps of CH_3NH_2 maser at 4.36 GHz superimposed on the continuum emission observed at 6.8 cm. The contours levels start at $4\,\sigma$ and up to the peak value with a step size of $2\,\sigma$. The peak value is 5.85, 4.88, 7.50 mJy beam^{-1} for the 84-, 73-, and 64-km s^{-1} component, respectively.

6.4 Discussion

The majority of the molecular lines observed toward the K4, K5, and K6 regions in Sgr B2(N) is in absorption (and reference therein Corby et al., 2015). The rotational temperatures constrained by these absorption features were reported to be <10 K (Hollis et al., 2006; Loomis et al., 2013; Zaleski et al., 2013; Thiel et al., 2017). In contrast, specific transitions of certain species cause emission in centimeter spectra (McGuire et al., 2012; Corby et al., 2015). The question was whether these emissions were thermal or maser. Empirically, a $T_{\rm B}$ much greater than the source's physical temperature is considered as an indication for a maser emission rather than a thermally-excited line (Voronkov et al., 2006; Gargaud et al., 2011). Based on non-LTE radiative transfer models, the best-fit kinetic temperature for the Sgr B2 region was found to be ~30 K Armijos-Abendaño et al. (2020), comparable to its dust temperature (Etxaluze et al., 2013). In the case of the molecular emission at cm wavelength reported in this study, as summarized in Table 6.2, the observed $T_{\rm B}$ are

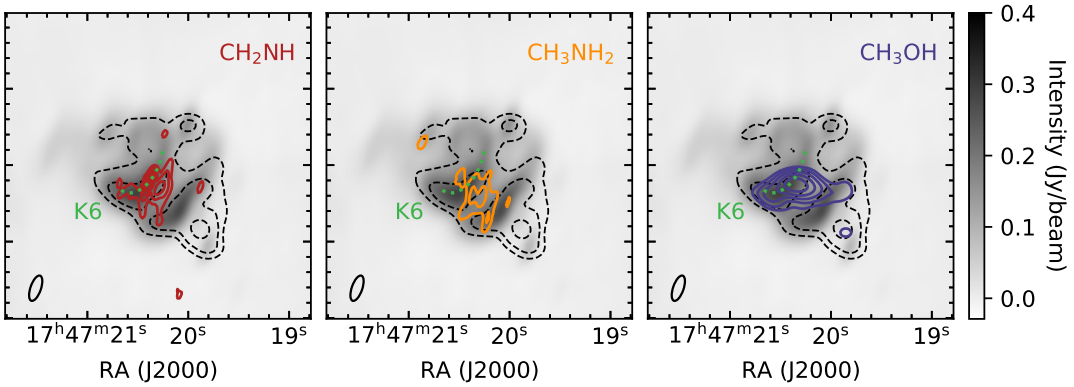

Figure 6.8: The 84-km s^{-1} components of the 5.29-GHz CH_2NH maser, 4.36-GHz CH_3NH_2 maser, and 84-GHz Class I CH_3OH are shown in red, orange, and blue contours respectively, superimposed on the 6.8-cm continuum emission. The arc-like K6 H II region is marked with green dotted line.

higher than both the cold rotational temperature and physical temperatures. Also, the emission spectral profiles deviate substantially from the thermal model, suggesting the observed non-thermal molecular emissions in the K4, K5, and K6 H II regions are astronomical masers.

By scrutinizing the VLA and ALMA observation, we found that the K6 source harbor maser emission of CH_2NH at 5.29 GHz, CH_3NH_2 at 4.36 GHz, and Class I CH_3OH at 84 GHz (Figure 6.8). A CH_3OH-rich gas that is energetic and moderately dense – just dense enough to turn on collisional pumping but well below the critical density for approaching LTE – can trigger Class I CH_3OH maser activities. The 84-km s^{-1} knot of the CH_2NH and CH3NH2 maser at K6 remarkably resemble those of the Class I CH_3OH maser. Their consistent morphology serves as strong evidence to support a similar collisionally pumping mechanism for the CH_2NH and CH_3NH_2 maser with the Class I CH_3OH as well as a common physical condition for triggering these masers. Therefore, these maser activities indicate that there are energetic events happening in the arc-like K6, which is far from strong infrared sources and has been

thought of as the ionization front of the H II regions (Gaume et al., 1995).

In addition to locating the regions where the masers emit, high-resolution images also provide information on the maser source sizes, which is critical for assessing the spectral profiles, i.e. proper treatment on beam dilution effects. While the single-dish PRIMOS observation had blended all components within the 2.5″ spatial scale into one single spectrum, we have resolved the distributed maser emission into three components with diverse source sizes toward Sgr B2(N). To connect the two cm observations, it is worth comparing the VLA spectra for the maser transitions with the corresponding spectra observed with GBT.

We first converted a VLA aperture-averaged specific intensity $I_{\nu,\mathrm{VLA}}$ into brightness temperature $T_{\mathrm{B,VLA}}$ using

$$T_{\mathrm{B,VLA}} = I_{\nu,\mathrm{VLA}} \frac{\lambda^2}{2k_{\mathrm{B}}} \frac{4\ln 2}{\pi\theta_{\mathrm{a}}\theta_{\mathrm{b}}}, \tag{6.1}$$

where $\theta_{\mathrm{a}}\theta_{\mathrm{b}}$ is the VLA synthetic beam size. Following that, to relate a GBT observed T_{B} with that of VLA, we considered the different beam dilution effect caused by difference in GBT beams and VLA aperture sizes. An undiluted $T_{\mathrm{B,GBT}}^{\mathrm{undiluted}}$ is obtained using

$$T_{\mathrm{B,GBT}}^{\mathrm{undiluted}} = T_{\mathrm{B,GBT}} \times \frac{\Omega_{\mathrm{GBT}} + \mathrm{ss}^2}{\mathrm{ss}^2} \tag{6.2}$$

while an undiluted $T_{\mathrm{B,VLA}}^{\mathrm{undiluted}}$ is obtained using

$$T_{\mathrm{B,VLA}}^{\mathrm{undiluted}} = T_{\mathrm{B,VLA}} \times \frac{\Omega_{\mathrm{VLA}}}{\mathrm{ss}^2}, \tag{6.3}$$

where Ω_{GBT} and Ω_{VLA} are the GBT beam and VLA aperture sizes and ss^2 is a source size. Since the source size of the maser emissions reported in this study is much smaller than the GBT beam, by relating $T_{\mathrm{B,GBT}}^{\mathrm{undiluted}}$ and $T_{\mathrm{B,VLA}}^{\mathrm{undiluted}}$ in Equations (6.2) and (6.3),

we can get the conversion factor

$$\frac{T_{\rm B,VLA}}{T_{\rm B,GBT}} = \frac{\Omega_{\rm GBT}}{\Omega_{\rm VLA}}. \tag{6.4}$$

Figure 6.9 shows example spectra of the CH_2NH 5.29-GHz maser transition observed with GBT and VLA (with an aperture of $16'' \times 16''$). In this example, the conversion factor between the GBT spectrum and VLA spectrum is ~80. The two observed spectra match to a large extent, although with non-trivial excess in the PRIMOS observation at $64\,{\rm km\,s^{-1}}$. The excess can be assigned to several sources since the observation field of GBT at 5.29 GHz is composed of both the North and Main clumps of Sgr B2 with overlapping velocity ranges. One of the possible sources is Sgr B2 (M), which has a $V_{\rm lsr}$ of $64\,{\rm km\,s^{-1}}$ (Pols et al., 2018); its emission could manifest as the excess. This excess might also be explained by that PRIMOS single-dish spectra have additional thermal contributions at the same $V_{\rm lsr}$ that are resolved out in the VLA interferometric observations. For example, the hot core N1 has a similar velocity of $64\,{\rm km\,s^{-1}}$. Thermal and maser emissions are not mutually exclusive to the each other. In some case, the thermal emission can coexist with non-thermal emission, further adding complexity to the multi-velocity components observations. Leveraging the theoretical calculations on collisional rate coefficients and cross sections, the spatial information will be incorporated into non-LTE spectral fitting and therefore assess the maser models.

6.5 Summary

We reported multi-wavelength interferometric observations of maser transitions toward Sgr B2 using ALMA and VLA. Enabled by the ALMA observation, we reported the first detection of the Class I CH_3OH maser at 84 GHz toward Sgr B2.

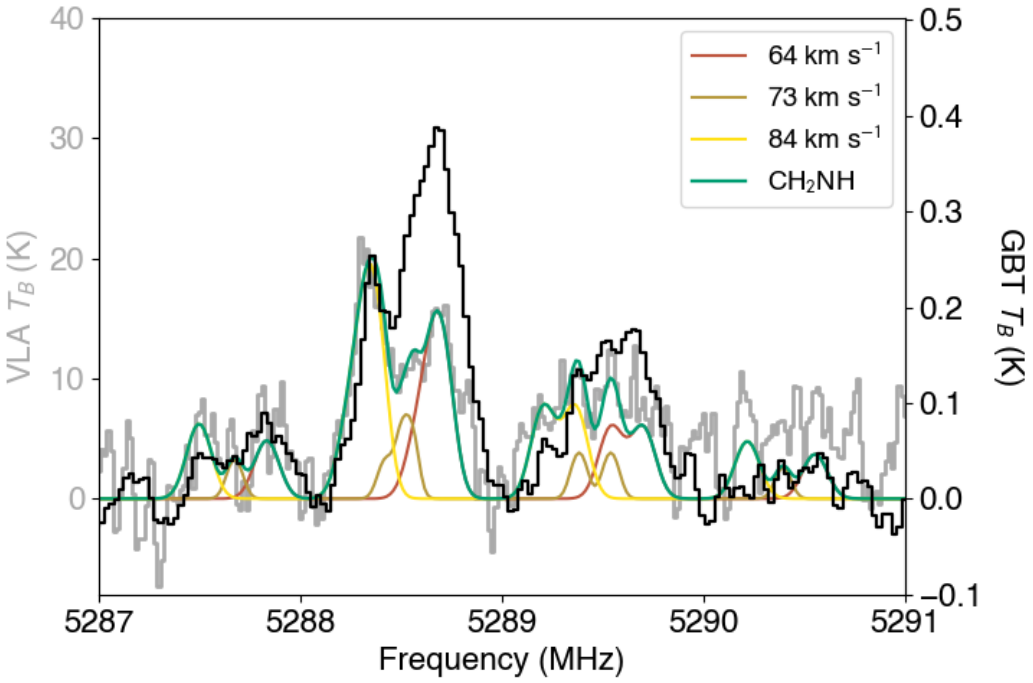

Figure 6.9: Observed spectra of the CH_2NH 5.29-GHz maser emission shown in grey for the VLA observation and in black for the GBT survey (i.e. PRIMOS). The VLA spectrum was extracted with an aperture of $16'' \times 16''$, larger than that used for Figure 6.4. See Figure 6.4 caption for details of the best-fitted spectra shown in colors.

Eight 84-GHz maser knots were resolved with the brightest spot located ~3″ west of the K4 free-free continuum emission core. Its peak brightness temperature reached 407.5 ± 0.2 K. Informed by the VLA observations, we reported the CH_2NH maser emission at 5.29 GHz with a peak brightness temperature of 121.7 ± 9.4 K as well as the CH_3NH_2 maser emission at 4.36 GHz with a peak brightness temperature of 75.8 ± 9.3 K. The asymmetric line profiles with multiple peaks revealed three components with distinct velocities for the CH_2NH and CH_3NH_2 maser. The peak intensity maps further enabled us to characterize the spatial origin and extent of maser emission in detail. The three velocity components display distinct fine-scale structures associated with the K5 and K6 bow-shaped H II regions.

We found a definite association between the maser emissions and the K6 H II region for the 5.29-GHz CH_2NH, 4.36-GHz CH_3NH_2, and 84-GHz CH_3OH masers. The spatial correlation between the three maser emissions suggested the CH_2NH and CH_3NH_2 masers were pumped by intense collisions, analogous to the Class I CH_3OH maser. By exploring the nature of the maser emission toward the galactic center, these preliminary results also demonstrate the thermal and non-thermal excitation regimes co-existing toward massive molecular clouds.

Part IV

Conclusion

Chapter 7

Conclusion

There is no denying that the molecular abundances are powerful tools for constraining the formation and chemical evolutionary processes. Many studies of large interstellar molecules have investigated the abundances of these species in both astrochemical observations and models and, in turn, used it to constrain chemical models. While the great contributions from these approaches are undeniable, information about the characteristic spatial distributions of molecules was less available, mostly due to the low abundance of these molecules, the poor spatial resolution of previous observations and the complexity of the majority of star-forming regions. Nevertheless, with the improved capabilities of modern telescopes, high-resolution images of complex-molecule emission regions open up a new field of astrochemical researches.

In this thesis, we investigated the molecular inventory of complex molecules in space and their spatial distribution through both single-dish and interferometric observations and chemical modeling. We detailed methods that process both dense and sparse spectra and uncovered very weak molecular signals, often buried under noise. This opens up the possibility of finding and understanding complex molecules in the most exotic environment.

7.1 Major Conclusions

7.1.1 Molecular Census

In Part II, we leveraged the GOTHAM high-sensitivity and high-spectral-resolution survey as well as cutting edge spectral line stacking and match filtering techniques to conduct molecular census towards TMC-1. We discussed one of the many first detections – HC_4NC – in Chapter 2 and the confirmation of H_2C_3S in Chapter 3. In particular:

- We reported the first astronomical detection of HC_4NC, the most complex isocyanide detected in the interstellar medium to date, in Chapter 2 and confirm the detection of H_2C_3S in Chapter 3. We identified a total of four distinct velocity components in both cases and provided the best-fit abundance, excitation temperatures, velocities, and line widths obtained from MCMC analysis. In the analysis, a strong degeneracy was found between abundance and source sizes.

- We found the spectra of HC_4NC best-fit with a total abundance of $3.29^{+8.60}_{-1.20} \times 10^{11}\,\mathrm{cm}^{-2}$, an excitation temperature of $6.7^{+0.3}_{-0.3}\,\mathrm{K}$ and a line width of $0.120^{+0.012}_{-0.010}\,\mathrm{km\,s}^{-1}$. The velocities of the four components range from $5.628^{+0.045}_{-0.038}$ to $6.009^{+0.044}_{-0.032}\,\mathrm{km\,s}^{-1}$ and the source sizes range from 9^{+11}_{-6} to 62^{+20}_{-20} arcsec.

- The abundance of HC_4NC and its cyanopolyyne counterpart HC_5N was compared against a chemical network constructed by considering dissociative recombination, ion-molecule reactions, reactions with atomic carbon, as well as other less dominant reactions. In turn, the rather less bounded reaction rates, branching fractions, and elemental abundance were constrained by fitting the simulated abundance to the observed abundance within an order of magnitude.

- The H_2C_nS family for n = 1, 2 and 3 was investigated systematically in Chapter 3. We were able to confirm the detection of H_2CS and H_2C_3S while an upper limit for H_2C_2S was derived. The total abundance of H_2C_3S was derived to be $(4.17 \pm 0.40) \times 10^{11}\,\mathrm{cm}^{-2}$; the best-fit excitation temperature and line width are $8.8 \pm 0.2\,\mathrm{K}$ and $0.125 \pm 0.003\,\mathrm{km\,s}^{-1}$ respectively. The four components have velocities ranging from 5.576 ± 0.025 to $6.020 \pm 0.012\,\mathrm{km\,s}^{-1}$ and source sizes ranging from $69.9''$ to $259.5''$.

- A complication in the confirmation of the detection of H_2C_3S due to a tentative detection of $DCC^{13}CN$ $J = 3 - 2$ transition blended with a H_2C_3S transition was examined. By considering the DC_3N:HC_3N and $HCC^{13}CN$:HC_3N ratios, we derived the expected abundance of $DCC^{13}CN$ that nicely matches the residual spectrum after subtracting the contribution from H_2C_3S.

- Analyzing the distinct emission-line profiles of H_2CS and H_2C_3S concluded the variation of sulfur chemistry among the four velocity components, which once again underlines the importance of spatial or morphological information of the sources.

7.1.2 Molecular Spatial Distribution

In Part III, three separate projects that utilized ALMA and VLA interferometric observations were discussed. We obtained and analyzed the spatial distribution of both thermal and maser emission towards two hot cores, Sgr B2 (N) and NGC 6334 I. More specifically:

- In Chapter 4, we described a quantitative data-filtering method that serves as a tool to assist and accelerate line identification by eliminating strongly contaminated features from a dense spectrum and a high level of spectral confusion over

a large bandwidth. This method is then applied on a spectrum extracted from ALMA Sgr B2 (N) and identified 26 least contaminated transitions for MF, 10 for GLA, and 5 for AcA.

- We imaged the peak emission maps of the clean transitions for each molecule, eliminated the spatially contaminated maps by comparing their morphology and stacked the remaining to obtain their chemical maps, which show more reliable distributions of the molecules with higher S/N ratios. From this, we found MF displays an extended distribution offset from the continuum emission. In contrast, GLA and AcA are more compact and co-spatial with the continuum emission.

- Four emission cores of MF are resolved, in which two of them, MF1 and MF2, have a $V_{\rm lsr}$ of $\sim$64 km s^{-1} and the other two, MF3 and MF4, have a $V_{\rm lsr}$ of $\sim$73 km s^{-1}. GLA displays two velocity components, with GLA1 at $\sim$64 km s^{-1} and GLA2 at $\sim$73 km s^{-1}. Only one velocity component of AcA, AcA1 at $\sim$64 km s^{-1}, is resolved.

- Through a thorough investigation into the prevalent formation mechanisms involving both grain-surface and gas-phase routes, we concluded that the current existing chemical theory can not explain the observed spatial distribution of the $C_2H_4O_2$ isomers. In addition, different desorption behaviors of the three isomers could contribute to the spatial distributions of the $C_2H_4O_2$ isomeric family.

- In the next chapter, we identified the first and second vibrationally excited states of CH_3COOH for the first time in the interstellar medium based on ALMA observations towards NGC 6334I. More than 100 transitions attributed to vibrationally excited CH_3COOH contribute to the emission features in the 130 –

352 GHz spectra, which seems to indicate that a large portion of unidentified spectral lines in observed interstellar spectra near chemically rich sources can be attributed to vibrationally excited states of detected interstellar molecules.

- We imaged the peak intensity map and pinpointed the emission regions of this molecule with a wide range of excitation energy toward NGC 6334I. Three emission peaks (AcA1, AcA2, AcA3) were identified. While there is not an obvious dependence of the positions of AcA1 and AcA2 on the excited energy levels, that of AcA3 could be explained by the effect of dust opacity or outflows.

- In the last chapter, we looked into the maser emissions of several complex molecules utilizing multi-wavelength observations towards Sgr B2 using ALMA and VLA. We reported the first detection of the Class I CH_3OH maser at 84 GHz as well as CH_2NH and CH_3NH_2 maser emissions at 5.29 and 4.36 GHz respectively.

- Enabled by interferometric imaging, we were able to characterize the spatial origin and extent of maser emission and associate them with the K5 and K6 bow-shaped H II regions. Their spatial correlation also suggested all the masers were pumped by collision like the Class I CH_3OH maser.

7.2 Future Work

7.2.1 Molecular Spatial Information in Dark Clouds

Recent single-dish observations with improved spectral resolution have demonstrated that the dark cloud, TMC-1, is not a quiescent and isotropic cloud as previously thought, but actually has multiple cloud components with distinct systematic velocities (e.g. Dobashi et al., 2018; Loomis et al., 2021, and Chapter 3). The dis-

cussion in Part II elucidated that the lack of spatial information poses a problem in estimating the abundance of molecules. Thus, to anchor the chemistry in this earliest stage of star formation, the spatial dependence of the chemistry must be considered.

A direct extension of the spectral analyses presented in this dissertation is to conduct a morphological investigation on TMC-1. Future interferometric observations are paramount to disentangling the detailed distribution of the underlying heterogeneous substructures inside TMC-1. While single-dish mosaic maps have explored the large-scale structures toward this source (Langston & Turner, 2007; Dobashi et al., 2019), TMC-1 CP has been the subject of virtually no attempts at high-resolution mapping, despite the fact that the CCS emission images toward other cores of the TMC complex obtained with EVLA indicated the existence of compact substructures (Roy et al., 2011).

7.2.2 From Molecular Clouds to the Solar System

Despite being the earliest stages of stellar and planetary formation, the complex molecular inventory of interstellar molecular clouds exhibits a great degree of similarity with those of comets and meteorites, particularly in terms of the large organic molecules relevant to life. In particular, methyl formate ($HCOOCH_3$), ethylene glycol ($HOCH_2CH_2OH$), ethanol (CH_3CH_2OH), glycolaldehyde (CH_2OHCHO), and formamide (NH_2CHO) have been detected toward both interstellar molecular clouds and comets (e.g. Zuckerman et al., 1975; Hollis et al., 2002; Crovisier et al., 2004; Biver et al., 2015). These species contain the same functional groups as the biotic building blocks of sugars, lipids, proteins, and other bio-macromolecules.

While molecules might be destroyed and undergo chemical evolutionary processes along with star-formation, the chemical ingredients in the dense molecular clouds, particularly the biologically related organic molecules, might survive during the voyage

of planetary assembly. These molecular species can enter the planetary system either as fresh streams of materials supplied from the interstellar medium or by residing in primitive meteorites that will eventually be incorporated into planets (Ehrenfreund & Charnley, 2000; Hsieh et al., 2020). In particular, studies enabled by the Rosetta Mission revealed that the comet 67P/C-G may have an origin in presolar clouds (Rubin et al., 2020). Hence, the chemistry in dense molecular clouds gives us clues to the origin of biological molecules in the Solar system.

There are a number of connections between interstellar and cometary chemistry, such as the overall bulk elemental budget and molecular contents. With the refined elemental ratios and the expanded molecular inventory in cold interstellar molecular clouds revealed by this dissertation, a detailed comparison of these properties with those in cometary particles and chondrites in the future will provide crucial information for examining the interstellar-heritage scenario. This line of research, namely tracing the full life cycle of the organics along the path from interstellar clouds to comets and meteorites, is essential to completing the picture of the origins and evolution of biotic chemical complexity.

Bibliography

Acharyya, K., & Herbst, E. 2017, Astrophysical Journal, 850, 105, doi: 10.3847/1538-4357/aa937e

Agúndez, M., & Wakelam, V. 2013, Chemical Reviews, 113, 8710, doi: 10.1021/cr4001176

Apponi, A. J., Halfen, D. T., Ziurys, L. M., et al. 2006, Astrophysical Journal, Letters, 643, L29, doi: 10.1086/504979

Araya, E., Hofner, P., Kurtz, S., Bronfman, L., & DeDeo, S. 2005, Astrophysical Journal, Supplement, 157, 279, doi: 10.1086/427187

Argon, A. L., Reid, M. J., & Menten, K. M. 2000, Astrophysical Journal, Supplement, 129, 159, doi: 10.1086/313406

Armijos-Abendaño, J., Banda-Barragán, W. E., Martín-Pintado, J., et al. 2020, Monthly Notices of the RAS, 499, 4918, doi: 10.1093/mnras/staa3119

Asplund, M., Grevesse, N., & Sauval, A. J. 2005, in Astronomical Society of the Pacific Conference Series, Vol. 336, Cosmic Abundances as Records of Stellar Evolution and Nucleosynthesis, ed. I. Barnes, Thomas G. & F. N. Bash, 25

Balucani, N., Ceccarelli, C., & Taquet, V. 2015, Monthly Notices of the RAS, 449, L16, doi: 10.1093/mnrasl/slv009

Batrla, W., Matthews, H. E., Menten, K. M., & Walmsley, C. M. 1987, Nature, 326, 49, doi: 10.1038/326049a0

Baudry, A., Forster, J. R., & Welch, W. J. 1974, Astronomy and Astrophysics, 36, 217

Bell, M. B., Watson, J. K. G., Feldman, P. A., & Travers, M. J. 1998, Astrophysical Journal, 508, 286, doi: 10.1086/306405

Belloche, A., Garrod, R. T., Müller, H. S. P., & Menten, K. M. 2014, Science, 345, 1584, doi: 10.1126/science.1256678

Belloche, A., Garrod, R. T., Müller, H. S. P., et al. 2019, Astronomy and Astrophysics, 628, A10, doi: 10.1051/0004-6361/201935428

Belloche, A., Menten, K. M., Comito, C., et al. 2008, Astronomy and Astrophysics, 482, 179, doi: 10.1051/0004-6361:20079203

Belloche, A., Müller, H. S. P., Garrod, R. T., & Menten, K. M. 2016, Astronomy and Astrophysics, 587, A91, doi: 10.1051/0004-6361/201527268

Belloche, A., Müller, H. S. P., Menten, K. M., Schilke, P., & Comito, C. 2013, Astronomy and Astrophysics, 559, A47, doi: 10.1051/0004-6361/201321096

Beltrán, M. T., Codella, C., Viti, S., Neri, R., & Cesaroni, R. 2009, Astrophysical Journal, Letters, 690, L93, doi: 10.1088/0004-637X/690/2/L93

Bennett, C. J., & Kaiser, R. I. 2007, Astrophysical Journal, 660, 1289, doi: 10.1086/513267

Beuther, H., Walsh, A. J., Thorwirth, S., et al. 2008, Astronomy and Astrophysics, 481, 169, doi: 10.1051/0004-6361:20079014

Bianchi, E., Chandler, C. J., Ceccarelli, C., et al. 2020, Monthly Notices of the RAS, 498, L87, doi: 10.1093/mnrasl/slaa130

Biver, N., Bockelée-Morvan, D., Moreno, R., et al. 2015, Science Advances, 1, 1500863, doi: 10.1126/sciadv.1500863

Blake, G. A., Sutton, E. C., Masson, C. R., & Phillips, T. G. 1987, Astrophysical Journal, 315, 621, doi: 10.1086/165165

Bøgelund, E. G., McGuire, B. A., Hogerheijde, M. R., van Dishoeck, E. F., & Ligterink, N. F. W. 2019, Astronomy and Astrophysics, 624, A82, doi: 10.1051/0004-6361/201833676

Bøgelund, E. G., McGuire, B. A., Ligterink, N. F. W., et al. 2018, Astronomy and Astrophysics, 615, A88, doi: 10.1051/0004-6361/201832757

Bonfand, M., Belloche, A., Menten, K. M., Garrod, R. T., & Müller, H. S. P. 2017, Astronomy and Astrophysics, 604, A60, doi: 10.1051/0004-6361/201730648

Botschwina, P., Heyl, Ä., Chen, W., et al. 1998, Journal of Chemical Physics, 109, 3108, doi: 10.1063/1.476515

Botschwina, P., Horn, M., FlÃŒgge, J., & Seeger, S. 1993, J. Chem. Soc., Faraday Trans., 89, 2219, doi: 10.1039/FT9938902219

Breen, S. L., Contreras, Y., Dawson, J. R., et al. 2019, Monthly Notices of the RAS, 484, 5072, doi: 10.1093/mnras/stz192

Brogan, C. L., Hunter, T. R., Cyganowski, C. J., et al. 2016, Astrophysical Journal, 832, 187, doi: 10.3847/0004-637X/832/2/187

—. 2018, Astrophysical Journal, 866, 87, doi: 10.3847/1538-4357/aae151

Brogan, C. L., Hunter, T. R., Towner, A. P. M., et al. 2019, Astrophysical Journal, Letters, 881, L39, doi: 10.3847/2041-8213/ab2f8a

Broten, N. W., Oka, T., Avery, L. W., MacLeod, J. M., & Kroto, H. W. 1978, Astrophysical Journal, Letters, 223, L105, doi: 10.1086/182739

Brouillet, N., Despois, D., Lu, X. H., et al. 2015, Astronomy and Astrophysics, 576, A129, doi: 10.1051/0004-6361/201424588

Brouillet, N., Despois, D., Baudry, A., et al. 2013, Astronomy and Astrophysics, 550, A46, doi: 10.1051/0004-6361/201219983

Brown, R. D. 1977, Nature, 270, 39, doi: 10.1038/270039a0

Brown, R. D., Burden, F. R., & Cuno, A. 1989, Astrophysical Journal, 347, 855, doi: 10.1086/168175

Brown, R. D., Crofts, J. G., Gardner, F. F., et al. 1975, Astrophysical Journal, Letters, 197, L29, doi: 10.1086/181769

Brown, R. D., Dyall, K. G., Elmes, P. S., Godfrey, P. D., & McNaughton, D. 1988, Journal of the American Chemical Society, 110, 789, doi: 10.1021/ja00211a018

Burke, D. J., Puletti, F., Brown, W. A., et al. 2015, Monthly Notices of the RAS, 447, 1444, doi: 10.1093/mnras/stu2490

Burkhardt, A. M., Herbst, E., Kalenskii, S. V., et al. 2018, Monthly Notices of the RAS, 474, 5068, doi: 10.1093/mnras/stx2972

Burkhardt, A. M., Loomis, R. A., Shingledecker, C. N., et al. 2021, Nature Astronomy, 5, 181, doi: 10.1038/s41550-020-01253-4

Butler, R. A. H., De Lucia, F. C., Petkie, D. T., et al. 2001, Astrophysical Journal, Supplement, 134, 319, doi: 10.1086/320859

Cabezas, C., Agúndez, M., Marcelino, N., et al. 2021, Astronomy and Astrophysics, 654, L9, doi: 10.1051/0004-6361/202142156

Calcutt, H., Viti, S., Codella, C., et al. 2014, Monthly Notices of the RAS, 443, 3157, doi: 10.1093/mnras/stu1363

Calcutt, H., Fiechter, M. R., Willis, E. R., et al. 2018, Astronomy and Astrophysics, 617, A95, doi: 10.1051/0004-6361/201833140

Carroll, P. B., Drouin, B. J., & Widicus Weaver, S. L. 2010, Astrophysical Journal, 723, 845, doi: 10.1088/0004-637X/723/1/845

Carroll, P. B., McGuire, B. A., Blake, G. A., et al. 2015, Astrophysical Journal, 799, 15, doi: 10.1088/0004-637X/799/1/15

Carvajal, M., Willaert, F., Demaison, J., & Kleiner, I. 2007, Journal of Molecular Spectroscopy, 246, 158, doi: 10.1016/j.jms.2007.08.009

Caswell, J. L. 1996, Monthly Notices of the RAS, 283, 606, doi: 10.1093/mnras/283.2.606

Caswell, J. L., Fuller, G. A., Green, J. A., et al. 2010, Monthly Notices of the RAS, 404, 1029, doi: 10.1111/j.1365-2966.2010.16339.x

Cazaux, S., Tielens, A. G. G. M., Ceccarelli, C., et al. 2003, Astrophysical Journal, 593, L51, doi: 10.1086/378038

Cernicharo, J., Cabezas, C., Endo, Y., et al. 2021a, Astronomy and Astrophysics, 646, L3, doi: 10.1051/0004-6361/202040013

Cernicharo, J., Velilla-Prieto, L., Agúndez, M., et al. 2019, Astronomy and Astrophysics, 627, L4, doi: 10.1051/0004-6361/201936040

Cernicharo, J., Cabezas, C., Agúndez, M., et al. 2021b, Astronomy and Astrophysics, 648, L3, doi: 10.1051/0004-6361/202140642

Chen, X., Sobolev, A. M., Ren, Z.-Y., et al. 2020, Nature Astronomy, 4, 1170, doi: 10.1038/s41550-020-1144-x

Chitarra, O., Martin-Drumel, M.-A., Gans, B., et al. 2020, Astronomy and Astrophysics, 644, A123, doi: 10.1051/0004-6361/202039071

Chuang, K. J., Fedoseev, G., Ioppolo, S., van Dishoeck, E. F., & Linnartz, H. 2016, Monthly Notices of the RAS, 455, 1702, doi: 10.1093/mnras/stv2288

Combes, F., & Wiklind, T. 1995, Astronomy and Astrophysics, 303, L61

Condon, J. J., & Ransom, S. M. 2016, Essential Radio Astronomy (Princeton University Press)

Contreras, Y., Sanhueza, P., Jackson, J. M., et al. 2018, Astrophysical Journal, 861, 14, doi: 10.3847/1538-4357/aac2ec

Corby, J. F., McGuire, B. A., Herbst, E., & Remijan, A. J. 2018, Astronomy and Astrophysics, 610, A10, doi: 10.1051/0004-6361/201730988

Corby, J. F., Jones, P. A., Cunningham, M. R., et al. 2015, Monthly Notices of the RAS, 452, 3969, doi: 10.1093/mnras/stv1494

Coutens, A., Rawlings, J. M. C., Viti, S., & Williams, D. A. 2017, Monthly Notices of the RAS, 467, 737, doi: 10.1093/mnras/stx119

Cragg, D. M., Sobolev, A. M., & Godfrey, P. D. 2002, Monthly Notices of the RAS, 331, 521, doi: 10.1046/j.1365-8711.2002.05226.x

—. 2005, Monthly Notices of the RAS, 360, 533, doi: 10.1111/j.1365-2966.2005.09077.x

Crovisier, J., Bockelée-Morvan, D., Biver, N., et al. 2004, Astronomy and Astrophysics, 418, L35, doi: 10.1051/0004-6361:20040116

Cummins, S. E., Linke, R. A., & Thaddeus, P. 1986, Astrophysical Journal, Supplement, 60, 819, doi: 10.1086/191102

Cyganowski, C. J., Brogan, C. L., Hunter, T. R., & Churchwell, E. 2009, Astrophysical Journal, 702, 1615, doi: 10.1088/0004-637X/702/2/1615

Cyganowski, C. J., Brogan, C. L., Hunter, T. R., et al. 2012, Astrophysical Journal, Letters, 760, L20, doi: 10.1088/2041-8205/760/2/L20

Daly, A. M., Bermúdez, C., López, A., et al. 2013, Astrophysical Journal, 768, 81, doi: 10.1088/0004-637X/768/1/81

Demyk, K., Wlodarczak, G., & Carvajal, M. 2008, Astronomy and Astrophysics, 489, 589, doi: 10.1051/0004-6361:200809354

Dobashi, K., Shimoikura, T., Nakamura, F., et al. 2018, Astrophysical Journal, 864, 82, doi: 10.3847/1538-4357/aad62f

Dobashi, K., Shimoikura, T., Ochiai, T., et al. 2019, Astrophysical Journal, 879, 88, doi: 10.3847/1538-4357/ab25f0

Ehrenfreund, P., & Charnley, S. B. 2000, Annual Review of Astron and Astrophys, 38, 427, doi: 10.1146/annurev.astro.38.1.427

El-Abd, S. J., Brogan, C. L., Hunter, T. R., et al. 2019, Astrophysical Journal, 883, 129, doi: 10.3847/1538-4357/ab3646

Elitzur, M., & Fuqua, J. B. 1989, Astrophysical Journal, Letters, 347, L35, doi: 10.1086/185601

Ellingsen, S. P. 2006, Astrophysical Journal, 638, 241, doi: 10.1086/498673

Etxaluze, M., Goicoechea, J. R., Cernicharo, J., et al. 2013, Astronomy and Astrophysics, 556, A137, doi: 10.1051/0004-6361/201321258

Fabricant, B., Krieger, D., & Muenter, J. S. 1977, Journal of Chemical Physics, 67, 1576, doi: 10.1063/1.434988

Faure, A., Lique, F., & Remijan, A. J. 2018, The Journal of Physical Chemistry Letters, 9, 3199, doi: 10.1021/acs.jpclett.8b01431

Faure, A., Remijan, A. J., Szalewicz, K., & Wiesenfeld, L. 2014, Astrophysical Journal, 783, 72, doi: 10.1088/0004-637X/783/2/72

Feng, S., Beuther, H., Zhang, Q., et al. 2016, Astrophysical Journal, 828, 100, doi: 10.3847/0004-637X/828/2/100

Fontani, F., Ceccarelli, C., Favre, C., et al. 2017, Astronomy and Astrophysics, 605, A57, doi: 10.1051/0004-6361/201730527

Forster, J. R., & Caswell, J. L. 1989, Astronomy and Astrophysics, 213, 339

Friberg, P., Hjalmarson, A., Guelin, M., & Irvine, W. M. 1980, Astrophysical Journal, Letters, 241, L99, doi: 10.1086/183369

Friedel, D. N., Snyder, L. E., Turner, B. E., & Remijan, A. 2004, Astrophysical Journal, 600, 234, doi: 10.1086/379765

Friesen, R. K., Di Francesco, J., Shirley, Y. L., & Myers, P. C. 2009, Astrophysical Journal, 697, 1457, doi: 10.1088/0004-637X/697/2/1457

Fuente, A., Navarro, D. G., Caselli, P., et al. 2019, Astronomy and Astrophysics, 624, A105, doi: 10.1051/0004-6361/201834654

Gargaud, M., Amils, R., Quintanilla, J. C., et al. 2011, Encyclopedia of Astrobiology (Springer Berlin Heidelberg), doi: 10.1007/978-3-642-11274-4

Garrod, R. T., & Herbst, E. 2006, Astronomy and Astrophysics, 457, 927, doi: 10.1051/0004-6361:20065560

Garrod, R. T., Widicus Weaver, S. L., & Herbst, E. 2008, Astrophysical Journal, 682, 283, doi: 10.1086/588035

Gaume, R. A., Claussen, M. J., de Pree, C. G., Goss, W. M., & Mehringer, D. M. 1995, Astrophysical Journal, 449, 663, doi: 10.1086/176087

Gensheimer, P. D. 1997, Astrophysical Journal, Letters, 479, L75, doi: 10.1086/310576

Geppert, W. D., Ehlerding, A., Hellberg, F., et al. 2004, Astrophysical Journal, 613, 1302, doi: 10.1086/422335

Gibb, A. G., Wyrowski, F., & Mundy, L. G. 2004, Astrophysical Journal, 616, 301, doi: 10.1086/424810

Gorski, M. D., Aalto, S., Mangum, J., et al. 2021, Astronomy and Astrophysics, 654, A110, doi: 10.1051/0004-6361/202141633

GOTHAM Collaboration. 2020, Spectral Stacking Data for Phase 1 Science Release of GOTHAM, 4.0, Harvard Dataverse, doi: 10.7910/DVN/PG7BHO

Graninger, D., Öberg, K. I., Qi, C., & Kastner, J. 2015, Astrophysical Journal, Letters, 807, L15, doi: 10.1088/2041-8205/807/1/L15

Graninger, D. M., Herbst, E., Öberg, K. I., & Vasyunin, A. I. 2014, Astrophysical Journal, 787, 74, doi: 10.1088/0004-637X/787/1/74

Gratier, P., Majumdar, L., Ohishi, M., et al. 2016, Astrophysical Journal, Supplement, 225, 25, doi: 10.3847/0067-0049/225/2/25

Gratier, P., Pety, J., Guzmán, V., et al. 2013, Astronomy and Astrophysics, 557, A101, doi: 10.1051/0004-6361/201321031

Gronowski, M., & Kołos, R. 2006, Chemical Physics Letters, 428, 245, doi: 10.1016/j.cplett.2006.07.041

Guarnieri, A., Hinze, R., Krüger, M., et al. 1992, Journal of Molecular Spectroscopy, 156, 39, doi: 10.1016/0022-2852(92)90091-2

Hacar, A., Bosman, A. D., & van Dishoeck, E. F. 2020, Astronomy and Astrophysics, 635, A4, doi: 10.1051/0004-6361/201936516

Halfen, D. T., Apponi, A. J., Woolf, N., Polt, R., & Ziurys, L. M. 2006, Astrophysical Journal, 639, 237, doi: 10.1086/499225

Halfen, D. T., Ilyushin, V. V., & Ziurys, L. M. 2015, Astrophysical Journal, Letters, 812, L5, doi: 10.1088/2041-8205/812/1/L5

Hatchell, J., Fuller, G. A., & Millar, T. J. 2001, Astronomy and Astrophysics, 372, 281, doi: 10.1051/0004-6361:20010468

Haykal, I., Margulès, L., Huet, T. R., et al. 2013, Astrophysical Journal, 777, 120, doi: 10.1088/0004-637X/777/2/120

Herbst, E., Terzieva, R., & Talbi, D. 2000, Monthly Notices of the RAS, 311, 869, doi: 10.1046/j.1365-8711.2000.03103.x

Herbst, E., & van Dishoeck, E. F. 2009, Annual Review of Astron and Astrophys, 47, 427, doi: 10.1146/annurev-astro-082708-101654

Hincelin, U., Wakelam, V., Hersant, F., et al. 2011, Astronomy and Astrophysics, 530, A61, doi: 10.1051/0004-6361/201016328

Hirota, T., Yamamoto, S., Mikami, H., & Ohishi, M. 1998, Astrophysical Journal, 503, 717, doi: 10.1086/306032

Hollis, J. M., Jewell, P. R., Lovas, F. J., & Remijan, A. 2004a, Astrophysical Journal, Letters, 613, L45, doi: 10.1086/424927

Hollis, J. M., Jewell, P. R., Lovas, F. J., Remijan, A., & Møllendal, H. 2004b, Astrophysical Journal, Letters, 610, L21, doi: 10.1086/423200

Hollis, J. M., Lovas, F. J., & Jewell, P. R. 2000, Astrophysical Journal, Letters, 540, L107, doi: 10.1086/312881

Hollis, J. M., Lovas, F. J., Jewell, P. R., & Coudert, L. H. 2002, Astrophysical Journal, Letters, 571, L59, doi: 10.1086/341148

Hollis, J. M., Lovas, F. J., Remijan, A. J., et al. 2006, Astrophysical Journal, Letters, 643, L25, doi: 10.1086/505110

Hollis, J. M., Vogel, S. N., Snyder, L. E., Jewell, P. R., & Lovas, F. J. 2001, Astrophysical Journal, Letters, 554, L81, doi: 10.1086/320930

Howk, J. C., Sembach, K. R., & Savage, B. D. 2006, Astrophysical Journal, 637, 333, doi: 10.1086/497352

Hsieh, C.-H., Lai, S.-P., Cheong, P.-I., et al. 2020, Astrophysical Journal, 894, 23, doi: 10.3847/1538-4357/ab7b69

Hung, T., Liu, S.-Y., Su, Y.-N., et al. 2019, Astrophysical Journal, 872, 61, doi: 10.3847/1538-4357/aafc23

Hunter, T. R., Brogan, C. L., Megeath, S. T., et al. 2006, Astrophysical Journal, 649, 888, doi: 10.1086/505965

Hunter, T. R., Zhang, Q., & Sridharan, T. K. 2004, Astrophysical Journal, 606, 929, doi: 10.1086/383181

Hunter, T. R., Brogan, C. L., MacLeod, G., et al. 2017, Astrophysical Journal, 837, L29, doi: 10.3847/2041-8213/aa5d0e

Hunter, T. R., Brogan, C. L., Bartkiewicz, A., et al. 2018, in Astronomical Society of the Pacific Conference Series, Vol. 517, Science with a Next Generation Very Large Array, ed. E. Murphy, 321

Ilyushin, V. V., Alekseev, E. A., Dyubko, S. F., & Kleiner, I. 2003, JMoSp, 220, 170, doi: 10.1016/S0022-2852(03)00073-0

Ilyushin, V. V., Endres, C. P., Lewen, F., Schlemmer, S., & Drouin, B. J. 2013, JMoSp, 290, 31, doi: 10.1016/j.jms.2013.06.005

Ilyushin, V. V., Alekseev, E. A., Dyubko, S. F., et al. 2001, JMoSp, 205, 286, doi: 10.1006/jmsp.2000.8270

Irvine, W. M., & Schloerb, F. P. 1984, Astrophysical Journal, 282, 516, doi: 10.1086/162229

Irvine, W. M., Friberg, P., Kaifu, N., et al. 1989, Astrophysical Journal, 342, 871, doi: 10.1086/167643

Jørgensen, J. K., van der Wiel, M. H. D., Coutens, A., et al. 2016, Astronomy and Astrophysics, 595, A117, doi: 10.1051/0004-6361/201628648

Kaifu, N., Ohishi, M., Kawaguchi, K., et al. 2004, Publications of the ASJ, 56, 69, doi: 10.1093/pasj/56.1.69

Karton, A., & Talbi, D. 2014, Chemical Physics, 436, 22, doi: 10.1016/j.chemphys.2014.03.010

Kawaguchi, K., Kasai, Y., Ishikawa, S.-I., & Kaifu, N. 1995, Publications of the ASJ, 47, 853

Kawaguchi, K., Ohishi, M., Ishikawa, S.-I., & Kaifu, N. 1992, Astrophysical Journal, Letters, 386, L51, doi: 10.1086/186290

Kobayashi, K., Ogata, K., Tsunekawa, S., & Takano, S. 2007, Astrophysical Journal, Letters, 657, L17, doi: 10.1086/512977

Kruger, M., Stahl, W., & Dreizler, H. 1993, Journal of Molecular Spectroscopy, 158, 298, doi: 10.1006/jmsp.1993.1074

Laas, J. C., Garrod, R. T., Herbst, E., & Widicus Weaver, S. L. 2011, Astrophysical Journal, 728, 71, doi: 10.1088/0004-637X/728/1/71

Langston, G., & Turner, B. 2007, Astrophysical Journal, 658, 455, doi: 10.1086/511332

Larsson, M., Geppert, W. D., & Nyman, G. 2012, Reports on Progress in Physics, 75, 066901, doi: 10.1088/0034-4885/75/6/066901

Lattelais, M., Pauzat, F., Ellinger, Y., & Ceccarelli, C. 2009, Astrophysical Journal, Letters, 696, L133, doi: 10.1088/0004-637X/696/2/L133

—. 2010, Astronomy and Astrophysics, 519, A30, doi: 10.1051/0004-6361/200913869

Lattelais, M., Pauzat, F., Pilmé, J., Ellinger, Y., & Ceccarelli, C. 2011, Astronomy and Astrophysics, 532, A39, doi: 10.1051/0004-6361/201016039

Lee, C. W., Cho, S.-H., & Lee, S.-M. 2001, Astrophysical Journal, 551, 333, doi: 10.1086/320062

Liechti, S., & Wilson, T. L. 1996, Astronomy and Astrophysics, 314, 615

Ligterink, N. F. W., El-Abd, S. J., Brogan, C. L., et al. 2020, Astrophysical Journal, 901, 37, doi: 10.3847/1538-4357/abad38

Linnartz, H., Ioppolo, S., & Fedoseev, G. 2015, International Reviews in Physical Chemistry, 34, 205, doi: 10.1080/0144235X.2015.1046679

Little, L. T., MacDonald, G. H., Riley, P. W., & Matheson, D. N. 1978, Monthly Notices of the RAS, 183, 45P, doi: 10.1093/mnras/183.1.45P

Liu, S.-Y., Girart, J. M., Remijan, A., & Snyder, L. E. 2002, Astrophysical Journal, 576, 255, doi: 10.1086/341620

Liu, S.-Y., Mehringer, D. M., & Snyder, L. E. 2001, Astrophysical Journal, 552, 654, doi: 10.1086/320563

Loison, J.-C., Wakelam, V., & Hickson, K. M. 2014a, Monthly Notices of the RAS, 443, 398, doi: 10.1093/mnras/stu1089

Loison, J.-C., Wakelam, V., Hickson, K. M., Bergeat, A., & Mereau, R. 2014b, Monthly Notices of the RAS, 437, 930, doi: 10.1093/mnras/stt1956

Loomis, R. A., McGuire, B. A., Shingledecker, C., et al. 2015, Astrophysical Journal, 799, 34, doi: 10.1088/0004-637X/799/1/34

Loomis, R. A., Zaleski, D. P., Steber, A. L., et al. 2013, Astrophysical Journal, Letters, 765, L9, doi: 10.1088/2041-8205/765/1/L9

Loomis, R. A., Burkhardt, A. M., Shingledecker, C. N., et al. 2021, Nature Astronomy, 5, 188, doi: 10.1038/s41550-020-01261-4

López, A., Tercero, B., Kisiel, Z., et al. 2014, Astronomy and Astrophysics, 572, A44, doi: 10.1051/0004-6361/201423622

Lorand, J.-P., Labidi, J., Rollion-Bard, C., et al. 2020, Meteoritics and Planetary Science, 55, 2097, doi: 10.1111/maps.13564

Lu, X., Li, S., Ginsburg, A., et al. 2021, Astrophysical Journal, 909, 177, doi: 10.3847/1538-4357/abde3c

Luo, G., Feng, S., Li, D., et al. 2019, Astrophysical Journal, 885, 82, doi: 10.3847/1538-4357/ab45ef

Mangum, J. G., & Shirley, Y. L. 2015, Publications of the ASP, 127, 266, doi: 10.1086/680323

Margulès, L., McGuire, B. A., Evans, C. J., et al. 2020, Astronomy and Astrophysics, 642, A206, doi: 10.1051/0004-6361/202038230

Margulès, L., Tercero, B., Guillemin, J. C., Motiyenko, R. A., & Cernicharo, J. 2018, Astronomy and Astrophysics, 610, A44, doi: 10.1051/0004-6361/201731515

Maris, A., Calabrese, C., Favero, L. B., et al. 2019, ACS Earth and Space Chemistry, 3, 1537, doi: 10.1021/acsearthspacechem.9b00084

McCarthy, M. C., Lee, K. L. K., Loomis, R. A., et al. 2021, Nature Astronomy, 5, 176, doi: 10.1038/s41550-020-01213-y

McCutcheon, W. H., Sandell, G., Matthews, H. E., et al. 2000, Monthly Notices of the RAS, 316, 152, doi: 10.1046/j.1365-8711.2000.03487.x

McElroy, D., Walsh, C., Markwick, A. J., et al. 2013, Astronomy and Astrophysics, 550, A36, doi: 10.1051/0004-6361/201220465

McGuire, B., Loomis, R. A., Charness, C., et al. 2013, in American Astronomical Society Meeting Abstracts, Vol. 221, American Astronomical Society Meeting Abstracts #221, 352.09

McGuire, B. A. 2018, Astrophysical Journal, Supplement, 239, 17, doi: 10.3847/1538-4365/aae5d2

—. 2021, arXiv e-prints, arXiv:2109.13848. https://arxiv.org/abs/2109.13848

McGuire, B. A., Burkhardt, A. M., Kalenskii, S., et al. 2018a, Science, 359, 202, doi: 10.1126/science.aao4890

McGuire, B. A., Burkhardt, A. M., Shingledecker, C. N., et al. 2017a, Astrophysical Journal, Letters, 843, L28, doi: 10.3847/2041-8213/aa7ca3

McGuire, B. A., Carroll, P. B., Loomis, R. A., et al. 2016, Science, 352, 1449, doi: 10.1126/science.aae0328

McGuire, B. A., Loomis, R. A., Charness, C. M., et al. 2012, Astrophysical Journal, Letters, 758, L33, doi: 10.1088/2041-8205/758/2/L33

McGuire, B. A., Shingledecker, C. N., Willis, E. R., et al. 2017b, Astrophysical Journal, 851, L46, doi: 10.3847/2041-8213/aaa0c3

McGuire, B. A., Brogan, C. L., Hunter, T. R., et al. 2018b, Astrophysical Journal, Letters, 863, L35, doi: 10.3847/2041-8213/aad7bb

McGuire, B. A., Shingledecker, C. N., Willis, E. R., et al. 2019, Astrophysical Journal, 883, 201, doi: 10.3847/1538-4357/ab3b01

McGuire, B. A., Burkhardt, A. M., Loomis, R. A., et al. 2020, Astrophysical Journal, Letters, 900, L10, doi: 10.3847/2041-8213/aba632

McGuire, B. A., Loomis, R. A., Burkhardt, A. M., et al. 2021, Science, 371, 1265, doi: 10.1126/science.abb7535

McMullin, J. P., Waters, B., Schiebel, D., Young, W., & Golap, K. 2007, in Astronomical Society of the Pacific Conference Series, Vol. 376, Astronomical Data Analysis Software and Systems XVI, ed. R. A. Shaw, F. Hill, & D. J. Bell, 127

Mehringer, D. M., & Menten, K. M. 1997, Astrophysical Journal, 474, 346, doi: 10.1086/303454

Mehringer, D. M., Snyder, L. E., Miao, Y., & Lovas, F. J. 1997, Astrophysical Journal, 480, L71, doi: 10.1086/310612

Melosso, M., Dore, L., Tamassia, F., et al. 2020, Journal of Physical Chemistry A, 124, 240, doi: 10.1021/acs.jpca.9b10803

Menten, K. M., Wyrowski, F., Keller, D., & Kamiński, T. 2018, Astronomy and Astrophysics, 613, A49, doi: 10.1051/0004-6361/201732296

Miao, Y., & Snyder, L. E. 1997, Astrophysical Journal, Letters, 480, L67, doi: 10.1086/310624

Millar, T. J., Ellder, J., Hjalmarson, A., & Olofsson, H. 1987, Astronomy and Astrophysics, 182, 143

Minier, V., Burton, M. G., Hill, T., et al. 2005, Astronomy and Astrophysics, 429, 945, doi: 10.1051/0004-6361:20041137

Minier, V., Conway, J. E., & Booth, R. S. 2001, Astronomy and Astrophysics, 369, 278, doi: 10.1051/0004-6361:20010124

Morata, O., Girart, J. M., & Estalella, R. 2005, Astronomy and Astrophysics, 435, 113, doi: 10.1051/0004-6361:20041829

Moscadelli, L., Sánchez-Monge, Á., Goddi, C., et al. 2016, Astronomy and Astrophysics, 585, A71, doi: 10.1051/0004-6361/201526238

Mottl, M., Glazer, B., Kaiser, R., & Meech, K. 2007, Chemie der Erde / Geochemistry, 67, 253, doi: 10.1016/j.chemer.2007.09.002

Müller, H. S. P., Schlöder, F., Stutzki, J., & Winnewisser, G. 2005, Journal of Molecular Structure, 742, 215, doi: 10.1016/j.molstruc.2005.01.027

Müller, H. S. P., Walters, A., Wehres, N., et al. 2016, Astronomy and Astrophysics, 595, A87, doi: 10.1051/0004-6361/201629309

Neill, J. L., Muckle, M. T., Zaleski, D. P., et al. 2012, Astrophysical Journal, 755, 153, doi: 10.1088/0004-637X/755/2/153

Nutter, D., Kirk, J. M., Stamatellos, D., & Ward-Thompson, D. 2008, Monthly Notices of the RAS, 384, 755, doi: 10.1111/j.1365-2966.2007.12750.x

Öberg, K. I., Bottinelli, S., Jørgensen, J. K., & van Dishoeck, E. F. 2010, Astrophysical Journal, 716, 825, doi: 10.1088/0004-637X/716/1/825

Öberg, K. I., Guzmán, V. V., Furuya, K., et al. 2015, Nature, 520, 198, doi: 10.1038/nature14276

Oesterling, L. C., Albert, S., De Lucia, F. C., Sastry, K. V. L. N., & Herbst, E. 1999, Astrophysical Journal, 521, 255, doi: 10.1086/307543

Ogata, K., Odashima, H., Takagi, K., & Tsunekawa, S. 2004, Journal of Molecular Spectroscopy, 225, 14, doi: 10.1016/j.jms.2004.02.004

Osamura, Y., Fukuzawa, K., Terzieva, R., & Herbst, E. 1999, Astrophysical Journal, 519, 697, doi: 10.1086/307406

Peng, T. C., Despois, D., Brouillet, N., et al. 2013, Astronomy and Astrophysics, 554, A78, doi: 10.1051/0004-6361/201220891

Peng, Y., Qin, S.-L., Schilke, P., et al. 2017, Astrophysical Journal, 837, 49, doi: 10.3847/1538-4357/aa5c81

Pickett, H. M., Poynter, R. L., Cohen, E. A., et al. 1998, Journal of Quantitiative Spectroscopy and Radiative Trasfer, 60, 883, doi: 10.1016/S0022-4073(98)00091-0

Plambeck, R. L., & Menten, K. M. 1990, Astrophysical Journal, 364, 555, doi: 10.1086/169437

Plambeck, R. L., & Wright, M. C. H. 1988, Astrophysical Journal, Letters, 330, L61, doi: 10.1086/185205

Pols, S., Schwörer, A., Schilke, P., et al. 2018, Astronomy and Astrophysics, 614, A123, doi: 10.1051/0004-6361/201732498

Pratap, P., & Menten, K. 1993, Interferometric observations of 95 GHz methanol masers., Vol. 412 (Springer Berlin Heidelberg), 211–214, doi: 10.1007/3-540-56343-1_245

Puletti, F., Malloci, G., Mulas, G., & Cecchi-Pestellini, C. 2010, Monthly Notices of the RAS, 402, 1667, doi: 10.1111/j.1365-2966.2009.16053.x

Qiao, H., Li, J., Shen, Z., Chen, X., & Zheng, X. 2014, Monthly Notices of the RAS, 441, 3137, doi: 10.1093/mnras/stu776

Qin, S. L., Schilke, P., Rolffs, R., et al. 2011, Astronomy and Astrophysics, 530, L9, doi: 10.1051/0004-6361/201116928

Quénard, D., Vastel, C., Ceccarelli, C., et al. 2017, Monthly Notices of the RAS, 470, 3194, doi: 10.1093/mnras/stx1373

Reid, M. J., Schneps, M. H., Moran, J. M., et al. 1988, Astrophysical Journal, 330, 809, doi: 10.1086/166514

Reid, M. J., Menten, K. M., Brunthaler, A., et al. 2014, Astrophysical Journal, 783, 130, doi: 10.1088/0004-637X/783/2/130

—. 2019, Astrophysical Journal, 885, 131, doi: 10.3847/1538-4357/ab4a11

Remijan, A., Snyder, L. E., Friedel, D. N., Liu, S. Y., & Shah, R. Y. 2003, Astrophysical Journal, 590, 314, doi: 10.1086/374890

Remijan, A., Snyder, L. E., Liu, S. Y., Mehringer, D., & Kuan, Y. J. 2002, Astrophysical Journal, 576, 264, doi: 10.1086/341627

Remijan, A. J., Hollis, J. M., Lovas, F. J., Plusquellic, D. F., & Jewell, P. R. 2005, Astrophysical Journal, 632, 333, doi: 10.1086/432908

Remijan, A. J., Snyder, L. E., McGuire, B. A., et al. 2014, Astrophysical Journal, 783, 77, doi: 10.1088/0004-637X/783/2/77

Requena-Torres, M. A., Martín-Pintado, J., Rodríguez-Franco, A., et al. 2006, Astronomy and Astrophysics, 455, 971, doi: 10.1051/0004-6361:20065190

Richards, A. M. S., Impellizzeri, C. M. V., Humphreys, E. M., et al. 2014, Astronomy and Astrophysics, 572, L9, doi: 10.1051/0004-6361/201425024

Roy, N., Datta, A., Momjian, E., & Sarma, A. P. 2011, Astrophysical Journal, Letters, 739, L4, doi: 10.1088/2041-8205/739/1/L4

Ruaud, M., Wakelam, V., & Hersant, F. 2016, Monthly Notices of the RAS, 459, 3756, doi: 10.1093/mnras/stw887

Rubin, M., Engrand, C., Snodgrass, C., et al. 2020, Space Science Reviews, 216, 102, doi: 10.1007/s11214-020-00718-2

Ruffle, D. P., Hartquist, T. W., Caselli, P., & Williams, D. A. 1999, Monthly Notices of the RAS, 306, 691, doi: 10.1046/j.1365-8711.1999.02562.x

Sakai, Y., Kobayashi, K., & Hirota, T. 2015, Astrophysical Journal, 803, 97, doi: 10.1088/0004-637X/803/2/97

Sánchez-Monge, Á., Schilke, P., Schmiedeke, A., et al. 2017, Astronomy and Astrophysics, 604, A6, doi: 10.1051/0004-6361/201730426

Sanna, A., Moscadelli, L., Cesaroni, R., et al. 2016, Astronomy and Astrophysics, 596, L2, doi: 10.1051/0004-6361/201629544

Schilke, P., Comito, C., Thorwirth, S., et al. 2006, Astronomy and Astrophysics, 454, L41, doi: 10.1051/0004-6361:20065398

Schilke, P., Walmsley, C. M., Pineau Des Forets, G., et al. 1992, Astronomy and Astrophysics, 256, 595

Schmiedeke, A., Schilke, P., Möller, T., et al. 2016, Astronomy and Astrophysics, 588, A143, doi: 10.1051/0004-6361/201527311

Shiao, Y. S. J., Looney, L. W., Remijan, A. J., Snyder, L. E., & Friedel, D. N. 2010, Astrophysical Journal, 716, 286, doi: 10.1088/0004-637X/716/1/286

Shingledecker, C. N., Lamberts, T., Laas, J. C., et al. 2020, Astrophysical Journal, 888, 52, doi: 10.3847/1538-4357/ab5360

Sinclair, M. W., Fourikis, N., Ribes, J. C., et al. 1973, Australian Journal of Physics, 26, 85, doi: 10.1071/PH730085

Skouteris, D., Balucani, N., Ceccarelli, C., et al. 2018, Astrophysical Journal, 854, 135, doi: 10.3847/1538-4357/aaa41e

Snyder, L. E., Kuan, Y. J., & Miao, Y. 1994, Where Is the Heavy Molecule Heimat in SgrB2?, Vol. 439 (Springer Berlin Heidelberg), 187, doi: 10.1007/3540586210_13

Snyder, L. E., Lovas, F. J., Hollis, J. M., et al. 2005, Astrophysical Journal, 619, 914, doi: 10.1086/426677

Sobolev, A. M., Cragg, D. M., & Godfrey, P. D. 1997, Astronomy and Astrophysics, 324, 211

Sobolev, A. M., & Deguchi, S. 1994, Astronomy and Astrophysics, 291, 569

Soma, T., Sakai, N., Watanabe, Y., & Yamamoto, S. 2018, Astrophysical Journal, 854, 116, doi: 10.3847/1538-4357/aaa70c

Stanton, J. F., Gauss, J., Cheng, L., et al. 2017, CFOUR, Coupled-Cluster techniques for Computational Chemistry, a quantum-chemical program package

Szymczak, M., Pillai, T., & Menten, K. M. 2005, Astronomy and Astrophysics, 434, 613, doi: 10.1051/0004-6361:20042437

Takagi, N., Fukuzawa, K., Osamura, Y., & Schaefer, Henry F., I. 1999, Astrophysical Journal, 525, 791, doi: 10.1086/307914

Takano, S., Masuda, A., Hirahara, Y., et al. 1998, Astronomy and Astrophysics, 329, 1156

Taniguchi, K., Ozeki, H., Saito, M., et al. 2016, Astrophysical Journal, 817, 147, doi: 10.3847/0004-637X/817/2/147

Tenenbaum, E. D., Dodd, J. L., Milam, S. N., Woolf, N. J., & Ziurys, L. M. 2010, Astrophysical Journal, Supplement, 190, 348, doi: 10.1088/0067-0049/190/2/348

Tennekes, P. P., Harju, J., Juvela, M., & Tóth, L. V. 2006, Astronomy and Astrophysics, 456, 1037, doi: 10.1051/0004-6361:20040294

Thiel, V., Belloche, A., Menten, K. M., Garrod, R. T., & Müller, H. S. P. 2017, Astronomy and Astrophysics, 605, L6, doi: 10.1051/0004-6361/201731495

Towner, A. P. M., Brogan, C. L., Hunter, T. R., et al. 2017, Astrophysical Journal, Supplement, 230, 22, doi: 10.3847/1538-4365/aa73d8

Townes, C. H., & Schawlow, A. L. 1975, Microwave spectroscopy. (Dover Publications)

Turner, B. E. 1991, Astrophysical Journal, Supplement, 76, 617, doi: 10.1086/191577

—. 2001, Astrophysical Journal, Supplement, 136, 579, doi: 10.1086/322536

Turner, B. E., Pirogov, L., & Minh, Y. C. 1997, Astrophysical Journal, 483, 235, doi: 10.1086/304228

van Dishoeck, E. F. 2018, IAU Symposium, 332, 3, doi: 10.1017/S1743921317011528

Vastel, C., Kawaguchi, K., Quénard, D., et al. 2018a, Monthly Notices of the RAS, 474, L76, doi: 10.1093/mnrasl/slx197

Vastel, C., Loison, J. C., Wakelam, V., & Lefloch, B. 2019, Astronomy and Astrophysics, 625, A91, doi: 10.1051/0004-6361/201935010

Vastel, C., Quénard, D., Le Gal, R., et al. 2018b, Monthly Notices of the RAS, 478, 5514, doi: 10.1093/mnras/sty1336

Vidal, T. H. G., Loison, J.-C., Jaziri, A. Y., et al. 2017, Monthly Notices of the RAS, 469, 435, doi: 10.1093/mnras/stx828

Vigren, E., Semaniak, J., Hamberg, M., et al. 2012, Planetary Space Science, 60, 102, doi: 10.1016/j.pss.2011.03.001

Voronkov, M. A., Brooks, K. J., Sobolev, A. M., et al. 2006, Monthly Notices of the RAS, 373, 411, doi: 10.1111/j.1365-2966.2006.11047.x

Voronkov, M. A., Caswell, J. L., Ellingsen, S. P., Green, J. A., & Breen, S. L. 2014, Monthly Notices of the RAS, 439, 2584, doi: 10.1093/mnras/stu116

Wächtershäuser, G. 2000, Science, 289, 1307, doi: 10.1126/science.289.5483.1307

Wakelam, V., Herbst, E., Loison, J. C., et al. 2012, Astrophysical Journal, Supplement, 199, 21, doi: 10.1088/0067-0049/199/1/21

Wakelam, V., Loison, J. C., Herbst, E., et al. 2015, Astrophysical Journal, Supplement, 217, 20, doi: 10.1088/0067-0049/217/2/20

Walsh, A. J., Macdonald, G. H., Alvey, N. D. S., Burton, M. G., & Lee, J. K. 2003, Astronomy and Astrophysics, 410, 597, doi: 10.1051/0004-6361:20031191

Walsh, A. J., Purcell, C. R., Longmore, S. N., et al. 2014, Monthly Notices of the RAS, 442, 2240, doi: 10.1093/mnras/stu989

Watanabe, N., & Kouchi, A. 2002, Astrophysical Journal, Letters, 571, L173, doi: 10.1086/341412

Widicus Weaver, S. L., Butler, R. A. H., Drouin, B. J., et al. 2005, Astrophysical Journal, Supplement, 158, 188, doi: 10.1086/429292

Williams, D. A., & Viti, S. 2014, Observational Molecular Astronomy (Cambridge University Press)

Winnewisser, M., & Schäfer, E. 1980, Zeitschrift für Naturforschung A, 35, 483, doi: doi:10.1515/zna-1980-0503

Woods, P. M., Kelly, G., Viti, S., et al. 2012, Astrophysical Journal, 750, 19, doi: 10.1088/0004-637X/750/1/19

Woon, D. E., & Herbst, E. 2009, Astrophysical Journal, Supplement, 185, 273, doi: 10.1088/0067-0049/185/2/273

Xue, C., Remijan, A. J., Brogan, C. L., et al. 2019a, Astrophysical Journal, 882, 118, doi: 10.3847/1538-4357/ab32e0

Xue, C., Remijan, A. J., Burkhardt, A. M., & Herbst, E. 2019b, Astrophysical Journal, 871, 112, doi: 10.3847/1538-4357/aaf738

Xue, C., Willis, E. R., Loomis, R. A., et al. 2020, Astrophysical Journal, Letters, 900, L9, doi: 10.3847/2041-8213/aba631

Yang, W., Xu, Y., Chen, X., et al. 2017, Astrophysical Journal, Supplement, 231, 20, doi: 10.3847/1538-4365/aa6ff3

Yates, J. A., Cohen, R. J., & Hills, R. E. 1995, Monthly Notices of the RAS, 273, 529, doi: 10.1093/mnras/273.3.529

Zaleski, D. P., Seifert, N. A., Steber, A. L., et al. 2013, Astrophysical Journal, Letters, 765, L10, doi: 10.1088/2041-8205/765/1/L10

Zeng, S., Quénard, D., Jiménez-Serra, I., et al. 2019, Monthly Notices of the RAS, 484, L43, doi: 10.1093/mnrasl/slz002

Zernickel, A., Schilke, P., Schmiedeke, A., et al. 2012, Astronomy and Astrophysics, 546, A87, doi: 10.1051/0004-6361/201219803

Ziurys, L. M., Clemens, D. P., Saykally, R. J., Colvin, M., & Schaefer, H. F. 1984, Astrophysical Journal, 281, 219, doi: 10.1086/162091

Zou, L., Guillemin, J.-C., Motiyenko, R. A., & Margulès, L. 2021, Astronomy and Astrophysics, 649, A60, doi: 10.1051/0004-6361/202040142

Zuckerman, B., Turner, B. E., Johnson, D. R., et al. 1975, Astrophysical Journal, Letters, 196, L99, doi: 10.1086/181753